

Application of Passive Drag Reduction Techniques on a Scaled-Down Underwater Vehicle
by

Desiree Reholon Inojosa

A thesis submitted in partial fulfillment of the requirements for the degree of

Master of Science

Department of Mechanical Engineering
University of Alberta

© Desiree Reholon Inojosa, 2018

Abstract

Natural Resources Canada (NRCan) has been using an autonomous underwater vehicle (AUV) to map the vast Canadian Arctic seabed. The logistics of under-ice survey is currently complicated due to limited lifetime of lithium-ion batteries of AUVs. An AUV with longer endurance would allow exploration of a larger seafloor area from a single Arctic camp, reducing costs and advancing the rate of exploration. A 1:15 scaled-down model of NRCan AUV was designed and manufactured to test different passive drag reduction techniques with the goal of improving its endurance in future.

The developed scaled-down underwater vehicle has a modular design consisting of the front edge, central body, and aft body sections. The main component of the aft body is a replaceable cylinder of 0.190 m length (l), where the different drag reduction techniques are applied. The aft body module is mounted on a submersible s-beam load cell for direct measurement of the axial force (i.e., drag) on this module. The vertical forces of weight and buoyancy in the aft body have been balanced in order to avoid off-axis forces and momentums on the load cell.

Three passives drag reduction methods were studied, including: superhydrophobic surfaces (SHS), air injection, riblets, and also their combinations. The experiments were carried out in the high-speed water loop of the University of Alberta, over a Reynolds number (Re) range of 5.0×10^5 to 1.5×10^6 (based on the free-stream velocity of 0.9 to 3.3 m/s and model length of 0.508 m. The test section of this facility is equipped with transparent walls for visualization and is 0.25 m wide, 0.45 m high and 2.1 meters long.

For the study of an SHS with random texture, direct measurement of the drag force is complemented with the simultaneous use of shadow-based long-range microscopic particle tracking velocimetry (micro-PTV). The use of the shadowgraph technique over the body-of-revolution allowed the visualization of the air plastron and its characteristic over time and with increasing Re number. Consistent with previous investigations, the water movement over the surface enhanced the air depletion. The largest air thickness was observed at the lowest $Re = 5.0 \times 10^5$, which also showed a larger value of drag reduction. Conversely, a faster air depletion rate was observed at higher velocities. The depletion of air exposed the SHS microstructures and reduced the drag reduction. The direct measurement of the drag force resulted in a maximum drag reduction (DR) of 36% at the lowest $Re = 5.0 \times 10^5$, and gradually decreased with higher velocities to a 5.6% at $Re = 1.5 \times 10^6$. The magnitude of slip velocity was estimated at the top of peaks of the SHS texture, showing a larger slip velocity with increasing Re number.

The use of the porous surface increased drag when compared with the smooth surface, and no improvement was observed with air injection. The efficiency of this technique was strongly influenced by the non-uniform distribution of the bubbles over the surface. The use of a superhydrophobic coating over the porous cylinder (porous SHS) reduced drag in comparison with the non-coated porous cylinder. Although the injection of air did not improve the porous SHS efficiency, it was possible to replenish the air layer that gradually dissolved into the flow stream. The replenished porous SHS could keep its superhydrophobicity as long as the air was supplied.

The use of rectangular riblets with normalized spanwise tip spacing of $s^+ = 15 - 40$ increased drag in comparison with the smooth surface. Yet, the use of the superhydrophobic coating over

the riblets reduced drag in comparison with the riblets surface without the coating. The combined effect of rectangular riblets ($s^+ = 30 - 80$) and a low air injection rates, did not result in the formation of grooves filled with air. This configuration also increased drag when compared with the smooth surface. Overall, the performance of riblets might have been adversely affected by the existence of a crossflow component around the AUV body, and manufacturing imperfections of the grooves.

Preface

The work in this thesis, including the experimental setup, data acquisition, processing, and analysis, was carried out by me under the supervision of Dr. Sina Ghaemi from the Mechanical Engineering Department of the University of Alberta.

The two riblets surfaces tested in this project were 3D printed in Dr. David Nobes' laboratory, from the Mechanical Engineering Department at the University of Alberta.

Acknowledgement

I want to express my gratitude to my supervisor Dr. Sina Ghaemi who provided his insight and expertise, for his useful comments, remarks, and engagement through the learning process of this master thesis.

Many thanks to everyone in the research group who supported me through the course of this project. I am especially grateful to Wagih Abu Rowin, Sadek Shaban, Farzad Ahmadi and Masoud Ebrahimian, with whom I had the pleasure to work during this journey and made my academic life enjoyable. Thanks to Max Ren and Findlay McCormick for their help in running the high-speed water loop.

Nobody has been more important to me in the pursuit of this master degree than the members of my family. I would like to thank my loved ones, who have supported me throughout the entire process, both by keeping me harmonious and helping me putting pieces together. I will be grateful forever to my mom, who taught me the value of knowledge; to my supporting cousins, Johana and Josmar, for encouraged me to pursue my education; and to my loving and supporting husband, Jorge, for join me in this adventure and help me to overcome any obstacle. Without your unconditional help, I couldn't have finished my thesis work without problems.

Table of Contents

Abstract	ii
Preface	v
Acknowledgement	vi
Table of Contents	vii
List of Figures	x
List of Tables	xviii
List of Symbols	xx
Chapter 1. Introduction.....	1
Chapter 2. Literature Review.....	5
2.1 Boundary Layer Theory	5
2.1.1 Flat plate.....	5
2.1.2 Axisymmetric Body	14
2.1.3 Coherent Structures.....	16
2.2 Drag Reduction Using Superhydrophobic Surfaces.....	20
2.2.1 Fundamentals	20
2.2.2 Wetting Phenomenon.....	21
2.2.3 Characterization of a Superhydrophobic Surface	23
2.2.4 Superhydrophobic Surfaces in Turbulent Flows.....	27
2.3 Drag Reduction Using Air Injection	29
2.3.1 Fundamentals	29
2.3.2 Bubble Drag Reduction.....	32
2.3.3 Air Layer Drag Reduction	36
2.4 Drag Reduction Using Riblets.....	38
2.4.1 Fundamentals	38
2.5 Measurement Techniques.....	42
2.5.1 Load Cell.....	42
2.5.2 Particle Tracking Velocimetry	43
Chapter 3. Experimental Setup and Methodology.....	50

3.1	Flow Facility.....	50
3.2	Design of the Test Model	53
3.2.1	Background and Motivation	53
3.2.2	Test Model	56
3.3	Test Surfaces	65
3.3.1	Smooth Surface:.....	65
3.3.2	Porous Surface	66
3.3.3	Riblets	67
3.4	Neutrally Buoyant Aft Body	70
3.5	Load Measurement	76
3.5.1	Pre-measurement and Measurement Procedure.....	77
3.5.2	Data processing.....	78
3.5.3	Propagation of Uncertainty	81
3.6	Shadow-Based Long-Range Microscopic Particle Tracking Velocimetry	84
3.6.1	Images Alignment.....	85
3.6.2	Images Pre-Processing and PTV Processing	85
3.6.3	Wall Detection	87
3.6.4	Air Plastron Visualization.....	89
3.7	Test Matrix	91
Chapter 4.	Effect of Superhydrophobic Coating on the Drag of a Smooth Surface.....	96
4.1	Introduction	96
4.2	Results and Discussion.....	99
4.3	Conclusions	106
Chapter 5.	Effect of Superhydrophobic Coating and Air Injection on the Drag of a Porous Surface.....	107
5.1	Introduction	107
5.2	Results and Discussion.....	110
5.2.1	Drag of the Porous Surface without Air Injection	111
5.2.2	Drag of the Porous Surface with Air Injection	113
5.2.3	Drag of the Porous Surface with Superhydrophobic Coating.....	121
5.2.4	Evaluation of the Effect of Air injection in Recovering a Superhydrophobic Surface.....	125
5.3	Conclusions	128

Chapter 6.	Effect of Superhydrophobic Coating and Air Injection on the Drag of Riblets Surfaces	130
6.1	Introduction	130
6.2	Results and Discussion.....	134
6.2.1	Drag of Riblets Model 1 (riblets span, $s = 0.3$ mm)	134
6.2.2	Drag of Riblets Model 2 (riblets span, $s = 0.6$ mm) with Air Injection.....	140
6.3	Conclusions	145
Chapter 7.	Slip and Plastron Morphology over an Axisymmetric Body with a Superhydrophobic Surface	146
7.1	Introduction	146
7.2	Results and Discussion.....	150
7.2.1	Load Measurement.....	150
7.2.2	Slip velocity	152
7.2.3	Plastron Morphology	159
7.3	Conclusions	163
Chapter 8.	Conclusions and Recommendations for Future Research	165
	Bibliography	168
	Appendix A. Drawings	181
	Appendix B. Data Distribution of the Drag Coefficient.....	208
	Appendix C. Pictures of the Porous Surface Tests	210
	Appendix D. Permissions for Use of Figures	223

List of Figures

Figure 2.1. Development of the boundary layer over a flat plate including the transition from laminar to turbulent (adapted from Cengel and Cimbala, 2014).	7
Figure 2.2. Sketch showing the various regions of the turbulent boundary layer in inner and outer variables. (adapted from George, 2013).	13
Figure 2.3. Flow coordinate system over an axisymmetric body (adapted from Cebeci <i>et al.</i> 1974).	14
Figure 2.4. Visualization of the low/high-speed streaks at $y^+=2.7$ (Kline <i>et al.</i> 1967, permission for use in Appendix D).	17
Figure 2.5. Sample space of the velocities fluctuations $u-v$. Location of sweeps and ejections events in the $u-v$ quadrants.....	18
Figure 2.6. Vortical structures: quasi-streamwise and transverse vortices (Robinson, 1991, permission for use in Appendix D).....	19
Figure 2.7. Sketch of a liquid drop showing the contact angle θ balanced by three interfaces. The letter A indicates the interfaces as well as their contact areas. SV, SL, and LV correspond to the interfaces between solid, liquid and vapor respectively (adapted from Yan <i>et al.</i> 2011).....	22
Figure 2.8. The homogeneous wetting state (a) and heterogeneous wetting state (b). The liquid drop in the homogeneous wetting state follows the solid surface and penetrates into the grooves caused by the protrusions; the liquid drop in the heterogeneous wetting state only contacts the top of the protrusions, leaving air below into grooves (adapted from Yan <i>et al.</i> 2011).....	22
Figure 2.9. A liquid drop that is theoretically sliding on a declination of θ_D without acceleration. α_A is the advancing angle, and α_R is the receding angle (adapted from Yan <i>et al.</i> 2011).	24
Figure 2.10. Schematic representation of the definition of (a) intrinsic, (b) apparent, and (c) effective slip lengths (Vinogradova and Belyaev, 2011, permission for use in Appendix D).	25

Figure 2.11. Three different choices of the reference surface to establish interfacial slip for a rough surface, and a structured surface containing fabricated pillars (adapted from Lee *et al.*, 2014). 26

Figure 2.12. Distribution of the air injected beneath a flat plate, (a) bubble drag reduction (BDR) and (b) air layer drag reduction (ALDR) 30

Figure 2.13. Drag reduction (DR) techniques using air injection and its sub-categories according to Murai (2014). 31

Figure 2.14. Classification of technical paper with successful drag reduction reports in horizontal channels, horizontal flat plates, and model ships (Murai, 2014, permission for use in Appendix D). The author indicates that the central position and diameter of each ellipse represent the average conditions and the estimated range of experimental tests in each article. 34

Figure 2.15. Example of canonical cavity flows for axisymmetric bodies (Ceccio, 2010, permission for use in Appendix D). σ is the cavitation number; L_c and d_c are the length scales of the air cavity. 37

Figure 2.16. Typical shapes of riblets. Cross-section geometries: a) sawtooth/V-shaped, b) blade, c) trapezoidal, d) semi-circular/ scalloped. Configurations: e) continuous, f) aligned segmented, and g) staggered segmented (adapted from Bechert *et al.* 1997, and Bixler and Bhushan, 2013). 39

Figure 2.17. General structure of a drag reduction (DR) curve over a riblets surface (Bechert *et al.* 1997, permission for use in Appendix D). 40

Figure 2.18. Models of load cell sensors (Loadstar™). 43

Figure 2.19. Experimental arrangement for particle tracking velocimetry (PTV). (adapted from Raffel *et al.* 2007) 44

Figure 2.20. Light scattering by a 10 μ m oil particle in air. (Raffel *et al.*, 2007, permission for use in Appendix D) 45

Figure 2.21. Sketch of the setup for shadow PTV over a body-of-revolution. (FOV = Field of View).....	49
Figure 3.1. A schematic view of the high-speed water loop showing the two levels of the facility, the settling chamber, flow straighteners, and the test section. (adapted from Cowar, A. 2004) ..	50
Figure 3.2. An image of the settling chamber of the high-speed water loop (left) followed by the test section (right).	51
Figure 3.3. A sketch of the main components of NRCan Explorer AUV (Crees <i>et al.</i> 2010).....	54
Figure 3.4. Sketch of the AUV model located on the test section: (a) side view; (b) top view of the test section; and (c) frontal view of the test section.	56
Figure 3.5. Two 3D views of the test model. (a) Displays the test model fully assembled, and (b) shows the three major sections of the modular design.	57
Figure 3.6. 3D views of the leading edge. The components are the nose, a thread insert, and an O-ring for the connection to the central body.	58
Figure 3.7. 3D views of the central body components. (a) Displays the main components, and (b) shows the hydrofoil attachments.....	58
Figure 3.8. 3D view of the load cell located between the hydrofoil and the aft body, and a sketch of the axial force to be measured by the load cell.....	59
Figure 3.9. Submersible S-Beam Junior Load Cell, LSB210 (Futek data sheet)	62
Figure 3.10. 3D view of the aft body main components.....	62
Figure 3.11. 3D views of the air distributor design (a) fully assembled and (b) disassembled components.	67
Figure 3.12. Riblets surfaces sleeves. The left column shows the 3D view, (a) for model 1 and (c) for model 2. The right column displays the riblets geometry and dimensions, (b) for model 1 and (d) for model 2.	68

Figure 3.13. Force balance in the center of mass of the AUV test model.	70
Figure 3.14. Diagram of the vertical forces acting on the aft body of the test model.	71
Figure 3.15. A 3D view of the balance weights designs for (a) the smooth surface assembly and (b) for the porous cylinder assembly. (c) Displays the installation of the balance weights in the front and back seals.....	74
Figure 3.16. Images captured during the verification of the balanced vertical forces and momentum. (a) Test of the balance weights without the load cell, using a hinge connection to the water tank wall. (b) Test of the balance weights in the fully assembled model, also in the water tank.....	75
Figure 3.17. AUV model installed in the test section of the high-speed water loop.	75
Figure 3.18. Voltage vs. Load plot used for the calculation of the load cell’s scale factor. The process was done by first adding weight (“Up”) and then removing it (“Down”).	76
Figure 3.19. Voltage vs. time plot used to visualize the effect of the low-pass filter over the raw data. The noise due to high frequency vibrations in the raw data is successfully filtered out.....	79
Figure 3.20. Voltage vs. Re number plot used to visualize the effect of the low-pass filter over the raw data. The change in the average is negligible. Conversely, the standard deviation is greatly reduced, especially at higher velocities where the vibrations are higher.....	80
Figure 3.21. Shadow-based long-range microscopic particle tracking velocimetry setup. The system is formed by a Nd:YAG laser, which pulse is guided by two laser mirrors through a diffuser, and a CCD camera located in front of the diffuser.....	85
Figure 3.22. Sample of velocity vector fields over (a) the smooth surface cylinder and (b) the SHS, at $Re = 5.0 \times 10^5$. The velocity vectors were obtained through shadow-based long-range microscopic particle tracking velocimetry.....	86
Figure 3.23. Wall detection over the smooth surface cylinder at $Re = 5.0 \times 10^5$. (a) A sample micro-PTV image over the smooth wall showing the interface of the solid surface and the liquid. This image corresponds to a reduced area of the total FOV. (b) The profile of wall normal	

distance y versus light intensity (in counts) averaged in the streamwise direction. (c) The profile of wall-normal gradient of the average light intensity. The peak value is selected as the location of the wall ($y = 0$). For this case, the uncertainty is equivalent to $0.6 \mu\text{m}$ (0.5 pixels)..... 88

Figure 3.24 Wall detection over the SHS cylinder at $Re = 5.0 \times 10^5$. (a) Presents a sample image of SHS displaying the recognition of the surface roughness peaks, the location of the average roughness height ($y = 0$) and the 95% cumulative distribution of the roughness height (y_{95}). (b) Shows the histogram for the height of surface roughness, and (c) displays the cumulative distribution of the height of surface roughness..... 89

Figure 3.25. Wall location on an image of the SHS model at a $Re = 5.0 \times 10^5$ with (a) a mostly uniform air-water interface (plastron full of air) and (b) SHS microstructures with air pockets (dissolved air plastron). Figure (c) displays the subtraction of image (b) from (a), with the location of the interface for each case to calculate the air plastron equivalent thickness..... 90

Figure 4.1. Average of the drag coefficient (C_D) versus Reynolds number (Re) for the smooth surface. The C_D is calculated using the drag force measured by a submersible load cell. The error bars, in both cases, correspond to one standard deviation (σ_{CD})..... 99

Figure 4.2. Average of the drag coefficient (C_D) versus Reynolds number (Re) for the superhydrophobic surface (SHS) in comparison with the smooth surface. The C_D is calculated using the drag force measured by a submersible load cell. The error bars, in both cases, correspond to one standard deviation (σ_{CD})..... 101

Figure 4.3. Test cylinder with the SHS in static water. 103

Figure 4.4. Test cylinder with the SHS. (a) The SHS displays the uniform shiny aspect of the air layer is seen at $Re = 5 \times 10^5$. (b) The image of the same surface at $Re = 1.5 \times 10^6$ and after 35 min operation of the flow loop. The shiny air-water interface is absent..... 104

Figure 4.5. The damaged coating area on the back section of the AUV module. (a) $Re = 1.5 \times 10^6$, and (b) in static water at the end of the test. 104

Figure 5.1. Average of the drag coefficient (C_D) versus Reynolds number (Re) for the porous and smooth surface. The error bars correspond to one standard deviation (σ_{CD})..... 111

Figure 5.2. Average of the drag coefficient (C_D) versus Reynolds number (Re) for low air injection rates (LAIR) over the porous surface. The porous surface (baseline) is compared with the cases of $Q_a = 0.15$ L/min, $Q_a = 0.25$ L/min, $Q_a = 0.5$ L/min, $Q_a = 1$ L/min, and $Q_a = 5$ L/min. The error bars correspond to one standard deviation (σ_{CD}). 114

Figure 5.3. Average of the drag coefficient (C_D) versus the air injection rate (Q_a) for the low air injection rates (LAIR) at the constant Re of: 5×10^5 , 7×10^5 , 1.0×10^6 , 1.2×10^6 , and 1.5×10^6 . The error bars correspond to one standard deviation (σ_{CD}). 115

Figure 5.4. Air injection with a rate (Q_a) of 5 L/min (a) in static water, (b) at the Re of: 5×10^5 , and (c) at the Re of 1.5×10^6 . The increase in velocity helped to keep the bubbles cloud near the surface. 116

Figure 5.5. Average of the drag coefficient (C_D) versus Reynolds number (Re) for the high air injection rates over the porous surface (HAIR). The porous surface (baseline) is compared with the cases of $Q_a = 10$ L/min, $Q_a = 15$ L/min, $Q_a = 20$ L/min, $Q_a = 25$ L/min, $Q_a = 30$ L/min, $Q_a = 35$ L/min, $Q_a = 40$ L/min, $Q_a = 45$ L/min, $Q_a = 50$ L/min. 117

Figure 5.6. Average of the drag coefficient (C_D) versus the air injection rate (Q_a) for the high air injection rates over the porous surface (HAIR) at the constant Re of: 5×10^5 , 7×10^5 , 1.0×10^6 , 1.2×10^6 , and 1.5×10^6 117

Figure 5.7. Air injection at the Re of 1.5×10^6 with an air injection rate (Q_a) of (a) 25 L/min, (b) 35 L/min, and (c) 45 L/min. The increase of Q_a was not enough to reduce the drag. 118

Figure 5.8. Average of the drag coefficient (C_D) versus Reynolds number (Re) for the combined effect of air injection and superhydrophobic surface (SHS). The following configurations are compared: porous surface, with and without air injection ($Q_a = 0.15$ L/min and $Q_a = 0.25$ L/min), SHS over the porous surface, with and without air injection (SHS $Q_a = 0.15$ L/min and SHS $Q_a = 0.25$ L/min), and the smooth surface. The error bars correspond to one standard deviation (σ_{CD}). 121

Figure 5.9. Porous SHS with (a) no air injection at the beginning of the test with a Re of 5×10^5 , and (b) at the end of the test with a Re of 1.5×10^6 . Images of the recovery and maintenance of

the shiny aspect of the porous SHS at the Re of 5×10^5 , with the injection rate (Q_a) of (c) 0.15 L/min, and (d) 0.25 L/min..... 123

Figure 5.10. Air injection effect on a wetted porous superhydrophobic surface (SHS)..... 126

Figure 6.1. Average of the drag coefficient (C_D) versus Reynolds number (Re) for the riblets Model 1 $s = 0.3\text{mm}$ in comparison with the smooth surface. The value of s^+ is indicated beside each data point. The error bars correspond to one standard deviation (σ_{CD}). 135

Figure 6.2. Particles trapped in the riblets ($s=0.3\text{mm}$) valleys. After the test in a dry environment 137

Figure 6.3. Average of the drag coefficient (C_D) versus Reynolds number (Re) for the combined effect of riblets model 1 and superhydrophobic surfaces (SHS) in comparison with the smooth surface. 138

Figure 6.4. Detail of the air injection, $Q_a=0.15\text{L/min}$. (a) Static water, (b) $Re = 5.0 \times 10^5$, and (c) $Re = 1.5 \times 10^6$ 141

Figure 6.5. Bubbles and air lines in the valleys of the riblets, $Q_a=0.15\text{L/min}$ at $Re = 7.0 \times 10^5$. (a) At the middle of the test model, and (b) downstream the front seal 141

Figure 6.6. Average of the drag coefficient (C_D) versus Reynolds number (Re) for the combined effect of air injection and riblets model 2 in comparison with the riblets model 1, and the smooth surface. The error bars correspond to one standard deviation (σ_{CD}). 143

Figure 7.1. Average of the drag coefficient (C_D) versus Reynolds number (Re) for the smooth surface in comparison with the superhydrophobic surface (SHS). The C_D is calculated using the drag force measured by a submersible load cell. The error bars, in both cases, correspond to one standard deviation (σ_{CD}). 150

Figure 7.2 Velocity of tracer particles from shadow-based long-range –micro-PTV over the baseline (left figures) and the SHS (right figures) at the specified Re numbers. The average velocity profile [m/s] seen as the continuous line is obtained by averaging the velocity of the tracer particles in bins with a wall-normal dimension of $30 \mu\text{m}$ and an overlap of 75%. 154

Figure 7.3. Plastron visualization in static water. (a) An image captured at the beginning of the test (before water flows). It shows a uniform and smooth air-water interface covering all the surface microstructures. (b) An image of the surface at the end of the test in still water (after the data was collected over five Re numbers within 45 min). The thick air plastron is absent, and the surface microstructures are visible..... 159

Figure 7.4. Plastron visualization with a flow at Re of (a-c) 5.0×10^5 in images, (d-f) Re of 7.0×10^5 in images, (g-i) Re of 1.0×10^6 , (j-l) Re of 1.2×10^6 , and (m-o) Re of 1.5×10^6 . The left column displays for each set an image at the beginning of the data recording period. The middle column shows images at the end of each set recording period. The right column displays the morphology of the air plastron and pockets by subtracting the inverted image of the left and middle column. 161

Figure B.1. Drag coefficient (C_D) as a function of time.....208

Figure B.2. Histogram for the drag coefficient (C_D) at Re number = 1.5×10^6 using the smooth surface.....209

Figure C.1. Low air injection rates (LAIR).....210

Figure C.2. High air injection rates (HAIR).....218

Figure C.3. Porous superhydrophobic surface (SHS).....221

List of Tables

Table 2.1. Wall regions, layers and their characteristics (George, 2013).....	12
Table 3.1. Description of Natural Resources Canada (NRCan) Explorer autonomous underwater vehicle (AUV) (Crees <i>et al.</i> 2010).....	54
Table 3.2. General description and dimensions of the test model geometry.	57
Table 3.3. Literature empirical, experimental and numerical drag coefficients (C_D) at 0° angle-of-attack, with the estimated drag force considering the test model submerged in a water flow stream at 6.25 m/s	61
Table 3.4. Parts summary of the test model main components, description, and materials.	64
Table 3.5. Balance weight description and force balance results.	74
Table 3.6. Results of a low-pass filter over the raw data	80
Table 3.7. Parameters of the micro-PTV system for the smooth surface cylinder	87
Table 3.8. Tests performed using load measurements per surface and its respective combinations. The number of data points collected for each configurations is indicated per Re number.	94
Table 3.9. Tests performed using shadow-based long range micro-PTV and load measurements. The number of data points collected for each configuration is indicated per Re number.	95
Table 4.1. Drag coefficient (C_D), standard deviation (σ_{CD}), average test velocity U [m/s], and drag reduction percentage (DR%) for the smooth surface and the superhydrophobic surface (SHS) cylinders.....	102
Table 5.1. Drag coefficient (C_D), standard deviation (σ_{CD}) and average test velocity U [m/s], for the smooth surface cylinder and the porous surface.	112
Table 5.2. Non-dimensional airflow C_v in the turbulent boundary layer (TBL) for each Re and air flow rate (Q_a) tested.....	113

Table 5.3. C_D and drag reduction percentage (DR%) of the porous surface with superhydrophobic coating (porous SHS) in comparison with the noncoated porous surface without air injection.	122
Table 5.4. Drag coefficient (C_D) and drag increase percentage (DI%) of the porous surface with superhydrophobic coating (porous SHS) with and without air injection.....	124
Table 6.1. Drag coefficient (C_D), standard deviation (σ_{CD}), average test velocity U [m/s] and drag increase percentage (DI%) for the smooth surface cylinder and the riblets model 1.	135
Table 6.2. Drag coefficient (C_D), standard deviation (σ_{CD}), average test velocity U [m/s], and drag reduction percentage (DR%) for the riblets model 1 and the SHS riblets model 1.....	138
Table 6.3. Drag coefficient (C_D), standard deviation (σ_{CD}), average test velocity U [m/s], and the drag increase percentage (DI%) for the smooth surface cylinder and the riblets model 2.	143
Table 7.1. Drag coefficient (C_D), standard deviation (σ_{CD}), average tests velocity U [m/s], and drag reduction percentage (DR%) for the smooth surface cylinder and the superhydrophobic surface (SHS) during the micro-PTV measurement.	151
Table 7.2. Summary of results obtained for the SHS during the experiment with long-range micro-PTV. Drag reduction percentage (DR %), wall units (η), dimensionless roughness (k^+_{rms}), slip length (b), slip velocity at y_{95} and $y = 0$, and the air plastron thickness (t).....	156

List of Symbols

Acronyms

AUV Autonomous Underwater Vehicles

ALDR Air Layer Drag Reduction

BDR Bubble Drag Reduction

CFD Computational Fluid Dynamics

CCD Charge Coupled Devices

DHM Digital Holographic Microscopy

DI Drag Increase

DNS Direct Numerical Simulation

DR Drag Reduction

FFT Fast Fourier Transform

FOV Field-of-View

Micro-PTV Microscopic Particle Tracking Velocimetry

NACA National Advisory Committee for Aeronautics

PIV Particle Image Velocimetry

PTV Particle Tracking Velocimetry

LV Liquid-Vapor interface

SHS Superhydrophobic Surfaces

SL Solid-Liquid interface

SNR signal-to-noise ratio

SV Solid-Vapor interface

RANS Reynolds-Averaged Navier-Stokes

TBL Turbulent Boundary Layer

Symbols

α Solid surface per a contact angle

α_A Advancing angle

α_C Equilibrium contact angle of the Cassie-Baxter state

α_R Receding angle

α_W Equilibrium contact angle of the Wenzel state

γ Surface tension

γ_W Water specific weight

γ_A Air specific weight

δ Boundary layer thickness

δ^* Displacement thickness

δ^+ Local Reynolds number

δ_z Depth-of-focus of the particle image

δ_{99} Boundary layer thickness at 99% of the free-stream velocity

η Inner length scale (wall units) – TBL theory

η_B Bulk viscosity – Apparent slip model

η_g Gas viscosity – Apparent slip model

$\Delta\alpha$	Contact angle hysteresis
Δp	Pressure difference
ΔU_o	Changes in the free-stream velocity U_o
Δt	Time interval in the micro-PTV measurement
Δx	Average particles displacement in the streamwise direction / Bin size in the streamwise direction
Δy	Average particles displacement in the wall-normal direction / Bin size in the wall-normal direction
θ	Momentum thickness
ϑ	Angle of the sawtooth/V-shaped riblets
λ	Laser wavelength
μ	Dynamic viscosity
ν	Kinematic viscosity
ρ	Water density
ρ_p	Density of the particles
σ_{CD}	Standard deviation
τ	Total shear stress
τ_w	Total shear stress at the wall
ϕ_s	Wetted area fraction of the surface roughness
A_w	Area of fluid in contact with the wall – Drag reduction using air injection
b	Slip length

b_{eff}	Effective slip
B_i	Injector span
C_D	Drag Coefficient
C_{DV}	Volumetric Drag Coefficient
C_f	Skin-Frictional Coefficient
\mathcal{C}	Center Line
d_i	Size of the particle image – PTV measurement fundamentals
d_{opt}	Optical limit of the particle image
d_p	Particle diameter – PTV measurement fundamentals
d_s	Diffraction limited of the particle image
D	Diameter of the AUV model
D_D	Diameter of the air distributor
e	Gas Film Thickness – Apparent slip model
e	Euler’s constant
F_D	Drag force
$f/\#$	f-number
F_B	Buoyancy force
F_D	Drag force
F_{FD}	Friction drag force – Drag reduction using air injection
g	Acceleration due to gravity
h	Height of the riblets cross-section geometry

h_{max}	Maximum height of the surface roughness
h_{min}	Minimum height of the surface roughness
h_{avg}	Average height of the surface roughness
I_{max}	Maximum illumination intensity
k^+	Non-Dimensional Surface Roughness
k_r	Roughness parameter
L	Total length of the AUV model
l	Length of the external surface of the replaceable cylinder (AUV model)
L_P	Variable to characterize the changes in the x -direction in the TBL theory
L_t	Total length of the AUV model tail
M	Magnification
M_z	Momentum in the z -axis
P	Local pressure
P_o	Free stream pressure
P_w	Pressure at the wall
Q_a	Air injection rates
QE	Quantum Efficiency
Q_w	Volumetric flux of the liquid in the TBL
r	Axisymmetric body curvature radius
r_t	Radius of the AUV model's tail at the streamwise position
r_w	Radius of the transverse section of the axisymmetric body

R	Main radius of the AUV model
Re	Reynolds number
$Re_{critical}$	Critical Reynolds number
Re_{cr}	Engineering critical Reynolds number
R_{rms}	Root-mean-square roughness
R_{PT}	and a peak-to-trough roughness
R_y	Vertical reaction on the load cell free edge – Neutrally buoyant aft body
s	Spacing between the grooves of riblets
S	Cross-section area of an axisymmetric body
s^+	Normalized spanwise tip spacing
t	Thickness of the riblets cross-section geometry
t_e	Air plastron estimated thickness
u_*	Friction velocity
u^+	Non-dimensional version of the velocity
u_τ	Friction velocity for smooth surfaces
u_τ^*	Friction velocity for rough surfaces
\mathbf{u}	Fluctuation of the velocity vector in the streamwise direction
u_s	Slip velocity
u_w	Velocity in the streamwise direction near the wall– TBL theory
\mathbf{U}	Instantaneous velocity vector
U	Velocity component parallel to the wall in the streamwise direction (x -axis)

U_g	Gravitational induced velocity
U_o	Free-stream velocity
U_w	Velocity of the moving wall – Drag reduction using air injection
U_f	Fluid velocity outside the boundary layer – Drag reduction using air injection
$\langle U \rangle$	Velocity ensemble average
V	Velocity component perpendicular to the wall in the wall normal direction (y -axis)
V_{AB}	Volume of the aft body
V_{AC}	Volume of air inside the replaceable cylinder
V_{AT}	Volume of air inside the tail
V_m	Volume of the axisymmetric body
w_c	Fluctuation of the velocity vector in the spanwise direction of the axisymmetric body
W_c	Circumferential velocity component, parallel to the wall, in the spanwise direction of the axisymmetric body (z -axis)
W	Weight
W_{A1}	Weight of air inside the replaceable test cylinder
W_{A2}	Weight of air inside the tail
W_B	Balance weight
W_1	Weight of the front seal and components installed on it
W_2	Weight of the replaceable module cylinder and air distributor (if applicable)
W_3	Weight of the back seal
W_4	Weight of the tail

x	Streamwise direction
x_t	Streamwise position in the longitudinal axis of the AUV model's tail
y	Wall normal direction
y^+	Non-dimensional distance perpendicular to the wall, inner and outer layer
\bar{y}	Non-dimensional distance perpendicular to the wall, for the outer layer
z	Spanwise direction

Chapter 1. Introduction

Underwater vehicles are being used in a wide range of applications including research, military operations, and commercial applications. For all these applications, the hydrodynamic performance of the underwater vehicle is a key factor as a large amount of their power is used to overcome the skin-friction drag (Samaha *et al.*, 2012). Therefore, it is of interest to study drag reduction (DR) methods such as superhydrophobic surfaces (SHS), air injection, riblets, and their combined effect over a simplified model of an autonomous underwater vehicle (AUV), which resembles an axisymmetric body in classical fluid mechanics.

The use of a superhydrophobic coating over a surface forms a water-repellent interface, which holds pockets of air in its nano/micro-pores. Hence, when the water flows over the surface, it is in contact with an air plastron instead of the solid surface, easing the no-slip boundary condition (Rothstein, 2010). The existence of a slip velocity in the air-water interface has proven to reduce skin-friction drag in both laminar and turbulent regimes (Ou and Rothstein, 2004, Gad-el-Hak, 2013). Balasubramanian *et al.* (2004) studied SHS over an ellipsoidal body in the laminar regime and obtained 14% DR at a Reynolds number (Re) of 5.5×10^5 . Zhang, S. *et al.* (2015) applied an SHS on a submarine model and obtained up to 15% DR, also in the laminar regime at $Re = 1.2 \times 10^5$. No previous investigations were found to report the use of SHS over axisymmetric bodies in the turbulent regime, neither the report of direct visualization of the air layer over a non-porous surface when exposed to a high shear flow. Moreover, the lack of accurate information regarding the air layer thickness, morphology, and lifetime has narrowed the interpretation and comparison of the results.

Injection of air into the turbulent boundary layer (TBL) of a liquid flow forms a two-phase mixture in the vicinity of the surface. The two-phase flow can remain as a bubbly mixture or become a continuous film. The air bubbles affect the formation and dynamics of the near-wall vortical structures (Madavan *et al.*, 1984 and Elbing *et al.*, 2008). The DR is obtained when the bubbles attenuate the formation of turbulent structures near the surface and decrease Reynolds stresses (Lu *et al.*, 2005). Merkle and Deutsch (1992) summarized several studies on microbubbles drag reduction. They found a maximum DR of 80-90% when the gas injection rate

is equivalent to the volumetric liquid flow in the boundary layer. Deutsch and Castano (1986) observed up to 20% DR over an axisymmetric body with 632 mm length, at flow speeds of 4.6 m/s, and with air injection rates of 90-150 L/min. However, at higher flow velocity, from 10.7 to 16.8 m/s, they observed 40-60% DR. In the latter case, DR was limited by the air flow rate required (> 240 L/min). The success of the latter technique requires a constant supply of a large amount of air. The bubbles have to overcome the buoyancy force and travel a long way until the end of the model. The amount of air could be reduced if the injection is done in multiple points along the body instead of using a single point. The experiments mentioned above used a single injection section located downstream the nose with an extension between 1-2% of the total model length. Therefore, it is of interest to study the effect of increasing the area of injection to reduce the amount of air required for drag reduction.

An alternative for underwater vehicles with limited space is the use of surfaces with streamwise microgrooves, which are referred to as riblets. These longitudinal grooves can reduce drag by keeping the quasi-streamwise vortices away from the surface (Walsh, 1990). The DR obtained by this method is a function of Re number, the groove geometry, and the groove spacing. Few investigations have reported the use of riblets over axisymmetric bodies underwater. Gillerist and Reidy (1989) tested the use of riblets on an axisymmetric buoyant vehicle. They obtained 8% DR using a v-grooved surface ($h/s = 1$) with a dimensionless spacing between the riblets (s^+) in the range of 13-15. Experiments in a wind tunnel also with v-grooved surfaces over an axisymmetric body resulted in a maximum of 8% DR with a $s^+ = 14$ (Konovalov *et al.*, 1991). Davari (2014) reported a 10% DR by using helical riblets over an axisymmetric body, also in a wind tunnel.

A novel application of the riblets and grooved surfaces can be to protect and hold the air plastron in its valley. The air can be introduced and kept in the valley of the grooves/riblets using superhydrophobic coating or air injection. The combined use of riblets and a superhydrophobic coating has shown DR in previous investigations (Barbier *et al.*, 2014, and Prince *et al.*, 2014). Hou (2016) proved, over a flat plate in the turbulent regime, that the use of a superhydrophobic coating can improve the performance of the riblets in the s^+ region where it would normally result in drag increase (DI). Regarding the combined effect of riblets and low air injection rates, Reed and Weinstein (1988, 1989) reported its potential in improving the efficiency of the current air injection technique by enhancing the air layer stability and reducing the amount of air

required. No investigation was found to report the use of riblets and SHS, neither the use of riblets and air injection, over an axisymmetric body in the turbulent regime.

A scaled-down model of the Natural Resources Canada (NRCan) Explorer autonomous underwater vehicle (AUV) is developed to investigate a variety of DR techniques. The current investigation aims to compare the individual and combined effect of SHS, air injection, and riblets, for DR over an axisymmetric body in the turbulent regime. The investigation details and results are presented in this manuscript.

This thesis is organized as follow:

Chapter 2 “*Literature Review*”: The chapter introduces basic concepts and background in turbulent boundary layer theory, the drag reduction techniques to be tested, and the measurement techniques used.

Chapter 3 “*Experimental Setup and Methodology*”: This section describes the flow facility, the test model design and calculations, details of the measurements methodology, and the tests performed.

Chapter 4 “*Effect of Superhydrophobic Coating on the Drag of a Smooth Surface*”: The use of an SHS is compared with a smooth surface. The performance is evaluated by measuring the resultant drag force with a submersible load cell.

Chapter 5 “*Effect of Superhydrophobic Coating and Air Injection on the Drag of a Porous Surface*”: The use of a porous surface, with and without air injection, is studied individually and in combination with a superhydrophobic coating. The resultant drag force is measured for each configuration and compared with the performance of the smooth surface.

Chapter 6 “*Effect of Superhydrophobic Coating and Air Injection on the Drag of Riblets Surfaces*”: Two designs of riblets surfaces are investigated, individually and in combination with a superhydrophobic coating and low air injection rates. The performance is assessed by measuring the resultant drag force.

Chapter 7 “*Slip and Plastron Morphology over an Axisymmetric Body with a Superhydrophobic Surface*”: The slip and the air plastron of an SHS over a smooth cylinder is further studied with

the simultaneous use of a load cell and the use of shadow-based long range microscopic particle tracking velocimetry (micro-PTV). The load cell measures the changes in the drag force, and the micro-PTV allows to study the slip velocity and the changes in the air plastron morphology when exposed to high shear flow.

Chapter 8 “*Conclusions and Recommendations for Future Research*”: This chapter considers the conclusions of the investigation performed and gives recommendations for future work.

Chapter 2. Literature Review

This chapter introduces basic concepts and background in turbulent boundary layer theory for a flat plate and an axisymmetric body. The fundamentals of the drag reduction techniques to be tested are also introduced, including the superhydrophobic coating, air injection, and riblets. Also, presents the measurement techniques used, which are the load cell and the shadow long range micro-PTV.

2.1 Boundary Layer Theory

Ludwig Prandtl (1904) introduced the boundary layer theory as an approximation to the Navier-Stokes solutions. The boundary layer approximation corrects some of the major deficiencies of the Euler equations by providing a way to enforce boundary conditions at the solid walls.

The classic example of a boundary layer flow is a uniform stream flowing parallel to a long flat plate. This study case can be extended to axisymmetric boundary layers and three-dimensional boundary layers. Therefore, the following discussion introduces first the boundary layer theory for a flat plate and then for an axisymmetric body. The explanation presented by George (2013) is used as a reference for the following discussion.

2.1.1 Flat plate

Prandtl (1904) stated that at high Reynolds number (Re) the flow could be divided into two regions: an outer flow region and an inner flow region called a boundary layer. The boundary layer refers to a thin region adjacent to a solid wall where the viscous forces dominate over the inertial forces. The successful application of the boundary layer approximation is based on the assumption that the inner region is very thin.

The solid surface provides two main boundary conditions. First, the normal flow velocity on the surface is equal to the normal velocity of the surface (also known as the kinematic boundary condition); therefore, there is no flow through the surface. In the same way, the second boundary condition is that the tangential component of the flow velocity at the surface is the same as the tangential velocity of the surface (also known as the no-slip boundary condition). Consequently,

in the case of a turbulent shear flow over a stationary solid surface, the fluid will have a zero velocity at the wall (Pope, 2000). The application of the boundary conditions allows the considerations of the viscous shear forces along walls, the drag force experienced by bodies immersed in a free stream, and helps to predict a more accurate flow separation in regions of adverse pressure.

The outer flow field is obtained by using the continuity and Euler equation. The Bernoulli equation is used to obtain the pressure field. If the flow field is rotational, the potential flow techniques can be applied to describe the flow. Either way, the outer flow region is solved first, and then the thin boundary layer. Therefore, this analysis of the turbulent boundary layer (TBL) starts with the characterization of the outer turbulent layer. For simplicity, only steady ($\partial/\partial t = 0$) and two dimensional flow is considered in the xy -plane in Cartesian coordinates.

The Cartesian coordinate system for a boundary layer along a solid wall can be described using x in the streamwise direction, it increases along the solid surface in the flow direction and y in the wall-normal direction, rising perpendicularly to the surface as seen Figure 2.1. As the flow is in continuous development, the statistics of the flow vary as a function of both the x and y -direction. Across the boundary layer, the instantaneous velocity vector is denoted by $\mathbf{U} = (U, V)$ and $\langle \mathbf{U} \rangle$ indicates its ensemble average. Considering the Reynolds decomposition, the fluctuation of the velocity vector $\mathbf{u} = (u, v)$ is:

$$\mathbf{u} = \mathbf{U} - \langle \mathbf{U} \rangle. \quad \text{Eq. 2.1}$$

The outer part of the boundary layer experience intermittent turbulent/non-turbulent motions, characterized by the free-stream velocity U_o . The higher the free-stream speed U_o , for a given fluid and plate, the thinner the boundary layer.

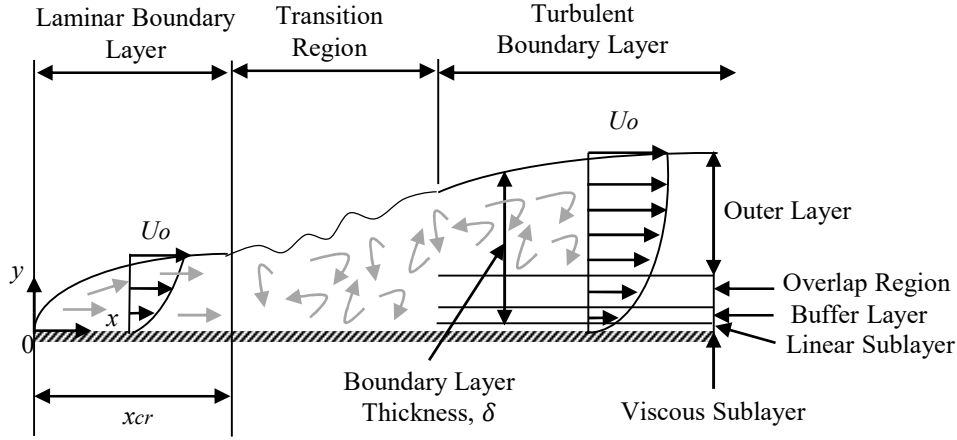


Figure 2.1. Development of the boundary layer over a flat plate including the transition from laminar to turbulent (adapted from Cengel and Cimbala, 2014).

As the boundary layer on a plate is continuously developing in the flow direction, its thickness $\delta(x)$ will increase along the x axis. The boundary layer thickness δ is usually defined as the distance away from the wall at which the velocity component parallel to the wall is 99% of the fluid speed outside the boundary layer. As mentioned before a key assumption for the application of the boundary layer approximation is that the boundary layer is very thin, which is considered to happen when $\delta/x \ll 1$.

The boundary layer displacement thickness is defined as

$$\delta^*(x) = \int_0^{\infty} \left(1 - \frac{\langle U \rangle}{U_o}\right) dy, \quad \text{Eq. 2.2}$$

and, the momentum thickness as

$$\theta(x) = \int_0^{\infty} \frac{\langle U \rangle}{U_o} \left(1 - \frac{\langle U \rangle}{U_o}\right) dy. \quad \text{Eq. 2.3}$$

The above concepts, displacement and momentum thickness, are also used to define different Re to characterize the boundary layer:

$$Re = \frac{U_o x}{\nu}, \quad Re_{\delta} = \frac{U_o \delta}{\nu}, \quad Re_{\delta^*} = \frac{U_o \delta^*}{\nu}, \quad Re_{\theta} = \frac{U_o \theta}{\nu}. \quad \text{Eq. 2.4}$$

In an ideal case of a smooth flat plate with a uniform free stream, the transition from laminar to turbulent regime starts at a critical Reynolds number ($Re_{critical}$) of 1×10^5 and continues until the

boundary layer is fully turbulent at $Re_{critical} \approx 3 \times 10^6$. However, in real life, the transition to turbulent flow usually occurs abruptly and at a lower Re than the values previously mentioned for a smooth flat plate with a calm, free stream. Some of the factors provoking an earlier transition location are roughness along the surface, free-stream disturbances, acoustic noise, flow unsteadiness, vibrations and curvature of the wall (Cengel and Cimbala, 2014). Because of these factors, an engineering critical Reynolds number (Re_{cr}) of 5×10^5 (Cengel and Cimbala, 2014) is used to determine if the boundary layer is mostly laminar ($Re < Re_{cr}$) or turbulent ($Re > Re_{cr}$). In some cases, rough sandpaper or wires called “trip wires” are installed along the surface to force the transition at the desired location. The vortices generated by the trip wire enhance the local mixing and create disturbances that rapidly lead to the formation of a TBL (Cengel and Cimbala, 2014).

The laws of conservation of mass and momentum of an incompressible and steady flow field are:

- Continuity equation:

$$\frac{\partial \langle U \rangle}{\partial x} + \frac{\partial \langle V \rangle}{\partial y} = 0, \quad \text{Eq. 2.5}$$

- Momentum equation:

$$U_j \frac{\partial U_i}{\partial x_j} = -\frac{1}{\rho} \frac{\partial P}{\partial x_i} + \nu \frac{\partial U_i}{\partial x_j \partial x_j}, \quad \text{Eq. 2.6}$$

where the material acceleration of the flow is related to the pressure gradient (P is the local pressure) and to the viscous diffusion. Applying the Reynolds decomposition to the x -component of the momentum equation, the result is:

$$\langle U \rangle \frac{\partial \langle U \rangle}{\partial x} + \langle V \rangle \frac{\partial \langle U \rangle}{\partial y} = -\frac{1}{\rho} \frac{\partial \langle P \rangle}{\partial x} - \frac{\partial \langle u^2 \rangle}{\partial x} - \frac{\partial \langle uv \rangle}{\partial y} + \nu \left(\frac{\partial^2 \langle U \rangle}{\partial x^2} + \frac{\partial^2 \langle U \rangle}{\partial y^2} \right). \quad \text{Eq. 2.7}$$

In the same way, the y - component of the momentum equation results in the following equation:

$$\langle U \rangle \frac{\partial \langle V \rangle}{\partial x} + \langle V \rangle \frac{\partial \langle V \rangle}{\partial y} = -\frac{1}{\rho} \frac{\partial \langle P \rangle}{\partial y} - \frac{\partial \langle uv \rangle}{\partial x} - \frac{\partial \langle v^2 \rangle}{\partial y} + \nu \left(\frac{\partial^2 \langle V \rangle}{\partial x^2} + \frac{\partial^2 \langle V \rangle}{\partial y^2} \right). \quad \text{Eq. 2.8}$$

Prandtl (1904) realized that at least one viscous stress term must remain in the momentum equation to apply the no-slip boundary condition. Hence, there must be at least two length scales

to characterize the changes in the flow direction (x) and normal direction (y). Considering the variable “ L_p ” to characterize the changes in the x -direction, and “ δ ” for the changes in the y -direction, a magnitude analysis of the terms in the previous equations can be performed to find an approximate solution. These length scales are used to estimate each term value. Those with small values are neglected and just the relevant terms are kept in the equation. U_o is used to scale the velocity and is considered to be equal to free-stream velocity, and ΔU_o is used to represent the changes in U_o .

The new length scales are replaced in the continuity equation and the x – component of the momentum equation to evaluate the relative importance of each of its terms. The analysis shows that at least one turbulent term must remain in the right side of the x – component of the momentum equation, and the largest turbulence term remaining in the equations is the one involving the Reynolds shear stress $\partial\langle uv \rangle / \partial y$. The prevalence of the Reynolds shear stress means that the boundary layer grows is relative to the turbulent intensity. As a result of the order of magnitude analysis, the Reynolds-averaged Navier-Stokes (RANS) equation of the outer layer in the x -direction is:

$$U \frac{\partial U}{\partial x} = -\frac{1}{\rho} \frac{\partial P}{\partial x} - \frac{\partial \langle uv \rangle}{\partial y}, \quad \text{Eq. 2.9}$$

Applying the same analysis to the y -component of the momentum equation results in the RANS equation of the outer layer in the y direction:

$$0 \approx -\frac{1}{\rho} \frac{\partial P}{\partial y} - \frac{\partial \langle v^2 \rangle}{\partial y}, \quad \text{Eq. 2.10}$$

Integrating the latter equation across the boundary layer, from a set value of y to infinity and considering that the free-stream value of $\langle v \rangle^2$:

$$P(x, y) = P(x, \infty) - \rho \langle v \rangle^2. \quad \text{Eq. 2.11}$$

If the free-stream is at a constant mean velocity, then: $P(x, \infty) = P_\infty$. Subsequently, the x -component of the momentum equation can be rewritten as:

$$U \frac{\partial U}{\partial x} = -\frac{1}{\rho} \frac{\partial P_\infty}{\partial x} - \frac{\partial \langle uv \rangle}{\partial y}, \quad \text{Eq. 2.12}$$

which is only valid on the outer layer, and it means that the pressure gradient is imposed on the boundary layer by the flow outside it.

After finding the approximate solution for the outer layer, it is now required to perform the order of magnitude analysis in the inner layer. No matter how small the viscous sublayer is, the mean velocity near the wall should change rapidly enough so that the viscous term remains in the governing equation and the no-slip condition is fulfilled. Thus, it requires the definition of a new length scale to characterize the changes in the y -direction close to the wall. The new length scale is defined by $\eta \ll \delta$. The changes in the x -direction will still be defined with L_P . To scale the velocity in the streamwise direction near the wall u_w ($u_w \ll U_o$) is defined. Moreover, as the turbulence intensities are high close to the wall, it is not relevant to distinguish the mean velocity from the fluctuation (u_w will be used for both).

The result of the magnitude analysis in the momentum equation reduces to:

$$0 = \frac{\partial}{\partial y} \left(-\langle uv \rangle + v \frac{\partial U}{\partial y} \right). \quad \text{Eq. 2.13}$$

Rewriting the later equation,

$$\frac{\partial \langle uv \rangle}{\partial y} = \frac{\partial}{\partial y} \left(v \frac{\partial U}{\partial y} \right), \quad \text{Eq. 2.14}$$

it can be integrated from $y = 0$ to a given value of y to obtain:

$$\langle uv \rangle|_y - \langle uv \rangle|_{y=0} = v \frac{\partial U}{\partial y} \Big|_y - v \frac{\partial U}{\partial y} \Big|_{y=0}. \quad \text{Eq. 2.15}$$

From the kinematic and the no-slip boundary conditions, it is known that $\langle uv \rangle|_{y=0} = 0$.

Additionally, the shear stress at the wall is given by:

$$\tau_w = \mu \frac{\partial U}{\partial x} \Big|_{y=0}. \quad \text{Eq. 2.16}$$

Replacing these values in Eq. 2.15, we obtain the equation for the inner layer (in the limit of infinite Re number):

$$\frac{\tau_w}{\rho} = -\langle uv \rangle + \nu \frac{\partial U}{\partial y}. \quad \text{Eq. 2.17}$$

The later equation shows that the total shear stress in the wall layer is constant in the limit of infinite Re (George, 2013). Following this same analysis in the y -component of the momentum equation, it is possible to prove that the outer region also defines the pressure in the near wall region. The streamwise pressure gradient disappears in the limit as $(u_w \eta)/\nu \rightarrow \infty$.

The definition of the scaled variables used, u_w and η , are defined using the friction velocity (u_*) which is:

$$u_*^2 \equiv \frac{\tau_w}{\rho}. \quad \text{Eq. 2.18}$$

Replacing this term in Eq. 2.17:

$$u_*^2 = -\langle uv \rangle + \nu \frac{\partial U}{\partial y}. \quad \text{Eq. 2.19}$$

Setting $u_w = u_*$, the friction velocity is the appropriate scale velocity for the near wall region. The inner length scale η can also be defined as function of the friction velocity as $\eta = \nu/u_*$. Consequently, the inner Re is unity and, the viscous and inertial terms are about the same.

Using the distance and the velocity length scale, it is possible to define the non-dimensional version of the velocity and the distance from the wall:

$$u^+ = \frac{U}{u_*} \quad \text{Eq. 2.20}$$

$$y^+ = \frac{y}{\eta} = \frac{yu_*}{\nu} \quad \text{Eq. 2.21}$$

Conversely, the dimensionless y coordinate for the outer layer can be defined as:

$$\bar{y} = \frac{y}{\delta} \quad \text{Eq. 2.22}$$

Using the dimensionless coordinates, the outer layer equations are applicable for $y^+ > 30$ and the inner layer equations for $\bar{y} < 0.1$. The ratio of y^+ to \bar{y} defines the local Reynolds number δ^+ :

$$\delta^+ = \frac{\delta u_*}{\nu} \quad \text{Eq. 2.23}$$

This local Reynolds number indicates that the inner layer is closer to the wall relative to δ . The influence of the viscous stress is said to decline from 100% at the wall ($y^+ = 0$) to 50% at $y^+ \approx 12$ and even lower (~10%) when $y^+ = 50$ (Pope, 2000). The variation of the viscous stress as a function of y^+ creates the division of the boundary layer in different regions according to the magnitude of its contribution (see Table 2.1).

Table 2.1. Wall regions, layers and their characteristics (George, 2013)

Region	Location	Characteristics	
Inner layer	Viscous sublayer	$y^+ < 30$, $y/\delta < 0.1$	The velocity's variation is fast enough for the viscous effects to be significant.
	Linear layer	$y^+ < 3$	Reynolds stress is negligible in comparison with the viscous stress.
	Buffer layer	$3 < y^+ < 30$	Adjustment region, both the viscous and the Reynolds stresses are significant in the momentum equation.
	Overlap region	$y^+ > 30$	The inner and outer layers are overlapped in this region.
Outer layer	$y^+ > 30$	The contributions of the viscous stress are negligible in comparison with the Reynolds stress.	

In the viscous sublayer, the viscous stress and Reynolds stress are not both important in all its extension. As mentioned in Table 2.1, near the wall ($y^+ < 3$) the Reynolds stress is negligible and Eq. 2.19 is reduced to:

$$u_*^2 \approx \nu \frac{\partial U}{\partial y}, \quad \text{Eq. 2.24}$$

which can be rewritten as:

$$1 = \frac{\partial U/u_*}{\partial y(\frac{u_*}{\nu})}. \quad \text{Eq. 2.25}$$

In terms of the inner variables, the latter equation reduces to:

$$u^+ = y^+ . \tag{Eq. 2.26}$$

Eq. 2.26 is one of the few exact solutions in turbulence, and it shows the reason why this region is named linear sublayer.

Moving away from the wall, the Reynolds stress rapidly develops until it overpasses the viscous stress. The buffer layer seen in Figure 2.2 is a region of adjustment. In this region the viscous and Reynolds stress are both significant in the momentum equation. Farther from the wall, the mean velocity gradient slowly falls until the viscous stress becomes negligible compared with the Reynolds stress (outer layer).

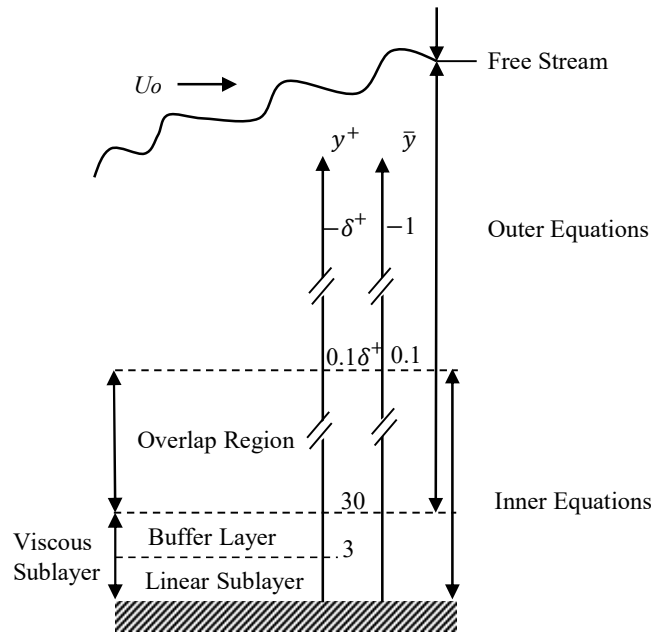


Figure 2.2. Sketch showing the various regions of the turbulent boundary layer in inner and outer variables. (adapted from George, 2013).

The understanding of the boundary layer theory is a key factor for the study of the drag over an object moving in a flow (Anderson, 2005), and is especially important for the analysis of the drag due to friction. Prandtl’s work explained that the viscosity has a critical role in a thin layer adjacent to the surface and gave the mathematical base for the calculation of the skin friction drag (Anderson, 2005). The equations of the inner layer are used in the current investigation to characterize and analyze the performance of the drag reduction techniques.

2.1.2 Axisymmetric Body

The main assumption in a wall-bounded TBL over an axisymmetric body is that at high values of Re ($Re \rightarrow \infty$) the boundary layer thickness δ in the radial direction is smaller than both the body length in the axial direction, and the body curvature radius r . In the situation where the boundary layer thickness has the same order of magnitude as the body curvature radius $\delta/r = O(1)$. For example, flow around a slender body, the effect of the transverse curvature must be considered as it affects the skin- friction and the heat transfer (Cebeci *et al.* 1974). The following discussion reflects the first case mentioned, where $\delta/r \ll 1$. The information to be presented follows the discussion of Schlichting *et al.* (2000) and Cebeci *et al.* (1974).

The flow over an axisymmetric body is described by the coordinate system shown in Figure 2.3. The x coordinate (streamwise) increases along the body arc length in the flow direction, y (wall-normal) rises perpendicular to the surface, and z is in the circumferential direction. The function $r_w(x)$, where r_w is the radius of the transverse section of the body, describes the body transverse curvature. Following the same velocity notation used in the previous section, the assumption can be made that U is the velocity parallel to the wall (in the streamwise direction, x axis), V is the wall normal component (y axis) and W_c , also parallel to the wall, is the circumferential velocity (z axis).

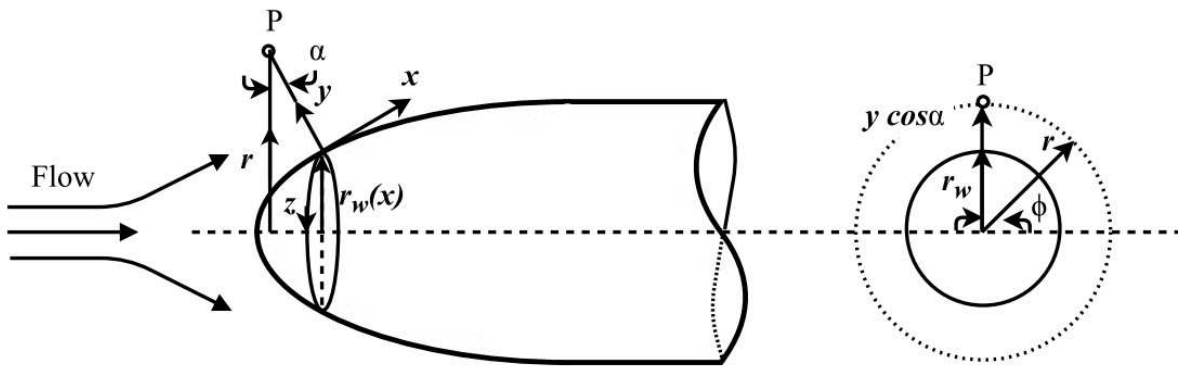


Figure 2.3. Flow coordinate system over an axisymmetric body (adapted from Cebeci *et al.* 1974).

The governing equations of flow over an axisymmetric body are not much different than those of a two-dimensional flow (Cebeci *et al.* 1974). The velocity and statistics within the boundary

layer will vary in y and x -direction and will be equally independent of the coordinate z ($\partial/\partial z = 0, \langle w_c \rangle = 0$) due to the assumption that $\delta/r \ll 1$.

In the boundary layer theory, the free stream pressure $P_o(x)$ is linked to the free stream velocity $U_o(x)$ through Bernoulli's equation [$P_o(x) + 1/2 \rho U_o(x)^2 = \text{const}$]:

$$-\frac{dP_o}{dx} = \rho U_o \frac{dU_o}{dx}, \quad \text{Eq. 2.27}$$

where an adverse pressure gradient would correspond to a negative velocity gradient ($\frac{dU_o}{dx} > 0$).

Moreover, considering a non-rotating flow, the governing equations can be written as:

- Continuity equation:

$$\frac{\partial(r^k \rho \langle U \rangle)}{\partial x} + \frac{\partial(r^k \rho \langle V \rangle)}{\partial y} = 0. \quad \text{Eq. 2.28}$$

- RANS equation:

$$\langle U \rangle \frac{\partial \langle U \rangle}{\partial x} + \langle V \rangle \frac{\partial \langle U \rangle}{\partial y} = -\frac{1}{\rho} \frac{\partial P}{\partial x} + \frac{1}{r^k} \frac{\partial}{\partial y} \left[r^k \left(\nu \frac{\partial \langle U \rangle}{\partial y} - \langle uv \rangle \right) \right], \quad \text{Eq. 2.29}$$

where,

$$r(x, y) = r_w(x) + y \cos \alpha \quad \text{Eq. 2.30}$$

and $k=1$ for the axisymmetric case, and $k=0$ for the two dimensional.

Comparing both cases ($k=1$ and $k=0$), Schlichting *et al.* 2000 highlights that, only the continuity equation is written in a different form. Subsequently, for a circular cylinder with $r_w(x) = \text{constant}$ (where $\delta/r_w \ll 1$) at a zero-incident angle-of-attack, Eq. 2.28 and Eq. 2.29 will reduce to the plate boundary layer equations (Schlichting *et al.* 2000). This is the reason why the plane and axisymmetric boundary layers are frequently discussed together.

Following the discussion of the TBL for a flat plate, the wall-normal mean momentum equation integrates to:

$$\langle P \rangle + \rho \langle v \rangle^2 = P_o(x) \quad \text{Eq. 2.31}$$

Considering that at the wall $\langle v \rangle^2 = 0$ (no penetration boundary condition) is possible to observe that the pressure at the wall $P_w(x)$ is equal to the free stream pressure $P_o(x)$.

Furthermore, the streamwise mean momentum equation (Eq. 2.29) can be rewritten considering Eq. 2.27 and the total shear stress $\tau(x, y)$ Eq. 2.17 as:

$$\langle U \rangle \frac{\partial \langle U \rangle}{\partial x} + \langle V \rangle \frac{\partial \langle U \rangle}{\partial y} = \frac{1}{\rho} \frac{\partial \tau}{\partial x} + U_o \frac{dU_o}{dx}. \quad \text{Eq. 2.32}$$

At the wall, the shear stress and the pressure gradient will balance; the no-slip and non-penetration conditions will make the convective and velocity terms zero. The integration of Eq. 2.32 for a zero-pressure gradient results in:

$$\tau_w = \rho U_o^2 \frac{d\theta}{dx}. \quad \text{Eq. 2.33}$$

Normalizing the wall shear stress by a reference velocity the skin-friction coefficient results in:

$$C_f = \frac{\tau_w}{\frac{1}{2} \rho U_o^2} = 2 \frac{d\theta}{dx}. \quad \text{Eq. 2.34}$$

2.1.3 Coherent Structures

Coherent structures are three-dimensional flow patterns with space and time coherence, which have a considerably larger scale than the smallest local turbulence (Robinson, 1991 and Pope, 2000). Different patterns occur at specific locations and times in the TBL; Robinson (1991) offers a classification and analysis of these structures. All are considered to play a key role in the turbulence-production cycle and the transport of momentum within the inner and outer layer (Robinson, 1991). Thus, the study of their kinematics (e.g., dimensions, shape, vorticity) and dynamic characteristics (e.g., origin, stability, growth), responds to the interest of getting a better understanding of the development of the TBL (Pope, 2000). The time-averaged statistics and scaling models help to design/improve control techniques and their applications for engineering problem solving (Robinson, 1991 and Pope, 2000). For example, avoiding the formation of these

coherent structures can diminish the turbulence production in a TBL and finally result in the reduction of the skin friction at the wall.

The basic coherent structures in a wall-bounded TBL are the low/high-speed streaks, ejections and sweep events, and the vortical structures (Pope, 2000). The general characteristics of these basic coherent structures are introduced in the following subsections.

2.1.3.1 Low/High-Speed Streak

The low/high-speed streaks are streamwise elongated meandering regions of slow-moving flow surrounded by the fast-moving flow. These structures are also described as regions of negative and positive fluctuations of the streamwise velocity.

These structures are visualized in the near wall region ($y^+ < 7$) and mostly independent of the Re . The distribution of the structures is typically uniform with a separation within the streaks around $100 \delta_v$. Moreover, their length, in the streamwise direction, can exceed 1000δ (Pope, 2000).

The first visualization of these structures patterns was reported by Kline *et al.* (1967) using tiny hydrogen bubbles, as displayed in Figure 2.4. Further experiments (Smith and Metzler, 1983) showed additional characteristics such as location and distribution.

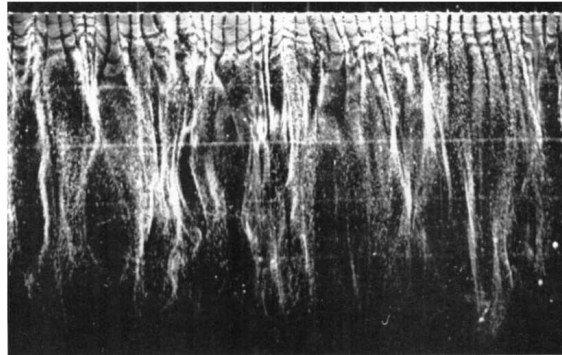


Figure 2.4. Visualization of the low/high-speed streaks at $y^+=2.7$ (Kline *et al.* 1967, permission for use in Appendix D).

2.1.3.2 Ejection and Sweep Events

The ejection and sweep events are a result of the characteristic movement of the low/high-speed streak. The movement of the low/high-speed streak is known as bursting and is thought to be responsible for a great amount of turbulent energy production (Blackwelder and Eckelmann,

1979, and Kim, 2011). Ejections are formed when the negative streaks ($u < 0$) start slowly moving away from the wall, and then, suddenly ($y^+ \sim 10$) turn and accelerate away from the wall ($v > 0$) (Pope, 2000). Ultimately, the structures break down into smaller motion patterns. Due to the flow moving upwards during the ejections, there will be regions of high-speed flow moving towards the wall ($u > 0$ and $v < 0$) that are known as sweeps events.

The relation between sweeps and ejections in turbulence production is shown in the u - v sample space of the velocities fluctuations. As displayed in Figure 2.5, the u - v sample space is divided in four quadrants; the sweeps and ejections are present in the regions where the product uv is negative (Q2 and Q4) and, consequently, the turbulence production is positive ($P = -\langle uv \rangle \partial \langle U \rangle / \partial y$) (Pope, 2000).

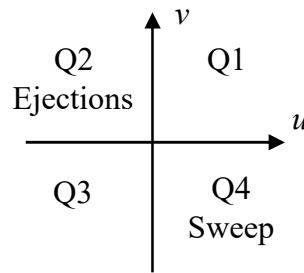


Figure 2.5. Sample space of the velocities fluctuations u - v . Location of sweeps and ejections events in the u - v quadrants.

The ejections and sweep events are distributed side-by-side in the spanwise direction (Kim *et al.* 1987). In the wall normal direction, the ejections contribution to the Reynolds shear stress prevails in the region $y^+ > 12$ and, the sweeps events are dominant near the wall (Kim *et al.* 1987, Wallace *et al.* 1972).

2.1.3.3 Vortical Structures

A vortical structure is defined as the circular or spiral pattern adopted by the flow streamlines around a midpoint when observed from a frame of reference that is moving with the center of the vortex core (Robinson 1991, and Spalart, 1988). The quasi-streamwise and transverse vortices (horseshoes and hairpins) are recognized as basic structures in the turbulence production and the generation of other coherent structures visualized in the TBL (Robinson 1991). The quasi-

streamwise vortices are mostly observed in the buffer layer; however, there is also supporting evidence of their presence in the logarithmic layer and, with less frequency, in the wake region (Robinson, 1991 and Adrian, 2007). These vortices, due to their location, have a major contribution to the Reynolds shear stress in the near-wall region and are closely related to sweeps and ejections events (Robinson, 1991). Conversely, the hairpins are commonly detected in the logarithmic layer, and, although they are less frequent when moving farther from the wall, it is possible to visualize some of them moving all across the TBL and forming bulges at the outer limit or TBL wake (Adrian, 2007). Figure 2.6 shows the formation of hairpins and the influence of the Re number in its dimensions. The hairpins can be found individually, but due to its auto-generation mechanism, it is also possible to observe them as a streamwise-organized package of hairpins (Adrian, 2007). Another notable aspect is the role of strong vortical structures as a source of pressure disruption due to their low-pressure centers that induce high-pressure regions in the neighboring flow (Robinson, 1991)

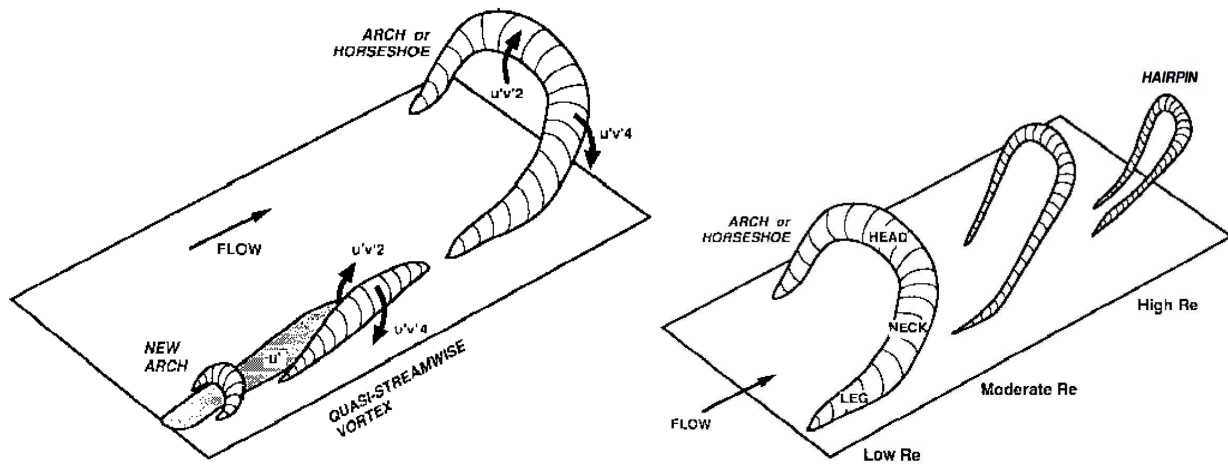


Figure 2.6. Vortical structures: quasi-streamwise and transverse vortices (Robinson, 1991, permission for use in Appendix D).

..

2.2 Drag Reduction Using Superhydrophobic Surfaces

The use of superhydrophobic surfaces (SHS) has proven to provide significant drag reduction without requiring the consumption of extra energy. The SHS originates an air-water interface between the solid surface and the main flow. At the interface the no-slip boundary condition is relaxed and the skin friction is reduced. This passive technique is reviewed by first introducing the fundamentals and working principles, followed by its characterization (contact angle, hysteresis and slip length) and its use in applications with turbulent flow.

2.2.1 Fundamentals

An SHS forms a water-repellent interface over a solid wall by holding pockets of air in its nano-/micro-pores. Hence, when the water flows over the surface, it is in contact with an air layer (also denominated air plastron) instead of the solid surface, easing the no-slip boundary condition (Rothstein, 2010). Its application has proven to reduce drag over a broad range of Re , in the laminar and turbulent regime (Bidkar *et al.* 2014).

The development of these surfaces was inspired by water-repellent properties seen in plants, animals, and insects. For example, lotus leaves, water-strider legs, and ducks feathers, among others (Golovin *et al.* 2016). Nowadays, these surfaces are usually manufactured by any of the following three procedures (Kim, 2008): i) roughening the surface of hydrophobic materials, ii) creating rough topographic features followed by hydrophobic treatments, and iii) depositing hydrophobic materials (e.g., aerosol spray coating) over surfaces with random roughness. The techniques requiring the manufacturing of surfaces with regular patterns, or accurate textures, are difficult to scale-up for large surfaces and are mainly used in microfluidics applications. Conversely, certain techniques, such as the aerosol spray coating, aerogel and thermal spray over random textures, are easily applicable in the manufacturing of large surfaces like in marine vessels (Bidkar *et al.* 2014).

Typically, the micro- or nano-sized roughness elements are organized in these surfaces (natural or synthetic) in one level or as hierarchical structures. These hierarchical structures are critical in preventing water from wetting the surface. The lotus leaf has a rough surface with a multilayer of micrometer-sized protrusions (sets of convex cells) covered in hydrophobic wax crystalloids

(Barthlott and Neinhuis, 1997). The water-striders have thousands of hydrophobic hairs (microsetas) with fine nano-grooves on their legs, which allow them to stand and move rapidly over water (Gao and Jiang, 2004).

Rothstein (2010) explains that surfaces will get partially or fully wet depending on the hydrophobicity of the material, the static pressure in the water and the particular geometry of the protrusions. All these factors contribute to the main challenge of using superhydrophobic surfaces in underwater applications: the longevity of the surface. Underwater, the air plastron formed in the superhydrophobic surface has a lifetime limited by the progressive dissolution of the air into the water. This effect worsens at higher flow rates and pressures (Peng *et al.* 2017).

2.2.2 Wetting Phenomenon

The wetting model for a drop on an ideal rigid, homogeneous, flat and inert surface is defined by Young's equation (Yan *et al.* 2011). The liquid is said to get in contact with the solid surface per a contact angle α , which is related to the interfacial tension. At each interface, the contact lines are formed with the purpose of reducing the surface area and balancing the tension forces in the direction of potential motion (equilibrium position attributed to Young):

$$\cos \alpha = \frac{\gamma_{SV} - \gamma_{SL}}{\gamma_{LV}}, \quad \text{Eq. 2.35}$$

where γ correspond to the surface tension of each interface (SV, SL, and LV correspond to the interfaces between solid, liquid and vapor respectively, as shown in Figure 2.7.

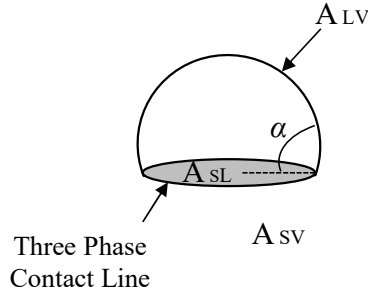


Figure 2.7. Sketch of a liquid drop showing the contact angle θ balanced by three interfaces. The letter A indicates the interfaces as well as their contact areas. SV, SL, and LV correspond to the interfaces between solid, liquid and vapor respectively (adapted from Yan *et al.* 2011).

Nevertheless, it is not possible to apply the ideal conditions of Young's model for all the cases. Hence, as shown in Figure 2.8, there are two types of wetting states (Rothstein, 2010, Yan *et al.*, 2011): the homogeneous state (or Wenzel state) and the heterogeneous state (Cassie-Baxter state).

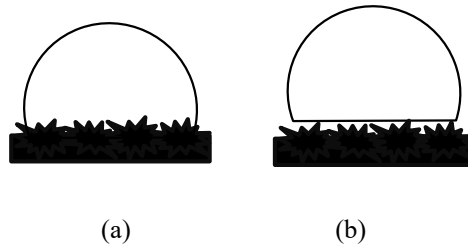


Figure 2.8. The homogeneous wetting state (a) and heterogeneous wetting state (b). The liquid drop in the homogeneous wetting state follows the solid surface and penetrates into the grooves caused by the protrusions; the liquid drop in the heterogeneous wetting state only contacts the top of the protrusions, leaving air below into grooves (adapted from Yan *et al.* 2011).

In the homogeneous state, or Wenzel state, the water enters the surface cavities. Wenzel (1936) related the contact angle to the surface roughness through the following equation:

$$\cos \alpha_W = k_r \cos \alpha ; \quad \text{Eq. 2.36}$$

where α_W is the equilibrium contact angle of the Wenzel state (which is different than the 'real' contact angle), and k_r is the roughness parameter, defined as the ratio of the actual wetted area to the projected area of the surface (Rothstein, 2010).

On the other hand, in the heterogeneous state (or Cassie-Baxter state), the hydrophobicity of the surface's roughness structures prevents water from filling the grooves. The hydrophobic property of the surface originates an air-water interface held in place by the roughness elements. The stability of this heterogeneous state will be limited by the maximum static pressure supported before the air-water interface fails and the water fills the surface grooves (Rothstein,2010). The equilibrium contact angle (α_C) in the Cassie-Baxter state is proportional to the amount of air in the air-water interface ($1-\phi_s$, where ϕ_s is the wetted area fraction of the surface roughness):

$$\cos \alpha_C = -1 + \phi_s(1 + \cos \alpha); \quad \text{Eq. 2.37}$$

2.2.3 Characterization of a Superhydrophobic Surface

The characterization of SHS is commonly done with the resulting contact angle, contact angle hysteresis and the slip length. The equilibrium contact angle (or static contact angle) and the contact angle hysteresis $\Delta\alpha$ are used to describe the wetting state of a surface. The $\Delta\alpha$ is defined as:

$$\Delta\alpha = \alpha_A - \alpha_R, \quad \text{Eq. 2.38}$$

where α_A is the advancing angle, and α_R is the receding angle (see Figure 2.9). In the case of a stable superhydrophobic state, the static contact angle (α_A) should be as high as possible, and at least greater than 150° . Additionally, the value of $\Delta\alpha$ should be as small as possible (Yan *et al.* 2011). Drops with small contact angle hysteresis $\Delta\alpha$ (within 5°) will roll easily over the surface without leaving material stuck to the surface.

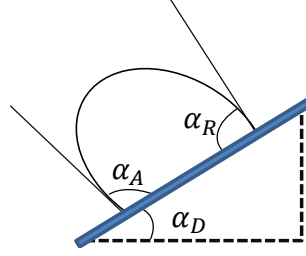


Figure 2.9. A liquid drop that is theoretically sliding on a declination of θ_D without acceleration. α_A is the advancing angle, and α_R is the receding angle (adapted from Yan *et al.* 2011).

The slip length corresponds to the distance inside the solid wall where the velocity is equal to zero when extrapolated (Vinogradova and Belyaev, 2011). Hence, a large slip length translates into a low friction force in the liquid-solid interface. The following equation describes the dependency between the slip length (b) and the slip velocity (u_s):

$$u_s = b \frac{\partial u}{\partial z}, \quad \text{Eq. 2.39}$$

where $\partial u / \partial z$ is the local shear rate. The no-slip condition would then correspond to $b = 0$.

There are three main categories of slip boundaries defined by the dynamic of the fluids at the interface (Vinogradova and Belyaev, 2011):

- i) Molecular (or intrinsic) slip: for liquid molecules slipping over the solid surface. The slip length b is estimated to be below 10 nm; it has not a major effect on large-scale flow phenomena (see Figure 2.10a).
- ii) Apparent slip: used to describe interfacial regions like the one formed by a lubricating “gas film” (see Figure 2.10b). Vinogradova and Belyaev (2011) presented the “gas cushion model” of hydrophobic slippage to calculate the apparent slip:

$$b = e \left(\frac{\eta_B}{\eta_g} - 1 \right) \cong e \frac{\eta_B}{\eta_g}; \quad \text{Eq. 2.40}$$

where e is the ‘gas film’ thickness, and η_g is the viscosity (different to its bulk viscosity η_B).

- iii) Effective slip, b_{eff} , is calculated in a complex heterogeneous surface by averaging the flow over the entire experimental configuration (see Figure 2.10c). Hence, instead of

evaluating the phenomenon at the micro-scale of a specific heterogeneous surface roughness, the problem is simplified by studying the fluid motion at a macro-scale (larger than the surface roughness patterns) using effective boundary conditions to describe an imaginary smooth surface that imitates the true surface (Vinogradova and Belyaev, 2011).

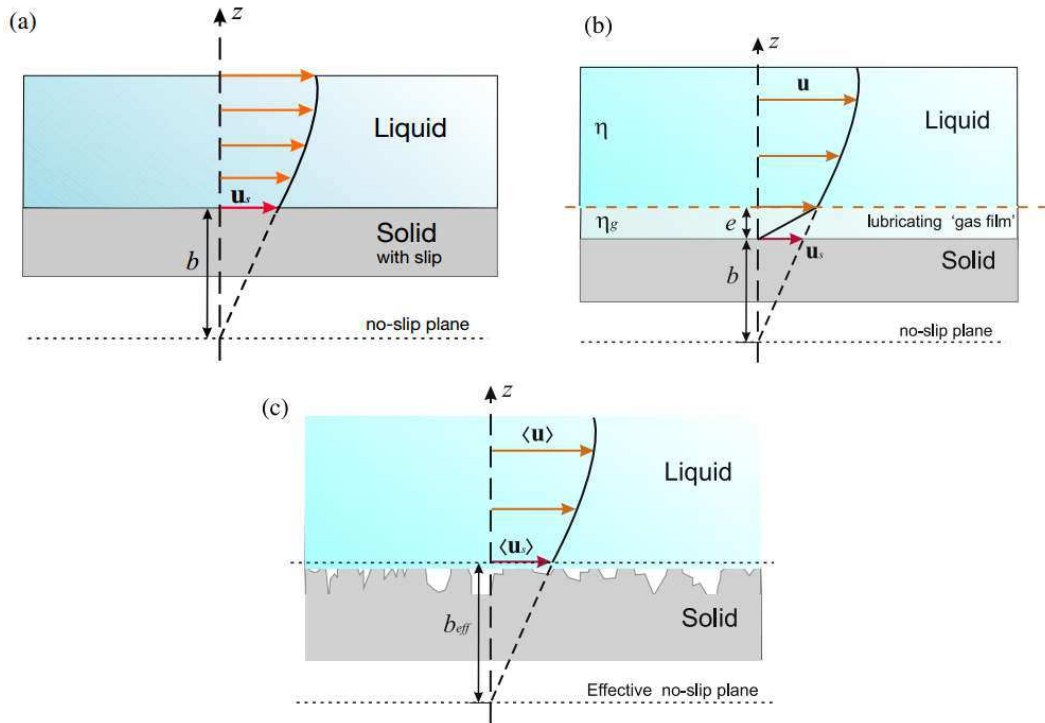


Figure 2.10. Schematic representation of the definition of (a) intrinsic, (b) apparent, and (c) effective slip lengths (Vinogradova and Belyaev, 2011, permission for use in Appendix D).

Depending on the disposition of SHS nano-/microfeatures, geometry, and distribution, the SHS might be considered as a rough surface. Nonetheless, this does not mean that the SHS will increase the drag when the surface is completely exposed; the performance of wetted SHS with random textures has been seen to be equivalent to a hydrodynamically smooth surface (Gad el Hak, 2013). Contrary to the intuitive definition of the slip length over a smooth surface, the definition of a slip length for a rough surface is still challenging. The uncertainty comes from the location selected for the reference surface used to locate the velocity profile and calculate the slip length. The location selected for the reference surface has an important impact on the magnitude of the slip reported (Lee *et al.*, 2014).

Figure 2.11 displays the different options reported in the literature for the location of the reference surface/boundary plane according to the characteristic of the surface nano-/microstructures. The definition of the boundary plane over the smooth surface is clear as it coincides with the solid surface; however, in a rough surface, its location can be selected at the top of the peaks/features, at the valleys/bottom of the features, or somewhere between these two limits. If it is located at the top of peaks/features, the resultant slip might be overestimated; however, if the boundary is located at the valleys within the peaks/features, the slip might be underestimated (Joseph, N. 2015; Lee *et al.*, 2014). Therefore, the results interpretation should always consider the location of the reference surface. In any case, the convention is that the slip velocity is positive if it is located below the reference surface.

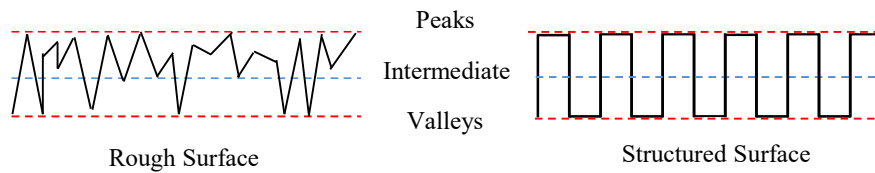


Figure 2.11. Three different choices of the reference surface to establish interfacial slip for a rough surface, and a structured surface containing fabricated pillars (adapted from Lee *et al.*, 2014).

Experiments working with a high magnification at the wall of SHS (Mongruel *et al.* 2012, Joseph, P. *et al.*, 2006, Ling *et al.*, 2016), have reported a better collapse of the data when treated as a rough surface regarding the selection of the reference plane $y = 0$. The selection of the roughness average height follows the discussion of Perry *et al.* (1969), Kunert *et al.* (2007), Brzek *et al.* (2008), and Chan *et al.* (2015) regarding TBL theory over rough surfaces (spheres, plates, and pipes).

Kunert and Harting (2007) introduced the term “effective no-slip plane” when studying different rough surfaces through DNS. Using this new term, the slip length is the distance between the reference $y = 0$ and the effective no-slip plane. In their investigation, the roughness of each surface was characterized with a maximum and minimum height (h_{max} and h_{min}), and an average height (h_{avg}). Their results showed that the location of the effective no-slip plane (h_{eff}) was higher than the h_{avg} for all the cases. Subsequently, some researchers have selected as a reference plane ($y = 0$) the top of the peaks to work in a range where the resultant slip length would always be

positive (Joseph, N. 2015). Kunert and Harting (2007) also argued that the instruments used to characterize surfaces textures would use the top of the roughness peaks as the location of the main surface reference. Investigations using atomic force microscopy (AFM) and research in microfluidics, have shown a good collapse of the data when the reference surface is located at the peaks of the roughness (Bonaccorso *et al.* 2003, Vinogradova and Yakubov, 2006 and 2011, Brzek *et al.* 2008). Lee *et al.* (2014) present a summary of the investigations (experiments and simulations) done in the past regarding interfacial slip on rough, patterned and soft surfaces. Yet, there is not a conclusion, or general agreement, about the best location to place the reference plane $y = 0$ and estimate the slip velocity in a rough surface, with or without superhydrophobic coating.

2.2.4 Superhydrophobic Surfaces in Turbulent Flows

Theoretical and numerical simulations have proven the direct impact of the SHS on the structures present in a TBL (Rothstein, 2010, Aljallis *et al.* 2013). Reports of the slip velocity have provided a better understanding of the DR mechanism in this regime. Min and Kim (2004) direct numerical simulation (DNS) showed the impact of the slip velocity direction: in the streamwise direction, the slip velocity resulted in a decrease of the drag and wall shear stress reduction; and in the spanwise direction, there was an increase of both drag and turbulence. Martell *et al.* (2009) DNS of micropost and microridges features on a turbulent channel flow resulted in a DR of 40%, and a slip of 75% the average flow velocity. Rastegari and Akhavan (2015) proposed an analytical expression to calculate DR as a function of the slip velocity. Their comparison with DNS data showed that the effective slip on the wall contributes to 80-100% of the total DR; leaving up to a 20% due to the attenuation of turbulence.

Even though most of the numerical simulations and theoretical analysis have predicted significant DR in the turbulent regime, the experimental results have been difficult to obtain. This is mainly due to the ideal assumptions of the DNS; such as the no air loss in the air-water interface (Hangjian *et al.* 2016).

Bidkar *et al.* (2014) reported a 30% DR in the turbulent regime using SHS with random textures. They concluded that the non-dimensional surface roughness k^+ needs to be considerably smaller (one order of magnitude as a minimum) than the non-dimensional viscous sublayer thickness.

They emphasized the importance of interconnected porosity on the surface to improve the capability of preserving the Cassie-Baxter state.

The experiment of Ling *et al.* (2016), using digital holographic microscopy (DHM), characterized the velocity profile, shear stresses, and turbulence intensities in the inner layer of a TBL. The magnitude of the slip velocity reached up to 38% of the bulk velocity over a nonporous surface, and a maximum DR of 36% was observed. Higher slip velocities lead to higher DR. Recently, Abu Rowin *et al.* (2017) characterized the inner and outer layers of a turbulent channel flow with a random textured SHS. A slip velocity of 13% the bulk velocity resulted in a DR of 19%. These experiments, among others, have reinforced the key role of the slip velocity in the DR results. The existence of a slip velocity at the wall modifies the turbulence statistics and the coherent structures (Ling *et al.*, 2016).

Balasubramanian *et al.* (2004) studied the use of an SHS over an ellipsoidal body in the laminar regime and obtained 14% DR at $Re = 5.5 \times 10^5$ and with a 0° angle-of-attack. However, the DR decreased at higher Re and with increasing angle-of-attack. Zhang, S. *et al.* (2015) applied a superhydrophobic coating on a submarine model and obtained up to 15% DR in the laminar regime at $Re = 1.2 \times 10^5$.

The effectiveness of the SHS in the turbulent regime has been seen to be directly related to the stability of the air layer (Samaha *et al.* 2001, Bidkar *et al.* 2014, Vajdi Hokmabad & Ghaemi 2016, and Abu Rowin *et al.* 2017). Additional to the time submerged in water, high shear rate flows enhance the dissolution of the air layer into the flow (Vajdi Hokmabad & Ghaemi, 2017). Although improvements are being sought, SHS retain the air layer for hours and not often for days (Xu *et al.* 2014). Further investigation of the air plastron morphology under high shear flow is required for a complete study of its efficiency and longevity.

2.3 Drag Reduction Using Air Injection

In the case of the air injection for drag reduction, the two-phase flow can remain as a continuous air layer or as a bubbly mixture over the surface. The requirements and working principle of each configuration is different. The drag reduction mechanism of the air layer work under the same principle of the SHS by creating a slip velocity at the wall. And, in the case of bubble drag reduction, the bubbles attenuate the formation of turbulent structures near the surface and decrease Reynolds stresses (Lu *et al.*, 2005). Both configurations are studied in the following subsections. The fundamentals, requirements, challenges, and previous applications are explored.

2.3.1 Fundamentals

The injection of air into the TBL has reduced drag among 80-90%. It has enabled the possibility of sustaining its effect over a long period and under continuous use (Elbing *et al.*, 2008).

Murai (2014) explained the DR mechanism of the air injection using the general mathematical definition of the friction drag force (F_{FD}) as follows:

$$F_{FD} = C_f \frac{1}{2} \rho (U_w - U_f)^2 A_w \quad \text{Eq. 2.41}$$

where C_f is the frictional coefficient, ρ is the density of the fluid, U_w the velocity of the moving wall, U_f is the fluid velocity outside the boundary layer, and A_w is the area of fluid in contact with the wall. An engineering approach, as Murai (2014) explains, dictates that the drag can be reduced by making any of the variables at the right of Eq. 2.41 smaller. However, a greater impact could be achieved by reducing the squared term, which is the relative velocity between the body wall and the fluid ($U_w - U_f$). Since reducing the speed of the moving object is not the goal, the following factors are means by which the injection of air reduces the drag (Murai, 2014):

- the local average density ρ decreases in the near-wall region due to the increased void fraction (this is known as the inertia effect of DR, the dynamic viscosity is reduced);
- the solid wall surface A_w is reduced by retaining large air bubbles over the surface;

- the full replacement of the solid-water interface by an air-water interface reduces the drag to a minimum due to the lower friction of the air. In consequence, it is possible to create a slip velocity close to the surface (Ceccio, 2010).

Sanders *et al.* (2006) and Elbing *et al.* (2008) identified three main regions according to the air distribution over a flat plate (see Figure 2.12):

- 1) bubble drag reduction (BDR) region: bubbles are initially formed and are seen individually distributed along the TBL,
- 2) the transition region: bubbles start grouping and coalescing, and
- 3) air layer drag reduction (ALDR) region: a continuous air layer is formed between the surface and the liquid.



Figure 2.12. Distribution of the air injected beneath a flat plate, (a) bubble drag reduction (BDR) and (b) air layer drag reduction (ALDR)

Murai (2014) collected and analyzed the data of technical papers (from 1963 to 2005) from a different research groups reporting successful DR using horizontal channel flows. Murai (2014) was able to identify seven different sub-categories among the BDR and ALDR (see Figure 2.13). Unique features characterize each sub-category/region. Hence, each of them has a different interaction with the TBL, a different drag reduction mechanism and an optimum operation range (flow stream speed, gas flow rate, etc.).

The sub-categories based on BDR are:

- i) microbubble regime: bubbles smaller than coherent structures,
- ii) mesoscopic bubble regime: bubbles comparable in size to coherent structures,
- iii) large bubbles regime: bubbles are larger than the coherent structures in the TBL,

- iv) rheological effect regime: the viscous properties of the bubbles influence its response to rapidly applied shear, and
- v) fat bubbles comparable to the boundary layer.

Conversely, the discussed sub-categories based on ALDR are:

- vi) gas cavity effect regime: the body geometry induces the formation of a stable air layer through flow separation within an air cavity (Ceccio, 2010), and
- vii) the gas layer effect regime: characterized by its natural formation; it does not use any geometrical feature (Elbing *et al.*, 2008).

This variability of mechanism has hampered the scaling up and, in some cases, the replication of drag reduction results.

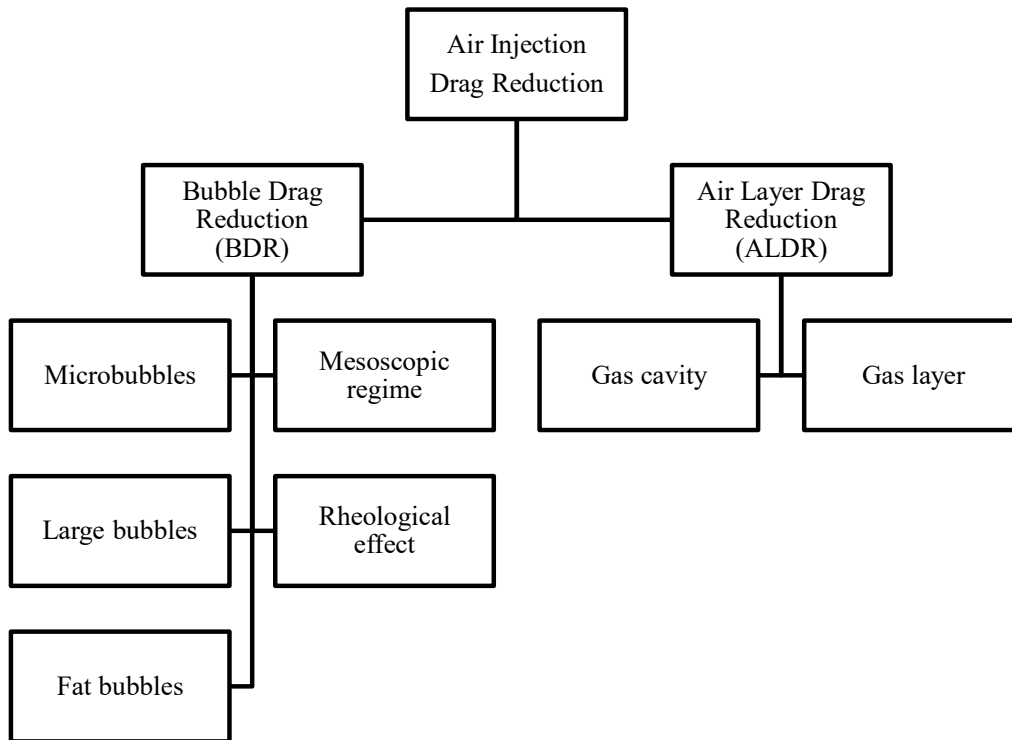


Figure 2.13. Drag reduction (DR) techniques using air injection and its sub-categories according to Murai (2014).

2.3.2 Bubble Drag Reduction

Several mechanisms of DR have been proposed to explain the bubble drag reduction (BDR), and there is a general agreement in that multiple mechanisms may be acting simultaneously (Elbing *et al.*, 2008). Based on Lumley's (1973, 1977) polymer DR hypothesis, it is said that the air bubbles change the momentum transport in the boundary layer by modifying its turbulent small-structures. Lu *et al.* (2005) observed, in the case of successful DR, that the bubbles avoided the formation of new turbulent structures near the surface and decreased the Reynolds stresses at the wall. Ceccio (2010) considers the following reasons for the bubbles effect on the drag reduction:

- the influence of the compressibility added by the air bubbles to the near wall region (Lo *et al.* 2006), and also
- the processes by which the bubbles interact with the boundary layer (splitting and coalescence - Meng and Uhlman (1998), scattering and clustering) as it can affect the production and dissipation of the turbulent kinetic energy.

In general, it is seen that the DR highly depends on how the bubbles mix into the boundary layer and interact in the near wall region. This is in agreement with the understanding that most of the turbulent transport processes (which have a direct influence on the production of friction drag) happen within a few tens of wall units of the surface (Ceccio, 2010 and Pope, 2000). Although the reduction of the bulk density in the near wall may have an important role decreasing the shear stress at the wall ($-\rho\langle uv \rangle$), the DR also depends on the bubbles effect over the turbulence production (Murai, 2014, Elbing *et al.*, 2008). Otherwise, the drag reduction would scale with the near-wall void fraction (Elbing *et al.*, 2008). The latter has been proven not to always be fulfilled. Gabillet *et al.* (2002) observed that the near wall turbulence increased linearly with the void fraction when injecting air in a horizontal channel. They concluded that the bubbles had a similar effect on DI as it would have the addition of surface roughness.

Different results have been obtained when the bubble-liquid interaction occurred in vertical and horizontal flows, in internal and external flow, in a fully developed and in spatially developing flows. Thus, it is important to consider all the roles that the bubbles might play in the TBL. This variability of the DR mechanism and the physical characteristics of the experiments makes

difficult the results comparison. A universal scaling law to collapse all the experimental results is still missing (Elbing *et al.* 2008).

Efforts have been made to obtain a proper correlation of the DR percentage with an independent parameter (liquid flow speed U , the effective air injection rate Q_a , the mean bubble size, etc.). In previous studies, the DR percentage has been vastly correlated with the void fraction (C_v or $\bar{\alpha}$) in the TBL. Madavan *et al.* (1985) proposed the following equation:

$$C_v = \frac{Q_a}{Q_a + Q_W} \quad \text{Eq. 2.42}$$

$$Q_W = UB_i(\delta_{99} - \delta^*) \quad \text{Eq. 2.43}$$

where Q_W is the volumetric flux of the liquid which is calculated as a function of the unmodified momentum boundary layer; δ_{99} is the boundary layer thickness, δ^* the displacement thickness, and B_i is the injector span. Elbing *et al.* (2008) explains that this correlation does not offer a good correlation with the data of different flow configurations as it neglects other parameters affecting the DR. Subsequently, the authors presented the scaling parameter used by Deutsch *et al.* (2003) and Sanders *et al.* (2006) proposed for BDR on plates with a rough surface:

$$C_v = \frac{Q_a}{Q_a + UB_i\theta_o} \frac{u_\tau}{u_\tau^*} \quad \text{Eq. 2.44}$$

where θ_o is the momentum thickness, u_τ friction velocity for smooth surfaces and u_τ^* for rough surfaces. Sanders *et al.* (2006) proposed another scaling law for the specific case of smooth surface:

$$C_v = \frac{Q_a}{Q_a + UB_i(\theta_{o,inj} - \theta_o)}. \quad \text{Eq. 2.45}$$

The bubbles size has also been a parameter of interest for researchers. Murai (2014) was able to classify past reports according to two main parameters: the size of the bubbles and the speed of the flow. The experiments involved horizontal channel flows, flows over flat plates, and model ships. The author separated the successful case of DR in two main groups shown in Figure 2.14 according to: i) use of relatively small bubbles at high flow speed (microbubbles and small

bubbles), and ii) use of large bubbles at low flow speed (large bubbles, and for viscosity-reducing bubbles). The failed experiments are also classified into other two groups: i) the “drag increase region”, where, even with a reduction of mixture density, the effect of the bubbles increased the friction; and ii) in the “unrealizing” region, where bubbles are not able to maintain their characteristic size due to fragmentation or coalescence processes.

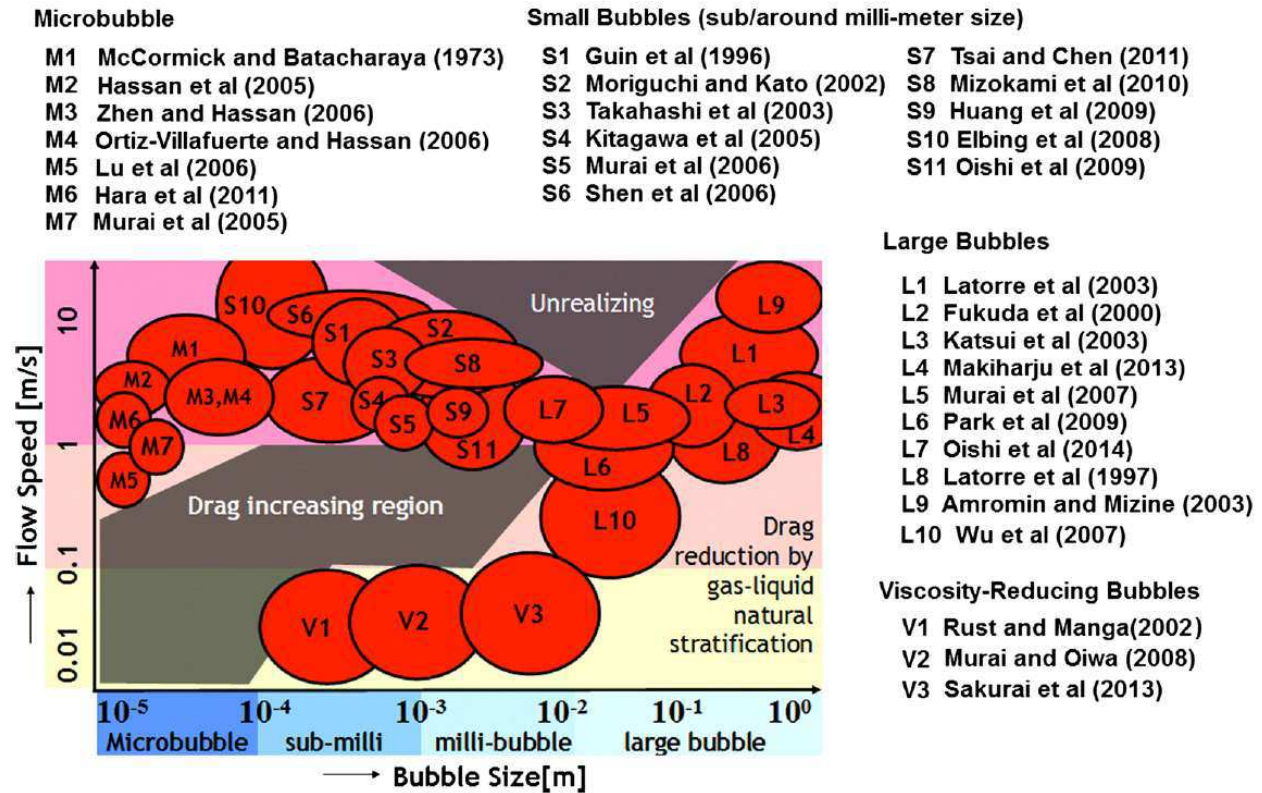


Figure 2.14. Classification of technical paper with successful drag reduction reports in horizontal channels, horizontal flat plates, and model ships (Murai, 2014, permission for use in Appendix D). The author indicates that the central position and diameter of each ellipse represent the average conditions and the estimated range of experimental tests in each article.

A small bubble is considered when its size is ten times the wall unit of the boundary layer. A large bubble is bigger than the former but smaller than the boundary layer thickness. Considering an air-water mixture, Murai (2014) explained that, at a flow speed of some meters per second, the wall unit would approximately result in $10\mu\text{m}$. Thus, a small bubble of approximately $100\mu\text{m}$, would internally modify the fluid characteristic of eddies. A large bubble ($>100\mu\text{m}$), due to its volume and compressibility, would directly affect the coherent structures in the boundary layer.

Conversely, some researchers have reported no change in the DR by using different bubbles sizes (Kawamura *et al.*, 2003, Winkel *et al.*, 2004, Elbing *et al.*, 2008). Murai (2014) presented an analysis focused on the deformability of the bubbles to explain this incongruence. The author describes that in the mesoscopic regime, regardless of the bubble size, the bubbles' deformability allows them to absorb kinetic energy and then released with a time lag. This phenomenon dampens the local acceleration of turbulence.

The first study involving the injection of air bubbles, specifically in the microbubbles region, was reported by McCormick and Bhattacharyya (1973). They obtained a 30% DR using hydrogen microbubbles (generated through electrolysis) over an axisymmetric body with a diameter of 127 mm and a length of 915 mm. The experiments were carried out in a tank with a flow speed ranging between 0.3 – 2.6 m/s. Merkle and Deutsch (1992) summarized several early studies on microbubbles DR. They found a maximum DR of 80-90% when the gas injection rate is equivalent to the volumetric liquid flow in the boundary layer.

Deutsch and Castano (1986) observed up to 20% DR over an axisymmetric body with 632 mm length at flow speeds of 4.6 m/s with air injection rates of 90-150 L/min. However, at higher flow velocity, from 10.7 to 16.8 m/s, they observed 40-60% DR. In the latter case, the DR was limited by the air flow rate required (240 L/min). The injection of air was done through a porous section, 5.17 mm wide and 6.35 mm long, with a pore size of 5 μ m.

Deutsch and Pal (1990) measured the resultant circumferential gradient of the local shear stress on an axisymmetric body while injecting microbubbles. They used the same test model of Deutsch and Castano (1986). The shear stream gradient showed maximum skin friction reduction of 80% and 92% at the top and bottom of the axisymmetric body cross-section. They confirmed that the DR is determined by the bubbles concentration and location in the boundary layer.

Clark and Deutsch (1991), studied the effects of axial pressure gradients with microbubbles. They explained, in agreement with Deutsch and Castano (1986) and Deutsch and Pal (1990), that at lower velocities, the DR is limited by the buoyancy effect over the bubbles; and at higher velocities, the DR is restricted by the required gas flow rate on the TBL. For their zero-pressure gradient, the maximum DR reached was approximately 75% at a flow stream of 10.7m/s and with an air injection rate around 600 L/min.

Shereena *et al.* (2013) used computational fluid dynamics to study the variation of the air injection rate, the angle of injection, and the angle-of-attack, in conjunction with the geometry of two axisymmetric bodies with blunt versus and streamlined tail. The model considered a ring of four air jets. The diameter of each jet represents 10% of the total model length. The highest values of DR were found at the maximum flow speed tested of 15 m/s, at 0° angle-of-attack and with an angle of injection of 30°. This condition resulted in 61% of DR with an air injection rate of 118 L/min at $Re = 4.6 \times 10^7$.

2.3.3 Air Layer Drag Reduction

The air layer drag reduction (ALDR) takes place when a continuous or a nearly continuous air layer is formed between a solid surface and the TBL (Elbing *et al.* 2008). The existence of this air layer reduces the friction to a minimum and originates a slip velocity in the air-liquid interface. This technique can offer a DR of around 90% (Ceccio, 2010). As Ceccio (2010) explained, the air layer can be formed by the permanent injection of a non-condensable gas, vaporization of the liquid (cavitation), or by the diffusion of dissolved gas from the liquid to the air cavity. The use of the air layer for DR has proven to require more technical effort as it is difficult to develop and maintain in time (Elbing *et al.* 2008, and Murai, 2014).

The formation of a stable air layer over an axisymmetric body, more specifically in underwater vehicles, has frequently been developed with the use of a cavitator at the tip of the body (Figure 2.15). As the flow moves over the body, the cavitator allows a clean separation of the flow and the formation of a cavity. This cavity can be filled by a non-condensable gas (ventilation through one or more vent ports) or with vapor (when the pressure of the cavity induces the flow vaporization). The pressure within the cavity is considered constant; however, the movement of gas into, within and out of the cavity, can produce some pressure differences (Ceccio, 2010). Moreover, the air cavity might be subject to wave oscillations that can disturb its stability.

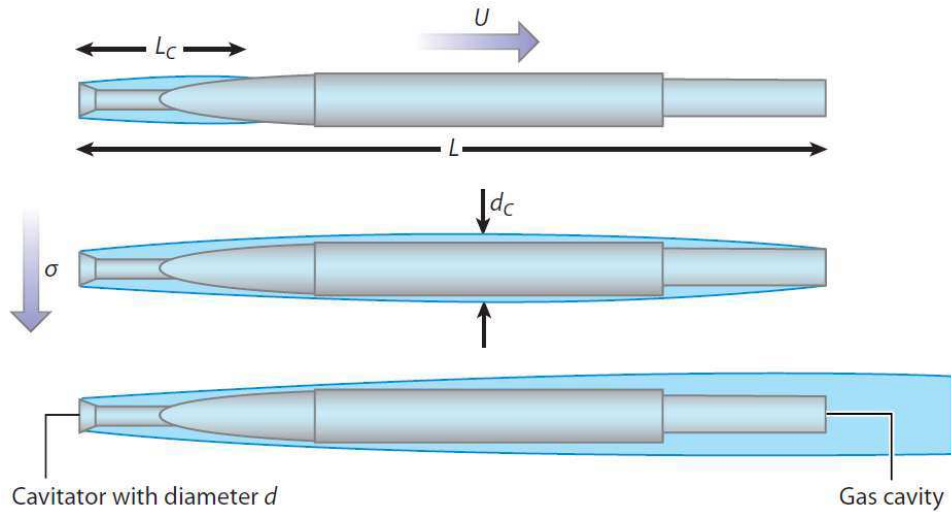


Figure 2.15. Example of canonical cavity flows for axisymmetric bodies (Ceccio, 2010, permission for use in Appendix D). σ is the cavitation number; L_c and d_c are the length scales of the air cavity.

The formation of an air supercavity (its length is larger than the body) in an underwater vehicle can offer a DR of 90% (Ceccio, 2010). However, some of the challenges are (Ceccio, 2010):

- the storage of the required amount of gas to be supplied in the case of a ventilated air cavity;
- the injection of the gas without disturbing the gas-liquid interface; and
- the control over the underwater vehicle to keep the entire body within the air cavity when maneuvering.

The formation of air layer without a cavitator has been observed in a high-speed underwater projectile (Yu *et al.*, 2015). The experimental model of Yu *et al.* (2015) had a length of 230mm and used two rows of nozzles in its elliptical head (16 nozzle per row, with a diameter of 2 mm). The air was injected by pressure difference after the projectile was launched. The air layer increased with time, but it was broken into bubbles clusters when moving to the after-body region. At 18 m/s, and after 10 ms of being launched, the length of the air layer covered approximately 55% of its total length and reduced the drag in a 25%. They concluded that the length and thickness of the air layer played a key role in the obtained DR.

2.4 Drag Reduction Using Riblets

Riblets are patterns of grooves used in aircrafts and water vehicles as a passive method to obtain drag reduction. These longitudinal grooves can reduce the drag by keeping the quasi-streamwise vortices away from the surface (Walsh, 1990). The fundamentals, characteristics, and applications are reviewed in the following section.

2.4.1 Fundamentals

The use of riblets is inspired by the skin of fast swimming sharks (e.g., Mako shark, Fu *et al.* 2017). Their skin is covered with microstructured features oriented parallel to the swimming direction; these microstructures are called dermal denticles (Fu *et al.* 2017). The shape, size, and configuration of the dermal denticles can vary among species; however, they will have the same effect (Bixler and Bhushan, 2013). These riblets surfaces naturally control turbulent vortices by preventing its formation or keeping them off the surfaces; the resulting low drag allows the shark to navigate faster in the water (Bixler and Bhushan, 2013, Fu *et al.* 2017).

The use of riblets on water vehicles and aircrafts consists of streamwise microgrooves displayed over their surface. Several geometries and configurations have been tested in the past, and a 10% DR has been obtained in the turbulent regime (Savari and Cheng, 2013, Fu *et al.* 2017). The grooves can be V-shaped/sawtooth, rectangular/blade, trapezoidal and semi-circular/scalloped, and can be displayed in continuous or segmented, with an aligned or staggered distribution (Bixler and Bhushan, 2013, see Figure 2.16). The geometry of the grooves is characterized according to its height (h), thickness (t) and the lateral riblets spacing (s). These structures lift the vortices over the surface and pin it at the riblets tip. The upward movement reduces the shear in the valleys areas and concentrates the high shear stress at the riblets tips. The cross-stream flow motion is reduced by the vortices retained above the riblets when compared with a flat plate (Bixler and Bhushan, 2013, Fu *et al.* 2017). The optimization of the riblets geometries requires a balance between a feasible fabrication process and the maximum drag reduction value that can be obtained under those conditions (Bixler and Bhushan, 2013).

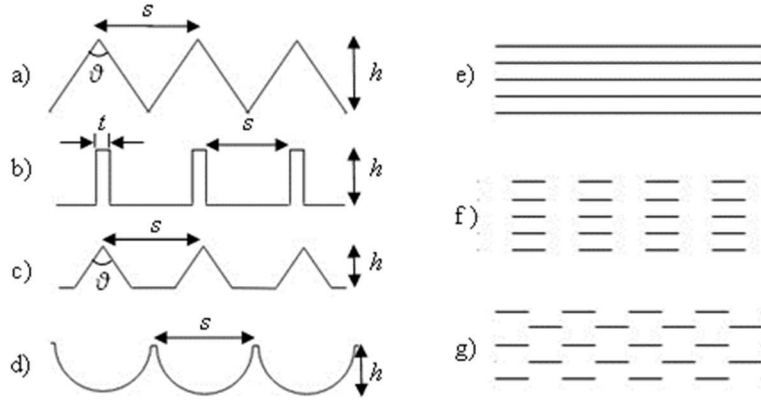


Figure 2.16. Typical shapes of riblets. Cross-section geometries: a) sawtooth/V-shaped, b) blade, c) trapezoidal, d) semi-circular/ scalloped. Configurations: e) continuous, f) aligned segmented, and g) staggered segmented (adapted from Bechert *et al.* 1997, and Bixler and Bhushan, 2013).

The DR obtained by this method is a function of the Re , the groove geometry, and the groove spacing. Walsh and Lindeman (1984) correlated the results in DR to the Re by defining the dimensionless spacing between the riblets $s^+ = s/(u_\tau/\nu)$, where s is the lateral riblets spacing, ν is the kinematic viscosity, and u_τ is the friction velocity over the smooth surface. Walsh (1979) tested sharp and curved riblets. The DR was limited to $s^+ < 30$, with maximum values of reduction at $s^+ = 15-20$.

Bechert *et al.* (1997) performed an extensive investigation optimizing riblets geometries, varying its cross-section shape and the ratio h/s . The highest values of DR, 9.9%, was obtained using the blade riblets with $h/s = 0.5$, $t/s = 0.2$, and $s^+ = 17$. This result was followed by an 8.2% DR found with the trapezoidal riblets, also at $s^+=17$, $h/s=0.5$, and with an angle $\vartheta = 60^\circ$. The sawtooth and the semi-circular scalloped riblets reduced the drag in 5%, also at $s^+=17$. The authors showed the curves of DR as a function of s^+ for all these riblets geometries. Figure 2.17 shows the general structure of a DR curve as a function of s^+ .

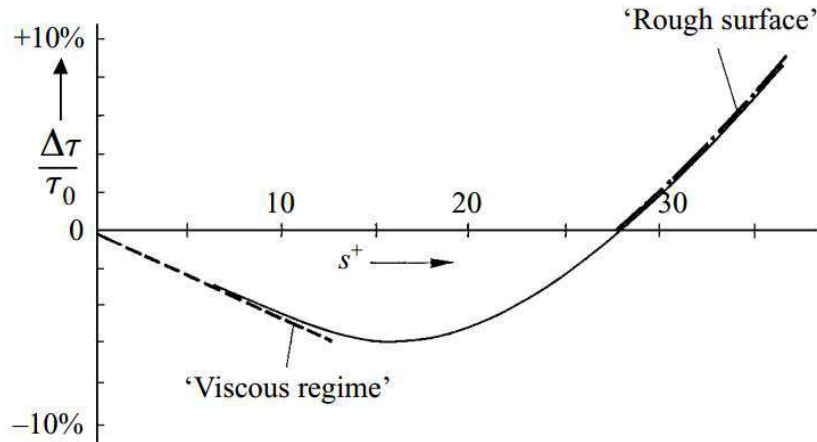


Figure 2.17. General structure of a drag reduction (DR) curve over a riblets surface (Bechert *et al.* 1997, permission for use in Appendix D).

In the region of drag reduction ($s^+ < 30$) the riblets spacing s^+ is smaller than the diameter of the longitudinal vortices. Hence, these vortical structures are lifted directly above the riblets tips, and the high shear stresses will only be present in these small areas (Koeltzch *et al.* 2002, Fu *et al.* 2017). Bechert *et al.* (1997) explain that at low s^+ the longitudinal structures hamper the crossflow near the wall, reducing the momentum exchange and the drag. As the viscous interactions are dominant near the riblets protrusions, and the non-linear terms of the flow are negligible in this region, the curve follows a linear behavior where the DR is proportional to s^+ . However, the viscous assumption breaks down in the region near the optimum spacing ($s^+ = s^+_{opt}$) where the maximum DR is obtained. After this point, the surface behavior will be similar to a rough surface, and the drag will increase (Bechert *et al.* 1997, Garcia-Mayoral and Jimenez, 2011). In the DI region ($s^+ > 30$) the vortical structures set inside the riblets grooves (Koeltzch *et al.* 2002) and the surface becomes wet. The growth of the wetted surface area boosts the interaction of the vortices and consequently increases the skin friction (Choi *et al.* 1993, Goldstein *et al.* 1995).

Recently, Hou *et al.* (2017) observed a reduction of the sweep and ejection events near the riblets by using planar PIV and quadrant analysis. This result is associated with the presence of weaker streamwise vortices over the riblets. Hou *et al.* (2017) also detected a decrease of the turbulent intensities over the riblets surface in comparison with the smooth case. If DR is obtained, the log region of the mean velocity profile shifts upward. This movement is associated with the reduction of the friction velocity and an increase in the thickness of the viscous sublayer (Walsh,

1990, Hooshmand *et al.*, 1983, Lee and Choi, 2008, Hou *et al.*, 2017). Conversely, the downward movement is related to the rise of the friction velocity and a thinner viscous sublayer.

The performance of the riblets will be affected by the quality of the machined surface and its durability. Nowadays, there is a great variety of materials (e.g., polymers, metals, etc.) and fabrication processes for its manufacturing (e.g., machining, laser etching, photolithography, extruded/coextruded polymer, 3D printing, etc.). The final result will depend on the geometry, configuration, scale, the material selected, precision, accuracy and budget (Bixler and Bhushan, 2013). As mentioned by Walsh (1990), poor quality in the manufacturing may affect the riblets geometrical parameters (rounding of the riblets tips, a variation on the riblets aspect ratios, etc.) and have an unknown influence on the performance comparison for specific geometries. Moreover, due to the small scale of the riblets, its performance is also affected by its contamination with external elements trapped between its valleys.

Gillerist and Reidy (1989) tested the use of riblets on an axisymmetric buoyant vehicle (length-to-diameter ratio of 14). The tests were performed in a lake at and involved the release of the model from a depth of 366 m directly to the surface. Then, the DR was estimated by measuring the velocity of the model when moving from the bottom of the lake to the surface. They obtained an 8% DR using a v-grooved surface ($h/s = 1$) with a $s^+ = 13-15$, and at a $Re = 14.9 \times 10^7$.

Some other experiments have been performed over axisymmetric bodies but in wind tunnels. Konovalov *et al.* (1991) tested in a wind tunnel an axisymmetric body with a v-grooved surface ($h/s = 0.5$) in the Re range of $4 \times 10^6 - 30 \times 10^6$. The maximum DR of 8% was obtained with an $s^+ = 14$, at a 0° angle-of attack. Davari (2014) reported a 10% DR by using helical riblets over an axisymmetric body in a wind tunnel.

In conclusion, the use of superhydrophobic surfaces, air injection, and riblets, in turbulent regime have shown promising results in the reduction of the skin friction drag. Further investigation is required using axisymmetric bodies to study the possibility of scaling these techniques to underwater vehicles. There is an extra interest in the study of the combined used of this techniques and see if it is possible to improve the results that each of them offer individually.

2.5 Measurement Techniques

The following section reviews the working principles of: a load cell, used for the measurement of the drag force in the test model; and the shadow-based long-range micro PTV (micro-PTV), used to study the mean velocity profile near the solid wall of the test model. Both techniques have been applied in different investigations, to measure acting forces on the tests models and study the turbulent boundary layer statistics, respectively (Balasubramanian *et al.*, 2004, Abu Rowin *et al.*, 2017).

2.5.1 Load Cell

A load cell is a transducer able to transform a force acting over the sensor into an electrical signal. These devices consist of a metal piece provided with at least one strain gauge per each of the component to be measured. The design of the strain gauge is based on W. Thomson work on electromechanical effect in 1856. He correlated the electrical resistance of a metal wire while a force is applied to it. The deformation of the strain gauge, due to the force applied, is showed as a change in the electrical resistance.

The different types of load cells are classified according to its operating principles (Tropea *et al.*, 2007):

- the number of force/momentum components that can measure simultaneously (from one to six), and
- working principle to measure the force: compression, tension, bending, shear, etc.

Some common shapes are: bending beam, s-beam, button, pancake, through holes, among others (see Figure 2.18).



Figure 2.18. Models of load cell sensors ([Loadstar™](#)).

2.5.2 Particle Tracking Velocimetry

Particle Tracking Velocimetry (PTV) is an experimental, non-intrusive, laser optical measurement technique used in fluid mechanics and aerodynamics. This technique helps to characterize flows, turbulence, spray atomization and combustion processes. The use of PTV makes possible to track the trajectories of individual tracer particles in consecutive images frames and to calculate the velocity vector of each particle (Baek and Lee 1996). The identification and location of each particle (a key step in the application of this technique) are possible due to the low number of particles per volume.

The particles are illuminated at least twice within a short time interval (Δt) by a pair of co-planar pulsed laser light sheets. The scattered light of the particles is captured by a high-resolution digital camera in two images with a Δt separation. Each image is sub-divided into small areas named interrogation windows. It is considered that the particles within a common interrogation window will show a uniform displacement. Thereafter, the average particles displacement (Δx) within the pair of PTV images is determined applying a cross-correlation and peak location algorithm within its interrogation windows. This cross-correlation process is repeated through all the interrogation areas of the recorded images. Finally, the velocity vector of each particle is derived as the displacement of the particles divided by the time delay within the pair of images ($U = \Delta x / \Delta t$). Figure 2.19 shows a schematic of an experimental arrangement for PTV.

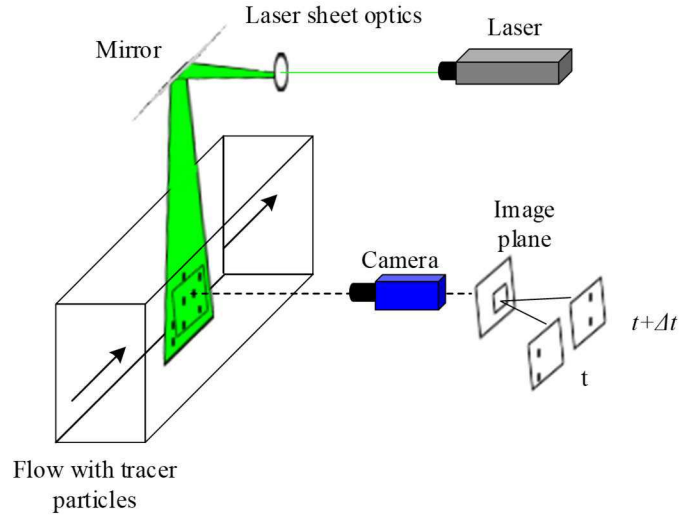


Figure 2.19. Experimental arrangement for particle tracking velocimetry (PTV). (adapted from Raffel *et al.* 2007)

The fundamentals of the seeding, illumination, imaging, processing and error analysis are presented in the following subsections. Additionally, the combined use of the shadowgraph technique with PTV is introduced.

2.5.2.1 Seeding

The selection of seeding particles should be made considering the flow characteristics, illumination and imaging requirements to guarantee a truthful representation of the flow field. Hence, the particles should faithfully follow the fluid motion without influencing it, and scatter enough light to be captured by the camera.

The gravitational forces are an important source of error on the particles motion when the density of the fluid (ρ) and the density of the particles (ρ_p) do not match. The particles' behavior under acceleration can be studied through the gravitational induced velocity U_g . This velocity can be derived using Stokes' drag law assuming spherical particles in a viscous flow at a very low Re .

$$U_g = d_p^2 \frac{(\rho_p - \rho)}{18\mu} g, \quad \text{Eq. 2.46}$$

where d_p is the particle diameter, μ is the viscosity and g is the acceleration due to gravity (Raffel *et al.* 2007). An effective particle size would offer a negligible U_g in comparison with the flow velocity (Prasad 2000a).

The size of the particle will also influence the amount of light scattered. Mie's scattering theory can be applied to particles with a diameter larger than the laser wavelength λ . Hereafter, the amount of scattered light of the particles will depend on the particles diameter, shape, and orientation, together with the ratio index of the particles to that of the surrounding medium (Raffel *et al.* 2007). Figure 2.20 shows the polar distribution of the scattered light intensity from a 10 μm oil particle in air, illuminated at a $\lambda=532\text{nm}$. The light spreads non uniformly in all the directions, showing the highest scattering intensity at the forward scattering position. However, a 90° viewing angle is commonly used to avoid a massive multi-scattering from all the particles on the field of view, and to work with a greater depth-of-field (Raffel *et al.* 2007).

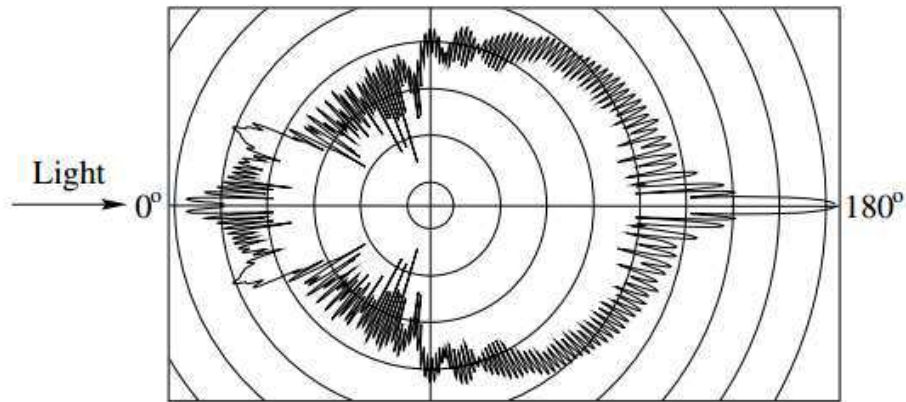


Figure 2.20. Light scattering by a 10 μm oil particle in air. (Raffel *et al.*, 2007, permission for use in Appendix D)

If the scattering light in the near-wall does not allow visualizing the characteristics of the fluid in this region, the particle concentration needs to be lower or the material to be changed. Conversely, where there are not enough resulting vectors to describe the flow, the particle concentration needs to be higher.

2.5.2.2 Illumination

The illumination is provided by a laser as light source. The laser pulse is required to be monochromatic, coherent, collimated and polarized (Raffel *et al.* 2007). Nd:YAG lasers are frequently applied for these measurements. This type of laser uses a crystal as the lasing medium, and its maximum wavelength is 1,064 nm in the infrared. However, when coupled with optics elements, it can provide a variety of different wavelengths (e.g., the green wavelength at 532nm, or the blue at 355nm). Usually, the laser is transformed into the green wavelength by a frequency

doubling crystal. The intensity of the laser is set considering the amount of light required to saturate a pixel of the camera and the amount of light scattered by the particles (Norconk, 2011). The intensity reflected by the particles cannot be higher than the intensity required to saturate the camera; if this happens, the camera can be damaged.

The beam alignment is done with mirrors and its polarization with a beam combiner. The pulse, which has a circular cross-section, is transformed into a light sheet with spherical and cylindrical lenses. This light sheet thickness is defined in conjunction with the depth-of-focus of the particle image (δ_z) to diminish blur and particles out of focus.

The pulse exposure should be short enough to freeze the particles motion and avoid distorted images (Raffel *et al.* 2007). The required two laser pulses should be independent and with a time difference (Δt). The synchronization of the two-laser pulses and the camera recording times are critical for the effectiveness of the measurement. The pulse delay is settled considering the displacement of the particles within the interrogation window. However, the pulse delay should be short enough to avoid the particles to go out of the image plane (Raffel *et al.* 2007). A general rule for setting this parameter is to consider a maximum displacement of a quarter (1/4) of the interrogation window (Keane and Adrian, 1990). Subsequently, as the flow velocity is known, the time required for this movement can be obtained from the velocity equation.

2.5.2.3 Imaging

The scattered light of the particles is captured by charge coupled devices (CCD). During the exposure time, the CCD sensors convert the light intensity into an electric charge. The charge is then stored in each of the sensor's individual elements named pixel (Raffel *et al.* 2007). A camera with high resolution, and large pixels, size is needed to obtain an image with detailed information. Moreover, when studying high speed flows, the exposure time required for the camera should be short enough to take two frames with a short time delay. The camera should also have a high spectral response, or Quantum Efficiency (QE); it offers a higher conversion rate of photons to electrons. A high conversion rate of photons to electrons is particularly helpful in adverse circumstances as: poor illumination or when using small particles.

The particle size is selected to obtain an optimal particle image size. The size of the particle in the images is affected by the light scattered, the camera sensor, and the characteristics of the lens.

Hence, to calculate the resultant size of the particle image (d_i) it is required to consider the optical (d_{opt}) and the diffraction-limited (d_s) effects over the real particle:

$$d_i = \sqrt{(d_{opt})^2 + d_s^2}. \quad \text{Eq. 2.47}$$

The effect of the optical elements is calculated as a function of the magnification (M) over the particle diameter (d_p):

$$d_{opt} = Md_p. \quad \text{Eq. 2.48}$$

The diffraction-limited (d_s) is computed considering the magnification (M), f-number ($f/\#$), and wavelength (λ) of the illumination source [15]:

$$d_s = 2.44 \times \lambda \times f/\# \times (1 + M). \quad \text{Eq. 2.49}$$

Similarly, the particle image depth-of-focus (δ_z) is calculated as function of the magnification (M), f-number ($f/\#$) and the diffraction-limited diameter (d_s).

$$\delta_z = 2 \times f/\# \times d_s(M + 1)/M^2 \quad \text{Eq. 2.50}$$

The depth of focus is used to define the laser sheet thickness. The later should be at least equal to the particle depth of focus to prevent blurred images of the particles out of focus.

2.5.2.4 Imaging processing

The images are first enhanced – in a pre-processing - by improving the contrast and illumination intensity of the particles. To run the analysis, the images are subdivided into interrogation areas which are also called “interrogation windows”. The cross-correlation, which uses a fast Fourier transform (FFT), estimates the displacement of the particles in each interrogation window by locating the highest peak of the correlation map. The peak is detected using sub-pixel peak fitting. Then, the velocity of the particles is obtained dividing the estimated particle displacement by the time interval between frames.

The veracity of the velocity vectors is finally placed in context and evaluated – post-processing. There might be false vectors due to background noise, errors in particles matching and/or in the window offset. The erroneous vectors are deleted, and the velocity profile is built with the

remaining vectors. The mean velocity profile is obtained by averaging the velocity vectors in small bins with an overlap of approximately 75%.

2.5.2.5 Error analysis

The estimation of the velocity vector field is affected by errors during the data collection and image processing. Some of the common errors explained by Raffel *et al.* (2007) and Feng *et al.* (2011) are:

- Calibration: the dimensions of objects in an image can vary from its actual values due to the limited resolution of the camera and errors in the scaling factor used to go from pixels to a physical dimension. The errors in the scaling factor come from mistakes in the calibration; the accuracy of this procedure is affected by the ability to select the center of two points separated by a known distance. This error can be reduced by using a calibration pattern with the proper scale (e.g., a small-scale pattern for a system with a large magnification) and by repeating the calibration few times to take the average of the scaling factors.
- Particle-position uncertainty: it can be originated by random noise in the data (seeding density, camera noise) or by a finite size of pixels (Feng *et al.* 2011). This will originate the peak-locking effect. Due to an error in the peak detection algorithm the location of the particle is bias to the nearest pixel, or located in a favored position (e.g., corners or middle of pixels, Feng *et al.* 2011). This error increases when working with particles smaller than 1 pixel. Nonetheless, with the proper considerations, it is possible to estimate the location of the correlation peak with subpixel accuracy (Raffel *et al.* 2007).
- Velocity errors due to acceleration: this can cause the loss of correlation information, which finally affects the accuracy of the peak detection. These errors can be due to a change on the linear acceleration, a rotational movement at a steady speed, or due to a collision with another particle (Feng *et al.* 2011). This change in the particle acceleration or trajectory will originate errors in the results of the cross-correlation applied to the pair of frames.
- Components of the setup: the measurement can be affected by the vibration of the camera and/or laser; variations in the laser pulses; noise due to changes in the temperature of the

camera sensor; optical defects and distortion. The calculations can also be influenced by the reflection of the light at the wall, the non-uniform distribution of the particles, and unknown particles in the water that might not follow the flow correctly.

2.5.2.6 Shadowgraph Particle Tracking Velocimetry

The shadowgraph technique is an optical method used to capture a media with different densities (Merzkirch, 1987). The technique uses a pulsed laser backlight illumination to cast the shadow of elements with different densities on a CCD camera (see Figure 2.21). The main differences with the traditional PTV are:

- instead of using a laser sheet to illuminate the tracer particles, the laser beam is passed through a diffuser to generate a low-intensity backlight illumination;
- the CCD camera is placed in front of the light source to capture the shadow of the tracer particles in the test volume defined by the field-of-view (FOV).

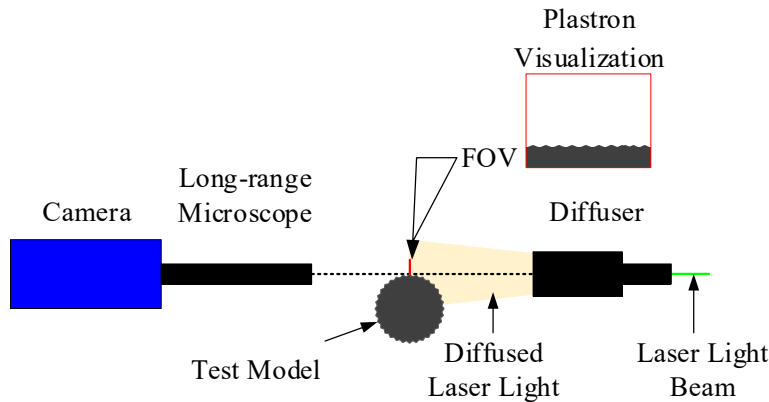


Figure 2.21. Sketch of the setup for shadow PTV over a body-of-revolution. (FOV = Field of View)

Previous researchers studying the hydrophobicity in flat surfaces have used the shadowgraph technique for the visualization of the water Cassie and Wenzel state (Jasikova *et al.* 2013, 2016). Moreover, the use of PIV and PTV techniques has been combined with shadowgraph for flow characterization (Lindken and Merzkirch, 2002, Ghaemi, *et al.* 2008).

Chapter 3. Experimental Setup and Methodology

The following chapter describes the experimental setup and measurement techniques used in the investigation. The first two subsections describe the flow facility where the experiments were carried out; and the design (background and characteristics) of the axisymmetric model used for the tests considering the characteristics of the flow facility. The following sub-sections describe the surfaces to be tested in the axisymmetric model, and the balance of the buoyancy force in the test model with the weight of its components. Additionally, the measurement techniques used to evaluate the effect of the different surfaces tested are described. The techniques considered are: load measurement and shadow-based long-range micro particle velocimetry (micro-PTV). Finally, the test performed are summarized.

3.1 Flow Facility

The experiments were carried out in the high-speed water loop located in the Department of Mechanical Engineering of the University of Alberta. This closed-water loop, displayed in Figure 3.1, is a two-floor facility equipped with a 100 hp axial pump that moves the flow to the second floor of the facility through a 0.48 m diameter pipe and vanned 90° elbows to change its direction.

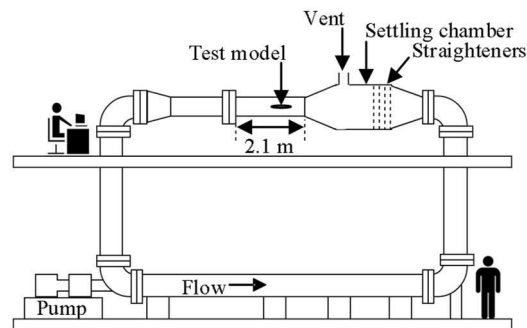


Figure 3.1. A schematic view of the high-speed water loop showing the two levels of the facility, the settling chamber, flow straighteners, and the test section. (adapted from Cowar, A. 2004)

Once the flow has reached the top floor, it goes through a diffuser section that expands the flow from the pipe to a settling chamber (height \times width \times length: $0.61 \times 0.91 \times 2.9$ m). At the beginning of this settling chamber, there are installed: a flow straightener, and a bank of eight

metal mesh screens (with two different open areas: 15 and 5 wires per inch) to generate a uniform flow through the test section.

After the settling chamber, the flow continues its trajectory to the test section through a 4:1 contraction. Before the contraction, the loop has a vent valve open to the atmosphere which avoids the pressurization of the system. Following the test section, the flow turns vertically downwards by a vanned 90° elbow and returns to the pump through a section of the 0.48 m diameter pipe.

The test section has a length of 2.1 m, as seen in Figure 3.1, and a cross-section of 0.25 m width by 0.45 m height. Figure 3.2 shows an image of the settling chamber followed by the test section. The latter section has removable transparent acrylic windows on each side, including top and bottom. The lateral windows were used to install the test model and for the outlet of an air hose and a load cell cable.

The test section was equipped with a pitot tube and a thermocouple, for velocity and temperature measurements. The pitot tube was installed in the bottom window, upstream the location of the test model, with a separation of 4 cm from the internal window surface. The thermocouple was placed at the same location as the pitot tube but in the top window.

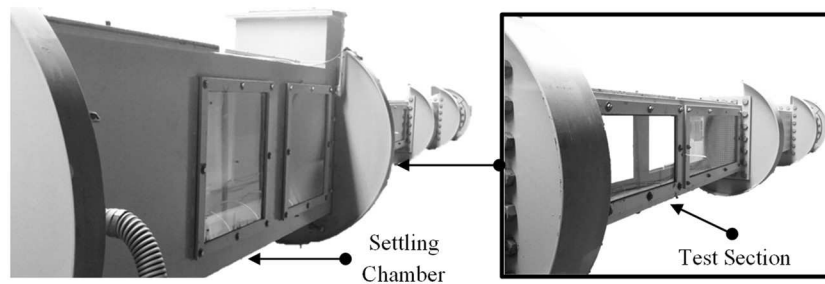


Figure 3.2. An image of the settling chamber of the high-speed water loop (left) followed by the test section (right).

The loop was filled to its maximum capacity for each test and was operated within the velocity range of 1 and 3.3 m/s. The data collection was performed at five Re : 5.0×10^5 , 7.0×10^5 , 1.0×10^6 , 1.2×10^6 and 1.5×10^6 , based on the total length of the model ($L = 0.508$ m). The Re was maintained through different tests by calculating the required flow velocity U [m/s] at the given

dynamic viscosity and density. The required value of U for each data point was calculated from the Re equation

$$U = \frac{Re \times \mu}{\rho \times L} \quad \text{Eq. 3.1}$$

This equation considers the changes in density (ρ [kg/m³]) and dynamic viscosity (μ [N s/m²]) due to the variation in the water temperature. The density and dynamic viscosity were calculated as a function of temperature using Eq.3.2 (McCutcheon *et al.*, 1993) and Eq. 3.3 (Al-Shemmeri, 2012), respectively:

$$\rho = 1000 \times \left(1 - \frac{T+288.9414}{508929.2 \times (T+68.12963)} (T - 3.9863)^2\right), \text{ where } T \text{ is in Celsius } [^{\circ}\text{C}], \text{ and} \quad \text{Eq. 3.2}$$

$$\mu = (2.414 \times 10^{-5}) \times 10^{247.8/(T-140)}, \text{ where } T \text{ is in Kelvins } [\text{K}]. \quad \text{Eq. 3.3}$$

Temperature change during the data collection period was negligible and did not have a significant effect on the velocity initially calculated.

The flow velocity upstream the test model was monitored in real time using the pressure difference measured by the pitot tube. The pressure difference (Δp) was used in Eq. 3.14 for the calculation of the flow velocity U .

$$U = \sqrt{\frac{2\Delta p}{\rho}} \quad \text{Eq. 3.4}$$

The pitot tube was connected to a pressure transducer (Valydine, DP15-30) which was in line with a sine wave carrier demodulator (Valydine, CD15). The demodulator analog output was read and converted to digital by the same data acquisition (DAQ) device (NI, USB-6000) that converts the analog input into a digital output. The signal was finally recorded using the software LabVIEW 2015 from National Instruments. The pressure transducer was calibrated using an Omega High Accuracy Portable Pressure Calibrator (DPI610).

3.2 Design of the Test Model

The following sub-sections present the design background and motivation, followed by the characteristics of the axisymmetric model used for the tests.

3.2.1 Background and Motivation

In 2009, Natural Resources Canada (NRCan) in partnership with International Submarine Engineering (ISE) developed an Explorer Autonomous Underwater Vehicle (AUV) suitable for undergoing under-ice bathymetric surveys. Given the potential of the Explorer AUV to endure in extreme cold conditions with minimum requirements, it has been used for mapping the Canadian Arctic in support of the United Nations Convention on the Law of the Sea, where the Government of Canada is committed to defining the outer limits of its continental shelf.

The Explorer AUV has a modular design, and its main sections are the nose, the variable ballast section, the pressure hull, the hydroplanes (two foreplanes, three aft planes) and the tail. A sketch is presented in Figure 3.3, and its general dimensions are shown in Table 3.1. The longitudinal section of the nose has an elliptical profile with a major-to-minor axis ratio of 2:1. The profile of the hydroplanes is a NACA0024¹. The tail's geometry, which has an important effect on the overall drag of the AUV, can be described as:

$$r_t = R \times \left(1 - \left(\frac{x_t}{L_t}\right)^2\right) \quad \text{Eq. 3.5}$$

where x_t is a variable along the tail's centerline measured from the beginning of this section, L_t is the total length of the tail, R is the main radius, and r_t is the radius at the position x_t . The ISE Explorer has a L_t/R ratio of 4.

¹ A NACA profile refers to an airfoil shape (generally used for aircraft wings) developed by the National Advisory Committee for Aeronautics (NACA)

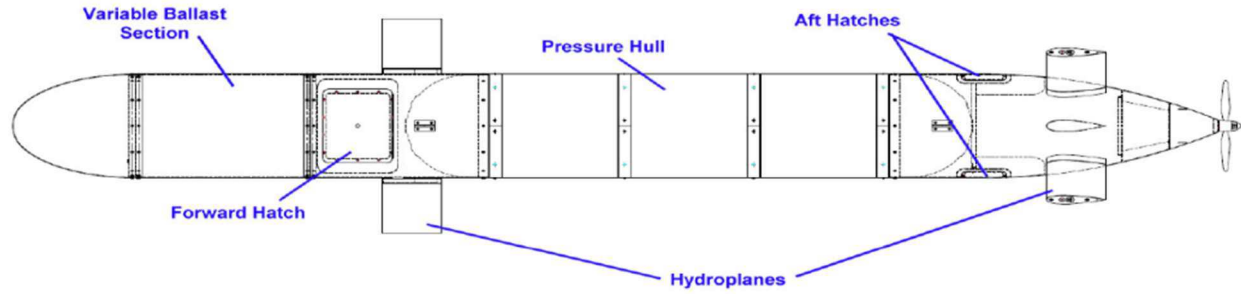


Figure 3.3. A sketch of the main components of NRCan Explorer AUV (Crees *et al.* 2010).

Table 3.1. Description of Natural Resources Canada (NRCan) Explorer autonomous underwater vehicle (AUV) (Crees *et al.* 2010)

Geometry	
Length, L_e	7.4 m
Body Diameter, D_e	0.74 m
L_e/D_e	10
Height	1.4 m (including antennas)
Width	1.5 m (including foreplanes)
Range	450 km at 1.5 m/s
Pressure Hull	Two hemispherical end domes + three cylindrical sections machined from cast aluminum
Hydroplanes	NACA 0024. Two foreplanes, three aft planes,
Performance	
Power Source	1.6 kWh Lithium-Ion Battery Modules
Endurance	24 - 85 Hrs
Effective Range	120 - 450 km
Speed Range	0.5 - 2.5 m/s

The logistics of exploring the vast Canadian Arctic seabed is currently complicated due to the limited lifetime of the lithium-ion batteries used by the Explorer AUV as a power source. In 2010, the AUV was deployed to Canada's high Arctic by NRCan. It approximately covered 1,000 km of the seabed in 3 missions during 10 days. The AUV operating range was limited to 450 km, which is equivalent to an endurance of 85 hours (Crees *et al.* 2010). The missions required two remote camps, located approximately 300 km apart. Each camp was provided with an 8 by 3 m ice hole where, without being removed from the water, the AUV was charged and the data collected was downloaded. During the missions, the AUV operated with an average speed of 1.5 m/s and reached depths of 3160 m (Crees *et al.* 2010). An AUV with longer endurance would allow exploration of a larger seafloor from a single Arctic camp, reducing exploration costs and advancing the rate of exploration. Therefore, it is of interest to study drag reduction methods such as SHS, air injection, riblets, and their combined effect over a simplified AUV model.

3.2.2 Test Model

The design of the experimental axisymmetric body, or AUV test model, follows the general hydrodynamic characteristics of the NRCan Explorer AUV. These common characteristics are: the geometry and aspect ratio of the front and rear ends, the cross-section profile of the hydroplanes, and the length (L) over diameter (D) ratio ($L/D = 10$). The model was designed to be located in the middle of a rectangular test section without being affected by the TBL developed on the walls of the test facility. The cross-section area of the model body represents 2% of the test cross-section area, and the minimum clearance between the TBL of the lateral walls and the TBL over the AUV model was at least 8 cm. Figure 3.4 displays a sketch of the AUV model in the test section.

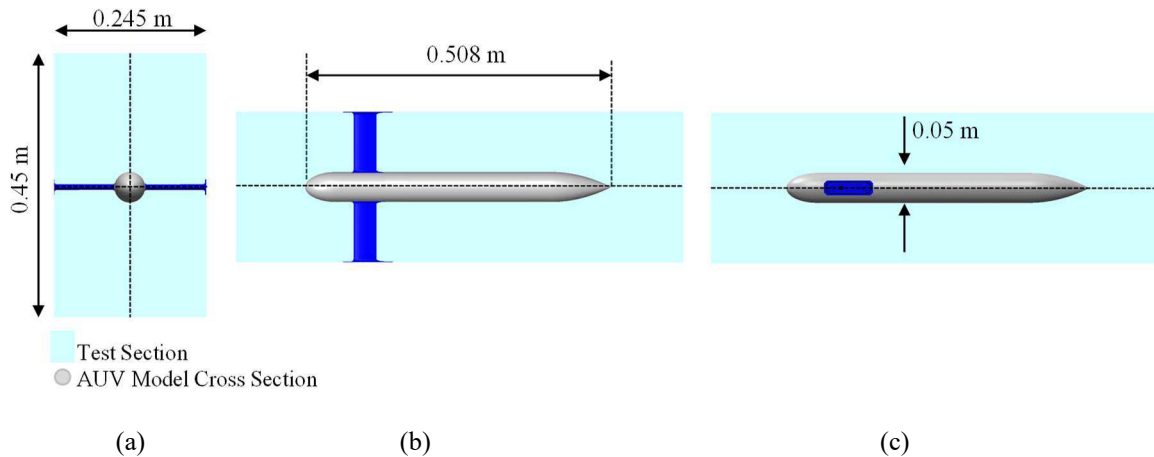


Figure 3.4. Sketch of the AUV model located on the test section: (a) side view; (b) top view of the test section; and (c) frontal view of the test section.

The test model can be divided into three major sections displayed in Figure 3.5: i) leading edge; ii) central body, which provides the model with a fixed support to the loop windows; and iii) aft body or experimental module, where the drag reduction techniques are applied. The aft planes were not considered for simplification. The general dimensions of the model are presented in Table 3.2. The AUV model was assembled and disassembled for each experiment using the same procedure. The design details are in the drawings displayed in Appendix A.

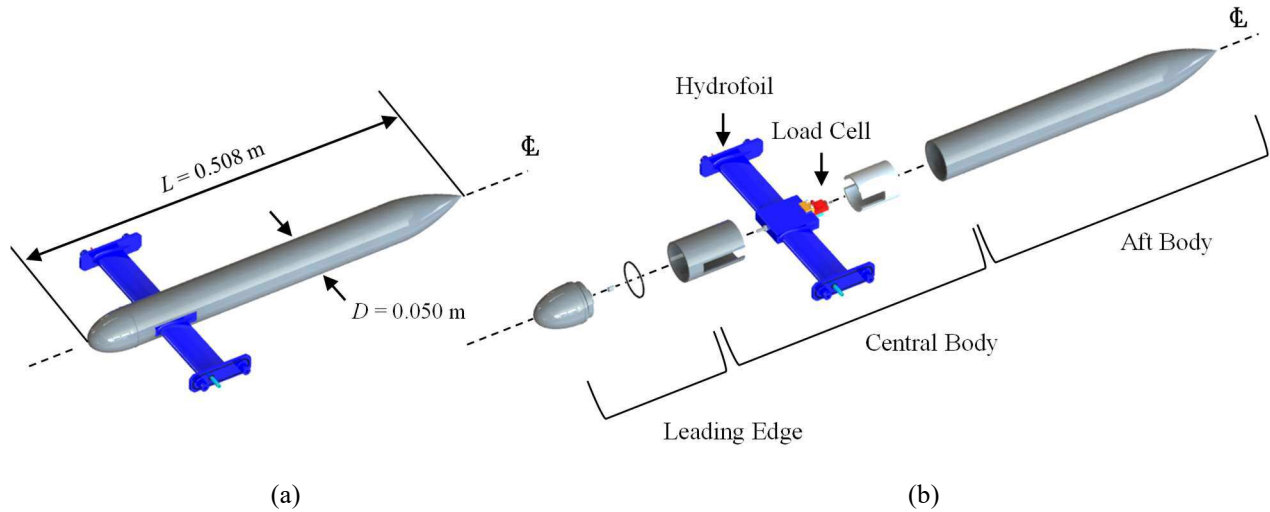


Figure 3.5. Two 3D views of the test model. (a) Displays the test model fully assembled, and (b) shows the three major sections of the modular design.

Table 3.2. General description and dimensions of the test model geometry.

Length, L	0.508 m
Body Diameter, D	0.050 m
L/D	10
Height	0.050 m
Width	0.245 m (including foreplanes)
Hydroplanes profile	NACA 0024, with maximum thickness of 17 mm

The front body, or leading edge, is displayed in Figure 3.6 and it corresponds to the nose of the submarine. This part was 3D printed in polyjet vero. It has the elliptical profile of the Explorer AUV nose, with a major-to-minor axis ratio of 2:1, and its purpose is purely hydrodynamic. The nose was provided with a 0.5 mm diameter step to enforce a laminar to turbulent transition. A threaded connection works as the union between the front and the central body.

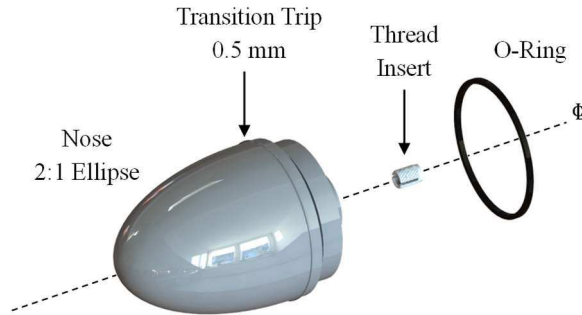


Figure 3.6. 3D views of the leading edge. The components are the nose, a thread insert, and an O-ring for the connection to the central body.

The central body was designed to provide support to the model and access to the interior of the AUV model. It is formed by the central body sleeve, the hydrofoil structure, the load cell sub-assembly, and a Teflon sleeve bearing. Figure 3.7 displays a 3D view of this module and its components.

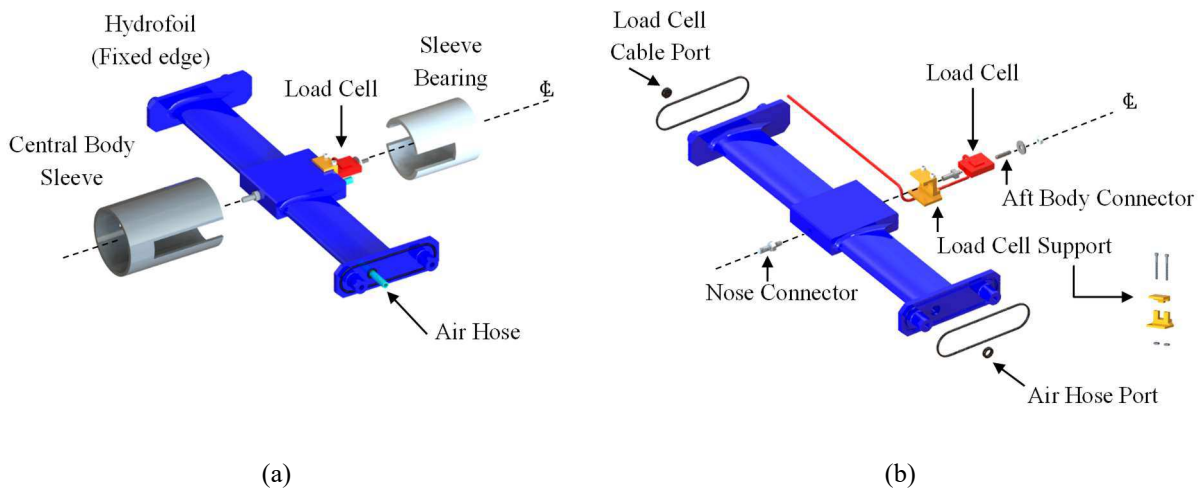


Figure 3.7. 3D views of the central body components. (a) Displays the main components, and (b) shows the hydrofoil attachments.

The central body sleeve outlines the outer surface of the AUV model front end; it covers the hydrofoil middle section and the load cell sub-assembly. This aluminum sleeve has a longitudinal rectangular groove for its installation in the middle section of the hydrofoil. The movement of the central body sleeve is restricted once the nose is screwed in the hydrofoil.

The hydrofoil extends to the windows of the test section and provides a fixed support for the model and load measurement. Both ends of the hydrofoil were provided with end-plates to be

inserted and fixed to the acrylic windows. The tolerance between the mating parts provides a gap with 3 degrees of freedom for leveling the AUV model (if required). The hydrofoil also has an internal and longitudinal cavity through which the load cell cable and an air hose pass from the exterior of the test section to the interior of the AUV model. The profile of the hydrofoil's cross-section is a NACA0024 with a maximum thickness of 17 mm.

The load cell sub-assembly works as a link between the central body and the aft body, making it possible to take a direct measurement of the drag force in the aft body (see Figure 3.8). This sub-assembly consists of a submersible load cell, two threaded connectors, a washer, and a support module. The submersible load cell is an s-beam strain gauge with a load capacity of 8.9 N in tension or compression. The load cell is centered in the longitudinal axis of the AUV model to measure the forces in this axis. As it only works in tension or compression, a large offset force or a momentum could affect the readings and damage the sensor. Two 3D printed modules are placed at the top and bottom of the threaded connection of the load cell and the hydrofoil to restrict the undesired rotation of the connector and the load cell. The forces acting on the load cell are further studied in section 3.4.

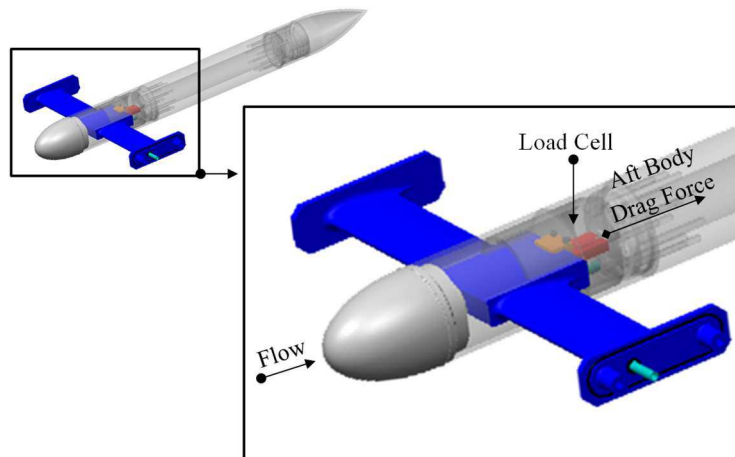


Figure 3.8. 3D view of the load cell located between the hydrofoil and the aft body, and a sketch of the axial force to be measured by the load cell.

The Teflon sleeve bearing is added to protect the load cell from a major bending. The bending of the load cell is prevented by having a press fit of the sleeve bearing between the hydrofoil and the central body sleeve and a sliding fitting with the front seal of the aft body. Thus, the sleeve

bearing allows the free movement of the aft body in the longitudinal axis, but it limits its movement in the vertical axis.

The nature of the experiment and the size of the model led to the selection of a miniature submersible load cell. This load cell is a strain gauge bonded onto a s-beam. This configuration can measure changes in the material strain/resistance when an acting force deforms the beam, and it reflects those changes with variations in its voltage output. In the test model configuration, where the hydrofoil works as a fixed edge, the load cell output only corresponds to the drag force in the aft body.

The capacity of the load cell was selected by performing an estimation of the drag force using a reference drag coefficient (C_D) and volumetric drag coefficient (C_{DV}) obtained from different researchers in previous studies. Jagadeesh *et al.* (2008) performed a study of variation in the coefficients of hydrodynamic forces over an AUV hull with different Re and values of angle-of-attack. Shereena *et al.* (2013) used computational fluid dynamics (CFD) to study the effects of air injection as drag reduction technique and showed the calculations of the C_{DV} . Nunes *et al.* (2014) used numerical analysis tools to optimize the AUV hull design with the C_D as the determining factor. Jiang *et al.* (2013) compared experimental C_D of an AUV using experimental procedures, empirical calculations, and CFD tools.

The investigations reporting the C_D used the cross-section area (S [m²]) of the axisymmetric bodies as input for Eq. 3.6.

$$C_D = \frac{F_D}{(0.5\rho U^2 S)} \quad \text{Eq. 3.6}$$

where F_D is the drag force [N], ρ is the flow density [kg/m³], and U is the flow stream velocity [m/s]. Conversely, the investigations reporting the C_{DV} (Eq. 3.7) are considering the wetted surface area, which is proportional to $V_m^{2/3}$, where V_m is the volume [m³] of the axisymmetric body.

$$C_{DV} = \frac{F_D}{(0.5\rho U^2 (V_m)^{2/3})} \quad \text{Eq. 3.7}$$

Making use of Eq. 3.6, Eq. 3.7, and the previous experimental values of C_D , an estimation of the drag force over the test model was done. For these calculations a velocity of 6.25 m/s was considered. This velocity value is two times higher than the expected maximum velocity to be used during the tests. The results are presented in Table 3.3, with the literature empirical, experimental, and numerical drag coefficients at 0° angle-of-attack.

Table 3.3. Literature empirical, experimental and numerical drag coefficients (C_D) at 0° angle-of-attack, with the estimated drag force considering the test model submerged in a water flow stream at 6.25 m/s

Authors	Type of Study	L/D	Re	Volumetric Drag Coefficient (C_{DV})	Drag Coefficient (C_D)	Estimated Drag Force [N]
Jagadeesh <i>et al.</i> (2008)	Experimental	10	3.67×10^5	0.0389	-	4.07
	CFD			0.0399	-	4.18
Shereena <i>et al.</i> (2013)	CFD	9.8	$6.6e \times 10^6$	0.0397	-	4.15
Nunes <i>et al.</i> (2014)	Numerical Analysis	9	4.2×10^6	-	0.123	4.49
Jiang <i>et al.</i> (2013)	Experimental	9.25	5.14×10^5	-	0.1726	6.30
	CFD			-	0.1673	6.10
	Empirical			-	0.165	6.02

The average of the drag forces estimated is 5.04 N, and the maximum force obtained is 6.3 N. Using these numbers as a reference, along with several manufacturers catalogs, a submersible s-beam from Futek (model LSB210) was selected. The load cell geometry, dimensions, and

working direction, are displayed in see Figure 3.9. The load cell has a capacity of 8.9 N (2 Lb) in tension and compression, which provides a safety margin of 2.6 N over the worst case scenario estimated.

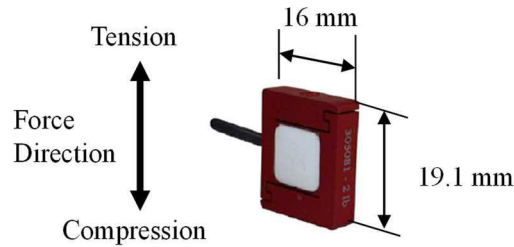


Figure 3.9. Submersible S-Beam Junior Load Cell, LSB210 (Futek data sheet)

The aft body sub-assembly is mounted on the load cell. This sub-assembly is displayed in Figure 3.10, and is constituted by the front seal, the balance weights, the replaceable body module, the aft seal and the tail. The aft body is connected to the load cell using a screwed connection in the front seal. During the assembly procedure, the sensor is attached to the front seal using the same torque every time.

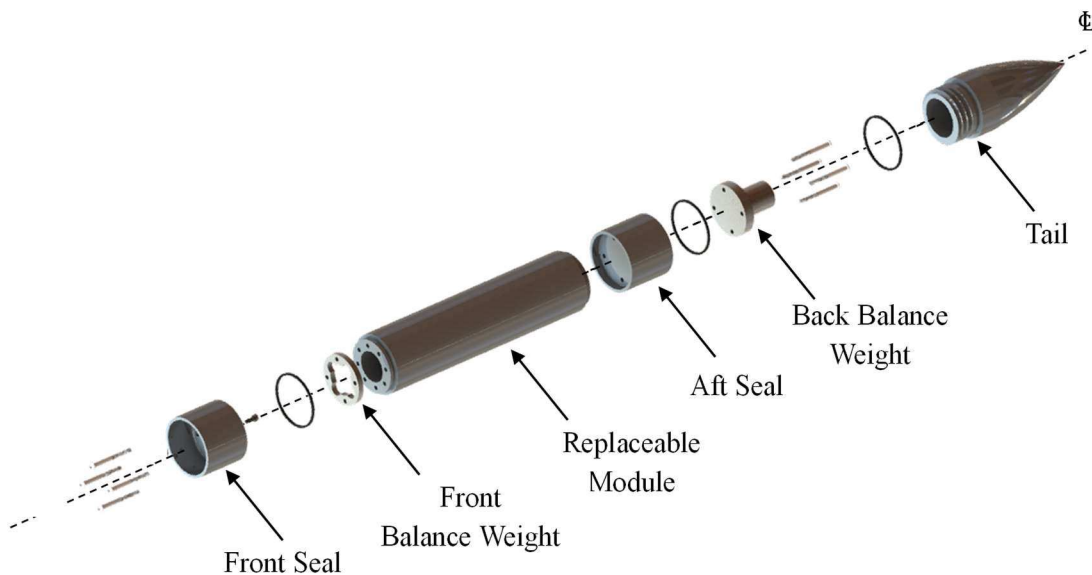


Figure 3.10. 3D view of the aft body main components

The replaceable module, where different surfaces can be tested, is held in place by the front and back seal; which also allow the pressurization of this module (if required). According to the

characteristics of the replaceable module used, the assembly requires different balance weights, or weight disks, to balance the buoyancy and gravitational forces acting in the aft body (further explanation in section 3.4). Lastly, the tail is attached to the aft seal by a threaded connection. Like the nose, the tail was 3D printed with polyjet vero, and its longitudinal profile is the same as in the Explorer AUV (Eq. 3.5).

The material for each component was selected considering its manufacturing process, wear and corrosion resistance, and its contribution to the total weight of the system. The material for the 3D printed parts was selected according to its low density (polyjet vero, 1.17 gr/cm^3) and low water absorption (polyjet vero, 1.1-1.5%). The central body sleeve, the hydrofoil, and seals were made of aluminum to take advantage of the strength of this material and its low density when compared with steel. The corrosion of these aluminum components was inhibited by the anodization of its surfaces. Table 3.4 displays a summary of the AUV main components, description, and materials. The design details are in the drawings displayed in Appendix A.

Table 3.4. Parts summary of the test model main components, description, and materials.

Sub-Assembly	Part	Main Function	Material
Leading edge	Nose	Hydrodynamic	Polyjet Vero
Central Body	Central Sleeve	Hydrodynamic	Aluminum with anodization
	Hydrofoils	Support and hydrodynamic	Aluminum with anodization
	Sleeve bearing	Protection for the load cell. Prevents the tilting of the aft body	Teflon
Load Cell	Submersible s-beam load cell, 2lb	Force measurement in the longitudinal axis of the AUV	Aluminum with anodization
	Support	Protection for the load cell. Prevents the rotation of the load cell and its threaded connection with the hydrofoil	ABS
Aft Body	Fore and aft Seals	Hydrodynamic and seals for the replaceable body modules	Aluminum with anodization
	Replaceable body module	Cylinder used to test different surfaces and drag reduction techniques (section 3.3)	Varies
	Tail	Hydrodynamic	Polyjet Vero.
	Fore and rear balance weight disk	Balance the buoyancy and gravitational forces	Aluminum with anodization

3.3 Test Surfaces

The design of the AUV model allows the use of different replaceable modules in the aft body to test various surfaces while keeping the rest of the test model unchanged. In this investigation, the replaceable module is used to test three drag reduction techniques (individually and combined): superhydrophobic surfaces (SHS), air injection, and riblets.

The drag reduction techniques are applied to three test cylinders with a test surface of 0.190 m length (l) and 0.05 m outer diameter (D). In the current investigation, the test cylinders used the following surfaces:

- i) Smooth surface: to be tested with and without a superhydrophobic coating.
- ii) Porous surface: to test the air injection, and its combined use with a superhydrophobic coating.
- iii) Riblets surfaces: two modules with different dimensions are considered to test the riblets, its combined use with a superhydrophobic coating, and with air injection.

Each of these surfaces is described in detail below.

3.3.1 Smooth Surface:

The replaceable module with the smooth surface was made with ultra-high-molecular-weight (UHMW) Polyethylene. The results obtained with this surface worked as a baseline to compare the efficiency of the different DR techniques tested. This same cylinder is used to test the effects of the SHS with random texture.

The SHS with random texture was produced using a commercial spray coating named Rust-Oleum Never Wet ®. The smooth surface module was covered with an adhesive paper (0.1 mm of thickness) to guarantee a surface without traces of coating for each SHS test. The preparation of the SHS first required the cleaning of the test cylinder. Then, the module was sprayed with an acrylic-based solution to enhance the adhesion of the superhydrophobic particles. Next, three layers of a hydrophobic coating were applied. Finally, after 12 hours of drying, each surface was

tested only one time. Vajdi Hokmabad and Ghaemi (2016) reported roughness measurements over a flat plate with the same coating and fabrication procedure used in the current study. The Ambios XP-300 surface profilometer used by them reported a root-mean-square roughness of $R_{rms} = 10.2 \mu\text{m}$ and a peak-to-trough roughness of $R_{PT} = 41 \mu\text{m}$.

3.3.2 Porous Surface

The AUV model is adapted for air injection. In the aft body sub-assembly, the front seal used is provided with a pressure fitting, and the replaceable module with a porous cylinder. The air was supplied through the hydrofoil by a hose (3/16" outside diameter, OD) connected to the front seal and distributed inside the test cylinder with an air distributor.

The replaceable module for the air injection was machined from a UHMW Polyethylene tube with 10 μm diameter pores. Previous studies of bubbles and air injection drag reduction over flat plates (Madavan *et al.* 1985, Merk and Deutsh 1989, and Elbing *et al.* 2008) concluded that the injector geometry and the porous size had little or none measurable differences on the results. The porous diameter should only influence the injection rate required to reach the most efficient point (Elbing *et al.* 2008).

Inside this porous cylinder, an air distributor was installed to guarantee a uniform air injection through the complete length of the module. The air distributor divides the interior of the cylinder in four chambers with the longitudinal panels shown in Figure 3.11. The air enters each chamber through a pattern of holes in the front face of the air distributor. As the air moves through the path of least resistance, the holes for the two top chambers are smaller than those for the two-bottom chambers. Moreover, the holes in the middle of the front face are larger than those close to the periphery. The holes in the middle, direct the air to the back of the cylinder by an internal division (similar to a tunnel) of the air distributor. The use of this air distributor improved the uniformity of the air injection.

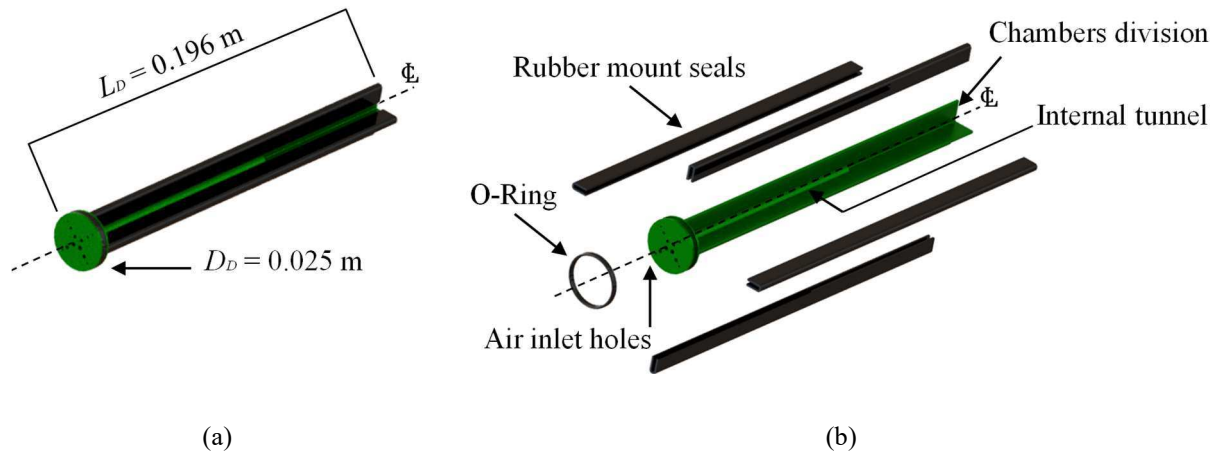


Figure 3.11. 3D views of the air distributor design (a) fully assembled and (b) disassembled components.

Two studies with the porous cylinder combined the effect of air injection and SHS. The porous material was coated with the superhydrophobic coating Rust-Oleum Never Wet ®. The preparation of the SHS first required the cleaning of the test cylinder. Then, three layers of a hydrophobic coating were applied. Based on the experiments performed by Abu Rowin *et al.* (2017), the step of spraying the acrylic-based solution was skipped because the roughness of the porous surface was good enough to retain the superhydrophobic particles. Finally, after 12 hours of drying, each surface was tested.

The laboratory's air supply line was used to feed the air injection system. The pressure and injection rate were set by a flowmeter and controller (Alicat) with a capacity of 500 slpm. The flowmeter was controlled using a data logging application in LabVIEW (Omega™ Flow Meter CPC). The air hose goes from the supply line, through an air filter, to the flowmeter and then into a control valve before going into the test section window. The air hose gets into the AUV model through a longitudinal cavity in the hydrofoil, till it reaches the fitting connection in the front seal of the test model.

3.3.3 Riblets

A UHMW Polyethylene tube, with 10 μm diameter pores, was used to obtain a base cylinder of 0.045 m diameter for the riblets modules. The riblets modules, shown in Figure 3.12, are two sleeves with an internal diameter of 0.0455 m and an external diameter of 0.05 m. These sleeves,

which slide over the base cylinder, were 3D printed in black resin and cover 37% of the total length of the model.

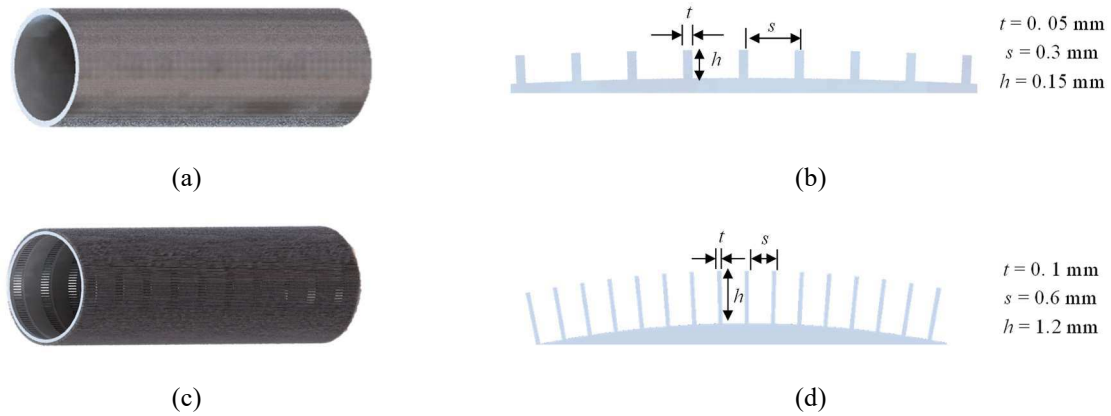


Figure 3.12. Riblets surfaces sleeves. The left column shows the 3D view, (a) for model 1 and (c) for model 2. The right column displays the riblets geometry and dimensions, (b) for model 1 and (d) for model 2.

The first riblets model (model 1) consists on rectangular grooves parallel to the longitudinal axis of the test cylinder, with a span (s) of 0.3 mm, height (h) of 0.15 mm, and thickness (t) of 0.05 mm; which correspond to the ratio $h/s = 0.5$ and a range of the dimensionless spacing of $s^+ = 15 - 40$. The geometry used here followed the non-dimensional characteristics ($h/s = 0.5$, $t/s = 0.2$) of the blade riblets used by Bechert *et al.* (1997). The effects of this riblets model are studied individually and in combination with an SHS. The sleeve surface was coated with the superhydrophobic coating Rust-Oleum Never Wet ®. The preparation of the SHS was the same used for the porous surface, which consists in the cleaning of the surface and the application of three layers of the hydrophobic coating. After 12 hours of drying, the surface was tested.

The combined effect of riblets and air injection was investigated with a second riblets model (model 2). This second riblets model also considers rectangular grooves parallel to the longitudinal axis of the test cylinder, with $s = 0.6$ mm, $h = 1.2$ and $t = 0.1$ mm, for a $h/s = 2$ and a range of $s^+ = 30 - 80$. This model was provided with staggered holes in the valleys of the riblets for air injection along the cylinder. The holes have a length of 5 mm and a width of 0.4 mm. These holes are uniformly distributed in the sleeve circumference, where a valley without a hole follows a valley with a hole. The pattern repeats along the cylinder every 10 mm, alternating the

holes location by one valley every time. Consequently, the holes are staggered in the longitudinal axis. This design intends to use the valleys of the riblets to retain the air bubbles and study the possibility of forming a stable air layer near the wall. The laboratory's air supply line was used to feed the air injection system. Moreover, the aft body was equipped with the air distributor and the front seal that has the pressure fitting. The geometry used follows Reed and Weinstein (1988, 1989) aspect ratio of $h/s = 2$ ($h=1.04$ mm and $s = 0.52$ mm); they tested their surfaces in the range of $s^+ = 40 - 75$, and a low air injection rate of 0.2 L/min.

All the replaceable modules described in section 3.3, with its different surfaces and configurations, were integrated into the aft body of the AUV model following a constant assembly procedure. The material of the replaceable modules, UHMW Polyethylene, has a density of 0.945 gr/cm³ for the smooth surface cylinder and 0.686 gr/cm³ for the porous cylinder. The water absorption of this material is 0.01%. The black resin used for the riblets sleeves has a density of 1.11 gr/cm³. The weight of each replaceable module and its related components was considered to balance the buoyancy force.

3.4 Neutrally Buoyant Aft Body

In the AUV model, as described in previous sections, the load cell is sandwiched between the hydrofoil (static edge of the load cell) and the front seal of the aft body (free edge) as seen in Figure 3.13. The presence of a large momentum, or a vertical force, in the connection point of the load cell with the aft body, can lead to errors in the drag force measurements and damage the load cell. Consequently, in order to avoid any off-axis load and moments on the load cell, it was required to balance the vertical forces acting on this section. These vertical forces, displayed in Figure 3.13, are the weight of the aft body components (W), and the buoyancy force (F_B).

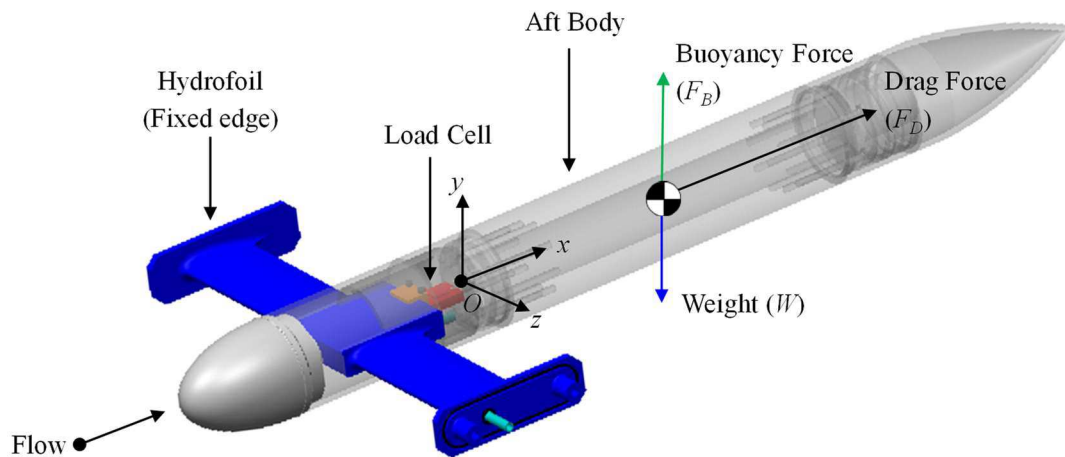


Figure 3.13. Force balance in the center of mass of the AUV test model.

The calculations were carried out by considering the weight of each component and the opposing buoyancy force at its corresponding center of mass. Moreover, the balance of the momentum around axis “z” was done in the connection point of the load cell with the aft body (point “O”) as displayed in Figure 3.14 to guarantee that both, the resultant momentum and the reaction force in the vertical axis, are zero. The equations of the sum of forces in the vertical axis, and the sum of momentums around axis “z”, allows us to calculate the required balance weights and its location on the assembly.

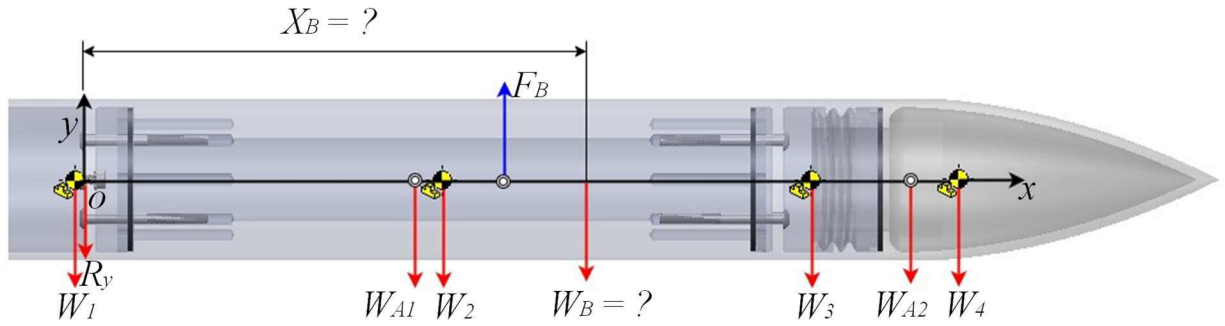


Figure 3.14. Diagram of the vertical forces acting on the aft body of the test model.

The equation of the sum of forces in the vertical axis is:

$$\sum F_y = 0, \quad F_B - W_{A1} - W_{A2} - W_1 - W_2 - W_3 - W_4 - W_B - R_y = 0 \quad \text{Eq. 3.8}$$

where:

F_B Buoyancy force

W_{A1} Weight of air inside the replaceable test cylinder

W_{A2} Weight of air inside the tail

W_1 Weight of the front seal and components installed on it

W_2 Weight of the replaceable module cylinder and air distributor (if applicable)

W_3 Weight of the back seal

W_4 Weight of the tail

W_B Balance weight

R_y Vertical reaction on the load cell free-edge

As the design requirement is $R_y = 0$, the required balance weight would be:

$$W_B = F_B - W_{A1} - W_{A2} - W_1 - W_2 - W_3 - W_4 - R_y \quad \text{Eq. 3.9}$$

The weight of each element was measured after its manufacture. Its corresponding center of mass was obtained using the Measure Module of the software SolidWorks® 2016.

Following Archimedes' principle, the buoyancy force was calculated by multiplying the volume of the aft body (V_{AB}) by the water specific weight (γ_w).

$$F_B = V_{AB} \times \gamma_w \quad \text{Eq. 3.10}$$

Similarly, the weight of the air trapped inside the assembly was obtained by calculating its volume and multiplying it by the specific weight of air. The weight of air inside the replaceable test cylinder is:

$$W_{A1} = V_{AC} \times \gamma_A \quad \text{Eq. 3.11}$$

where: V_{AC} is the volume of air inside the replaceable cylinder, and γ_A is the air specific weight. And, the weight of air inside the tail section is:

$$W_{A2} = V_{AT} \times \gamma_A \quad \text{Eq. 3.12}$$

where: V_{AT} is the volume of air inside the tail.

The buoyancy force and the weights of the air were considered to act in the centroid of the assembly (center of the volume). The exact location and volumes values were obtained using the Measure Module of the software SolidWorks® 2016.

The location of the balance weights was calculated from the momentum equation in the “z” axis. Once again, the design requirement is $M_z = 0$.

$$\begin{aligned} \sum M_z = 0, \quad & a\hat{i} \times F_B\hat{j} + b\hat{i} \times W_{A1}(-\hat{j}) + c\hat{i} \times W_{A2}(-\hat{j}) + d(-\hat{i}) \times W_1(-\hat{j}) \\ & + e\hat{i} \times W_2(-\hat{j}) + f\hat{i} \times W_3(-\hat{j}) + g\hat{i} \times W_4(-\hat{j}) + X_B\hat{i} \times W_B(-\hat{j}) \\ & = 0 \end{aligned} \quad \text{Eq. 3.13}$$

$$X_B = a \times FB - b \times W_{A1} - c \times W_{A2} - d \times W_1 - e \times W_2 - f \times W_3 - g \times W_4 \quad \text{Eq. 3.14}$$

The calculations are performed for each replaceable module to be tested:

- i. smooth surface cylinder,
- ii. the porous cylinder,

- iii. model 1 of riblets, and
- iv. model 2 of riblets;

The results for the two first cases were the following:

- i. Smooth surface: Required a balance weight of $W_B = 1.5$ N, which is equivalent to 152 gr; and it should had be located at 201 mm away from the load cell free-edge.
- ii. Porous surface: Required a balance weight of $W_B = 2.0541$ N, which is equivalent to 210 gr; and it should had be located at 185 mm away from the load cell free-edge.

The location of that amount of weight, in those exact locations, would have required a complete modification of the model. Consequently, an iterative process was used to evaluate the addition of weight in the areas where the design was more flexible, vigilant to maintain an approximately zero resultant force and momentum. The calibration tolerance able to implement was 1 gr.

The geometry and weight of the aft body elements were finally matched to counterbalance the buoyancy force in each assembly (see Figure 3.15). The addition of weight was done with stainless steel disks attached to the front and back seal. These disks modified the location of the center of mass for the front and back seal, and also the volume of air inside the assembly ($\therefore W_{A1}$ and W_{A2}). Considering these changes, the results of the final force balance are shown in Table 3.5.

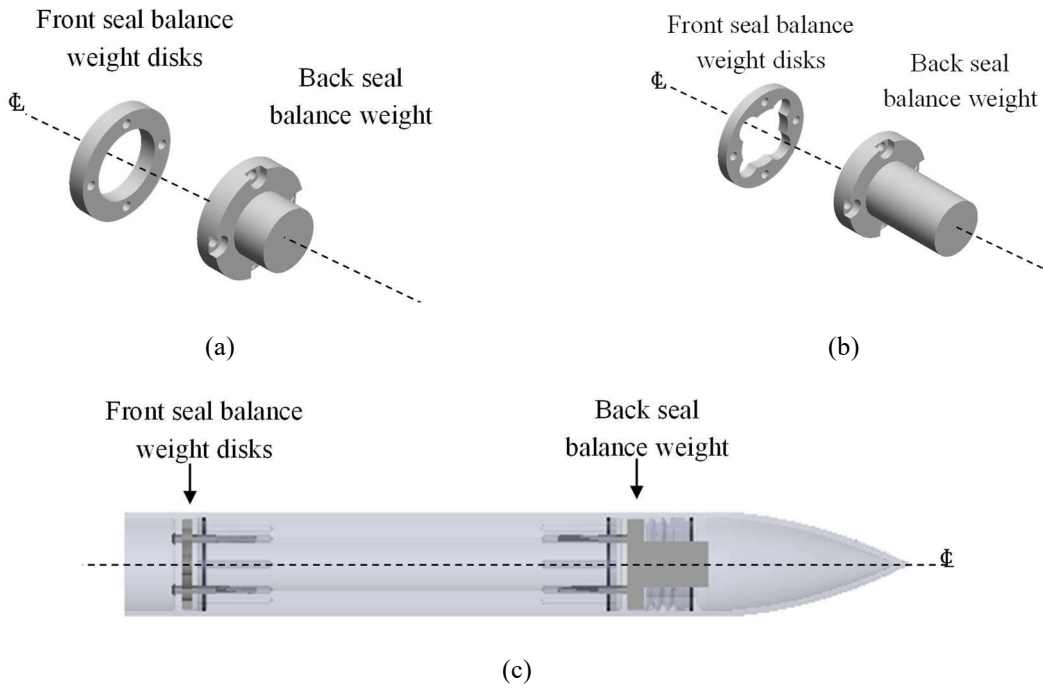


Figure 3.15. A 3D view of the balance weights designs for (a) the smooth surface assembly and (b) for the porous cylinder assembly. (c) Displays the installation of the balance weights in the front and back seals.

Table 3.5. Balance weight description and force balance results.

Assembly	Location	Weight	Resultant Force and Momentum	Variation ¹
Baseline cylinder	Front Disk	40 gr	$R_y = 0.006 \text{ N}$	+7%
	Back Disk	135 gr	$M_z = -0.022 \text{ Nm}$	-0.04%
Porous cylinder	Front Disk	20 gr	$R_y = 0.006 \text{ N}$	+4%
	Back Disk	170 gr	$M_z = 0.056 \text{ Nm}$	+0.09%
Riblets model 1	Front Disk	40 gr	$R_y = 0.005 \text{ N}$	+6%
	Back Disk	143 gr	$M_z = -0.019 \text{ Nm}$	-0.03%
Riblets model 2	Front Disk	20 gr	$R_y = 0.006 \text{ N}$	+4%
	Back Disk	155 gr	$M_z = 0.06 \text{ Nm}$	+0.10%

¹Variation after adjusting the final air volumes and the location of the front and back seal center of mass.

The results were tested without the load cell in a water tank with clear windows for visualization. A hinge connection to the tank wall was used to verify the balance of the buoyancy force with the aft body weight; the test result is displayed in Figure 3.16(a). Then, the balance of the fully assembled model was tested in the same water tank as seen in Figure 3.16(b). Finally, it is possible to use the full assembly of the AUV model to test the different drag reduction techniques in the high-speed water loop (Figure 3.17).

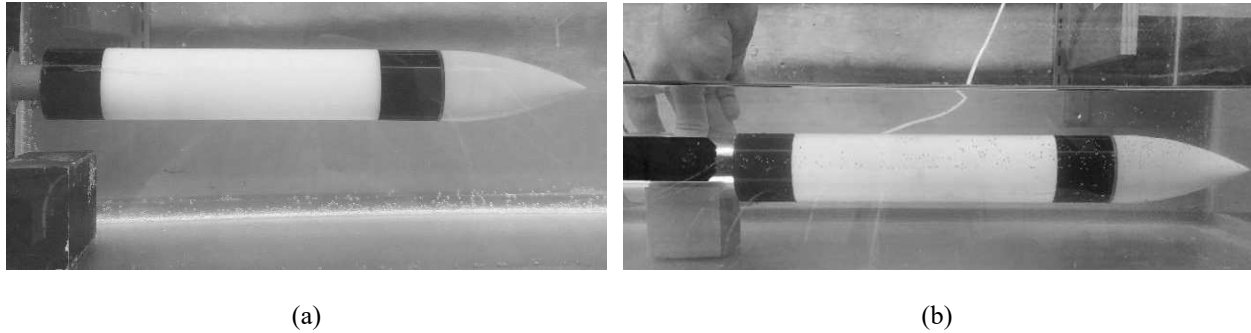


Figure 3.16. Images captured during the verification of the balanced vertical forces and momentum. (a) Test of the balance weights without the load cell, using a hinge connection to the water tank wall. (b) Test of the balance weights in the fully assembled model, also in the water tank.

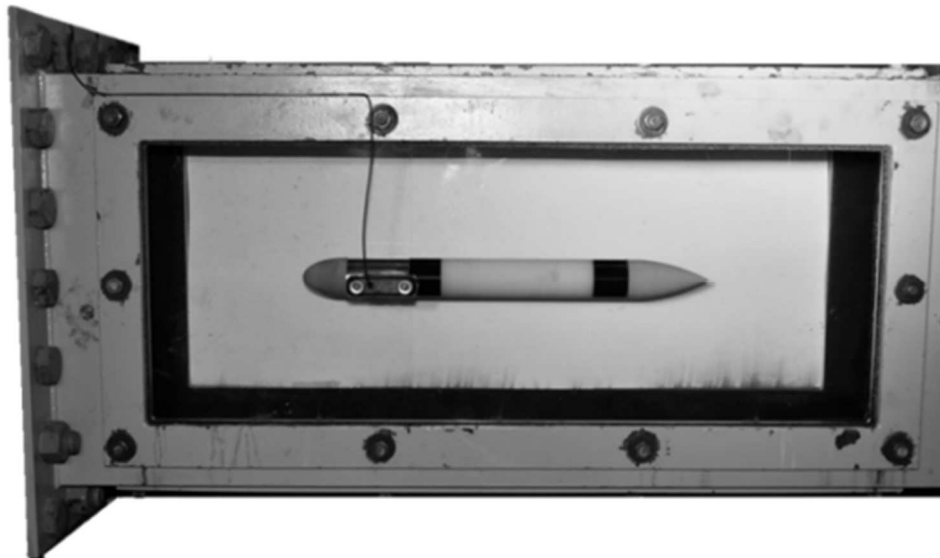


Figure 3.17. AUV model installed in the test section of the high-speed water loop.

3.5 Load Measurement

The effect of each replaceable module in the drag force experienced by the aft body is measured with the submersible load cell installed in the AUV model. All the experiments performed involved the measurement of the drag force. To implement the load measurement, the load cell was connected to an analog amplifier with a voltage output of 10 V (model IAA100, Futek), which is also used to provide the power required for the load cell. The output of the amplifier is collected into a data acquisition (DAQ) device (USB-6000, National Instrument Inc.) that converts the analog input into a digital output. The signal was finally recorded using the software LabVIEW 2015.

The real scale factor of the load cell was obtained by installing it in a calibration bench. The calibration bench allowed the load cell to be in the same position as during operation. The process was done by adding known loads in the range of 100 - 800 gr and recording its output. The process is repeated five times, first adding weight (“Up”) and then removing it (“Down”). The resultant calibration factor is 91.1238 gr/Volt. This test also confirmed the linear behavior of the load cell (Figure 3.18).

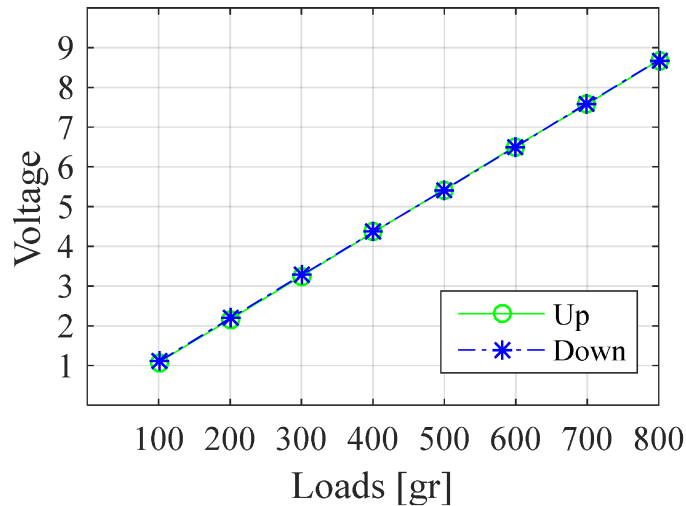


Figure 3.18. Voltage vs. Load plot used for the calculation of the load cell’s scale factor. The process was done by first adding weight (“Up”) and then removing it (“Down”).

The results of the drag force measurement with the submersible load cell are expressed as a function of the C_D , which was defined in Eq. 3.6, versus Re number. The water density and viscosity for the calculation of the C_D and the Re are estimated at the temperature of the flow during the experiment.

The load cell performance can be affected by disturbing factors such as concentric angular loading, eccentric loading, and side loading (VPG Transducers, 2015). Although these forces can be reduced, they cannot be completely eliminated. There will always be a deflection of the load cell member and a certain amount of friction between the mating parts. Although the vertical forces and moments about the load cell hinge were balanced, there still is an error associated to the procedure. Moreover, vibrations and errors in the alignment of the surface can transmit side and even concentric loads into the sensor. The effect of these factors translates into the bias error of the measurement. The following description of pre-measurement, measurement and data processing were applied to all the tests with the purpose of reducing the bias error and guaranteeing repeatability.

3.5.1 Pre-measurement and Measurement Procedure

Once the AUV model has been assembled, and before installing it in the test section, the load cell reading was tested. The AUV model was placed in the vertical position with the hydrofoil in two lateral supports (one at each side); the aft body was only in contact with the load cell. A vertical force was applied to the aft body while monitoring the load cell measurement. As soon as the force was stopped, the load cell measurement should have returned to its equilibrium value. This step guarantees that the load cell measurement was not being affected by friction forces between components.

After the model had been installed in the test section, and the water level was approximately 5 cm over its surface, the angle-of-attack was reviewed with two levels, one of 0.60 m and other of 0.20 m. Both levels were required to show their reference in the middle of their vials to obtain a 0° angle-of-attack. If necessary, the angle-of-attack was corrected using the tolerance between the hydrofoil and the lateral windows. If air injection was required during the experiment, the verification of the 0° angle-of-attack of the model was done while the injection rate of interest

was being applied to the porous cylinder. After the experiment, the angle-of-attack was reviewed again; only those tests where the final alignment matched 100% with the initial configuration were considered for analysis in this study.

Before starting a test, a momentary tension force was applied to the aft body to assess the load cell measurement when submerged in water. As mentioned before, the load cell reading had to return to its equilibrium value to proceed with the experiment. As soon as the high-speed loop was filled to the limit, and the model was submerged in static water, the equilibrium value of the load cell was used as a reference to set the zero of the measurements to be performed. If air injection was required during the experiment, the reference value was obtained while the injection rate of interest was being applied to the porous cylinder. Finally, the data collection was performed for all the range of Re during the same experiment; first, increasing the velocity from $Re = 5 \times 10^5$ up to 1.5×10^6 , and then reducing it from the highest value to the lowest Re . The data was recorded at a rate of 100 Hz during 1 minute per Re . Subsequently, each data collection period gathered 6,000 data points. When returning to a flow velocity equal to zero, the load cell measurement also returned to 0 ± 0.01 Volts. If the load cell measurement did not return to approximately zero, the experiment was discarded because the results would not demonstrate repeatability.

3.5.2 Data processing

The data of the drag force measurement was processed using Matlab 2017. Before performing any calculation, a low-pass filter was applied to the data. Knowing that the load cell measurement is affected by the radial vibrations of the aft body, a low-pass filter with a 1 Hz frequency cutoff is used to remove high-frequency vibrations. The cutoff frequency is determined empirically and is within a range that allows the removal of vibrations without affecting the desired measurements. The effect of the filter on a sample data collected at the highest Re of 1.5×10^6 can be observed in Figure 3.19. The noise due to high frequency vibrations in the raw data is successfully filtered out. It can be seen in Figure 3.20 and Table 3.6 that the average was not significantly affected by the application of this filter, and that the standard deviation was significantly reduced (especially at higher velocities, where the vibrations are higher). The standard deviation quantifies the dispersion of the data; a high value indicates that

the data is spread over a wide range of values (in this case due to vibrations), while on the contrary case the values are closer to the mean. Table 3.6 shows the mean value and the standard deviation of 12,000 raw data points and the matching filtered results. The filter decreases the mean value by a 0.03%, and it reduces the standard deviation by approximately 80%. A signal-to-noise-ratio (SNR), also defined as the mean-to-standard deviation ratio, higher than 1:1 indicates more signal than noise. In the current measurements, at a $Re = 5.0 \times 10^5$ the SNR increased from 9.6 to 61.4; and at $Re = 1.5 \times 10^6$ it increased from 11.5 to 75.2. Hence, the filter helped to reduce the signal noise.

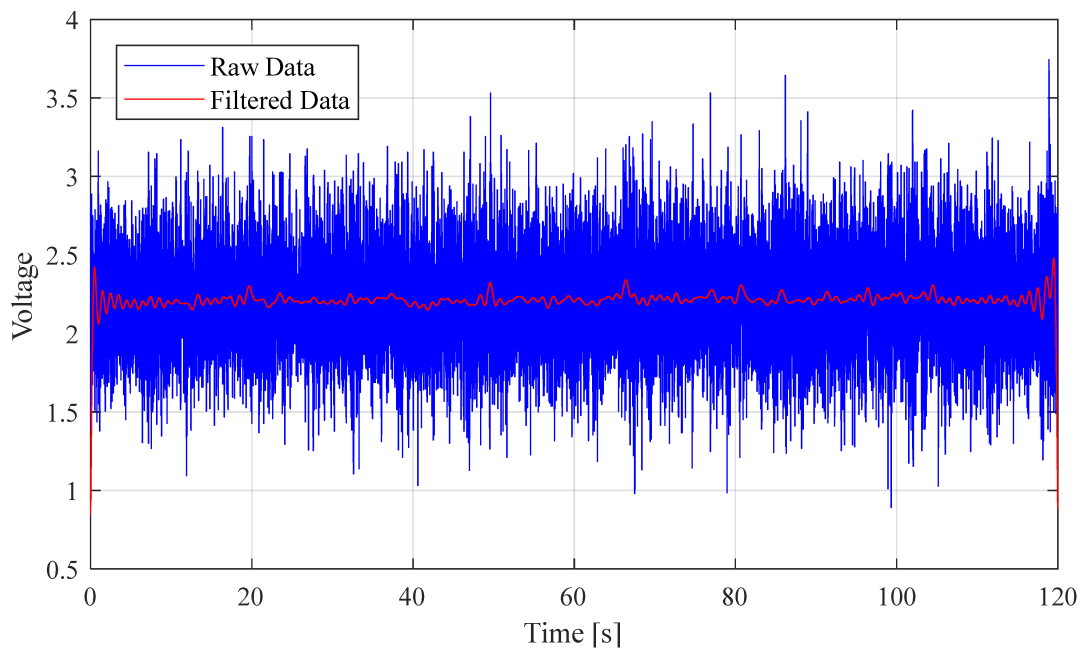


Figure 3.19. Voltage vs. time plot used to visualize the effect of the low-pass filter over the raw data. The noise due to high frequency vibrations in the raw data is successfully filtered out.

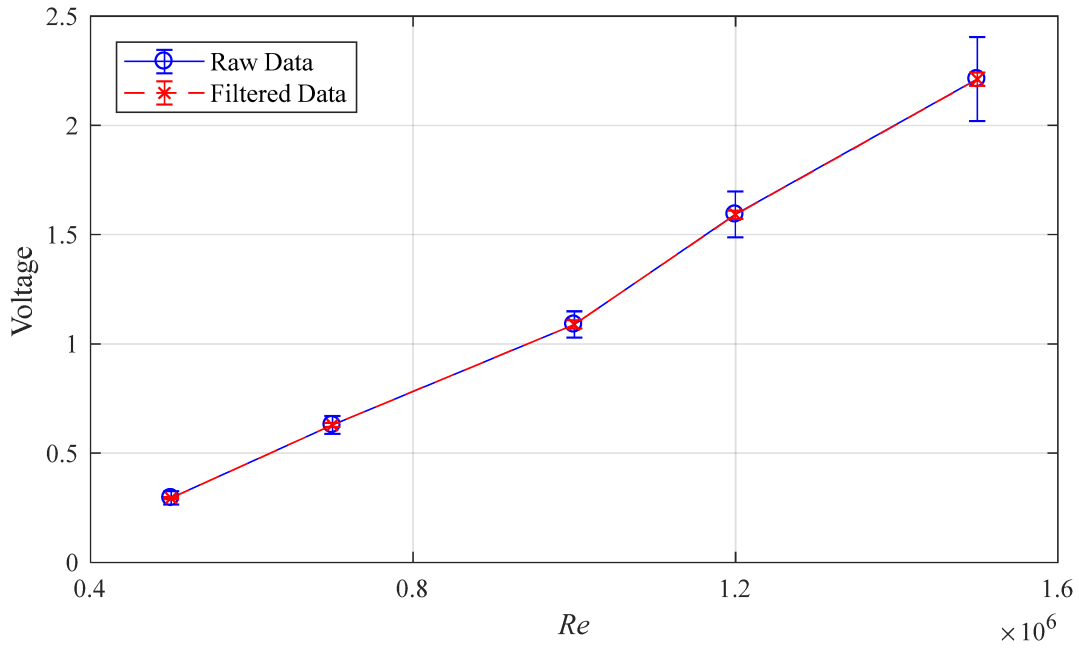


Figure 3.20. Voltage vs. Re number plot used to visualize the effect of the low-pass filter over the raw data. The change in the average is negligible. Conversely, the standard deviation is greatly reduced, especially at higher velocities where the vibrations are higher.

Table 3.6. Results of a low-pass filter over the raw data

Re number	Location	5.0×10^5	7.0×10^5	1.0×10^6	1.2×10^6	1.5×10^6
Raw data	Mean [Volts]	0.2948	0.6294	1.0896	1.5923	2.2121
	Std. deviation [Volts]	0.0306	0.0405	0.0599	0.1054	0.192
Filtered data	Mean [Volts]	0.2947	0.6292	1.0893	1.5918	2.2115
	Std. deviation [Volts]	0.0048	0.0088	0.0189	0.0189	0.0294
Change rate	Mean	-0.03%	-0.03%	-0.03%	-0.03%	-0.03%
	Std. deviation	-84.3%	-78.3%	-68.4%	-82.1%	-84.7%

Finally, the data collected is used to compute in Matlab 2017 the C_D at each Re using Eq. 3.6. The velocity used in the equation corresponds to the magnitude measured with the pitot tube, and the value of the density is calculated as a function of the temperature measured during the data

collection period of each Re number. The dispersion of the load measurements among experiments with the same configuration is calculated using the standard deviation (σ_{CD}). This statistic is expressed in the same units of the C_D .

3.5.3 Propagation of Uncertainty

The measurements limitations, which are related to the instruments precision, propagated along the calculations are considered in this uncertainty analysis. The general equation for uncertainty propagation (ε_Q) in a function $Q(x, \dots, z)$ is:

$$\varepsilon_Q = \sqrt{\left(\frac{\partial Q}{\partial x} \varepsilon_x\right)^2 + \dots + \left(\frac{\partial Q}{\partial z} \varepsilon_z\right)^2} \quad \text{Eq. 3.15}$$

The uncertainty analysis requires the independence of the variables (x, \dots, z) and random uncertainties ($\varepsilon_x, \dots, \varepsilon_z$).

Applying this analysis to the Eq. 3.6 used for the calculations of C_D , is possible to obtain the uncertainty of the C_D calculations:

$$\varepsilon_{CD} = \sqrt{\left(\frac{\partial C_D}{\partial F_D} \varepsilon_{F_D}\right)^2 + \left(\frac{\partial C_D}{\partial \rho} \varepsilon_{\rho}\right)^2 + \left(\frac{\partial C_D}{\partial U} \varepsilon_U\right)^2 + \left(\frac{\partial C_D}{\partial S} \varepsilon_S\right)^2} \quad \text{Eq. 3.16}$$

where: ε_{F_D} Uncertainty in the measurement of the drag force [N]

ε_{ρ} Uncertainty in the estimation of the density [kg/m³]

ε_U Uncertainty in the estimation of the velocity [m/s]

ε_S Uncertainty in the estimation of the reference area [m²]

and the partial derivatives of each term are equal to:

$$\frac{\partial C_D}{\partial F_D} = \frac{1}{(0.5\rho U^2 S)} \quad \text{Eq. 3.17}$$

$$\frac{\partial C_D}{\partial \rho} = -\frac{2F_D}{(\rho^2 U^2 S)} \quad \text{Eq. 3.18}$$

$$\frac{\partial C_D}{\partial U} = -\frac{4F_D}{(\rho U^3 S)} \quad \text{Eq. 3.19}$$

$$\frac{\partial C_D}{\partial S} = -\frac{2F_D}{(\rho U^2 S^2)} \quad \text{Eq. 3.20}$$

The value of ε_{F_D} corresponds to the precision factor reported in the load cell data sheet; this value is equivalent to 0.002 N and is constant for all the measurements. The nonlinearity factor of the load cell (1% of the rated output) has a negligible effect on the resultant drag force (2×10^{-5} N). The value of ε_ρ is related to the uncertainty in the temperature measurement, and it is calculated applying the previous analysis to Eq. 3.2:

$$\varepsilon_\rho = \left(\frac{\partial \rho}{\partial T} \varepsilon_T \right) = 0.002, \varepsilon_T = 0.01 \text{ }^\circ\text{C} \quad \text{Eq. 3.21}$$

where ε_T is the error in the measurement of the temperature, and

$$\frac{\partial \rho}{\partial T} = -0.00196 \times \frac{(2T^3 + 485.3577T^2 + 38284.6008T - 160453.2123)}{(x + 68.12963)^2} \quad \text{Eq. 3.22}$$

Similarly, the uncertainty of the velocity is calculated applying this analysis to Eq. 3.4 and considering a steady flow. As it is required that the variables involved in Eq. 3.16 are independent, the density is considered constant for this estimation. In this case the uncertainty will vary among high (~ 3.3 m/s) and low velocities (~ 1 m/s) because the magnitude of the pressure difference is required in the Eq. 3.24; lower velocities will offer the highest values of error.

$$\varepsilon_U = \left(\frac{\partial U}{\partial \Delta P} \right) \varepsilon_{\Delta P} \approx 0.02 - 0.01 \text{ m/s}, \varepsilon_{\Delta P} = 22 \text{ Pa} \quad \text{Eq. 3.23}$$

where $\varepsilon_{\Delta P}$ is the accuracy in the measurement of the pressure transducer (0.25% of the full scale), and:

$$\frac{\partial U}{\partial \Delta P} = \frac{\partial}{\partial \Delta P} \left(\sqrt{\frac{2\Delta p}{\rho}} \right) = \frac{1}{\sqrt{2\Delta P \rho}} \quad \text{Eq. 3.24}$$

The uncertainty for the area estimation ($S = \pi D^4/4$) is calculated by:

$$\varepsilon_S = \left(\frac{\partial S}{\partial D} \varepsilon_D \right) = 7.78 \times 10^{-7} \text{m}^2, \quad \varepsilon_D = 0.00001 \text{m} \quad \text{Eq. 3.25}$$

where ε_D is the precision in the measurement of the diameter, and

$$\frac{\partial S}{\partial D} = \frac{\pi D}{2}. \quad \text{Eq. 3.26}$$

The parameters and results of the smooth surface case are used as a reference to obtain the error of the measurement. Replacing all the above values in Eq. 3.16 the uncertainty on the C_D estimation varies from 0.5% at high velocities ($Re = 1.5 \times 10^6$) up to 0.9% at low velocities ($Re = 5 \times 10^5$).

3.6 Shadow-Based Long-Range Microscopic Particle Tracking Velocimetry

A shadow-based long range microscopic particle tracking velocimetry (micro-PTV) was applied to obtain the mean velocity profile in the inner layer for the smooth surface and the SHS. The shadow-based technique also allowed the visualization of the air plastron, and air pockets, formed in the SHS. This technique provides the means to observe the morphology of the air-water interface and its evolution in time and with increasing flow stream velocities.

The characterization of the flow velocity is done using tracer particles in the water stream. For the smooth surface, the flow was seeded with a polyamide 12 fine powder (VESTOSINT 2070, natural color) of 5 μm diameter and a density of 1.016 gr/cm^3 . In the case of the SHS, the flow was seeded with hollow glass spheres (Spherical® 110P8) with a 10 μm diameter and a density of 1.10 gr/cm^3 . The effect of the gravitational forces on the particles is studied through the gravitational induced velocity U_g (Eq. 2.57). An effective particle size would have a negligible U_g in comparison with the flow velocity (Prasad 2000a). For the particles of 5 μm , U_g results in 2.2×10^{-7} m/s; and for the particles of 10 μm , U_g results in 5.4×10^{-6} m/s. In both cases, U_g is significantly smaller than the lowest flow velocity tested of 0.9 m/s. Hence, the velocity measurements will not be considerably affected by the gravitational forces over the particles.

The same setup was implemented for the study of both surfaces Figure 3.21. A Nd:YAG laser (Gemini PIV, New Wave Research Inc.), with 90 mJ energy per 3-5 ns pulse, was used to generate the backlight for the flow particles and the top surface of the test model. The laser beam was directed through a pair of mirrors to a light diffuser located in front of a 12-bit digital camera (FlowMaster, LaVision) with a $1,280 \times 1,024$ pix CCD sensor (pixel size $6.7 \times 6.7 \mu\text{m}^2$). The camera was equipped with a 12X zoom lens (Navitar), allowing a magnification of $M = 5.3$ and a field-of-view (FOV) of $1,621 \times 1,297 \mu\text{m}^2$. The image acquisition was performed at three-quarter of the total cylinder length (l) and, a set of 900 pairs of double-frame images was collected at 4 Hz per Re . The time delay between frames (Δt) resulted in a maximum particle displacement of 30 pixels in the top region of the FOV. The synchronization of the camera frames and the laser pulses was done with the commercial software DaVis 7.4 (LaVision GmbH).

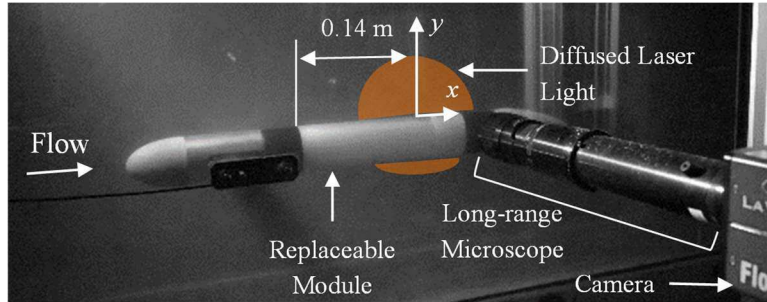


Figure 3.21. Shadow-based long-range microscopic particle tracking velocimetry setup. The system is formed by a Nd:YAG laser, which pulse is guided by two laser mirrors through a diffuser, and a CCD camera located in front of the diffuser

3.6.1 Images Alignment

Once the data was collected, the images of each set were aligned in the wall-normal direction. The cylindrical body has a small vibration due to the small flexibility of the load cell. The vertical displacement of the body varies from a few μm at low velocities (~ 1 m/s) up to $200 \mu\text{m}$ at the highest velocity (~ 2.9 m/s) as seen in the images collected. The images were extracted from DaVis 7.4 (LaVision GmbH) and aligned with Matlab 2017.

The alignment process began with the rotation of the images, guaranteeing the horizontal orientation of the surface shadow in all the data set during its processing. Then, the wall alignment in the images was carried out by selecting a characteristic feature on a reference image. In the smooth surface images, the characteristic feature used was a mark present in the shadow of the smooth surface cylinder. For the SHS cylinder, the characteristic feature used is a roughness peak on the wall. An area of interest was selected around this feature in the subsequent images and the displacement was estimated using a cross-correlation algorithm. The location of each cross-correlation peak indicated the displacement required to align the specific feature with the reference image.

3.6.2 Images Pre-Processing and PTV Processing

The aligned images were transferred back to DaVis 8.3 (LaVision GmbH) for improving the signal-to-noise ratio and the PTV processing. The intensity matrix of the images is first inverted and the minimum intensity of the ensemble of images is subtracted from each image. The images

are further improved using a sliding minimum filter and normalization over a kernel of 7 pixels. A Gaussian filter with kernel of 5×5 pix for the smooth surface, and 9×9 pix for the SHS, is also applied to smoothen the intensity profile of the particles.

The PTV algorithm first detected the particles based on an initial intensity threshold; this value is set using the 50% of the maximum intensity within the inverted images. Particle peak detection was performed with subpixel accuracy using a 5×5 pix Gaussian fit. The size of the detected particles was limited to 10 pixels to avoid detection of out-of-focus particles. The displacement range was limited from 0 to 30 pix in the streamwise direction and from -5 to 5 pix in the wall-normal direction. Sample micro-PTV images showing the velocity vectors of the detected particles over the smooth and the SHS are displayed in Figure 3.22. The background color shows the effects of the filters applied to improve the particle detection. Finally, the mean velocity profile was obtained by averaging the velocity vectors in bins of 570×24 pix ($720 \times 30 \mu\text{m}^2$) in the x and y -direction with an overlap of 75%, respectively. The number of particles per bin varied from minimum of 125 particles to a maximum of 850 particles per bin. The details of the PTV system and the processing parameters are shown in Table 3.7.

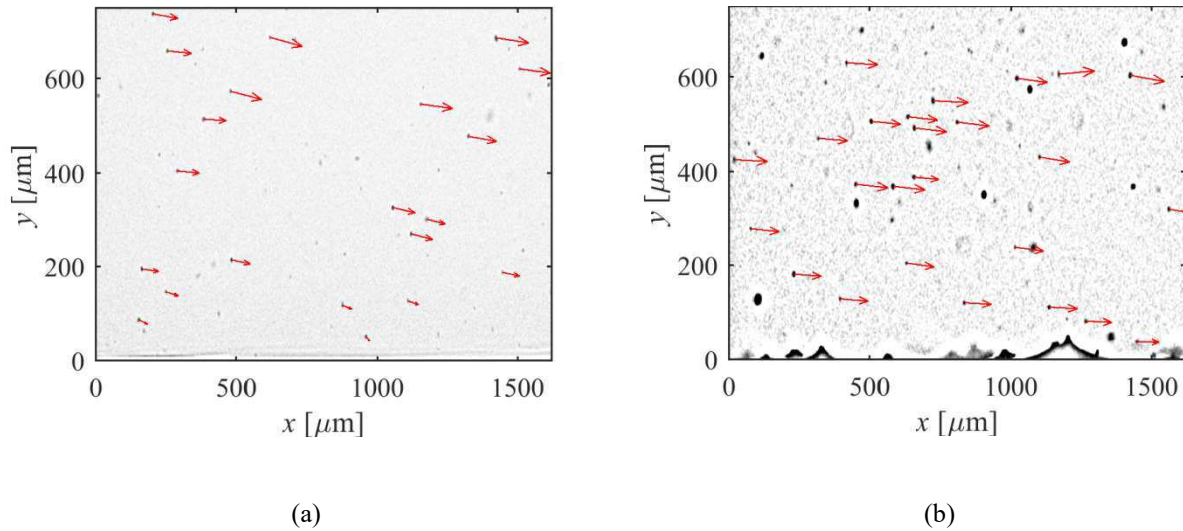


Figure 3.22. Sample of velocity vector fields over (a) the smooth surface cylinder and (b) the SHS, at $Re = 5.0 \times 10^5$. The velocity vectors were obtained through shadow-based long-range microscopic particle tracking velocimetry.

Table 3.7. Parameters of the micro-PTV system for the smooth surface cylinder

Magnification	5.3
Digital resolution	1.267 $\mu\text{m}/\text{pix}$
Measurement field	1,280 \times 1,024 pix 1,621 \times 1,297 μm^2
Velocity evaluation	Correlation of double-frames
Bin size (Δx , Δy)	570 \times 24 pix 720 \times 0.03 μm^2
Bin overlap (%)	75

3.6.3 Wall Detection

In the aligned images, a wall detection algorithm developed in Matlab 2017 was used. All the images showed the shadow of the model in the horizontal direction. Hence, for simplicity in the calculations of the velocity profile, the wall was considered as a horizontal line in the limit of the solid surface shadow and the illuminated flow field. In case of the smooth wall, the shadow of the cylinder forms a straight edge at the solid-water interface as seen in Figure 3.23a. In the case of the SHS, the detection of the wall was more difficult due to the roughness of the surface and the presence of air pockets seen in the sample micro-PTV image of Figure 3.22b.

In order to detect the wall location for the smooth surface, the light intensity of the two-dimensional matrix, shown in Figure 3.23a, is first averaged in the streamwise direction (x) to generate a profile of the average intensity (I) versus wall-normal distance (y) as seen in Figure 3.23b. The peak of the wall-normal gradient ($\partial I / \partial y$) in Figure 3.23c is used to identify the wall location as the point with the fastest change of intensity from the dark shadow to the bright background. The wall location is detected in each image and then averaged to define the reference $y = 0$ for the set of images at each Re number. The uncertainty associated with this method corresponds to the thickness of the glare region in the interface and is equal to 0.6 μm (0.5 pixels); the value is estimated as the width of the intensity peak at the base (I_{max} / e^2 , where “ I_{max} ” is the maximum intensity and “ e ” is Euler’s constant = 2.71828).

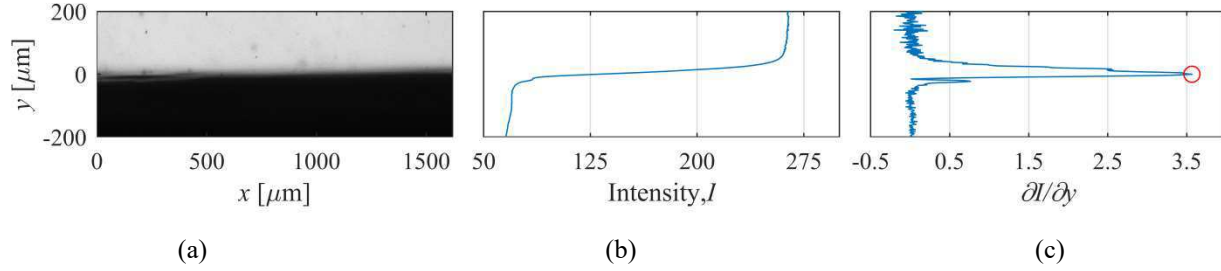


Figure 3.23. Wall detection over the smooth surface cylinder at $Re = 5.0 \times 10^5$. (a) A sample micro-PTV image over the smooth wall showing the interface of the solid surface and the liquid. This image corresponds to a reduced area of the total FOV. (b) The profile of wall normal distance y versus light intensity (in counts) averaged in the streamwise direction. (c) The profile of wall-normal gradient of the average light intensity. The peak value is selected as the location of the wall ($y = 0$). For this case, the uncertainty is equivalent to $0.6 \mu\text{m}$ (0.5 pixels).

The detection of the wall location plays a crucial role in the accurate estimation of the slip velocity over SHS. The magnitude of the resultant slip velocity will highly depend on the position of the reference surface $y = 0$. The location of this reference surface is not straightforward as the surface has a mixed-boundary condition due to the existence of air-water and solid-water interface in an irregular pattern.

The SHS is characterized from the projection of the roughness peaks that are in focus in the image. The silhouette of the surface roughness and the air-water interface seen in Figure 3.24(a) is detected using the wall-normal gradient of the light intensity every $1.3 \mu\text{m}$ in the x -direction. The profile of light intensity every $1.3 \mu\text{m}$ is obtained by averaging I in steps of $15 \mu\text{m}$ with an overlap of 90%. The peak of the wall-normal gradient ($\partial I / \partial y$) is used to identify the local position of the wall every $1.3 \mu\text{m}$ and finally construct the complete silhouette of the surface roughness. The location of $y = 0$ is set at the average height (h) of the roughness peaks from all the images of the Re number set. The distribution of the roughness height (h) for the case of $Re = 5.0 \times 10^5$ is seen in Figure 3.24(b) showing the location of $y = 0$ at the average height. The selection of the roughness average height follows the information presented in section 2.2.3 and the discussion of Ling *et al.* (2016), Perry *et al.* (1969), Kunert *et al.* (2007), Brzek *et al.* (2008), and Chan *et al.* (2015) regarding turbulent boundary layer theory over rough surfaces (spheres, plates and pipes). Similar to Ling *et al.* (2016), in the current investigation the slip velocity is estimated where the cumulative distribution of the roughness height reached 95% (y_{95}). The cumulative distribution of the roughness heights is displayed in Figure 3.24(c) indicating the 95% cumulative roughness height.

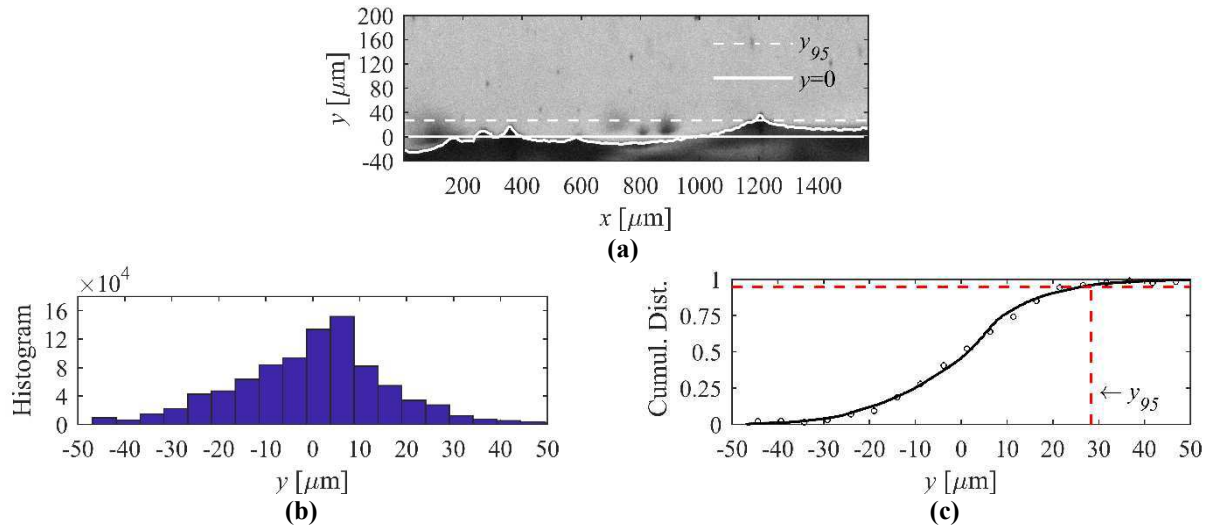


Figure 3.24 Wall detection over the SHS cylinder at $Re = 5.0 \times 10^5$. (a) Presents a sample image of SHS displaying the recognition of the surface roughness peaks, the location of the average roughness height ($y = 0$) and the 95% cumulative distribution of the roughness height (y_{95}). (b) Shows the histogram for the height of surface roughness, and (c) displays the cumulative distribution of the height of surface roughness

The reference planes $y = 0$ and y_{95} consider the combined effect of the air-water and the solid-water interface areas seen in Figure 3.24a. These selections guarantee a maximization of the slip values in all the range of Re tested, and the magnitude will always be positive. However, some data will be lost for the $Re > 1.0 \times 10^6$ as the flow moving in the valleys will not be considered. If the valleys were selected as a reference, the slip velocity at the $Re < 1.0 \times 10^6$ would be considerably reduced, and negative slip length might have arisen. In any case, the interpretation of the results should always consider the location of the reference planes.

3.6.4 Air Plastron Visualization

The comparison of the amount of air present on the SHS surface at different Re numbers is difficult due to the constant movement of the air and the irregularities of the surface. The cross-section area of the air plastron in each image is calculated by manually selecting a reference image with the lowest level of air through the ensemble of images as shown in Figure 3.25a. As there is no reference image of the surface completely without air, this estimation would be below the real amount of air present within the peaks and in the surface microstructures. Subsequently, a sample of 50 aligned images is selected from each Re data set; these 50 images have an equal time step between them. Next, the exact location of the interface is calculated for all the images

using the peak of the intensity gradient profile. Sample images of an SHS with air pockets (dissolved air plastron) and with a continuous air layer are displayed in 3.23a and 3.23b. The amount of air at each streamwise location (x) is then determined, as seen in Figure 3.25c, by subtracting the location of the interface in the reference image (y_{ref}) from the interface detected at each image (y_i) to obtain the local thickness of the air layer as $t_e = y_i - y_{ref}$. The thickness is averaged over the ensemble of images to obtain the mean thickness $\langle t_e \rangle$.

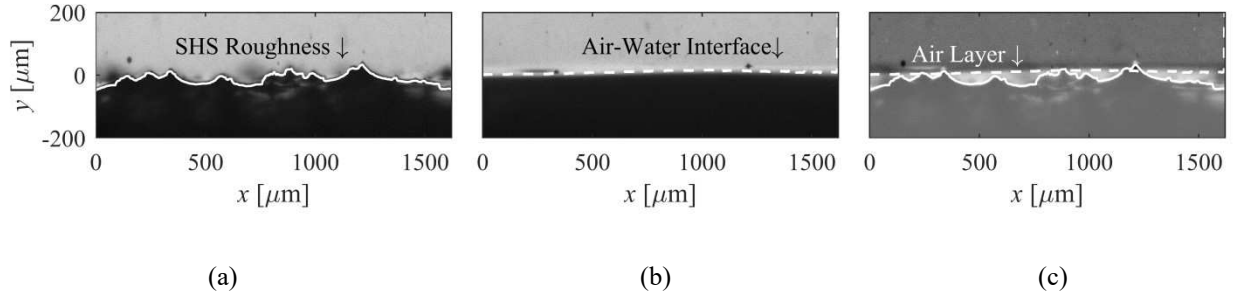


Figure 3.25. Wall location on an image of the SHS model at a $Re = 5.0 \times 10^5$ with (a) a mostly uniform air-water interface (plastron full of air) and (b) SHS microstructures with air pockets (dissolved air plastron). Figure (c) displays the subtraction of image (b) from (a), with the location of the interface for each case to calculate the air plastron equivalent thickness

3.7 Test Matrix

The use of the three types of surfaces described in section 3.3 allows us to study the effect of the SHS, air injection, riblets, and their combination, over the aft body of the AUV simplified model. This section summarizes the tests performed with each surface configuration using the load cell, and it specifies those that were further studied with shadow-based long range micro-PTV.

The following surfaces and drag reduction techniques were studied with the load cell. The data collection was performed at five Re numbers: 5.0×10^5 , 7.0×10^5 , 1.0×10^6 , 1.2×10^6 and 1.5×10^6 for almost all the configurations tested.

i. Smooth surface:

- a. Baseline (smooth surface without superhydrophobic coating)
- b. SHS

The body remained submerged in static water at least 30 minutes before the test would begin. Then, the model was exposed to 45 minutes of running water while the data was collected for the five Re numbers.

ii. Porous surface:

- a. Baseline (porous surface with no air injection, and without superhydrophobic coating)
- b. Porous surface with air injection:

- Low air injection rates (LAIR)

With air injection rates $Q_a = 0.15$ L/min, 0.25 L/min, 0.5 L/min, 1 L/min and 5 L/min.

- High air injection rates (HAIR)

With Q_a values going from 10 L/min up to 50 L/min with increments of 5 L/min. At these high values of Q_a , the loop was rapidly pressurized, and it

was only possible to do the drag measurements in a limited number of Re . For the range of $10 \text{ L/min} < Q_a < 35 \text{ L/min}$, the data was collected at $Re = 5.0 \times 10^5$ and $Re = 1.5 \times 10^6$. In the range of $40 \text{ L/min} < Q_a < 50 \text{ L/min}$, the data was only collected at $Re = 1.5 \times 10^6$.

c. Porous surface with superhydrophobic coating (porous SHS):

- Without air injection.

The body remained submerged in static water at least 30 minutes before the test would begin. Then, the model was exposed to 45 minutes of running water while the data was collected for the five Re numbers.

- With low air injection rates ($Q_a = 0.15 \text{ L/min}$, and 0.25 L/min)

Consecutively, the model was exposed to 45 minutes of running water and air injection at $Q_a = 0.15 \text{ L/min}$. Followed by another 45 minutes of running water with $Q_a = 0.25 \text{ L/min}$.

d. Effect of air injection in recovering an SHS.

The porous cylinder used in the previous tests was coated again to be tested a second time. The objective of this second experiment was to observe the effect of the air injection in a wetted SHS. A “wetted” SHS is one that has lost a great portion of the air plastron, and it cannot offer DR on its own. The stability analysis of Abu Rowin *et al.* (2017) using the same superhydrophobic coating over a flat plate, showed that an unstable SHS gradually lost its capacity on reducing DR after 5 minutes at a $Re = 4400$ based on the channel height (25 mm) and a velocity of 0.2 m/s. In the current study, the coated cylinder was exposed for 12 minutes to a high shear flow ($Re = 1.5 \times 10^6$) to obtain the wetted SHS before beginning to inject the air. The experiment considered the discrete injection of air per periods of 30 s and the continued injection of air for a period of 300 s to try the recovering of SHS air layer. This experiment was performed at

$Re = 1.5 \times 10^6$ during 52 min, and the data was collected in periods of 30 s every 30 s.

- Discrete air injection per periods of 30 s: $Q_a = 0.15$ L/min at the minute 13 of the test, $Q_a = 0.25$ L/min at the minute 19 of the test, $Q_a = 0.5$ L/min at the minute 23 of the test.
- Continued air injection of $Q_a = 0.15$ L/min for 300 s, from the minute 43 to the minute 48 of the test.

ii. Riblets:

a. Riblets model 1 ($s = 0.3$ mm, $h/s = 0.5$ and $s^+ = 15 - 40$)

- Baseline (without superhydrophobic coating)
- With superhydrophobic coating (SHS Riblets model 1)

The body remained submerged in static water at least 30 minutes before the test would begin. Then, the model was exposed to 45 minutes of running water while the data was collected for the five Re numbers.

b. Riblets model 2 with air injection ($s = 0.6$ mm, $h/s = 2$, $s^+ = 30 - 80$ and $Q_a = 0.15$ L/min)

Table 3.8 displays a summary of the tests done with load measurements, the Re number considered, and the number of data points collected for each study case. The baseline case of the smooth surface has the highest number of data points due to the repeatability assessment done to the experimental system at the beginning of the investigation.

Table 3.8. Tests performed using load measurements per surface and its respective combinations. The number of data points collected for each configurations is indicated per Re number.

Test Surface	Re number	5.0×10^5	7.0×10^5	1.0×10^6	1.2×10^6	1.5×10^6
Smooth Surface	Baseline	30	30	30	30	30
	SHS	18	18	18	18	18
Porous Surface	Baseline	12	12	12	12	12
	LAIR	4	4	4	4	4
	HAIR	2				2
	SHS	6	6	6	6	6
	SHS + LAIR	6	6	6	6	6
	Wetted SHS + LAIR					104
Riblets	Model 1 Baseline	18	18	18	18	18
	Model 1 + SHS	6	6	6	6	6
	Model 2 +LAIR	18	18	18	18	18

The smooth surface, with and without the superhydrophobic coating, was evaluated using shadow-based long range micro-PTV. The use of this technique allowed the characterization of the mean velocity profile in the inner layer of each configuration and the visualization of the air plastron/pockets present in the SHS. The image acquisition was performed at three-quarter of the total cylinder length (l). A set of 900 pairs of double-frame images was collected at 4 Hz per Re number, and the FOV of each frame is $1,621 \times 1,297 \mu\text{m}^2$. Table 3.9 summarizes the tests done with the later technique together with the load cell measurements, indicating the Re number

considered and the number of data points collected. The data collection was performed at five Re : 5.0×10^5 , 7.0×10^5 , 1.0×10^6 , 1.2×10^6 and 1.5×10^6 .

Table 3.9. Tests performed using shadow-based long range micro-PTV and load measurements. The number of data points collected for each configuration is indicated per Re number.

Test Surface	Re number	5.0×10^5	7.0×10^5	1.0×10^6	1.2×10^6	1.5×10^6
Smooth Surface	Baseline	1	1	1	1	1
	SHS	1	1	1	1	1

Chapter 4. Effect of Superhydrophobic Coating on the Drag of a Smooth Surface

This chapter evaluates the use of a superhydrophobic coating on a smooth surface of an axisymmetric body. The coating formed a superhydrophobic surface (SHS) with a random pattern of nano-/microstructures. The effect of the SHS in the drag force and with increasing Re number is measured with a submersible load cell.

The data collection was performed at five Reynold numbers (Re): 5.0×10^5 , 7.0×10^5 , 1.0×10^6 , 1.2×10^6 and 1.5×10^6 . The SHS reduced the drag in comparison with the smooth surface; nonetheless, the drag reduction (DR) declined with increasing Re number. Consistent with previous investigations, the water movement over the SHS at high velocities enhanced the air depletion and degraded the coating.

4.1 Introduction

There is a general agreement in the literature that the drag reduction mechanism of the SHS is based on creating a slip velocity at the wall. When water flows over the surface, it is in contact with an air layer instead of the solid surface, easing the no-slip boundary condition. This method is of special interest as it does not require the storage and continuous provision of air neither requires the consumption of extra energy to work properly.

The effectiveness of SHS in reducing drag in the laminar regime was experimentally demonstrated by Ou and Rothstein (2005) among other early investigators. They obtained a maximum DR of 40% based on measurements of pressure difference in a microchannel flow. Balasubramanian *et al.* (2004) tested a superhydrophobic coating over a flat plate in the laminar regime using particle image velocimetry (PIV). A 20% DR was estimated based on the ratio of the momentum thickness calculated for the uncoated and coated flat plate. The momentum thickness considered the integration of the velocity profile obtained from the PIV technique. Henoeh *et al.* (2006) used a patterned silicon nanograss over a plate suspended in a water tunnel by flexible steel strips. Applying an optical proximity sensor to measure the plate displacement, they observed 50% DR in the laminar regime. Nonetheless, the DR decreased 34% when tested

in the turbulent regime. Zhao *et al.* (2007) used random-textured plates in a water tunnel and obtained 9% DR in the laminar regime. Conversely, at higher Re drag increased. All these experimental data have proven that SHS can reduce the skin-friction drag in the laminar regime. However, further understanding of the DR mechanism in the turbulent regime is required to scale up its use.

In the turbulent regime, the effectiveness of the SHS has been seen to be directly related to the stability of the air layer (Samaha *et al.* 2001, Vajdi Hokmabad & Ghaemi 2016, and Abu Rowin *et al.* 2017). Besides the time factor, high shear rate flows enhance the dissolution of the air layer into the flow (Moreira *et al.* 2016, Vajdi Hokmabad & Ghaemi, 2017). Even though most of the numerical simulations and theoretical analysis have predicted significant DR in the turbulent regime, the experimental results have been difficult to obtain.

Few experiments have reported the use of load cells to measure changes in the drag force. Bidkar *et al.* (2014) used a direct force measurement and reported 30% DR in the turbulent regime using superhydrophobic surfaces with random textures. To obtain satisfactory turbulent DR, Bidkar *et al.* (2014) explained that the dimensionless surface roughness (k^+_{rms}) needs to be considerably smaller (at least one order of magnitude) than the dimensionless viscous sublayer thickness. Lyu *et al.* (2013) compared the use of a smooth surface with the use of a superhydrophobic coating over aluminum plates with the measured the drag force with a load cell. They observed a DR around 50% in the range of $1 \times 10^5 < Re < 2 \times 10^5$, but it then decreased to values around zero with higher Re ($\sim 2.6 \times 10^5$). Also using SHS with a random pattern, Zhang, J. *et al.* (2015) reported an increase of the mean velocity profile, and DR, due to the slip velocity at the interface and the modification of the turbulent structures. They reported the loss of the air layer at high Re , which affected the effectivity of the SHS. Moreover, it was seen that these surfaces with random textures were more susceptible to elevated hydrostatic pressure than the surfaces with ordered microstructures.

Using PIV and pressure drop measurement, Daniello *et al.* (2009) demonstrated that micropatterned SHS also reduced drag in the turbulent regime. A maximum DR around 50% was obtained. Nevertheless, the effect of the SHS decreased as the microfeatures spacing became wider than the viscous sublayer thickness. Zhang J. *et al.* (2015) reported an increase of the mean

velocity profile, and DR, due to the slip velocity at the interface and the modification of the turbulent structures. Other experiments using PIV (Woolford *et al.* 2009, Vajdi Hokmabad & Ghaemi 2016) showed a DR among 10-20% in the turbulent regime, together with a mild shift upward of the mean velocity profile.

The DR performance of the surfaces in the turbulent regime with ordered and random structures seems not to be the same. The use of surface with random structures has shown a decrease of the DR with increasing Re number; conversely, the DR has been seen to increase with higher Re number for surfaces with ordered structures. The contrast of the results obtained with these different SHS (organized patterns versus random textures) has been related to the hierarchical arrangement of the structures. It is considered that the longevity of the SHS with random texture could be improved by creating, during its manufacturing, a hierarchical structure of the hydrophobic particles, going from micro- to nano-scale (Verho *et al.*, 2011). There is still a necessity for further characterization of the turbulent flow over a random SHS (Gad-el-Hak, 2013).

SHS with random structures are of special interest for the manufacturing of large-scale surfaces like marine vessels as it only requires the use of spray coatings (Bidkar *et al.* 2014). Furthermore, no previous work was found on axisymmetric bodies in the turbulent regime. Balasubramanian *et al.* (2004) studied an ellipsoidal body completely covered by an SHS in the laminar regime. The results showed 14% DR at $Re = 5.5 \times 10^5$ and with a 0° angle-of-attack. The DR percentage decreased at higher Re numbers. Zhang S. *et al.* (2015) applied an SHS on a submarine model and obtained up to 15% drag reduction, also in the laminar regime at $Re = 1.2 \times 10^5$.

The current investigation uses the direct measurement of the drag force to study the effect of superhydrophobic coating with random texture on a smooth surface of an axisymmetric model in the turbulent regime. The load measurements are performed at five Re : 5.0×10^5 , 7.0×10^5 , 1.0×10^6 , 1.2×10^6 and 1.5×10^6 , and the results are expressed in terms of the C_D as a function of Re number. The results for the smooth surface and the SHS are shown together to facilitate the comparison of the SHS performance.

4.2 Results and Discussion

The values of the C_D as a function of Re are presented for both smooth and SHS, in Figure 4.1. The test body with the smooth surface has a drag coefficient of $C_D = 0.250$ at the lowest $Re = 5.0 \times 10^5$ with a standard deviation of $\sigma_{CD} = 0.009$. The σ_{CD} is estimated based on 18 independent experiments. The drag coefficient over the smooth surface gradually reduces to $C_D = 0.206$ at the highest $Re = 1.5 \times 10^6$, with a σ_{CD} of 0.005. This translates into a 17.6% reduction of the C_D while Re number increases three times. Appendix B presents the visualization of the calculated C_D as function of time for a sample set at $Re = 1.5 \times 10^6$, together with the histogram and normal density function for the C_D .

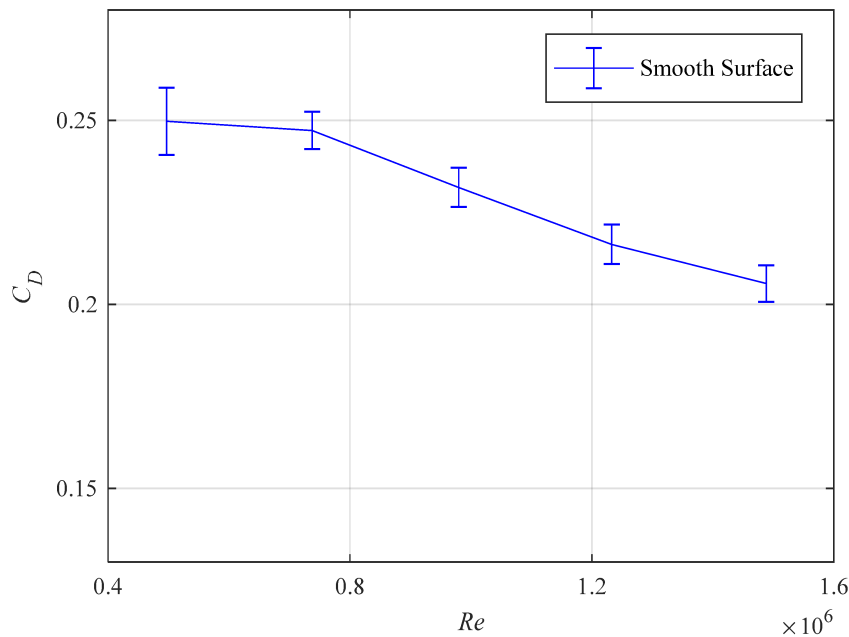


Figure 4.1. Average of the drag coefficient (C_D) versus Reynolds number (Re) for the smooth surface. The C_D is calculated using the drag force measured by a submersible load cell. The error bars, in both cases, correspond to one standard deviation (σ_{CD}).

This tendency of decreasing C_D with rising Re agrees with the trend of the numerical and experimental data reported by Cebeci *et al.* (1970). They compared the accuracy of different methods used for calculation of the viscous drag and the location of the flow separation for two-dimensional and axisymmetric bodies in incompressible flows. In the specific case of the total

drag coefficient, they used Young's (Young, 1939) and Granville's formulas (Granville, 1953); taking into consideration the boundary layer momentum and the test model cross-section area for normalizing. The Douglas boundary-layer method (Cebeci *et al.* 1968), an implicit finite-difference technique valid in the laminar and turbulent regime, was used to account for the transverse curvature effects in the calculation of the boundary layer. The drag coefficients were calculated for several airfoils and axisymmetric bodies. For one of their axisymmetric models, which has an $L/D = 10$ and was tested in the Re number range of $2 \times 10^6 - 26 \times 10^6$ based on the model length, the C_D decayed $\sim 44\%$ over the complete range. In the reduced Re number range of $2 \times 10^6 - 6 \times 10^6$ (also an increase of three times the Re number, as in the current experiment) the C_D decreased by $\sim 20\%$. The reduction of C_D is associated with the location of the separation point on the trailing-edge of the axisymmetric body.

The values of the C_D as a function of Re are presented for the SHS in comparison to the smooth surface in Figure 4.2 and Table 4.1. The test cylinder covered by the SHS with random texture resulted in a C_D value of 0.159 at the lowest Re number of 5.0×10^5 , while it gradually increases to 0.195 at the largest Re number of 1.5×10^6 . A maximum DR of 36.4% was obtained at $Re = 5.0 \times 10^5$, while at $Re = 1.5 \times 10^6$ the DR was reduced to 5.6%. The texture of the SHS (R_{rms}) is about $10.2 \mu\text{m}$ which is 9% relative to the viscous sublayer thickness ($y^+ = 5$) at $Re = 5.0 \times 10^5$. However, the surface may act as a rough wall at $Re = 1.5 \times 10^6$ with a viscous sublayer thickness of $49.4 \mu\text{m}$. The wall units ($\eta = \nu/u_*$) were obtained for each flow velocity by calculating the friction velocity (u_*) as a function of the shear stress at the wall (τ_w) using Eq. 2.18; the latter term is found with Eq. 2.34, where the local skin-friction coefficient (C_f) is estimated from the Re number ($C_f = 0.59/(Re_x)^{0.2}$).

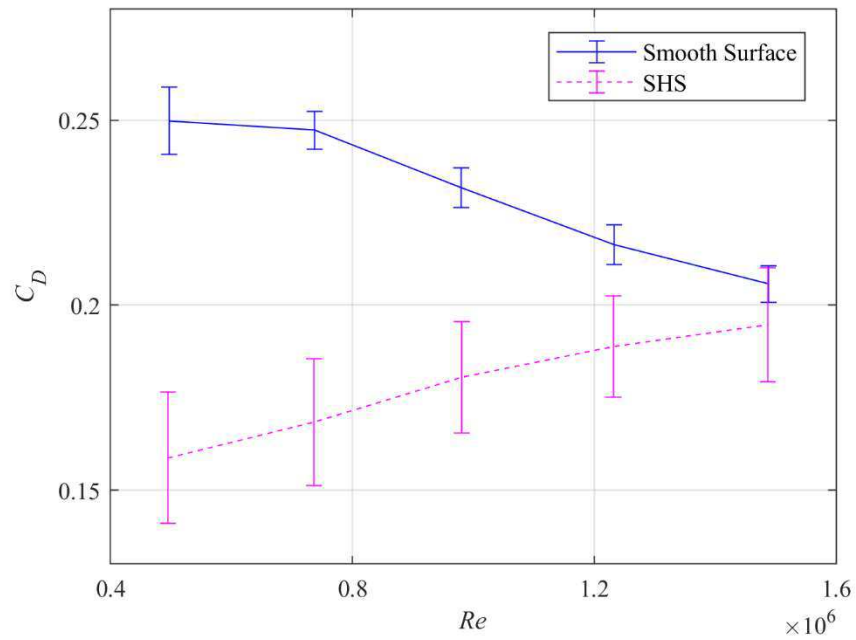


Figure 4.2. Average of the drag coefficient (C_D) versus Reynolds number (Re) for the superhydrophobic surface (SHS) in comparison with the smooth surface. The C_D is calculated using the drag force measured by a submersible load cell. The error bars, in both cases, correspond to one standard deviation (σ_{C_D}).

Table 4.1. Drag coefficient (C_D), standard deviation (σ_{CD}), average test velocity U [m/s], and drag reduction percentage (DR%) for the smooth surface and the superhydrophobic surface (SHS) cylinders.

Test Surface	Re number	5.0×10^5	7.0×10^5	1.0×10^6	1.2×10^6	1.5×10^6
Smooth Surface	Drag Coefficient, C_D	0.250	0.247	0.232	0.216	0.206
	Standard deviation, σ_{CD}	0.009	0.005	0.005	0.005	0.005
	U [m/s]	1.09	1.62	2.15	2.70	3.26
SHS	Drag Coefficient, C_D	0.159	0.168	0.181	0.189	0.195
	Standard deviation, σ_{CD}	0.018	0.017	0.015	0.014	0.015
	U [m/s]	0.98	1.45	1.93	2.43	2.92
	Dimensionless root-mean-square surface roughness $k^+_{rms} = R_{rms} / \eta$	0.46	0.66	0.85	1.04	1.23
Drag Reduction, DR [%]		36.4	32	22	12.5	5.6
Skin friction drag with respect the total drag [%]		58.2	54.6	55.1	56.4	57.1

Overall, the percentages of DR are higher than the previous experiments performed in the laminar regime over an axisymmetric body. Zhang S. *et al.* (2015) applied a superhydrophobic coating on a submarine model of 1-ft-long, with a ratio $L/D = 8.9$, and obtained up to 15% DR at a $Re = 1.2 \times 10^5$. Balasubramanian *et al.* (2004) tested a superhydrophobic surface on a 3-ft-long ellipsoid model, $L/D = 6$. A 14% of DR was obtained at a $Re = 5.5 \times 10^5$ with a 0° -angle-of-attack.

The longevity of this technique remains a challenge for scale-up applications in the turbulent regime. Although improvements are being sought, SHS retain the air layer for hours and not often for days (Xu *et al.* 2014). During the experiments, and simultaneously with the decay in the DR, the shiny aspect displayed by the surface at the beginning of the test was gradually lost over time and with increasing velocity; at the end of the tests, the surfaces exhibited an opaque color. The flow movement over the SHS not only enhanced the depletion of the air in the SHS (this

effect is further studied in Chapter 7), but it also removed part of the coating in the last 2 cm of the test cylinder when the flow velocity was increased beyond 1.5 m/s. Figure 4.3 shows the test cylinder with SHS at the beginning of the test in static water with a uniform air layer and bubbles at the top of the cylinder. Figure 4.4(a) displays the same SHS at the $Re = 5 \times 10^5$ still with a shiny aspect, and Figure 4.4(b) displays the same module at the $Re = 1.5 \times 10^6$ with a depleted air layer and a surface exhibiting an opaque color. Figure 4.5 shows the damaged section of the coating at $Re = 1.5 \times 10^6$ and in static water. The last 2 cm of the test cylinder was considered damaged as it was possible to see the wet regions. After finishing the tests, which involved 45 minutes in running water, the surface of the coated cylinder was exposed to the ambient air for an hour and submerged in the water again. Except for the section where the coating was damaged (it remained wet), a new air layer was formed along the cylinder. Hence, the change in the surface appearance during the data collection period is attributed to the loss of the air entrapped on the surface. The process of air depletion has been studied before by monitoring the amount of light reflected by the surface with a non-invasive optical technique based on total internal reflection. The loss of the light intensity reflected has matched the decrease in DR (Bobji *et al.* 2009, Samaha *et al.* 2011, Vajdi Hokmabad and Ghaemi, 2017).

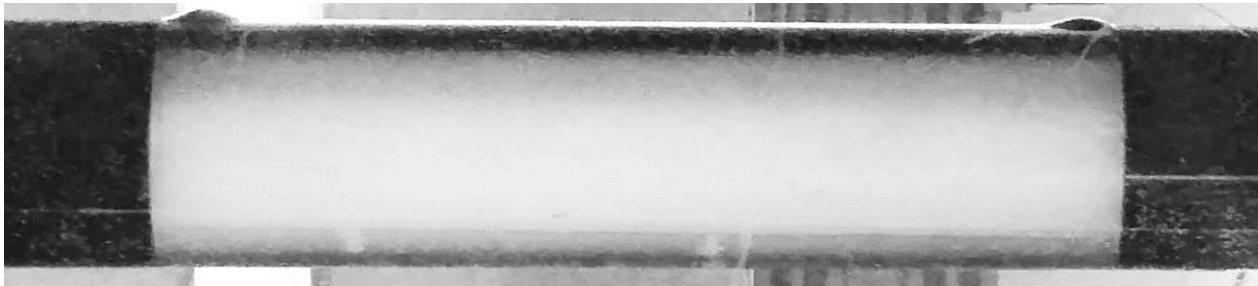


Figure 4.3. Test cylinder with the SHS in static water.

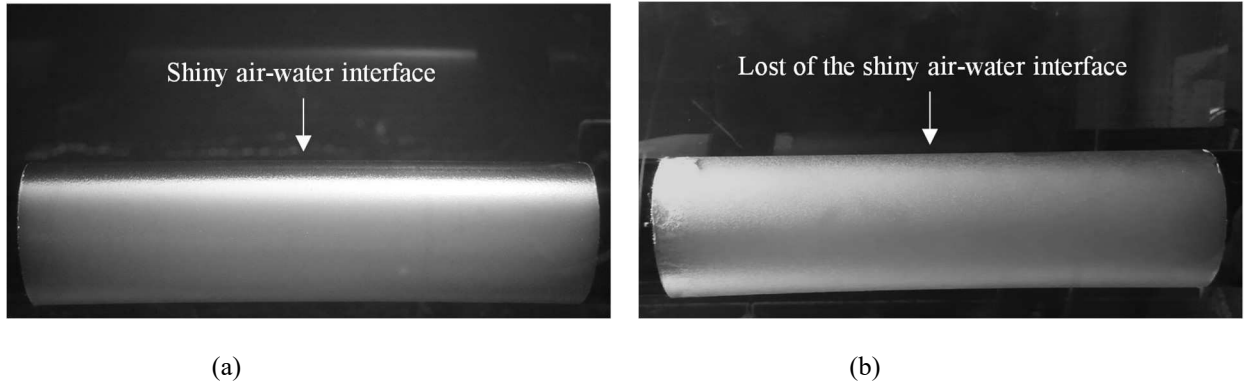


Figure 4.4. Test cylinder with the SHS. (a) The SHS displays the uniform shiny aspect of the air layer is seen at $Re = 5 \times 10^5$. (b) The image of the same surface at $Re = 1.5 \times 10^6$ and after 35 min operation of the flow loop. The shiny air-water interface is absent.

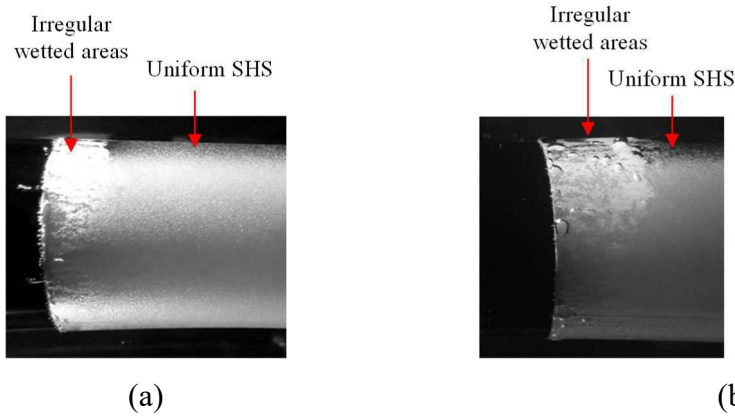


Figure 4.5. The damaged coating area on the back section of the AUV module. (a) $Re = 1.5 \times 10^6$, and (b) in static water at the end of the test.

In comparison with the SHS of random textures over flat plates in the turbulent regime, the results show a similar trend. The highest value of DR (36%) was obtained with the lowest dimensionless roughness k^+_{rms} of 0.46, and decreased to a minimum of 5.6% DR with increasing Re and a $k^+_{rms} = 1.23$. Bidkar *et al.* (2014) used a direct force measurement to test different textures in the SHS. Higher DR was obtained when the surface k^+_{rms} was at least one order of magnitude smaller than the dimensionless viscous sublayer thickness. Samples with high porosity (40%), coated with fluorosilane, and with a dimensionless roughness in the range of $0.06 < k^+ < 0.45$, showed a maximum DR of 25% at $Re = 2.5 \times 10^6$. However, they observed a decrease in the DR values with increasing Re when the surface roughness became comparable in size with the viscous sublayer thickness. The DR decreased up to 5% at $Re = 8.7 \times 10^6$. Similarly,

Lyu *et al.* (2013) coated aluminum plates with heptadecafluoro-1,1,2,2-tetrahydrodecyl trimethoxysilane (HDFS) and measured the changes in the drag force with a load cell. They reported a DR around 50% in the range of $1 \times 10^5 < Re < 2 \times 10^5$, but it then decreased to values around zero with higher Re .

The measurement of drag using the load cell includes the skin-friction drag of the boundary layer over the cylindrical body and also the drag due to the velocity deficit in the wake. The flow over the cylindrical body remains attached and experiences a pressure gradient only at the far back of the cylinder in the vicinity of the trailing-edge. Hence, the skin friction force can be estimated from the calculation of the wall-shear stress based on the integration of the momentum thickness and the assumption of the one-seventh-power law for the boundary layer thickness (Cengel and Cimbala *et al.*, 2014). The skin friction of the test model is estimated to contribute to about 54 to 58 % of the total drag when Re number varies from 5.0×10^5 to 1.5×10^6 . Assuming that there was no significantly change in the wake of the test model, the 36% DR obtained from the load cell at $Re = 5.0 \times 10^5$ would translate into about 63% reduction of the skin friction over the cylindrical body.

4.3 Conclusions

The C_D for the aft body of the test model is obtained for the smooth surface and the SHS case. The C_D value decreases with rising Re over the smooth surface; this same trend has been seen in previous experiments studying TBL over axisymmetric bodies (Cebeci *et al.*, 1970).

The use of the SHS proved to be an effective technique to reduce the drag in an axisymmetric model in the turbulent regime. Direct drag measurements showed a maximum reduction of 36.4% at a $Re = 5 \times 10^5$, with a k^+_{rms} of 0.46, and a minimum of 5.6% at a $Re = 1.5 \times 10^6$, with a k^+_{rms} of 1.23. The increase of the flow velocity produced a constant displacement of the air layer (enhancing its dissolution into the stream), deterioration of the coating, and also reduction of the boundary layer thickness. Subsequently, the DR decreased over time and with increasing Re numbers; this tendency is in agreement with the results reported in the turbulent regime for SHS over flat plates with the use of load cells (Bidkar *et al.* 2014, Lyu *et al.* 2013).

The use of SHS over axisymmetric bodies is promising for reduction of the drag of underwater vehicles. The DR obtained in this study was higher than the results obtained in previous work done in the laminar regime (Balasubramanian *et al.*, 2004 and Zhang *et al.*, 2015). It is still required to evaluate the wake of the axisymmetric body to properly quantify the reduction of the skin friction drag. There is a necessity for further study of the turbulent flow over the SHS (Gad-el-Hak, 2013) and the characterization of the air layer. The resultant slip and the air plastron of the SHS are further investigated in Chapter 7.

Chapter 5. Effect of Superhydrophobic Coating and Air Injection on the Drag of a Porous Surface

In this chapter, the use of a porous surface for air injection over the axisymmetric body is evaluated. Moreover, the air injection is combined with the use of a superhydrophobic coating over the porous surface.

The data collection was performed at five Re : 5.0×10^5 , 7.0×10^5 , 1.0×10^6 , 1.2×10^6 and 1.5×10^6 ; except those cases with high air injection rates, which rapidly pressurized the high-speed water loop. The use of the porous surface resulted in drag increase (DI) when compared with the smooth surface, and no improvement was observed with air injection. The use of the superhydrophobic coating over the porous cylinder (porous SHS) caused drag reduction (DR) relative to the non-coated porous surface. Although the injection of air did not improve the efficiency of the SHS, it was possible to replenish the air of the SHS plastron/pockets and maintain its performance. It was also possible to replenish the air layer over a wetted SHS. The surface kept its hydrophobic properties as long as the air was being supplied.

5.1 Introduction

The injection of air into the TBL of a liquid flow forms a two-phase mixture between the surface and the main flow. The two-phase flow can remain as a bubbly mixture or become a continuous film. The air bubbles affect the formation and the dynamic of the near-wall vortical structures (Madavan *et al.*, 1984 and Elbing *et al.*, 2008). Drag reduction is obtained when the bubbles attenuate the formation of turbulent structures near the surface and decrease Reynolds stresses (Lu *et al.*, 2005).

Merkle and Deutsch (1992) summarized several studies on microbubbles drag reduction. They found a maximum drag reduction of 80-90% when the gas injection rate is equivalent to the volumetric liquid flow in the boundary layer. Deutsch and Castano (1986) observed up to 20% drag reduction over an axisymmetric body with 632 mm length, at flow speeds of 4.6 m/s, and with air injection rates of 90-150 L/min. However, at higher flow velocity, from 10.7 to 16.8 m/s, they observed 40-60% drag reduction. In the latter case, drag reduction was limited by the air

flow rate required (240 L/min). The injection of air in their model was done through a small porous section of 5.17 mm wide and 6.35 mm long, with a pore size of 5 μ m. These results in an axisymmetric body are opposed to the observations made on a flat plate (Madavan *et al.*, 1984 & 1985a), where higher DR is obtained at lower flow stream velocities. The authors attributed this difference to the effect of the geometry in the buoyancy of the bubbles. Hence, they concluded that in axisymmetric bodies higher flow streams velocities are required to keep the bubbles near the surface of the axisymmetric body.

Deutsch and Pal (1990) measured the resultant circumferential gradient of the local shear stress on the same axisymmetric body previously used by Deutsch and Castano (1986). The local shear stress was measured with 12 flush-mounted hot film probes. The shear gradient showed maximum skin friction reduction (80-92%) at the top and bottom of the axisymmetric body cross-section at velocities above 10 m/s. At flow velocities below 10 m/s, the flow field was influenced by a double vortex structure located on each side of the body. These structures entrained the gas bubbles and pushed them from the bottom to the top of the body; the early separation of the air bubbles cloud from the wall directly affected the efficiency of the technique. Consequently, it was confirmed that the skin friction reduction is determined by the bubble concentration and location in the boundary layer.

Clark and Deutsch (1991), using the same test model, studied the effects of axial pressure gradients with microbubbles. They explained (in agreement with Deutsch and Castano, 1986 and Deutsch and Pal, 1990) that at lower velocities DR is limited by the buoyancy effect over the bubbles, and that at higher velocities drag is restricted by the required gas flow rate on the TBL. Moreover, they reported that the bubbles must reside above the viscous sublayer and below $y^+ < 100$ to be effective. For their zero-pressure gradient, the maximum DR reached was 80% at a flow stream of 10.7m/s and with an air injection rate around 660 L/min.

Shereena *et al.* (2013) used CFD to study the variation of the air injection rate, the angle of injection, and the angle-of-attack, in conjunction with the geometry of two axisymmetric bodies (blunt versus and streamlined tail). The model considered a ring of four air jets. The diameter of each jets represented 10% of the total length of the model. The results showed agreement with previous studies; highest DR was obtained at high flow speeds. The best results were found at

the maximum flow speed tested of 15 m/s, at 0 angle-of-attack and with an angle-of-injection of 30°. This configuration resulted in 61% of DR with an air injection rate of 118 L/min at the $Re = 4.6 \times 10^7$.

As previous experiments have proven, the success of this technique requires a constant supply of large amounts of air. The bubbles not only have to overcome the buoyancy force and the effect of the turbulent structures that push them away, but they also have to travel a long way until the end of the model. The amount of required air might be reduced if the injection is done in multiple points along the body instead of using a single point. The experiments mentioned above used a single injection section located downstream the nose with an extension between 1-2% of the total model length. Subsequently, it is of interest to study the effect of a larger area of injection and reduce the amount of air supplied. The current study injects air at lower rates (from 0.15 L/min up to 50 L/min) through the test cylinder of the aft body, which represents 37% of the total length of the AUV model. The average size of the pores is 10 μm .

As the amount of air required to obtain DR makes this method a challenge for underwater vehicles with limited space, it is of interest to study the combined effect of low injection rates and SHS. The injection of small amounts of air into SHS could improve the effective lifetime of the hydrophobic properties. As mentioned in previous sections, the effective lifetime of the SHS is limited due to the unstable air layer and its gradual dissolution into the flow stream. Although improvements are being sought, superhydrophobic surfaces retain the air layer for hours and not often for days (Xu *et al.* 2014). Hence, this study aims to evaluate if the injection of air can keep an SHS active, and if it is possible to recover a wetted SHS surface.

The porous surface module is tested with and without air injection. The combined effect of air injection with a superhydrophobic coating is also investigated. The data collection was performed at five Re : 5.0×10^5 , 7.0×10^5 , 1.0×10^6 , 1.2×10^6 and 1.5×10^6 .

5.2 Results and Discussion

The results of the load measurements performed with the porous surface, and the different configurations, are presented in the following order:

- a. Porous surface (baseline. No air injection, and without superhydrophobic coating)
- b. Porous surface with air injection:
 - Low air injection rates (LAIR)
Air injection rates: $Q_a = 0.15$ L/min, 0.25 L/min, 0.5 L/min, 1 L/min and 5 L/min.
 - High air injection rates (HAIR)
 Q_a values go from 10 L/min up to 50 L/min, with increments of 5 L/min.
- c. Porous surface with superhydrophobic coating (porous SHS):
 - Without air injection.
 - With low air injection rates ($Q_a = 0.15$ L/min, and 0.25 L/min)
- d. Effect of air injection in recovering an SHS:
 - Discrete air injection per periods of 30 s: $Q_a = 0.15$ L/min at the minute 13 of the test, $Q_a = 0.25$ L/min at the minute 19 of the test, $Q_a = 0.5$ L/min at the minute 23 of the test.
 - Continued air injection of $Q_a = 0.15$ L/min for 300 s, from the minute 43 to the minute 48 of the test.

Images of each experiment are displayed in Appendix C.

5.2.1 Drag of the Porous Surface without Air Injection

Due to the difference in the surface roughness among the smooth and porous surfaces, it was required to characterize the aft body C_D as a function of Re when the porous module is used without air injection. Figure 5.1 and Table 5.1 display the comparison of the porous surface results with those of the smooth surface. The direct measurement of the drag force showed a $C_D = 0.381$, with a $\sigma_{CD} = 0.011$, at the $Re = 5.0 \times 10^5$. Moving into higher velocities, at $Re = 1.5 \times 10^6$, the $C_D = 0.309$ and $\sigma_{CD} = 0.003$. Similar to the smooth surface results, the C_D values declined with increasing Re . However, the rough finish of the porous surface produced DI in comparison with the smooth surface: 52.7% and 50.3%, at the lowest and highest Re respectively.

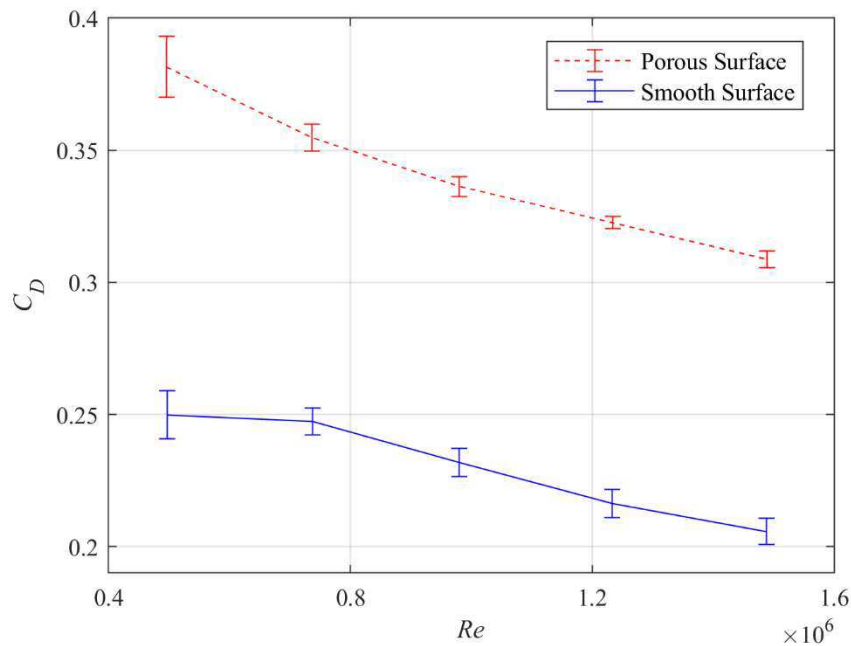


Figure 5.1. Average of the drag coefficient (C_D) versus Reynolds number (Re) for the porous and smooth surface. The error bars correspond to one standard deviation (σ_{CD}).

Table 5.1. Drag coefficient (C_D), standard deviation (σ_{CD}) and average test velocity U [m/s], for the smooth surface cylinder and the porous surface.

Test Surface	Re number	5.0×10^5	7.0×10^5	1.0×10^6	1.2×10^6	1.5×10^6
Smooth Surface	Drag Coefficient, C_D	0.250	0.247	0.232	0.216	0.206
	Standard deviation, σ_{CD}	0.009	0.005	0.005	0.005	0.005
	U [m/s]	1.09	1.62	2.15	2.70	3.26
Porous Surface with No Air Injection	Drag Coefficient, C_D	0.381	0.355	0.336	0.323	0.309
	Standard deviation, σ_{CD}	0.011	0.005	0.004	0.002	0.003
	U [m/s]	0.97	1.45	1.92	2.42	2.92
Drag Increase, DI [%]		52.6	43.4	45.1	49.1	50.3

5.2.2 Drag of the Porous Surface with Air Injection

The air injection rates Q_a were divided into two categories: low air injection rates (LAIR), $Q_a = 0.15$ L/min, 0.25 L/min, 0.5 L/min, 1 L/min and 5 L/min; and high air injection rates (HAIR), from 10 L/min up to 50 L/min, with increments of 5 L/min. Table 5.2 shows the non-dimensional airflow C_v in the TBL as a function of the Re and the air flow rate Q_a . The values of C_v were estimated using Eq. 2.42. If no C_v values are reported, no data was collected at that flow velocity.

Table 5.2. Non-dimensional airflow C_v in the turbulent boundary layer (TBL) for each Re and air flow rate (Q_a) tested.

Q_a [L/min]	$Re = 5 \times 10^5$	$Re = 7 \times 10^5$	$Re = 1 \times 10^6$	$Re = 1.2 \times 10^6$	$Re = 1.5 \times 10^6$
LAIR C_v	0.15	0.003	0.002	0.001	0.001
	0.25	0.005	0.003	0.002	0.002
	0.5	0.01	0.006	0.005	0.004
	1	0.019	0.013	0.01	0.008
	5	0.09	0.06	0.05	0.04
HAIR C_v	10	0.16			0.06
	15	0.22			0.09
	20	0.28			0.12
	25	0.33			0.15
	30	0.37			0.17
	35	0.40			0.2
	40				0.22
	45				0.24
50				0.25	

The results for LAIR are displayed as C_D versus Re in Figure 5.2, and as C_D versus Q_a in Figure 5.3. All the injection rates tested showed DI when compared with the C_D values of the porous surface without air injection. For a constant Q_a , DI was greater at lower flow stream velocities, $Re = 5.0 \times 10^5$, than at higher velocities ($Re = 1.5 \times 10^6$). Moreover, increasing Q_a caused a higher DI; except $Q_a = 0.15$ L/min, which displays a similar trend to $Q_a = 1$ L/min.

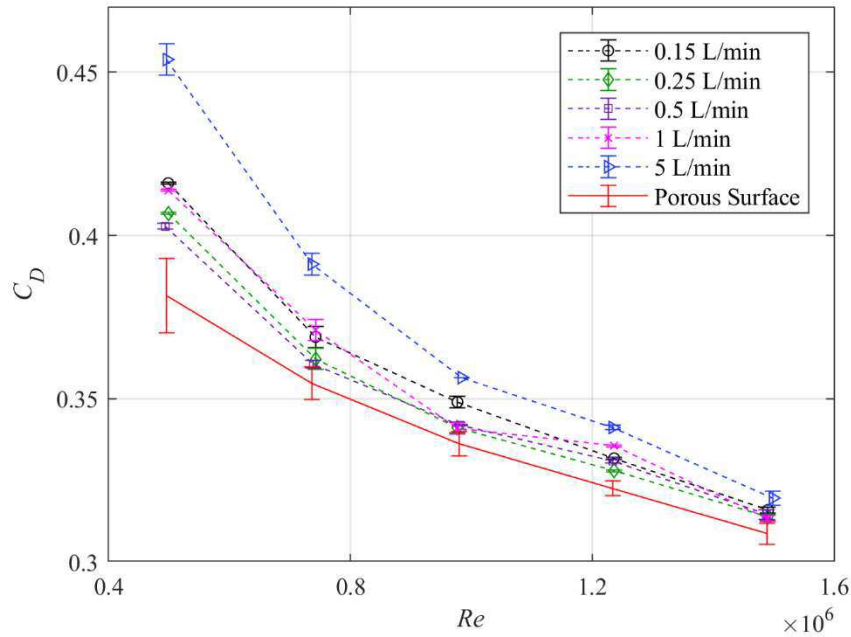


Figure 5.2. Average of the drag coefficient (C_D) versus Reynolds number (Re) for low air injection rates (LAIR) over the porous surface. The porous surface (baseline) is compared with the cases of $Q_a = 0.15$ L/min, $Q_a = 0.25$ L/min, $Q_a = 0.5$ L/min, $Q_a = 1$ L/min, and $Q_a = 5$ L/min. The error bars correspond to one standard deviation (σ_{C_D}).

Figure 5.3 shows the C_D versus Q_a at constant Re . There is a slight reduction (between 1 to 3%) of the C_D when injecting air at 0.25 L/min and 0.5 L/min. However, from 1 L/min upward, the C_D increased. That slight reduction of the C_D at $Q_a = 0.25$ L/min and $Q_a = 0.5$ L/min, gradually decreases with higher Re .

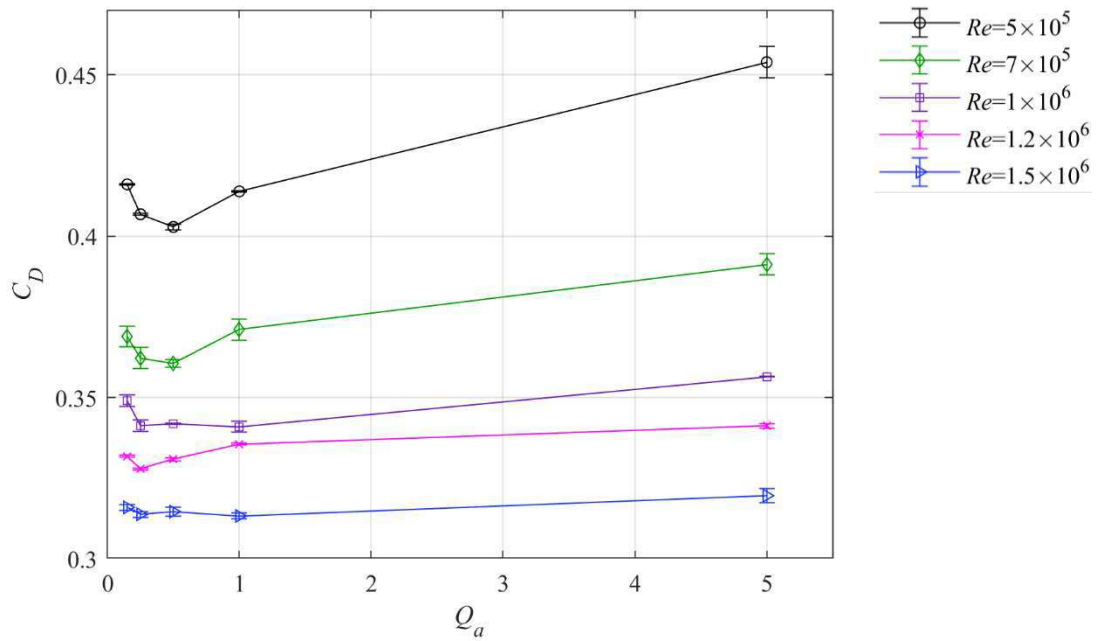
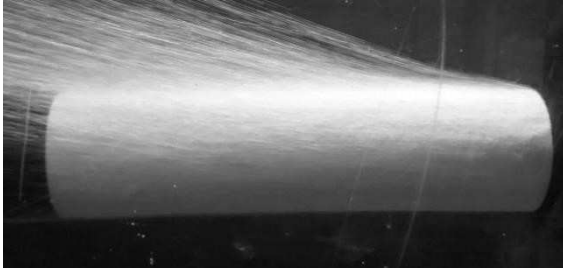


Figure 5.3. Average of the drag coefficient (C_D) versus the air injection rate (Q_a) for the low air injection rates (LAIR) at the constant Re of: 5×10^5 , 7×10^5 , 1.0×10^6 , 1.2×10^6 , and 1.5×10^6 . The error bars correspond to one standard deviation (σ_{CD}).

Pictures of the experiments are gathered in the Appendix C.1. Figure 5.4 shows sample images for $Q_a = 5$ L/min in static water, at $Re = 5.0 \times 10^5$ and $Re = 1.5 \times 10^6$. In Figure 5.4(a) with static water, is possible to see slightly more bubbles being injected at the top than at the bottom of the test cylinder. As soon as we start moving the flow, the buoyancy effect on the bubbles produced an upward movement of the bubbles at the bottom and side of the model to the top surface, as displayed in Figure 5.4(b). Increasing the velocity diminished this effect. As show in Figure 5.4(c) the flow at the $Re = 1.5 \times 10^6$ helped to maintain the bubbles cloud near the surface for a longer section. However, the effect of the highest flow velocity on the bubbles buoyancy was not enough to decrease the drag.



(a)



(b)



(c)

Figure 5.4. Air injection with a rate (Q_a) of 5 L/min (a) in static water, (b) at the Re of: 5×10^5 , and (c) at the Re of 1.5×10^6 . The increase in velocity helped to keep the bubbles cloud near the surface.

Similar to the previous results, in case of HAIR, all the values of Q_a tested showed DI. A higher DI was observed at the lowest flow stream velocity with $Re = 5.0 \times 10^5$, than at the highest velocity with $Re = 1.5 \times 10^6$. Increasing the injection rate generally resulted in higher DI. The exception was the injection rate of $Q_a = 15$ L/min at $Re = 5.0 \times 10^5$, which showed a higher C_D than $Q_a = 20$ L/min and $Q_a = 25$ L/min. These changes in the C_D are displayed in Figure 5.5, considering the C_D versus Re , and in Figure 5.6 considering the C_D as a function of the Q_a .

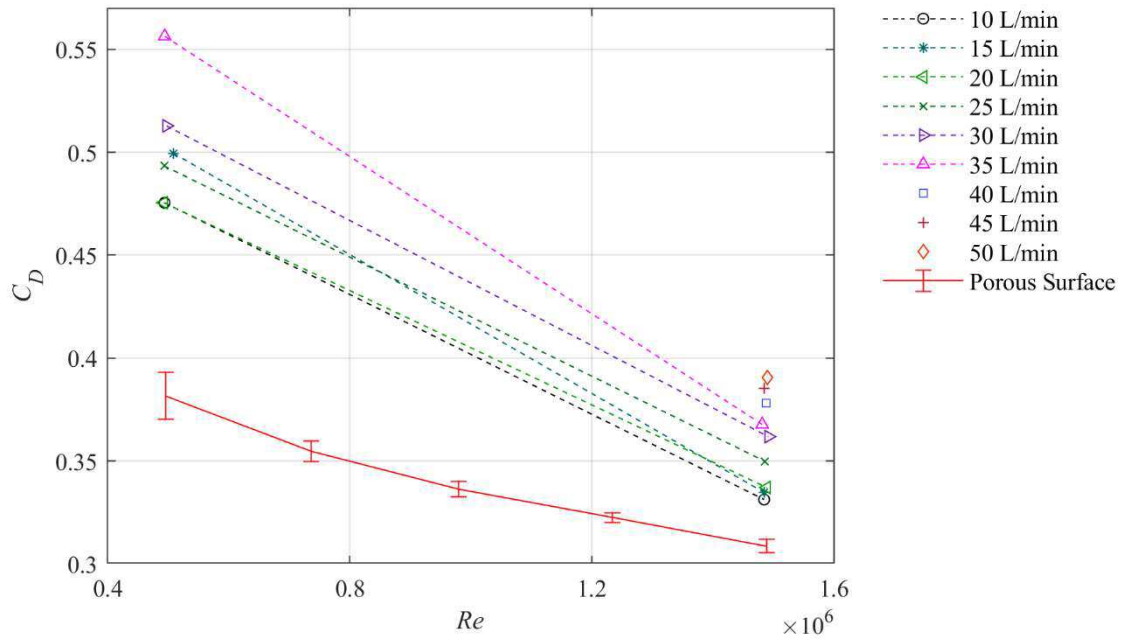


Figure 5.5. Average of the drag coefficient (C_D) versus Reynolds number (Re) for the high air injection rates over the porous surface (HAIR). The porous surface (baseline) is compared with the cases of $Q_a = 10$ L/min, $Q_a = 15$ L/min, $Q_a = 20$ L/min, $Q_a = 25$ L/min, $Q_a = 30$ L/min, $Q_a = 35$ L/min, $Q_a = 40$ L/min, $Q_a = 45$ L/min, $Q_a = 50$ L/min.

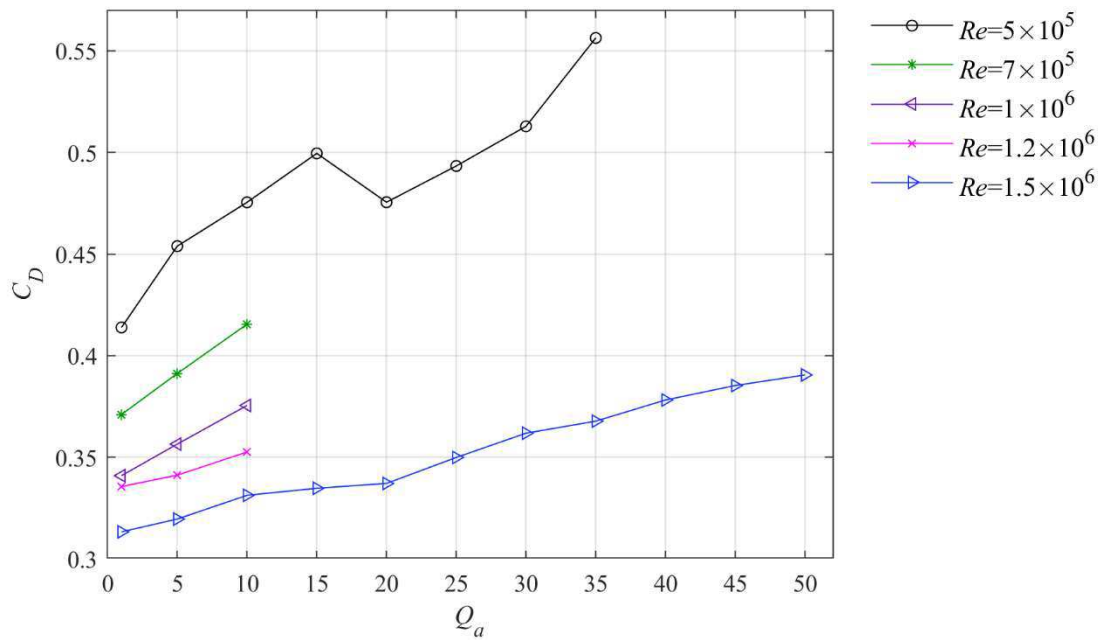


Figure 5.6. Average of the drag coefficient (C_D) versus the air injection rate (Q_a) for the high air injection rates over the porous surface (HAIR) at the constant Re of: 5×10^5 , 7×10^5 , 1.0×10^6 , 1.2×10^6 , and 1.5×10^6 .

Pictures of the experiments are gathered in the Appendix C.2. Figure 5.7 shows sample images for $Q_a = 25, 35$ and 45 L/min, at the constant $Re = 1.5 \times 10^6$. The increase of Q_a helped to increase the number of bubble near the surface at the bottom and sides. Similar to the experiments with LAIR, the effect of the highest flow velocity on the bubbles buoyancy was not enough to decrease the drag. For all the images is possible to observe a higher concentration of bubbles at the top surface than on at the bottom and sides of the test cylinder.

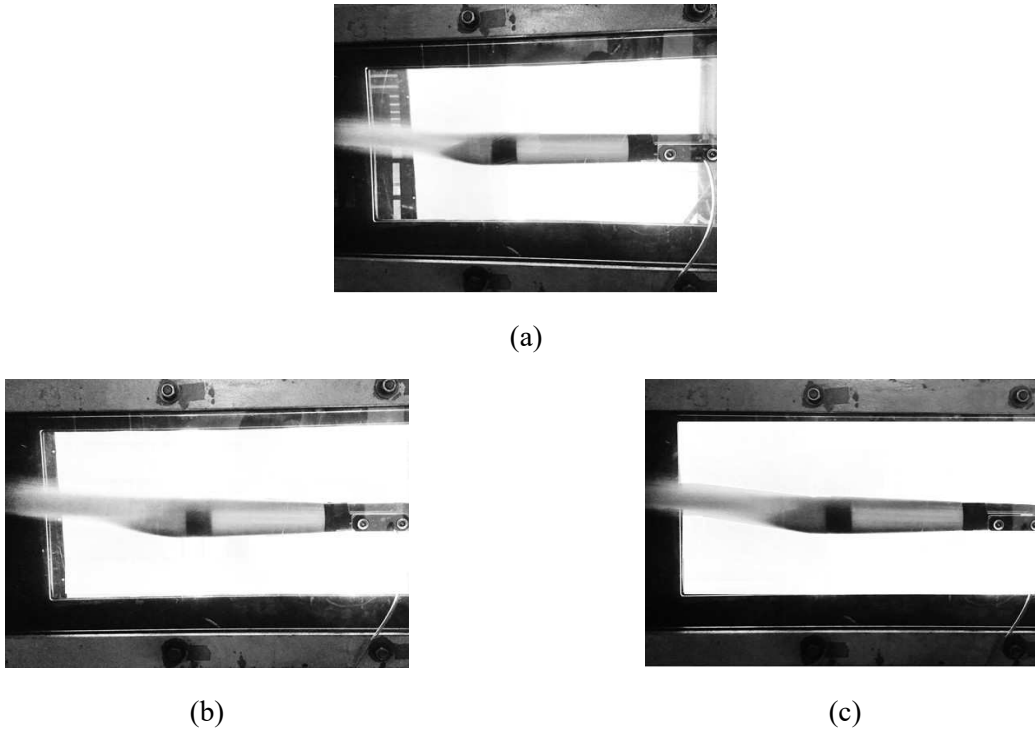


Figure 5.7. Air injection at the Re of 1.5×10^6 with an air injection rate (Q_a) of (a) 25 L/min, (b) 35 L/min, and (c) 45 L/min. The increase of Q_a was not enough to reduce the drag.

Overall, the extension of the air injection area and the use of low air injection rates did not offer DR. For all the air injection rates (Q_a) there was a DI in comparison with the porous surface without air injection, and even higher in contrast to the smooth surface.

In agreement with Murai (2014) and Elbing *et al.* (2008), the DR is seen to depend on the bubbles effect over the turbulence production, and not only on the reduction of the bulk density. Even though the reduction of the bulk density in the near wall may have an important role decreasing the shear stress at the wall ($-\rho \langle uv \rangle$), it is not enough to result in DR. The C_v range tested in the current investigation were in the range of 0.001 to 0.40. Previous successful work of

Deutsch and Castano (1986) obtained a 40% DR at a $Re = 6.7 \times 10^6$ with a C_v of 0.23; and Shereena *et al.* (2013) obtained 62% DR at a $Re = 4.6 \times 10^6$ with a C_v of 0.22. Although the range of C_v used in the current investigation covered the values applied in previous literature with successful DR, the tests were performed at lower velocities ($Re < 1.6 \times 10^6$) than the works mentioned above ($Re > 4.6 \times 10^6$). Gabillet *et al.* (2002) observed that the near wall turbulence increased linearly with the C_v when injecting air in a horizontal channel. They concluded that the bubbles had a similar effect on the resultant DI as it would have the addition of surface roughness. They attributed DI to the relative motion of the bubbles and the augmentation of the turbulent shear stress in the bubble layer.

The injection of the bubbles in multiple points along the TBL might have enhanced the pressure drag and the turbulence production. The increase of the pressure drag could have been due to the effects of the bubbles in the separation the flow from the surface in the multiple points of injection; previous successful work had used a single and small injection area at the beginning of their test model. Turbulence production could have been affected by the non-uniform distribution of the bubbles over the AUV model. Two factors affecting the air bubbles distribution were the injection uniformity and the upward buoyancy-driven motion of the bubbles. In the current experiment the bubble distribution was denser at the top of the porous cylinder than at the bottom, as previously described. Although the distribution improved with increasing air rates, the bubbles injected at the bottom, and sides of the AUV model were rapidly moved upward. This is analogous to the observations done by Deutsch and Pal (1990) at low flow stream speeds (< 10.7 m/s). They reported that the flow field around the axisymmetric body was influenced by a double vortex structure located on each side of the body. These structures entrained the gas bubbles and pushed them from the bottom to the top of the body. Further investigation is required to determine if the upward movement of the bubbles mixture in the present experiments are due to these (or similar) structures, or if it is only due to the buoyancy force over the bubbles.

Similar to the observation reported by Merkle and Deutsch (1992), the flow stream velocity affected the buoyancy of the bubbles over the surface. At the lowest Re tested, 5×10^5 , the cloud of bubble rapidly separated from the test model. Conversely, increasing the flow stream velocity improved the attachment of the cloud of bubbles to the surface. Nonetheless, higher Q_a would be

necessary to reproduce the conditions of successful previous works. Higher flow stream velocity and air injection rates were not tested due to limitations in the facility.

Further investigation is required with higher injection rates and flow stream velocities to compare the performance of this technique with the use of a small single injection section at the leading edge of the axisymmetric body, and to determine if the design of the AUV model needs to be modified.

5.2.3 Drag of the Porous Surface with Superhydrophobic Coating

The data of the porous SHS was collected in three parts with the following order during the same test: 1) without air injection, 2) $Q_a = 0.15$ L/min, and 3) $Q_a = 0.25$ L/min. Figure 5.8 shows the average C_D versus Re for the porous SHS (with and without air injection) in comparison with the porous surface (with and without air injection, $Q_a = 0.15 - 0.25$ L/min) and the smooth surface.

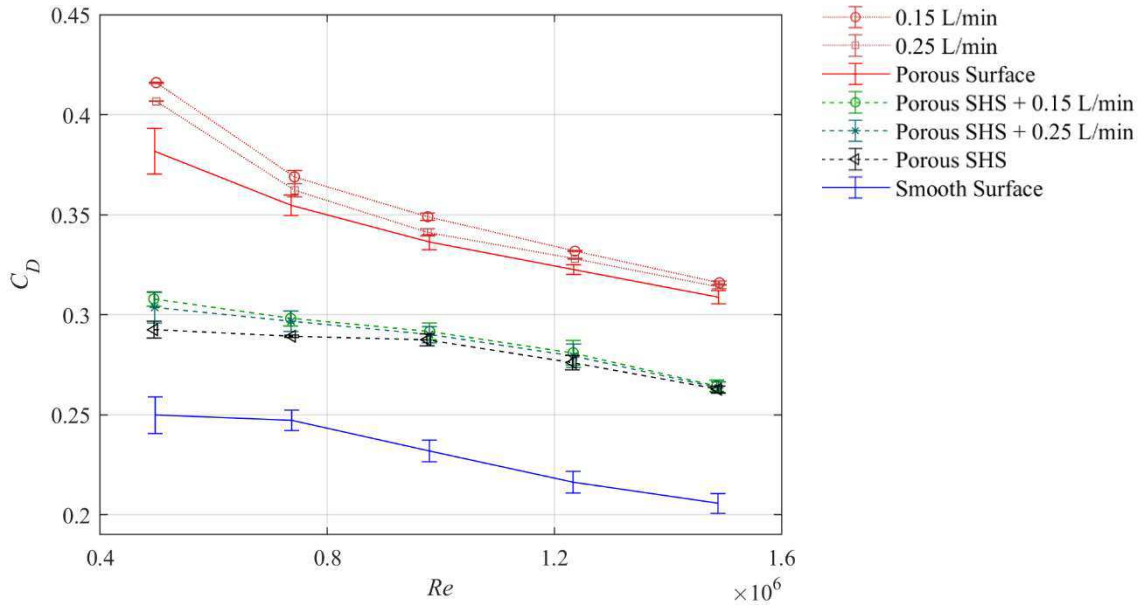


Figure 5.8. Average of the drag coefficient (C_D) versus Reynolds number (Re) for the combined effect of air injection and superhydrophobic surface (SHS). The following configurations are compared: porous surface, with and without air injection ($Q_a = 0.15$ L/min and $Q_a = 0.25$ L/min), SHS over the porous surface, with and without air injection (SHS $Q_a = 0.15$ L/min and SHS $Q_a = 0.25$ L/min), and the smooth surface. The error bars correspond to one standard deviation (σ_{CD}).

Although the results of the porous SHS showed DR in comparison with the porous surface, the C_D values are still higher than those for the smooth surface. Considering the most favorable case of the porous SHS (the one with the maximum DR), the C_D is 17% higher than the value of the smooth surface at $Re = 5.0 \times 10^5$, and 28% higher than the C_D value of the smooth surface at $Re = 1.5 \times 10^6$. Furthermore, in comparison with the DR percentage obtained by the smooth SHS, the averaged result decreased approximately 13% at low velocities and improved approximately 9% at the highest velocity $Re = 1.5 \times 10^6$. It was observed that the adhesion of the superhydrophobic coating to the porous material was better than for the smooth surface. Moreover, the surface was

not damaged at the end of the replaceable module, as happened with the smooth surface. Consequently, the porous surface performed better than the smooth surface in retaining the air pockets at high velocities. Bidkar *et al.* (2014) emphasized the importance of having a textured surface able to preserve the Cassie-Baxter state (e.g., using a surface with interconnected porosity). Surfaces with low porosity ($< 20\%$) and large values of roughness ($0.35 < k^+_{rms} < 5.83$) showed a neutral or small DR at low flow velocities, and a DI at higher Re . Samples with high porosity (40%) coated with fluorosilane, and with a dimensionless roughness in the range of $0.06 < k^+_{rms} < 0.45$, showed a maximum DR of 25% at $Re = 2.5 \times 10^6$. However, DR eventually decreased with increasing Re (Bidkar *et al.*, 2014).

Overall, in the current experiment the results of the porous SHS without air injection showed the highest averaged DR in comparison with the porous surface: 23.4% at the lowest Re of 5.0×10^5 , and a 14.9% at the highest Re of 1.5×10^6 . Table 5.3 gathers the averaged C_D values and the percentage of DR obtained by the porous SHS in comparison with the porous surface.

Table 5.3. C_D and drag reduction percentage (DR%) of the porous surface with superhydrophobic coating (porous SHS) in comparison with the noncoated porous surface without air injection.

Re number	5×10^5		7×10^5		1.0×10^6		1.2×10^6		1.5×10^6	
Test Surface	C_D	DR	C_D	DR	C_D	DR	C_D	DR	C_D	DR
Porous Surface	0.382	-	0.355	-	0.336	-	0.323	-	0.309	-
U [m/s]	0.97		1.45		1.92		2.42		2.92	
Porous SHS	0.293	23.4%	0.289	18.5%	0.288	14.5%	0.276	14.4%	0.263	14.9%
U [m/s]	0.94		1.39		1.85		2.33		2.81	
Porous SHS + $Q_a = 0.15$ L/min	0.304	20.4%	0.297	16.4%	0.290	13.8%	0.279	13.4%	0.264	14.6%
U [m/s]	0.92		1.37		1.83		2.30		2.77	
Porous SHS + $Q_a = 0.25$ L/min	0.308	19.3%	0.298	16.0%	0.292	13.3%	0.281	12.9%	0.264	14.3%
U [m/s]	0.92		1.36		1.81		2.28		2.75	

The shiny aspect observed at the beginning of the test with no air injection was gradually lost and the surface displayed an opaque aspect at the end of the test. This change in the surface aspect can be seen in Figure 5.9(a) and (b). Conversely, the continuous injection of air kept the shiny look of the SHS during all the experiment and this effect can be observed in Figure 5.9(c) and (d). Similar to the observations done by Peng *et al.* (2017) over a flat plate, the hydrophobic surface was able to maintain the air bubbles within the SHS. The air injected spread through the surface and moved in the same direction of the flow stream within the air plastron. Furthermore, it was possible to observe a strong flow pattern in the air-water interface.

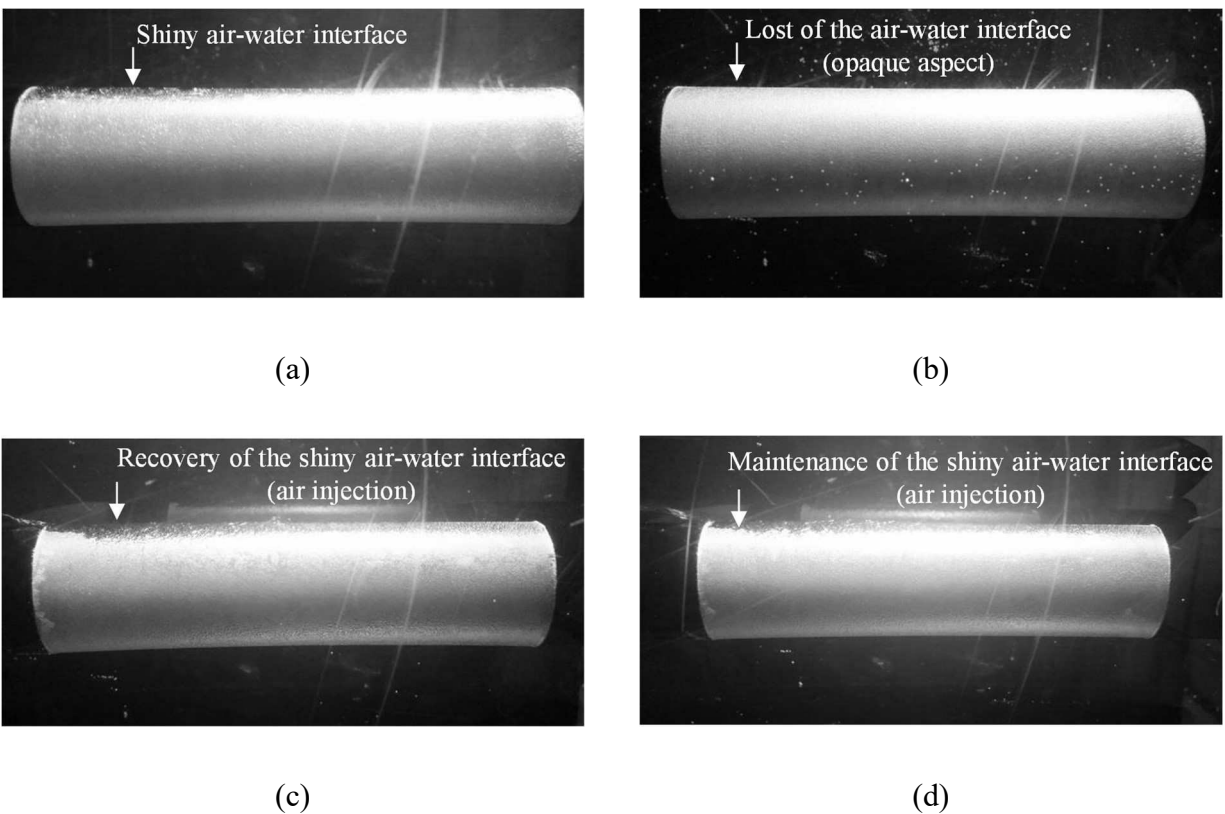


Figure 5.9. Porous SHS with (a) no air injection at the beginning of the test with a Re of 5×10^5 , and (b) at the end of the test with a Re of 1.5×10^6 . Images of the recovery and maintenance of the shiny aspect of the porous SHS at the Re of 5×10^5 , with the injection rate (Q_a) of (c) 0.15 L/min, and (d) 0.25 L/min.

Even though the injection of air over the porous SHS did not improve the results obtained by the porous SHS by itself, nor there was a significant DI. Note that a slight increase in drag, among 0 to 5% as seen in Table 5.4, was measured as the time elapsed throughout the experiment and the air injection rate increased. The total time of the experiment was 135 min, 45 min for each configuration in subsequent order. Consequently, this slight increase in the drag might be a result

of the degradation of the coating due to the flow movement over the surface over time, and not necessarily a consequence of the injection of air.

Table 5.4. Drag coefficient (C_D) and drag increase percentage (DI%) of the porous surface with superhydrophobic coating (porous SHS) with and without air injection.

Re number	5×10^5		7×10^5		1.0×10^6		1.2×10^6		1.5×10^6	
	C_D	DI	C_D	DI	C_D	DI	C_D	DI	C_D	DI
Porous SHS	0.293	-	0.289	-	0.288	-	0.276	-	0.263	-
Porous SHS + $Q_a = 0.15$ L/min	0.304	3.8%	0.297	2.6%	0.290	0.9%	0.279	1.2%	0.264	0.3%
Porous SHS + $Q_a = 0.25$ L/min	0.308	5.3%	0.298	3.1%	0.292	1.4%	0.281	1.8%	0.264	0.6%

When the coating was not used over the porous surface, the injection of the air produced a DI within 2 - 9% with the same Q_a . The difference in DI might be related to the trajectory of the bubbles and their synergy with the TBL. During the injection of air over the porous surface (without the coating), the bubbles were rapidly moving away from the surface, interacting in their trajectory with the TBL structures. When the air was injected into the porous SHS, no bubbles were seen to come out from the air-water interface. Hence, the bubbles were not interacting with the TBL structures beyond the interface region. This behaviour of the bubbles might explain why the increase in drag was lower in the latter case than when injecting air over the porous surface (without coating). Pictures of the experiments are gathered in the Appendix C.3.

In conclusion, the injection of air in a submerged SHS can help to maintain its hydrophobicity; as long as the air pockets are present the surface will be hydrophobic (Samaha *et al.* 2012). Nonetheless, further investigation is required to find an optimal injection rate to form a robust air layer. The use of high rates of air injection might destabilize the SHS due to the formation of strong flow patterns in air-water interface. Hence, it is also recommended to study the effect of the air injection rate on the stability of the air-water interface.

5.2.4 Evaluation of the Effect of Air injection in Recovering a Superhydrophobic Surface

The objective of this second experiment was to observe the effect of the air injection on a wetted SHS in a high shear flow. To obtain the wetted SHS, the coated cylinder was exposed for 12 minutes to a flow at $Re = 1.5 \times 10^6$ before beginning to inject the air. The stability analysis of Abu Rowin *et al.* (2017) using the same superhydrophobic coating over a flat plate, showed that an unstable SHS gradually lost its capacity on reducing DR after 5 minutes at a $Re = 4400$ based on the channel height (25 mm) and a velocity of 0.2 m/s. The current investigation with the SHS, over the smooth and the porous surface, also showed that the exposure of the surfaces to high velocity rapidly diminished its efficiency. Additionally, the load cell measurement was being monitored in real time and it was showing no DR in comparison with the porous surface without the coating.

The experiment considered discrete injection of air per periods of 30 s, and the continued injection of air for a period of 300 s, to try the recovering of the air layer in the porous SHS. The pattern of air injection is described in the following scheme (outside those times, no air was being injected). The results are displayed in Figure 5.10.

- Discrete air injection per periods of 30 s:
 - $Q_a = 0.15$ L/min at the minute 13 of the test,
 - $Q_a = 0.25$ L/min at the minute 19 of the test, and
 - $Q_a = 0.5$ L/min at the minute 23 of the test.
- Continued air injection of $Q_a = 0.15$ L/min for 300 s, from the minute 43 to the minute 48 of the test.

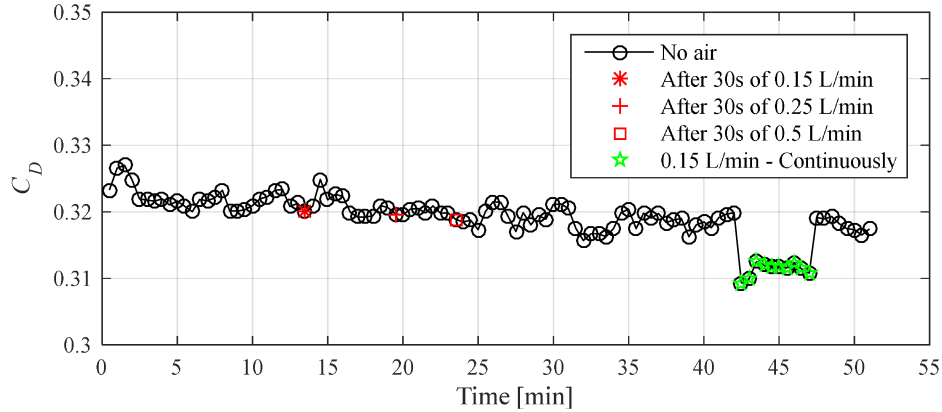


Figure 5.10. Air injection effect on a wetted porous superhydrophobic surface (SHS)

This first observation is that the porous SHS lost its capacity of reducing drag. For the data points without air injection the average C_D is 0.320, which represents a slight increase of the drag ($\sim 3\%$) in comparison with the porous surface without the coating. This slight increase in the drag might be due to the intensification of the SHS roughness when exposed for a large period of time to a high shear flow at $Re = 1.5 \times 10^6$. The depletion of the air layer might have exposed the microstructure of the superhydrophobic coating (for this cylinder the coating had been applied two times).

Regardless of the air rate, the discrete injection of air over the wetted SHS only showed DR while the air was being supplied. It is not possible to see any effect when the injection was stopped. Peng *et al.* (2017), who tested the injection of air during small periods of time over an SHS of a flat plate, also observed the rapid dissolution of the air into the water when the air injection was stopped. Specially, at this high velocity, the bubbles are quickly taken away by the flow.

Consequently, the DR improvement was only visualized during the continuous injection of air. Similar to the observations done with the injection of air in the porous SHS, the continuous injection of air kept the shiny look of the SHS during the exposure time. The air injected spread through the surface and moved in the same direction of the flow stream; no bubbles were seen to come out from the air-water interface. Using $Q_a = 0.15$ L/min, the C_D improved a maximum of 3.5% and an average a 2.7% ($C_D=0.311$). After the air injection was stopped, the C_D increased and reached the same average value observed before the air was injected.

Although it is not possible for the wetted SHS to retain the air, it is possible to restore the air layer as long as the air supply is maintained. The combined use of the SHS and low air injection rate is promising on improving the longevity of the SHS used under high flow speed and pressure conditions.

5.3 Conclusions

There was no DR with the use of air injection over a porous surface. Although the range of C_v covered the values applied in the previous literature with successful DR, the tests did not result in DR due to lower freestream velocity. Due to the facilities capabilities, it is not possible to reproduce higher Re and neither fulfill the requirement of air flow rate to obtain the same C_v at those flow velocities.

The DR mechanism of the air bubbles is seen to be strongly influenced by the bubbles effect over the turbulence production and not only on the reduction of the bulk density in the TBL. Hence, the turbulence production could have been affected by the non-uniform distribution of the bubbles over the AUV model. Two factors affecting the air bubbles distribution were: i) the injection uniformity, and ii) the upward buoyancy driven motion of the bubbles.

Further investigation is required to evaluate if the air distribution over the surface can be improved with higher injection rates and flow stream velocities, or if the design of the AUV model needs to be modified. A supplementary investigation at low velocities is to evaluate the effect of the bubbles injected along the aft body, in comparison with the bubbles injected at a single point located at the beginning of the test model.

The use of a porous SHS proved its effectiveness in reducing the drag in the aft body of the test model in comparison with the non-coated porous surface. The rough surface prevented the damage of the coating at high shear flow. Although there was DR in comparison with the porous surface, the resultants C_D are still higher than those of the smooth surface.

Overall, the highest DR values were obtained at the beginning of the test without air injection. The maximum DR obtained was 25.0% at the lowest $Re = 5.0 \times 10^5$, and 14.5% at the $Re = 1.5 \times 10^6$. Although the injection of air replenished the SHS, it was not observed an improvement of the SHS efficiency. Nonetheless, the combined effect of air injection and SHS can improve the longevity of the hydrophobic properties.

The injection of air over a wetted SHS can restore the air plastron as long as the air supply is maintained. As soon as the air injection is stopped, the air bubbles will be taken away by the flow. In the experiments performed at $Re = 1.5 \times 10^6$, the C_D improved a maximum of 3.5% and

an average a 2.7%. After the air injection was stopped, the C_D increased and reached the same average value observed before the air was injected. Further investigation is required to find an optimal injection rate to form a robust air layer.

Chapter 6. Effect of Superhydrophobic Coating and Air Injection on the Drag of Riblets Surfaces

The use of riblets, and also riblets in combination with superhydrophobic coating and air injection, is evaluated over an axisymmetric body in this chapter. Two riblets sleeves with rectangular grooves are considered. Model 1 has riblets with a span (s) of 0.3 mm, height (h) of 0.15 mm, and thickness (t) of 0.05 mm; which correspond to the ratio $h/s = 0.5$ and a range of the dimensionless spacing of $s^+ = 15 - 40$. This module is tested with and without a superhydrophobic coating (SHS riblets model 1). Model 2 considers rectangular grooves with $s = 0.6$ mm, $h = 1.2$ mm and $t = 0.1$ mm, for a $h/s = 2$ and a range of $s^+ = 30 - 80$. This model was provided with staggered holes in the valleys of the riblets for air injection along the cylinder.

The data collection was performed at five Re : 5.0×10^5 , 7.0×10^5 , 1.0×10^6 , 1.2×10^6 and 1.5×10^6 . Overall, the use of both riblets modules increased the drag in comparison with the smooth surface. Consistent with previous tests in this project, the use of the SHS over the riblets reduced the drag in comparison with the riblets module without the coating.

6.1 Introduction

Surfaces with streamwise microgroove are referred to as riblets and can reduce the drag by keeping the quasi-streamwise vortices away from the surface (Walsh, 1990). There is a general agreement on the effect of riblets on the vortical structures: in the region of DR ($s^+ < 30$) the riblet spacing s^+ is smaller than the longitudinal vortices diameter, hence, these vortical structures just interact with the riblet's tip. Consequently, the high shear stresses are only present in these small areas (Koeltzch *et al.* 2002, Fu *et al.* 2017). The DR obtained by this method is a function of the Re (expressed in terms of $s^+ = s/(u\tau/\nu)$), the groove geometry, and the groove spacing. Hence, its performance might be affected by external elements that get trapped between the valleys.

Bechert *et al.* (1997) performed an extensive investigation optimizing riblets geometry; varying its cross-section shape and the ratio h/s . They used a direct force measurement on flat plates with a shear-stress balance. The highest values of DR is 9.9%, and was obtained using the blade riblets with $h/s = 0.5$, $t/s = 0.2$, and $s^+ = 17$. An 8.2% DR was obtained with the trapezoidal

riblets, also at $s^+ = 17$ and $h/s = 0.5$. The sawtooth and the semi-circular scalloped riblets reduced the drag in a 5%, also at $s^+ = 17$.

Recently, also in the turbulent regime, Bezuijen (2017) performed drag force measurements on a plate with riblets. Three models of riblets were tested: a sample of 3D printed riblets ($s = 400\mu\text{m}$), a sample of stiff riblets ($s = 100\mu\text{m}$), and a sample of riblets able to deform with the flow motion ($s = 100\mu\text{m}$). The highest results of DR were obtained by testing the riblets in its optimal value of $s^+ = 17$, based on Bechert (1997) design of trapezoidal riblets. A DR of 5% was obtained for the sample of 3D printed riblets, 4 - 7% DR for the sample of stiff riblets, and 3-4% DR for the flexible riblets. The author attributed the limited performance of the riblets to manufacturing defects. A great precision is required for the good performance of small riblets, the rounding of the riblets tips and contours can presumably affect the DR results (Walsh, 1990).

Konovalov *et al.* (1991) tested in a wind tunnel an axisymmetric body of 2.6 m long and a diameter of 0.3 m with a v-grooved surface ($h/s = 0.5$). The measurements were performed with a six-component aerodynamic balance installed in the platform attached to the model. The amount of surface area covered with the riblets was not reported, but it is possible to see that the nose and tail were not covered. Their experiments were performed at a Re range from 4×10^6 to 30×10^6 and with an angle-of-attack range from 0° to 12° . A maximum DR of 8% was obtained with $s^+ = 14$ at a 0° angle-of-attack. They reported that the efficiency of the riblets decreased by a factor of two when changing the angles-of-attack from 0° to 9° . Also in a wind tunnel, Davari (2014) reported a 10% DR by using helical riblets over an axisymmetric body at a $Re = 1.3 \times 10^6$. The helical riblets were done with a steel wire of 0.5 mm in diameter, and a pitch-to-diameter ratio of 1.0.

Few investigations have reported the use of riblets over axisymmetric bodies underwater. Gillerist and Reidy (1989) from the Naval Ocean Systems Center, tested in a deep freshwater lake the use of a v-grooved surface ($h/s = 1$) on an axisymmetric buoyant vehicle of 7.5 m long and 0.53 m in diameter. The riblets, manufactured by the 3M Company in an adhesive-backed vinyl film, were displayed along the longitudinal axis of the vehicle. The riblets covered 76% of the vehicle surface. They obtained an 8% DR with a value of $s^+ = 13-15$, at $Re = 14.9 \times 10^7$. The

DR decreased to a value of 4.4-4.8% when reducing the values of the Re ($12-13 \times 10^7$) and with a $s^+ = 11-13$.

The combined use of riblets and SHS has shown DR in previous investigations. Barbier *et al.* (2014) tested the combined effect of riblets with SHS over a cone-and-plate rheometer system in the transitional and turbulent regime. The superhydrophobic finish was obtained using anodized nanopores in conjunction with a hydrophobic coating. The geometry of the riblets was v-shaped, and its depth varied among 10 to 1000 μm . A maximum DR of 20% was obtained with $h = 100$ μm in the transition to the turbulent regime (with a rotational speed of 44 rad/s), which represented a 75% improvement with respect the use of riblets alone. They reported that the geometries used for successful DR should not be either too small or too large; unfortunately, the geometries used were not described as a function of s^+ .

Prince *et al.* (2014) tested both of these techniques, individually and combined, over the top and bottom walls of a water channel. The surfaces were manufactured using photolithographic processes. The riblets had a rectangular geometry and were aligned with the flow direction. The DR at low Re ($5 \times 10^3 - 1.5 \times 10^4$) improved 5% using the combined effect of the riblets and the SHS, with a maximum DR of 7% at a $Re = 7 \times 10^3$. At higher Re , the DR decreased to a 2.7% at $Re = 1.5 \times 10^4$. However, the confidence of their results is questioned by the large variation of their pressure measurements.

Due to the difference in the optimal length scale of the riblets and the SHS, Golovin *et al.* (2016) questioned the effectivity of the combined use of riblets and SHS. Hou (2016) highlighted that the use of SHS should not affect the performance of the riblets if the SHS roughness is lower than the viscous sublayer. Moreover, several investigations (Gad-el-Hak, 2013, Vajdi Hokmabad and Ghaemi, 2016, Abu Rowin *et al.* 2017) have reported that SHS with the later characteristic are hydrodynamically smooth in the Wenzel state (wet). Hou (2016) proposed that the use of SHS could improve the efficiency of the riblets in the range of $s^+ > 30$, where the streamwise vortices move into the valleys of the riblets. If the valleys are coated, the vortical structures will be in contact with the air pockets of the SHS instead of the solid surface.

Hou (2016) tested the use of SHS over three riblets samples: $s^+ = 8.5$ (small), 17 (medium) and 34 (large). No improvement was obtained for the riblets with $s^+ = 8.5$ and 17. Conversely, for the

over-sized riblets, $s^+ = 34$, the Reynolds stresses were suppressed in comparison with the control case (smooth plate), the turbulence intensities were reduced, and there was an increment of the mean velocity profile in the near wall region. The results confirmed the initial assumption; that the use of SHS can improve the performance of the riblets in the s^+ region where it would normally get DI.

Additionally, the riblets can also be used to improve the efficiency of DR by air injection. The longitudinal grooves may be used to protect and hold an injected stream of air near the wall. As mentioned in the previous sections, the DR by air injection has proven to be effective (up to 80% DR) but limited by the amount of air required, the buoyancy effect over the bubbles, and the existence of interfacial instabilities. Moreover, the instabilities of the air injection are intensified with high shear flows and when the flow stream is over the surface (the air layer tends to be more stable when the flow is below the surface).

The use of longitudinal grooves to stabilize a gas layer was first studied at NASA Langley by Reed and Weinstein (1988, 1989). They injected small amounts of air (0.2 L/min) into the valleys of millimeter-sized v-grooves. The combined effect of surface tension and local dynamic forces helped to fill the grooves with air layers stretching from peak to peak. The air in the grooves was significantly more stable to buoyancy and interfacial instabilities. The stability of the air layer was improved by using surfactants materials with high contact angles, deep narrow grooves, and a tangential air injection. In the laminar regime, the ratio of $h/s = 2$ had the best results in stability. The results showed that the amount of air required to obtain a 50% of DR was at least one order of magnitude lower than just injecting air over a smooth surface. Further investigation is required in the turbulent regime regarding the optimal geometry and air injection rate.

The present work evaluates the use of riblets over an axisymmetric body underwater and in the turbulent regime. Moreover, there is interest in studying the combined effect of the riblets with SHS, and riblets with air injection. Two models of surfaces with rectangular shaped grooves are tested in the ranges of $s^+ = 15 - 40$ and $s^+ = 30 - 80$, which correspond to the data collection at five Re : 5.0×10^5 , 7.0×10^5 , 1.0×10^6 , 1.2×10^6 and 1.5×10^6 .

6.2 Results and Discussion

The load measurements performed with the riblets models and the different configurations are compared with the results of the smooth surface, and are presented in the following order:

- a. Riblets model 1 ($s = 0.3$ mm, $h/s = 0.5$ and $s^+ = 15 - 40$)
 - Baseline (without superhydrophobic coating)
 - With superhydrophobic coating (SHS Riblets model 1)
- b. Riblets model 2 with air injection ($s = 0.6$ mm, $h/s = 2$, $s^+ = 30 - 80$ and $Q_a = 0.15$ L/min)

6.2.1 Drag of Riblets Model 1 (riblets span, $s = 0.3$ mm)

The results of the direct measurement of the drag force are displayed in Figure 6.1 and Table 6.1. The C_D values show an increase of the drag in all the range of velocity tested when compared with the smooth surface. A DI of 34.4 and 44.8% were obtained at $Re = 5.0 \times 10^5$ and 1.5×10^6 , respectively.

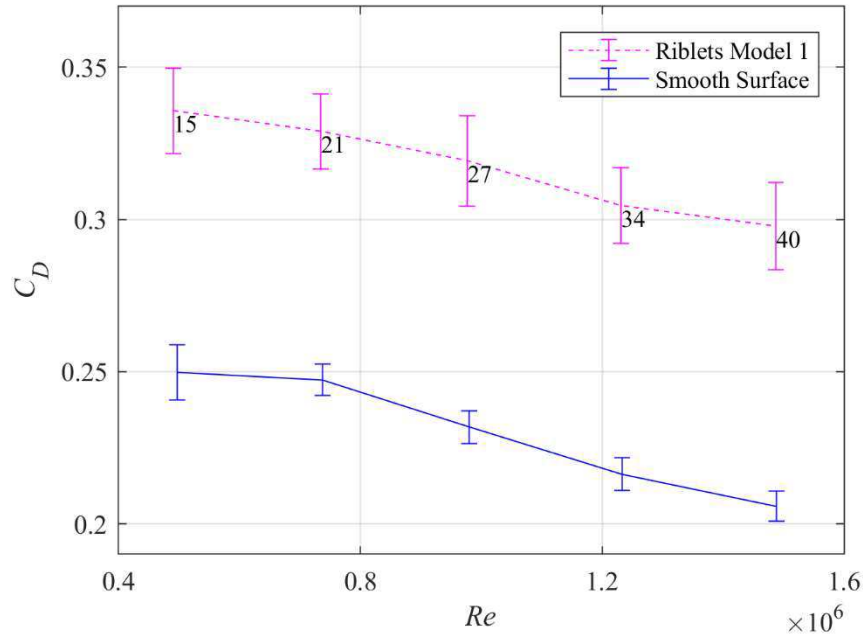


Figure 6.1. Average of the drag coefficient (C_D) versus Reynolds number (Re) for the riblets Model 1 $s = 0.3\text{mm}$ in comparison with the smooth surface. The value of s^+ is indicated beside each data point. The error bars correspond to one standard deviation (σ_{CD}).

Table 6.1. Drag coefficient (C_D), standard deviation (σ_{CD}), average test velocity U [m/s] and drag increase percentage (DI%) for the smooth surface cylinder and the riblets model 1.

Test Surface	Re number	5.0×10^5	7.0×10^5	1.0×10^6	1.2×10^6	1.5×10^6
Smooth Surface	Drag Coefficient, C_D	0.250	0.247	0.232	0.216	0.206
	Standard deviation, σ_{CD}	0.009	0.005	0.005	0.005	0.005
	U [m/s]	1.09	1.62	2.15	2.70	3.26
Riblets, Model 1	Drag Coefficient, C_D	0.336	0.329	0.319	0.305	0.298
	Standard deviation, σ_{CD}	0.014	0.012	0.015	0.013	0.014
	U [m/s]	0.94	1.41	1.87	2.36	2.85
Drag Increase, DI [%]		34.4	33.0	37.7	40.8	44.8

The results are different to previous successful work on axisymmetric bodies. Previous work showed an 8% of DR using v-grooved riblets in the range of $s^+=13-15$ over more than 70% of test model surface (Gillerist and Reidy, 1989, Konovalov *et al.*, 1991). These differences might be related to the range of s^+ tested in the current study, which was in the upper limit of the optimum values of previous work, the geometry of the riblets, and the lower area covered by the riblets in this case (37% of the total length of the test model).

The geometry used in the current investigation followed the non-dimensional characteristics of the blade riblets used by Bechert *et al.* (1997). They reported a DR = 9.9% using blade riblets with $h/s = 0.5$, $t/s = 0.2$, and $s^+ = 17$. Nonetheless, after their optimum point ($s^+ = 17$), the authors explained that the viscous assumption breaks down and the surface behavior is similar to a rough surface which results in DI. Following the experience of Bechert *et al.* (1997), in the current experiment was expected to obtain DR in the range around $s^+ = 15-20$, followed by a gradually DI. The results showed no DR, and the DI progressively augmented for $s^+ < 27$.

The dissimilarity in the performance of using the same riblets geometry might be due to the existence of a crossflow around the axisymmetric body. If the flow is not straight over the entire surface of the axisymmetric body, the interaction of the riblets with the coherent structures of the TBL will change, and its efficiency would be affected (Konovalov *et al.*, 1991, Ng and Lou, 2016). A misalignment up to 15° from the horizontal flow in a flat plate would not affect the performance of riblets; however, a flow pattern with a greater deviation would make the use of riblets ineffective (Ng and Lou, 2016). The use of helical riblets might offer a more flexible interaction between the riblets and possible flow pattern over the axisymmetric body. Davari (2014) obtained a 10% of DR with helical riblets, 2% higher than the DR reported by Konovalov *et al.* (1991) who used v-grooved riblets parallel to the longitudinal axis of the body.

The performance of small riblets requires a great precision (Walsh, 1990). Hence, other important factors affecting the performance of the riblets is the quality of the groove after manufactured and being exposed to high shear flow. Visual assessment confirmed the characteristics of the riblets geometry. Although the surface showed a good demarcation of the riblets geometry, there are further concerns related to the riblets contamination and degradation when exposed to the flow. After the AUV model was removed from the test section, particles

were seen embedded between the surface grooves as displayed in Figure 6.2. Compressed air was used to clean the surface after each experiment. Lazos (1989) studied the impact of the contamination of riblets in aircraft. The author reported a loss of 2% in the riblets efficiency when the particles covered from 0.4-0.7% of the surface. Choi *et al.* (1989) found practical limitations when testing polymer coated riblets on a scaled-down yacht. They reported the deterioration of the coating and the riblets due to particles present in the water.

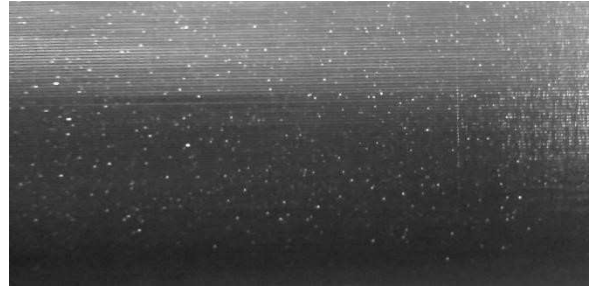


Figure 6.2. Particles trapped in the riblets ($s=0.3\text{mm}$) valleys. After the test in a dry environment

The combined effect of the SHS and the riblets produced a DR in comparison with the riblets sleeve without the coating; 12% and 9.8% DR at the $Re = 5.0 \times 10^5$ and $Re = 1.5 \times 10^6$, respectively (Figure 6.3 and Table 6.2). The DR obtained is in agreement with the observation done by Prince *et al.* (2014), Barbier *et al.* (2014), and Hou (2016) that the performance of the riblets can be improved with the use of SHS. However, in comparison with the smooth surface, there is an 18% DI at $Re = 5.0 \times 10^5$, and 31% DI at the $Re = 1.5 \times 10^6$.

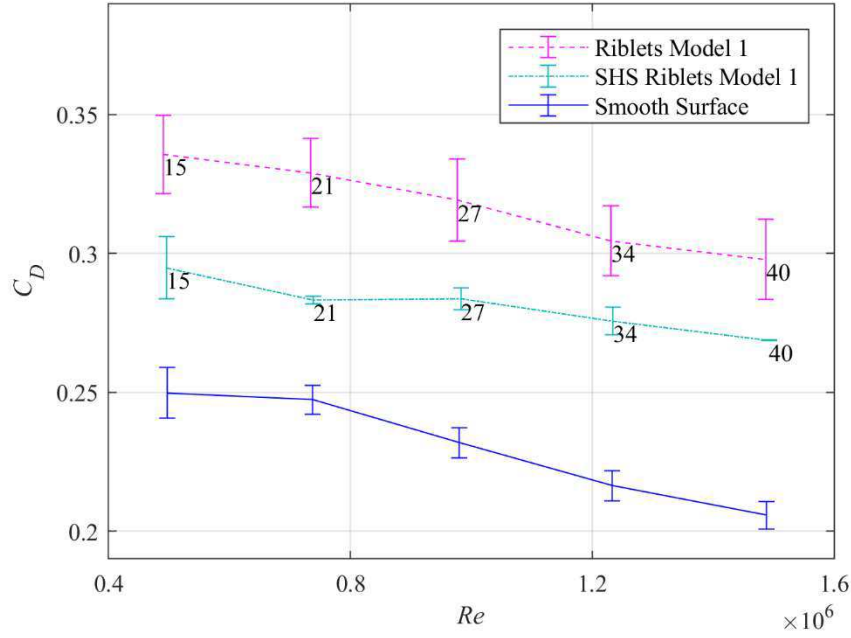


Figure 6.3. Average of the drag coefficient (C_D) versus Reynolds number (Re) for the combined effect of riblets model 1 and superhydrophobic surfaces (SHS) in comparison with the smooth surface.

Table 6.2. Drag coefficient (C_D), standard deviation (σ_{CD}), average test velocity U [m/s], and drag reduction percentage (DR%) for the riblets model 1 and the SHS riblets model 1.

Test Surface	Re number	5.0×10^5	7.0×10^5	1.0×10^6	1.2×10^6	1.5×10^6
Riblets, Model 1	Drag Coefficient, C_D	0.336	0.329	0.319	0.305	0.298
	Standard deviation, σ_{CD}	0.014	0.012	0.015	0.013	0.014
	U [m/s]	0.94	1.41	1.87	2.36	2.85
SHS Riblets, Model 1	Drag Coefficient, C_D	0.295	0.283	0.284	0.276	0.269
	Standard deviation, σ_{CD}	0.011	0.001	0.004	0.005	0.001
	U [m/s]	0.93	1.39	1.85	2.33	2.81
Drag Reduction, DR [%]		12.2%	13.9%	11.1%	9.5%	9.8%

Similar to the observations of Prince *et al.* (2014), DR decayed with the increase of velocity. Additional to the factors affecting the riblets performance, the performance of the SHS was reduced by degradation of the coating on the last 2 cm of the test module. Analogues to the smooth SHS, the coating displayed wetted areas after increasing the flow speed beyond 1.5 m/s. After getting in contact with air, and being submerged again in water, the coating still looked wet in the damaged parts. Further investigation is required to study the effect of the riblets in the stability of the air layer/pockets of the SHS.

6.2.2 Drag of Riblets Model 2 (riblets span, $s = 0.6$ mm) with Air Injection

The objective of using the combined effect of riblets with air injection is to form a stable air-water interface in the valleys of the riblets. The longitudinal grooves would be used to protect the air being injected into the wall from the effect of buoyancy and interfacial instabilities. Thus, the loss of air could be reduced and the amount of air required for DR would decrease.

The work of Reed and Weinstein (1988, 1989) over a flat surface was taken as reference for this test. They used v -grooves with an aspect ratio of $h/s = 2$ ($h = 1.04$ mm and $s = 0.52$ mm), a range of $s^+ = 40 - 75$, and an air injection rate around $Q_a = 0.2$ L/min. The current investigation considered rectangular grooves with an aspect ratio of $h/s = 2$ ($h = 1.2$ mm and $s = 0.6$ mm), a range of $s^+ = 30 - 80$, and an air injection rate of $Q_a = 0.15$ L/min.

The objective of filling the riblets grooves with air was not accomplished. Figure 6.4 displays the outcomes of the air injection method. The air tended to come out in the form of jets in one or two spots that constantly moved along the test cylinder. This phenomenon was not observed in the air injection test reported in Chapter 5, where the bubbles came out over all the porous surface. Thus, the use of the riblets sleeve over the porous surface might have affected the distribution of the pressure in the interior of the test cylinder, forcing the air to come out through the less resistive path in a jet shape. Some of the grooves near the air jets and the front seal were partially filled with air, but it was not possible to see a uniform distribution of the air layers. The front seal worked as a protection to the air being injected in the near region of this component as seen in Figure 6.5. Hence, a recommendation for future research is to add cross-section walls in the riblets valleys to break long grooves into several small sections. Some air bubbles were seen between the valleys of the riblets surface; however, the number of bubbles decreased with higher Re .

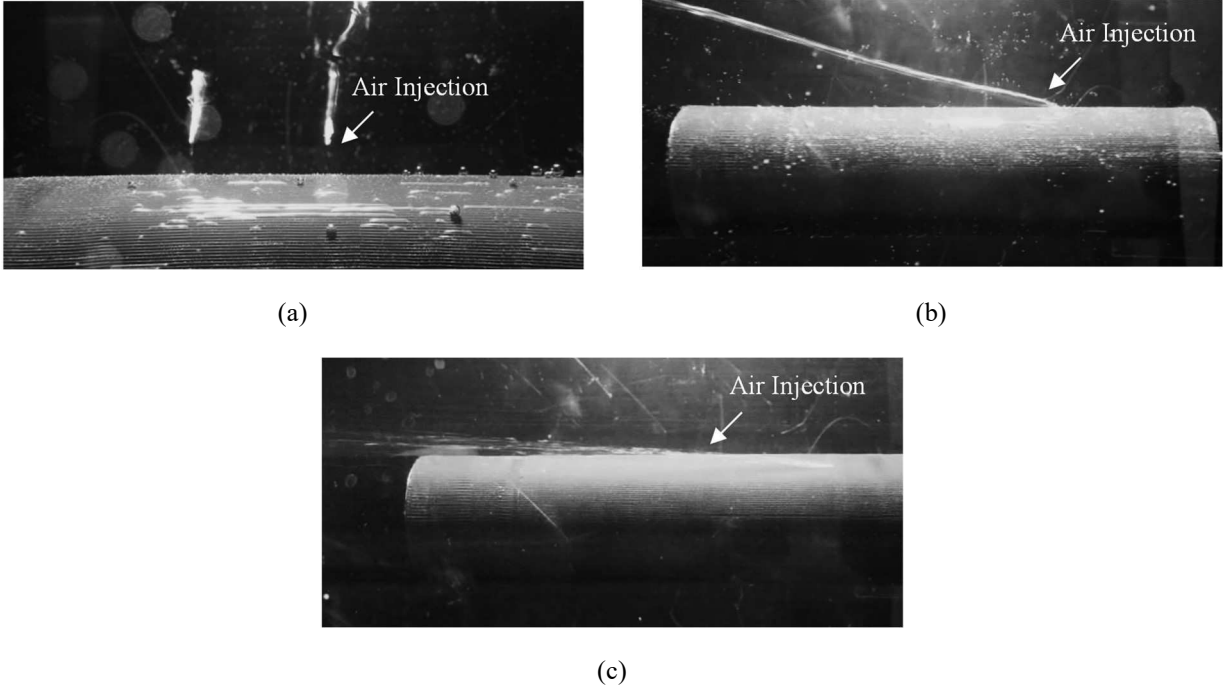


Figure 6.4. Detail of the air injection, $Q_a=0.15\text{L}/\text{min}$. (a) Static water, (b) $Re = 5.0 \times 10^5$, and (c) $Re = 1.5 \times 10^6$

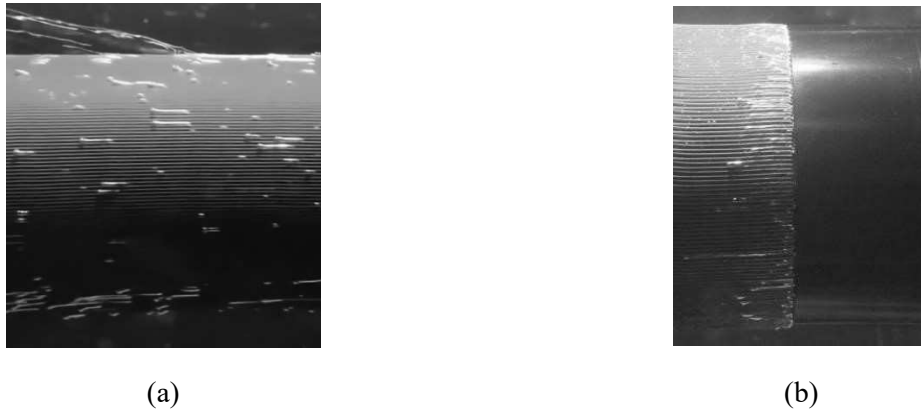


Figure 6.5. Bubbles and air lines in the valleys of the riblets, $Q_a=0.15\text{L}/\text{min}$ at $Re = 7.0 \times 10^5$. (a) At the middle of the test model, and (b) downstream the front seal

The formation of the air layer might have been affected by alterations of the grooves geometries. Similar to the case of the riblets model 1, although the surface showed a good demarcation of the riblets geometry, there are further concerns related to the riblets contamination and degradation when exposed to the flow. Reed and Weinstein (1988, 1989) reported that the reduction of the groove span beyond their optimal dimension (in their case 0.26 mm) reduces the ratio of drag force to surface tension. Consequently, there was not enough “activation energy” for the air layer to establish itself within the groove (Reed, 1994). The “activation energy” refers to the amount

of energy required to alter the surface tension, displace the water inside the valley, and hold the air being injected inside the grooves (Reed and Weinstein, 1989).

Reed and Weinstein (1988, 1989) also highlighted the importance of using a tangential injection of air ($< 10^\circ$) in the downstream direction. This configuration helped to decrease the local dynamic pressure on the air-water interface near the injector. Additionally, they reported the use of a plastic shroud, which was placed over the injection ports to improve the initial formation of the air layer. The volumetric flow rate was also controlled by the authors to avoid the over-pressurization of the air layer within the grooves and its consequent detachment from the surface. Hence, it would be required to vary the injection rate according to the flow velocity. Differently from Reed and Weinstein (1988, 1989), in the current test model, the air injection ports were located perpendicular to the flow stream and over the entire length of the test surface. Moreover, a uniform air injection was not achieved, and the resultant injection of the air as a jet flow impeded the distribution of the air along the grooves. Variations in the injection rate, within the range of $Q_a = 0.1 - 0.5$ L/min, did not show improvement. Some of the grooves were partially filled with air, but none of them achieved a length higher than 20 mm; not even near the front seal, which worked as the plastic shroud used by Reed and Weinstein (1988, 1989) and contributed to the formation of some small air layers near its edge.

Figure 6.6 display the comparison of the C_D values as a function of the Re in comparison with the smooth surface and the riblets model 1. Table 6.3 summarize the results and compares them with the smooth surface. Relative to the smooth surface a DI of 49% was obtained at $Re = 5.0 \times 10^5$, and a DI of 59% at $Re = 1.5 \times 10^6$.

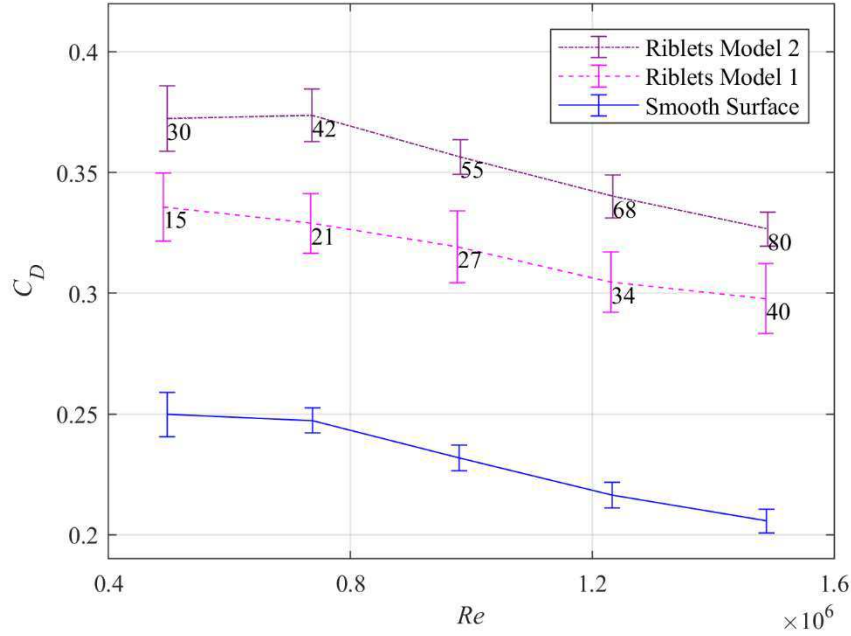


Figure 6.6. Average of the drag coefficient (C_D) versus Reynolds number (Re) for the combined effect of air injection and riblets model 2 in comparison with the riblets model 1, and the smooth surface. The error bars correspond to one standard deviation (σ_{CD}).

Table 6.3. Drag coefficient (C_D), standard deviation (σ_{CD}), average test velocity U [m/s], and the drag increase percentage (DI%) for the smooth surface cylinder and the riblets model 2.

Test Surface	Re number	5.0×10^5	7.0×10^5	1.0×10^6	1.2×10^6	1.5×10^6
Smooth Surface	Drag Coefficient, C_D	0.250	0.247	0.232	0.216	0.206
	Standard deviation, σ_{CD}	0.009	0.005	0.005	0.005	0.005
	U [m/s]	1.09	1.62	2.15	2.70	3.26
Riblets, Model 2	Drag Coefficient, C_D	0.372	0.374	0.357	0.340	0.327
	Standard deviation, σ_{CD}	0.014	0.011	0.007	0.009	0.007
	U [m/s]	0.98	1.45	1.93	2.43	2.93
Drag Increase, DI [%]		49.0	51.1	53.8	57.2	58.7

Additional investigation is required to determine the optimum groove geometry and size for axisymmetric bodies. It is also required to study the effect of the injection rate as a function of the flow stream velocity, the number of ports, and their location to form a stable air layer. Furthermore, it is of special interest to develop a method to surpass the required energy for the formation of air layers in small grooves.

6.3 Conclusions

The riblets surfaces, in the ranges of $s^+ = 15 - 40$ and $s^+ = 30 - 80$, did not reduce the drag. The highest DI, relative to the smooth surface, was obtained by model 2 ($s^+ = 30 - 80$) with an injection of air at a rate of 0.15 L/min. The performance of riblets might have been affected by the existence of an azimuthal flow component, and imperfections in the geometry of the grooves due to manufacturing limitation, contamination, and deterioration of the riblets.

The combined effect of riblets with the superhydrophobic coating showed a limited benefit in comparison with the no coated riblets surface. The maximum DR obtained with the coated surface was 13.9% for a riblet with $s^+ = 21$ in comparison with the same module without the coating. However, there was no DR in comparison with the smooth surface. The performance of the SHS was also affected by the degradation of the coating on the last 2 cm of the test module. Contrary to the porous surface, the riblets structures did not improve the adhesion of the superhydrophobic coating over the surface. Further investigation is required to investigate the effect of the riblets in the stability and longevity of the SHS.

The injection of air through the holes of module 2 was not effective in filling the grooves. The air injected was not distributed over the entire cylindrical surface. Instead, the air came out in the form of jets in one or two spots that constantly moved along the cylinder. Although it was possible to see some air bubbles trapped in the valleys of riblets, and some grooves partially filled with air, the configuration of the air injection was not adequate to fully displace the water in the grooves and replace it with air. A recommendation for future research is to add cross-section walls in the riblets valleys to break long grooves into several small sections. Further investigation is required to optimize the geometrical parameters, determine the most effective configuration for air injection, estimate the variations of the volumetric flow as a function of the flow velocity, and evaluate the stability of the air layers, all of them for axisymmetric bodies in the turbulent regime.

Chapter 7. Slip and Plastron Morphology over an Axisymmetric Body with a Superhydrophobic Surface

The use of a superhydrophobic surface (SHS) is further studied in this chapter with an emphasis in the slip velocity and the characterization of the air plastron morphology. The smooth surface is used as the basis for the comparison. The direct measurement of the drag force is complemented with the simultaneous characterization of the velocity vector field over the surface. The velocity vector field is obtained with shadow-based long range microscopic particle tracking velocimetry (micro-PTV). The use of the latter visualization technique allowed the observation of the SHS structures when exposed to a high shear flow. The air plastron and air pockets morphology were characterized for each of the flow stream velocities by estimating the average thickness ($\langle t_e \rangle$).

The data collection was performed at five Reynold numbers (Re): 5.0×10^5 , 7.0×10^5 , 1.0×10^6 , 1.2×10^6 and 1.5×10^6 . Similar to the results of Chapter 4, the SHS reduced the drag in comparison with the smooth surface. However, the water movement over the SHS enhanced the air depletion, and the drag reduction (DR) decayed with increasing Re . The largest air thickness ($\langle t_e \rangle$) was estimated at the lowest $Re = 5.0 \times 10^5$, which also showed the largest value of DR (23%). Inversely proportional to the DR tendency, the slip velocity increased with higher Re number. This incongruence is related to the selection of the 95% cumulative roughness (y_{95}) for the estimation of the slip velocity. The selection of a location near the top of the roughness peaks enhance the magnitude of the slip velocity as the liquid can still move at the bottom of the valleys

7.1 Introduction

The air trapped by the SHS when submerged in water, stretches along the surface nano-/microstructures due to the tension forces. The air can be seen as a mostly continuous air plastron/layer, or as curved meniscus within the peaks of the surface. These sections of air-water interface originate the slip boundary condition near the wall, while the solid sections exposed to

the water will impose the no-slip boundary condition. Consequently, as long as the proportion of the air –water interface is higher than the area of solid surface exposed, the SHS will effectively relax the no-slip boundary condition and reduce the DR (Samaha *et al.* 2012). Hence, the efficiency and longevity of the surface is determined by its capacity of maintaining the entrapped air.

Reports of the slip velocity have provided a better understanding of the drag reduction mechanism. Ou and Rothstein (2004) were among the first in reporting the proportional relation between the slip velocity and the total area covered by the shear-free air-liquid interface. Min and Kim (2004), using a DNS, showed the impact of the slip velocity direction in the resultant DR. The slip velocity in the streamwise direction reduced the drag and the wall shear stress. Conversely, a slip velocity in the spanwise direction increased both drag and turbulence. Rastegari and Akhavan (2015) developed an analytical expression to calculate DR as a function of the slip velocity. Their comparison with DNS data showed that the effective slip on the wall contributed from 80 to 100% of the total DR; thus, only up to a 20% was due to the attenuation of turbulence.

Experiments using PIV (Woolford *et al.* 2009, Vajdi Hokmabad and Ghaemi 2016) showed a negligible DR in the turbulent regime, together with a mild shift upward of the mean velocity profile. Woolford *et al.* (2009) tested surfaces with small-scale ridges. They reported up to 11% DR and detected a decrease of the turbulence intensities in general. Vajdi Hokmabad and Ghaemi (2016) noted the suppression of the sweep and ejection events and the reduction of the spanwise vertical structures in the buffer layer. Vajdi Hokmabad and Ghaemi (2017) reported that the existence of particles in the flow enhanced the air layer dissolution and limited the DR obtained (up to 15%).

Ling *et al.* (2016) characterized the velocity profile, shear stresses, and turbulence intensities in the inner layer of a TBL by using digital holographic microscopy (DHM). The magnitude of the slip velocity over a smooth surface reached up to 38% the bulk flow velocity, and a maximum of 36% DR was observed. Higher slip velocities, resulted in the higher DR. Moreover, opposing previous experiments (Woolford *et al.* 2009, Vajdi Hokmabad & Ghaemi 2016), Ling and

colleagues found an increase of the Reynolds stress in the inner layer which directly affected their DR results.

Recently, Abu Rowin *et al.* (2017) characterized the inner and outer layers of a turbulent channel flow with a random textured SHS. The study of the boundary layer was done with the simultaneous use of long-range micro-particle tracking velocimetry (micro-PTV) and PIV. A slip velocity of 13% the average flow velocity resulted in a DR of 19%. The investigators reported a negligible increase of the Reynolds shear stress at the wall, a reduction of the sweep motions at $y^+ < 15$, and an attenuation of the ejections in the buffer layer ($y^+ = 20 - 30$). Additionally, an analysis of the surface stability through time was provided. They defined a “stable” SHS when the DR performance was maintained in time, and an “unstable” SHS, when it rapidly lost its DR effect. Although at the beginning both surfaces (the stable and an unstable SHS) showed a slip velocity larger than the control surface, the performance was different as the time progressed. The average velocity at the wall remained fairly constant over the stable SHS in a period of 800 s. However, in the unstable SHS the air plastron was lost after 300 s; consequently, the velocity at the wall started decreasing. Further investigation of the air plastron morphology under high shear flow is required for a complete study of its efficiency and longevity.

The lack of accurate information regarding the air layer thickness, morphology, and lifetime has narrowed the results interpretation and comparison. Bobji *et al.* (2009) used an optical technique based in the light scattered by the air-water interface to study the longevity of the air plastron over regular and random surface patterns in quiescent conditions. Regardless of the texture pattern, the surfaces had a limited lifetime due to the diffusion of air into the water. Similar observations were reported by Poetes *et al.* (2010). The reflection of light from the plastron showed that the lifetime of the plastron highly depends on the immersion height (hydrostatic pressure). Additionally, the air depletion process was explained as a two stages process: (i) the thickness of the air layer is reduced due to diffusion of air into water, and (ii) the plastron reached a critical thickness and broke up into spherical cup-shaped bubbles. Once the air layer broke into bubbles, the latter rapidly dissolved into the water due to the Laplace pressure.

Using a similar technique based on light reflection, Vajdi Hokmabad and Ghaemi (2017) studied the longevity of the superhydrophobicity. The superhydrophobicity was affected by the

convection with high shear rate flows, particles – plastron collisions, levels of oxygen in the water, and the overall submersion time. All these factors had a direct impact on the dissolution of the air layer into the flow stream. Nevertheless, there is still no direct visualization of the air layer thickness and morphology of an SHS under the effect of high shear flow; neither an observation of the transition from the Cassie state to Wenzel state. Some of the challenges to overcome are the light reflected by the surface, the obstruction of the field-of-view FOV by the surface structures, and the microscopic scale of the phenomenon.

The simultaneous measurement of the drag force and the slip velocity has not been broadly used despite the key information that each of them provides for a full characterization of the DR mechanism in terms of force and velocity. In the current study, the direct measurement of the drag force is complemented by the use of shadow-based long-range micro-PTV to study the slip and characterize the air plastron morphology. The images obtained with the shadowgraph technique provided the tools required to obtain the average velocity profile over the surface. Moreover, it allowed the visualization of the air plastron morphology and monitoring of its evolution with increasing Re .

7.2 Results and Discussion

The SHS is further studied with the simultaneous use of the load cell and long-range micro-PTV measurement. The results from the load measurement are introduced first, followed by the calculations of the velocity profile, the slip velocity, and slip length. Finally, the visualization of the air plastron and air pockets under high shear flow is presented.

7.2.1 Load Measurement

The values of the C_D as a function of Re are presented for both surfaces, smooth and SHS, in Figure 7.1 and Table 7.1. The test body with the SHS reduced the drag in 23, 16, 8, 1, and -3% (drag increase) at $Re = 5 \times 10^5$, 7×10^5 , 1×10^6 , 1.2×10^6 , and 1.5×10^6 , respectively. Compared with the averaged results of Chapter 4, the DR decreased in a 13% at $Re = 5 \times 10^5$ and 9% at $Re = 1.5 \times 10^6$. Once again, the gradual decrease of the DR with increasing Re is associated with the depletion of the air layer and also the reduction of the boundary layer thickness (details in section 7.2.2 and 7.2.3).

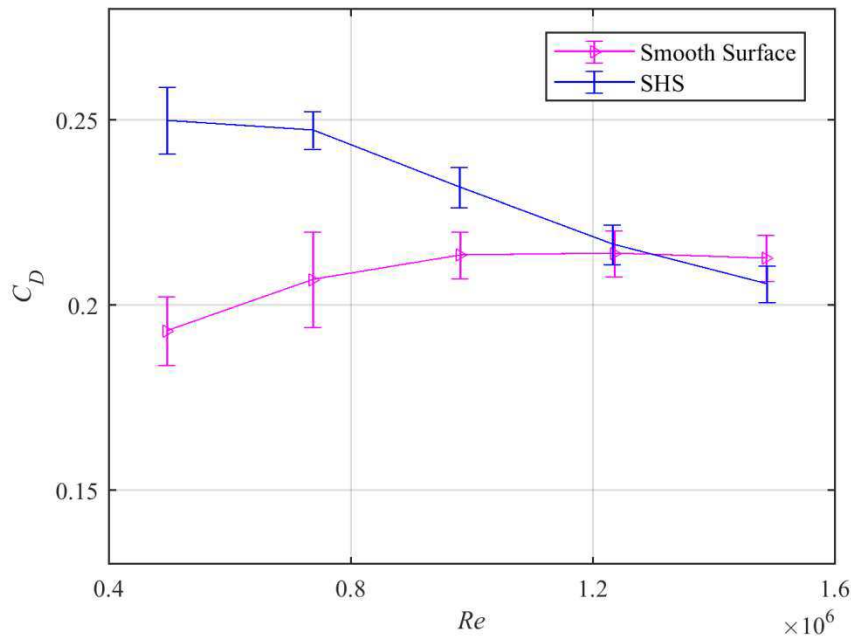


Figure 7.1. Average of the drag coefficient (C_D) versus Reynolds number (Re) for the smooth surface in comparison with the superhydrophobic surface (SHS). The C_D is calculated using the drag force measured by a submersible load cell. The error bars, in both cases, correspond to one standard deviation (σ_{C_D}).

Table 7.1. Drag coefficient (C_D), standard deviation (σ_{CD}), average tests velocity U [m/s], and drag reduction percentage (DR%) for the smooth surface cylinder and the superhydrophobic surface (SHS) during the micro-PTV measurement.

Test Surface	Re number	5.0×10^5	7.0×10^5	1.0×10^6	1.2×10^6	1.5×10^6
Smooth Surface	Drag Coefficient, C_D	0.250	0.247	0.232	0.216	0.206
	Standard deviation, σ_{CD}	0.009	0.005	0.005	0.005	0.005
SHS	Drag Coefficient, C_D	0.193	0.207	0.214	0.214	0.213
	Standard deviation, σ_{CD}	0.009	0.013	0.006	0.006	0.006
	Dimensionless root-mean-square surface roughness $k^+_{rms} = R_{rms}/\eta$	0.40	0.56	0.75	0.88	1.03
U [m/s]		0.98	1.45	1.93	2.43	2.92
Wall units, $\eta = f(\tau_w)$, where is the τ_w shear stress at the wall		22.1	15.6	12.0	9.8	8.3
Drag Reduction, DR [%]		22.7	16.4	7.9	1.1	-3.4 (DI)

Overall, the same comparison done with previous experiments are still valid. The texture of the SHS (R_{rms}) is about $10.2\mu\text{m}$ which is 8% relative to the viscous sublayer thickness ($y^+ = 5$) at $Re = 5.0 \times 10^5$. However, the surface may act as a rough wall at $Re = 1.5 \times 10^6$ with a viscous sublayer thickness of $41.5\mu\text{m}$. The DR at $Re = 5.0 \times 10^5$ is still higher than the results obtained with axisymmetric bodies in the laminar regime. In comparison with the flat plates studied with load cells, the same trend is observed; the DR also decays with increasing velocities and higher k^+_{rms} .

7.2.2 Slip velocity

Detailed measurement of the near-wall velocity is carried out using the long-range micro-PTV measurement. The velocity of individual tracers is captured by the micro-PTV in the vicinity of the wall for the baseline and the SHS surfaces at five different Re numbers of 5.0×10^5 , 7.0×10^5 , 1.0×10^6 , 1.2×10^6 and 1.5×10^6 . The processing of the long-range micro-PTV images is explained in section 3.6.

The scatter plots over the smooth surface (left side graphics in Figure 7.2) show that the velocity of tracers becomes smaller with reduction of the wall normal distance. The average velocity is calculated for each Re number using bins which are 30 μm long in the y -direction, and is displayed with a solid line in Figure 7.2 (left side). The number of particles per bin varied from minimum of 122 particles to a maximum of 1000 particles per bin; and the total number of particles considered for the average velocity ranged from 13500 to 18000 for all the range of Re numbers tested. Although there is a small gap with missing data ($y^+ < 1$) in the plots, the extrapolation of the lines would tend to zero as it is expected due to the no-slip boundary condition over the smooth surfaces. The gap of missing data is due to the overlap of the particles with the region of high light reflection at the wall. With increasing velocities, the difficulty of determining particles near the wall is higher. The velocity profile in the linear viscous sublayer is defined up to $y^+ = 5$ using as reference a theoretical approximation of the wall units as a function of the velocity and the wall shear stress. The average velocity profile in the linear viscous sublayer, displayed as a dashed line in Figure 7.2, is fitted to a line and extrapolated up to $y^+ = 12$ for visualization purposes. The wall units for the baseline are recalculated using the obtained slope (dU/dy) in the linear region; the resultant magnitude varies from a minimum of 4 to 13% in comparison with the theoretical approximation initially done at the lowest and highest Re respectively.

The velocity of the tracer particles over the SHS (right side graphics in Figure 7.2) does not tend to zero with the same trend as the particles over the smooth surface. The tracers still have a significant velocity at the y_{95} location, which is termed as the slip velocity (Ling *et al.* 2016). The average velocity is also calculated using bins which are 30 μm long in the y -direction, and the result is displayed with the solid line in Figure 7.2 (right side). The number of particles per bin

varied from minimum of 125 particles to a maximum of 850 particles per bin; and, the total number of particles considered for the average velocity ranged from 16000 to 28000 for all the range of Re numbers tested. The limit of the linear viscous sublayer ($y^+ = 5$) is defined using as reference the wall units of the baseline cases as a function of the linear viscous sublayer slope. The velocity profile in the linear section, displayed as a dashed line in Figure 7.2, is fitted to a line and extrapolated up to $y^+ = 12$ for visualization purposes. The wall units for the SHS are recalculated using the obtained slope (dU/dy) in the linear region, and the resultant magnitude varies from a minimum of 4 to 10% in comparison with the experimental wall units of the baseline. Overall, the results of the SHS show a gradual increase of the slip velocity with higher Re numbers; from a slip velocity of ~ 0.13 m/s at $Re = 5.0 \times 10^5$, it increases up to ~ 0.90 m/s at $Re = 1.5 \times 10^6$. Higher slip velocities should show higher DR, but in this case, the increase in the magnitude of the slip is inversely proportional to the percentages of DR measured with the load cell. This incongruence of the results is related to the selection of the equivalent flat interface at y_{95} for the estimation of the slip velocity. The definition of the y_{95} location follows the work of Ling *et al.* 2016 and is explained in section 3.6.3.

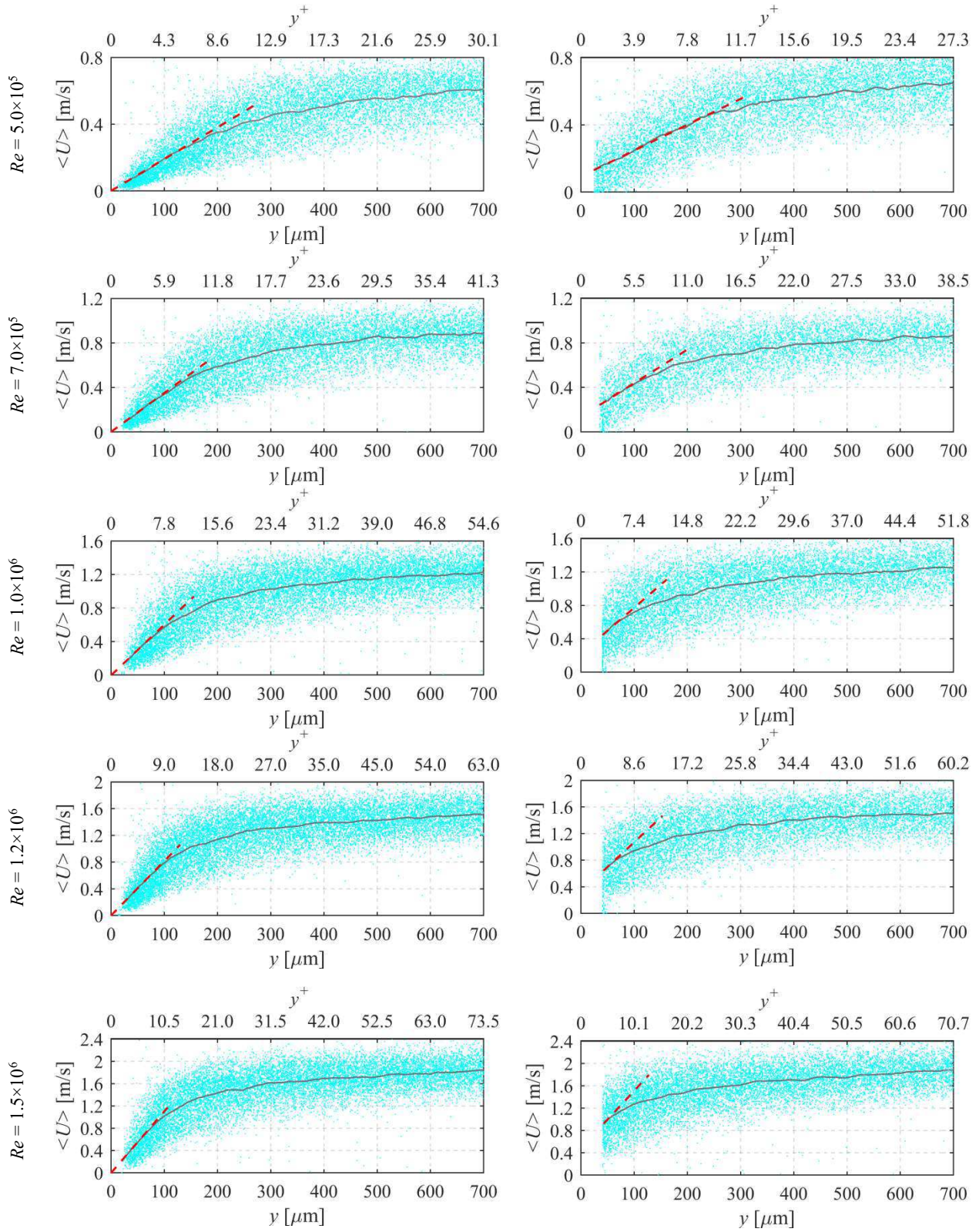


Figure 7.2 Velocity of tracer particles from shadow-based long-range –micro-PTV over the baseline (left figures) and the SHS (right figures) at the specified Re numbers. The average velocity profile [m/s] seen as the continuous line is obtained by averaging the velocity of the tracer particles in bins with a wall-normal dimension of $30\ \mu\text{m}$ and an overlap of 75%.

Table 7.2 summarizes the values of DR obtained during this test, the surface dimensionless roughness (k^+_{rms}), the slip length (b), slip velocity estimated at y_{95} and at $y = 0$, and the estimated air thickness ($\langle t_e \rangle$) for each Re number. In general, the slip length is fairly similar for all the Re number tested; the results show $b = 85 \mu\text{m}$ at the $Re = 5.0 \times 10^5$ and $b = 87 \mu\text{m}$ at the $Re = 1.5 \times 10^6$. In terms of wall units, the dimensionless slip length (b^+) goes from 3.3^+ to 8.9^+ at the $Re = 5.0 \times 10^5$ and $Re = 1.5 \times 10^6$, respectively. The increase in wall units of the slip length with higher Re numbers helps to understand the increase in the magnitude of the slip velocity when moving up in velocity; it indicates that the location in the viscous sublayer where the slip velocity is being estimated increases with the flow velocity. The results show that the slip velocity augmented in an average of 84% for $Re \leq 1.0 \times 10^6$, and in an average of 42% for $Re > 1.0 \times 10^6$. The increase rate of the slip velocity slowed down from the $Re = 1.2 \times 10^6$ up, where the DR is seen to decline, the k^+_{rms} increases, and the air layer ($\langle t_e \rangle$) is highly reduced as seen in Table 7.2. Evaluating the slip velocity at $y = 0$, its magnitude also increased with higher velocities.

Table 7.2. Summary of results obtained for the SHS during the experiment with long-range micro-PTV. Drag reduction percentage (DR %), wall units (η), dimensionless roughness (k^+_{rms}), slip length (b), slip velocity at y_{95} and $y = 0$, and the air plastron thickness (t)

Re number	5.0×10^5	7.0×10^5	1.0×10^6	1.2×10^6	1.5×10^6
DR [%]	23%	16%	8%	1%	-3% (DI)
Wall units, $\eta = f(du/dy)$ [μm]	25.6	18.2	13.5	11.6	9.9
Dimensionless root-mean-square surface roughness $k^+_{rms} = R_{rms}/\eta$	0.40	0.56	0.75	0.88	1.03
y_{95} [μm]	26.6	27.2	27.9	30.4	31.7
Dimensionless, y_{95}^+	1.0 ⁺	1.5 ⁺	2.1 ⁺	2.6 ⁺	3.2 ⁺
Slip length [μm], b	85	80	81	85	87
Dimensionless slip length, b^+	3.3 ⁺	4.4 ⁺	6.0 ⁺	7.3 ⁺	8.9 ⁺
Slip velocity at y_{95} [m/s]	0.131	0.242	0.445	0.629	0.899
Slip velocity at $y = 0$ [m/s]	0.094	0.136	0.223	0.328	0.482
Air plastron thickness, $\langle t_e \rangle$ [μm]	10.8	9.6	3.4	2.4	1.1

Previous studies with rough and SHS (Bonaccorso *et al.*, 2003, Vinogradova and Yakubov, 2006, 2011, Brzek *et al.*, 2008), have shown the high influence of the reference plane location (y_{95}) in the magnitude of the resultant slip velocity. The selection of a location near the top of the roughness peaks enhances the magnitude of the slip velocity as the liquid can still move at the bottom of the valleys (Joseph, 2015, Lee *et al.*, 2014). With increasing roughness height (greater peak-to-peak distance) the effect in the slip will be higher as it is estimated farther away from the wall (Lee *et al.*, 2014). Ling *et al.* (2016) reported, for flat plates with porous SHS, larger slip velocities for the samples tested at higher flow velocities and with larger roughness. The slip velocities were also estimated at the 95% of the cumulative distribution of the roughness height. At the lowest flow velocities of 2 m/s, their porous samples with a $k^+_{rms} = 0.43 - 0.62$ showed slip velocities around 15 to 17.5% of the bulk velocity with a 9 to 12% DR based on the wall shear stress. However, samples with a $k^+_{rms} = 1.71-3$ tested at a flow velocity of 5.5 m/s and 5.9 m/s, showed higher values of slip velocity (34-35% the bulk velocity) while displayed negligible

DR (~3%) and DI (~10%). Conversely, the results of Ling *et al.* (2016) with samples of SHS over aluminum plates that were polished in the flow direction ($k^+_{rms} = 0.68 - 0.75$) displayed a proportional relation between the slip velocity and the DR obtained. The slip velocities ranged from 14.5% to 36.5% of the bulk velocity, and the DR varied between 10% - 36%. For the latter polished samples, higher slip velocity values resulted in higher DR results. Hence, this difference in trends when using different types of surface roughness is attributed to the selection of the reference location for the estimation of the slip velocity.

The challenge of defining the boundary plane for an SHS is based on the existence of a mixed – slip boundary conditions (Joseph, N. 2015). In an SHS, there are areas of air-water interface (seen as an air layer or curved meniscus within the peaks of the surface) which offer a slip condition; and there are areas of solid-water interface which have a no-slip boundary condition. As long as the proportion of the air-water interface is higher than the solid-water, the combined effect of these two areas will offer a resultant slip condition applied at an equivalent flat plane of the mixed-interface (Samaha *et al.* 2012). As we can see in Table 7.2, the air thickness decreases with increasing Re number. In comparison with the initial value, the averaged air thickness decreased up to a 90% at the $Re = 1.5 \times 10^6$. Subsequently, is not physically possible for the SHS to offer a higher slip velocity at the $Re = 1.5 \times 10^6$ than at the lowest Re number of 5.0×10^5 . The increasing magnitude of slip velocity is due to the reference selected in the wall-normal direction for its calculation, and not due to the effect of the SHS. The air plastron thickness is further studied in section 7.2.3.

Although the existence of DR implies the presence of a slip velocity at the wall, the contrary case is not necessarily true: the presence of a slip velocity does not indicate a resultant DR. Further statistics in the inner and outer layer are required to improve the understanding of the phenomena in rough surfaces. Woolford *et al.* (2009), using PIV, characterized the turbulent flow over a pattern of ribs and cavities made superhydrophobic with a Teflon coating. Two ribs patterns, one with longitudinal and other with transversal orientation, were tested in the Re number range of 4800 up to 10000. The results from a smooth bottom wall were used as the basis for comparison. In the spatial resolution of their PIV measurement, and considering $y = 0$ at the top of the ribs, their time-averaged velocity profiles revealed no discernible slip velocity at the superhydrophobic walls. Nonetheless, the SHS influenced changes in the flow field. The SHS

with the ribs aligned in the flow direction reduced the fluctuation in the streamwise velocity, the friction resistance and the turbulence production, while the wall-normal turbulence intensity remained unaffected. The same surface pattern was tested without the coating, and the previous DR of 11% was not obtained; this confirmed the necessity of a slip velocity at the wall. The influence of the surface structures configurations was observed when the SHS with the ribs aligned in the transverse direction increased the friction resistance, the turbulence production, and the wall-normal fluctuations. Consequently, the momentum transport in the wall-normal direction was boosted, and the drag increased. The influence of the orientation of the SHS structures in the resultant magnitude of the slip velocity and DR was also observed by Min and Kim (2004). Lee *et al.* (2014) present a summary of the investigations (experiments and simulations) done in the past regarding interfacial slip on rough, patterned, and soft surfaces.

7.2.3 Plastron Morphology

This section presents the visualization of the air plastron morphology over the SHS and its variation with Re numbers. Figure 7.3 shows the SHS in static water at the beginning and the end of the test. At the beginning of the test, the SHS exhibited a shiny surface as observed by visual inspection and a uniform air plastron as seen in Figure 7.3(a). As the flow velocity increased and the time progressed, the air constantly moved within the plastron and eventually dissolved into the flow stream. The loss of air exposed the SHS microstructures/peaks observed in Figure 7.3(b).

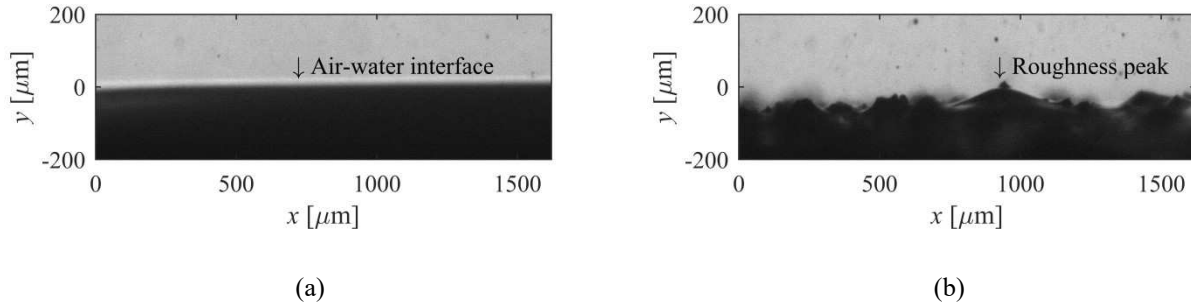


Figure 7.3. Plastron visualization in static water. (a) An image captured at the beginning of the test (before water flows). It shows a uniform and smooth air-water interface covering all the surface microstructures. (b) An image of the surface at the end of the test in still water (after the data was collected over five Re numbers within 45 min). The thick air plastron is absent, and the surface microstructures are visible.

The process of air depletion at each Re is presented in Figure 7.4. Each row of images belongs to the same Re , starting from the lowest Re of 5.0×10^5 at the top of the figure and continuing up to the highest $Re = 1.5 \times 10^6$ at the bottom images. The air layer is thicker at the beginning of the tests and then gradually depletes as the bubbles pinch-off or air dissolves into the water. The left column of Figure 7.4 displays a surface image at the beginning of the recording period, and the middle column shows an image at the end of the same recording period. The right column of Figure 7.4 shows a sample of the morphology of the air plastron and air pockets. The plastron thickness and the air pockets morphology are obtained by the inversion and subtraction of the images in the left and middle column. The observation of the image sets reveals a constant movement of the air within the plastron, especially at the lower Re numbers of 5.0×10^5 and 7.0×10^5 . At the latter two Re numbers, it is common to see the air layer covering all the SHS microstructures/peaks as seen in Figure 7.4(a) and Figure 7.4(d). Nonetheless, at these same Re numbers (5.0×10^5 and 7.0×10^5), there are also images with a reduced air layer that partially exposes the surface microstructures/peaks as displayed in Figure 7.4(b) and Figure 7.4(e). This

mixture of images demonstrates the movement of the air and its variable thickness. Over time and with increasing Re numbers ($> 1.0 \times 10^6$), the air plastron progressively dissolves into the flow stream and the SHS microstructures/peaks are permanently uncovered. The remaining air is seen in Figure 7.4 (l and o) as curved meniscus extended from peak-to-peak, these areas are known as air pockets. The sets of images at high velocities ($Re > 1.0 \times 10^6$) also showed the movement of the air pockets among the surface structures.

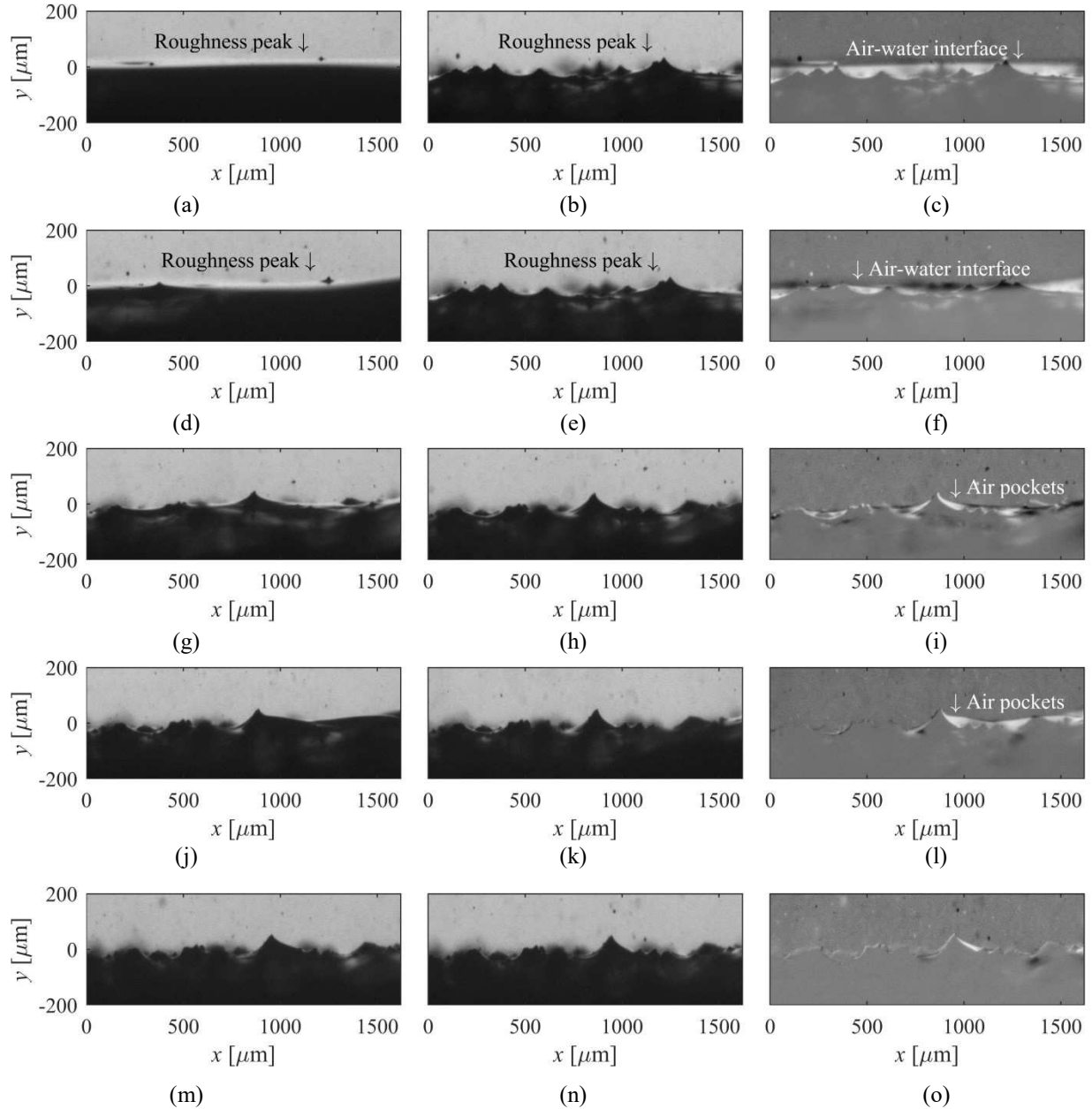


Figure 7.4. Plastron visualization with a flow at Re of (a-c) 5.0×10^5 in images, (d-f) 7.0×10^5 in images, (g-i) 1.0×10^6 , (j-l) 1.2×10^6 , and (m-o) 1.5×10^6 . The left column displays for each set an image at the beginning of the data recording period. The middle column shows images at the end of each set recording period. The right column displays the morphology of the air plastron and pockets by subtracting the inverted image of the left and middle column.

Similar to Poetes *et al.* (2010) observations, the thickness of the continuous air layer progressively decreased until it broke and formed air pockets. From the plastron visualization, it is possible to obtain an approximation of the air thickness within the surface. This approximation does not consider the air trapped within the surface microstructures, and neither considers the changes in the roughness of the surface due to the effect of the flow stream.

Table 7.2 gathers the estimation of the thickness of the air plastron and air pockets corresponding to a sample of 50 images from each set displayed in Figure 7.4. The estimation of the air plastron thickness is described in section 3.6.4. In conformity with the results presented before, the average thickness ($\langle t_e \rangle$) of the air plastron decreased as the Re raised and the SHS properties were lost. These results are also consistent with the trend of the DR as a function of the Re showed in Table 7.2. Higher values of DR were obtained at the $Re = 5.0 \times 10^5$, which displayed an averaged equivalent thickness of 10.8 μm . In comparison with this initial value, the averaged equivalent thickness decreased by ~11, 69, 78, and 90% at the $Re = 7.0 \times 10^5$, 1.0×10^6 , 1.2×10^6 and 1.5×10^6 . In agreement with the observations of Samaha *et al.* (2012b), Bidkar *et al.* (2014), Vajdi Hokmabad & Ghaemi 2016, and Abu Rowin *et al.* 2017, the effectivity of the SHS in the turbulent regime is directly related to the stability of the air layer. The highest values of DR were obtained when the surface displayed a commonly constant air layer.

7.3 Conclusions

The dependency of the drag reduction on the slip velocity and the equivalent thickness of the air plastron were further investigated using shadow-based long-range microscopic PTV. The SHS showed a relaxation of the no-slip boundary condition that gradually increased at higher velocities. At $Re = 5.0 \times 10^5$, the dimensionless roughness k^+_{rms} is 0.40, the slip velocity is 0.13 m/s, and the slip length b is 85 μm . In this case, the surface roughness R_{rms} represents 8% of the viscous sublayer thickness ($y^+ = 5$, 127.8 μm). These conditions reduced the drag by a 23%. Increasing the flow velocity, at $Re = 1.5 \times 10^6$, the k^+_{rms} increased to 1.03 and the slip velocity to 0.90 m/s. Although b remained fairly equal in 87 μm , the R_{rms} increased to 21% in relation to the viscous sublayer thickness (49.4 μm). These conditions resulted in an increase of the drag in 3%.

The slip velocity is seen to be inversely proportional to the DR. The value of the slip velocity is greatly affected by the selection of the distance from the wall used for its estimation, in this case y_{95} . The location of y_{95} depends on the characteristic roughness of the surface. At higher velocities, the surface roughness increases at the same pace that the air is reduced, and the location of y_{95} is defined farther away from the wall. In wall units, the location of y_{95} corresponds to 1^+ at $Re = 5.0 \times 10^5$ and 3.2^+ at $Re = 1.5 \times 10^6$. Consequently, the slip velocity increases with higher velocities. The same trend is seen if the slip velocity is estimated at $y = 0$, as it also depends on the characteristic roughness of the surface. Further statistics in the inner and outer layer are required to improve the understanding of the micro-scale phenomena in SHS with random texture.

The use of the shadowgraph technique provided visualization of the air plastron morphology and an estimation of the air layer thickness. At the $Re = 5.0 \times 10^5$, the surface exhibited a shiny and mostly continuous air plastron. These surfaces with a mostly constant air plastron had the best results in DR. However, the movement of the flow produced a constant displacement of the air layer enhancing its dissolution into the stream. Hence, the DR decreased over time and with increasing velocities. At the highest $Re = 1.5 \times 10^6$ the air plastron reduced by 90% when compared with its initial value. Consequently, the DR vanished.

In summary, the use of SHS over axisymmetric bodies is promising for the reduction of drag in scale-up applications. Specially the SHS with random structures, which are easily applicable in the manufacturing of large-scale surfaces like marine vessels by using spray coatings (Bidkar *et al.* 2014). However, there is still a necessity for further characterization of the turbulent flow over a random SHS. The use of the shadowgraph technique with the combined use of microscopic PTV with PIV could provide the missing turbulence statistic in the inner and outer layer over a body-of-revolution. A detailed studied of the air layer longevity would also provide a further understanding of the DR mechanism.

Chapter 8. Conclusions and Recommendations for Future Research

A promising method for DR in underwater vehicles with limited space is the use of SHS. The use of a superhydrophobic coating over the smooth, porous, and riblets surfaces reduced the drag in comparison with the same baseline module without the coating. However, for all the configurations tested the DR decayed with increasing Re . The highest DR, 36.4%, was obtained by the SHS over the smooth surface at $Re = 5 \times 10^5$; it then decreased to a 5.6% at $Re = 1.5 \times 10^6$. The efficiency of the smooth and riblets surfaces with the superhydrophobic coating might have been affected by the deterioration of the coating in the last 2 cm of the cylinders when the flow velocity was increased above 1.5 m/s. Conversely, the porous SHS did not show a severe deterioration of the coating and retained the air layer for a larger time than the smooth surface. At $Re = 1.5 \times 10^6$, the porous SHS reduced the drag in a 14.9% in comparison with the porous surface without the coating.

The use of the shadow-based long-range micro-PTV technique over the SHS provided a good visualization of the air plastron morphology and the required information to monitor the amount of air present at the wall with increasing Re numbers. The maximum DR was obtained at the beginning of the test where the amount of air at the surface was higher. The slip condition at the wall was also evaluated with long-range micro-PTV. At $Re = 5.0 \times 10^5$, the dimensionless roughness k^+_{rms} was 0.40 and the slip velocity is 0.13 m/s. These conditions reduced the drag by a 23%. Increasing the flow velocity, at $Re = 1.5 \times 10^6$, the k^+_{rms} increased to 1.03 and the slip velocity to 0.90 m/s. A DI of 5.6% was observed. This increasing trend of the slip velocity with Re is inversely proportional to the reduction of DR. This incongruence of the results is related to the selection of equivalent flat interface (located at y_{95}) for the estimation of the slip velocity. As the flow can still move within the valleys of the roughness peaks, the slip velocity is enhanced when estimated far from the wall ($y = 0$).

Although the injection of air did not improve the efficiency of the SHS, it was possible to replenish the air over the SHS plastron/pockets and maintain its performance. It was also possible to replenish the air of a wetted SHS. The surface kept its hydrophobic properties as long

as the air was being supplied. All the air injected remained within the SHS and no bubbles were seen to come out and interact beyond the air-water interface.

Conversely, the use of a larger porous surface over the axisymmetric body for the injection of air did not reduced the drag. The current study observed, for all the air injection rates Q_a tested (0.15 – 50 L/min), a DI in comparison with the porous surface without air injection, and an even higher in contrast to the smooth surface. The pressure drag could have been increased by the non-uniform distribution of the bubbles over the AUV model. Two factors influencing the air bubbles distribution were: i) the injection uniformity, and ii) the upward buoyancy-driven motion of the bubbles. Higher flow stream velocities and air injection rates would be necessary to improve the attachment of the bubbles cloud to the test model surface, and to replicate the conditions of successful previous works. These conditions were not tested due to limitations in the facility.

The use of rectangular riblets, in the ranges of $s^+ = 15-40$ and $s^+ = 30-80$, did not offer DR over an axisymmetric body in the turbulent regime. The performance of the riblets might have been affected by the existence of a flow pattern around the AUV body, and imperfections in the geometry of the grooves. Regarding the combined effect of riblets with the SHS, the results showed a limited improvement in comparison with the riblets surfaces without coating. The maximum DR obtained with the coated surface was 13.9% with a $s^+=21$. However, there was no DR in comparison with the smooth surface. Furthermore, the performance of the riblets in combination with low air injection neither offer DI. The method of air injection used limited the performance of this combined technique. Although it was possible to see some air bubbles trapped in the valleys of the riblets, and some grooves were partially filled with air, the configuration of the air injection was not adequate to displace the water in all the grooves and replace it with air.

Recommendations for Future Research

The following aspects are recommended for the future work considering the results of this investigation and the literature:

- Estimation of slip velocities in SHS with random textures: further investigation is required to develop a methodology to properly set the location for the reference surface ($y = 0$).

- SHS over axisymmetric bodies in the turbulent regime: carry out the combined use of PTV and PIV. The measurements of micro-PTV for the characterization of the inner layer, and the PIV for the characterization of the complete TBL. The use of these techniques could provide the missing turbulence statistic in the inner and outer layer over a body-of-revolution.
- SHS stability: a detailed study of the SHS longevity in the axisymmetric body would also provide a further understanding of the DR mechanism in action, and how the coating degradation could be avoided or slow it down. The injection of air might help to extend its effective lifetime, but it is required to study its optimum range and effects in the air-water interface.
- DR with low air injection rates: further investigation is required to optimize the injectors and the surface geometrical parameters. Additionally, is necessary to determine the most effective configuration for air injection, estimate the variations of the volumetric flow as a function of the flow velocity, and evaluate the stability of the air layers.
- DR with helicoidal riblets over an axisymmetric body: a performance comparison of longitudinal and helicoidal riblets would help to evaluate the impact of flow misalignment in the DR mechanism of the riblets over an axisymmetric body.
- DR with riblets and low air injection rates: add cross-section walls in the riblets valleys to break long grooves into several small sections. It is also recommended to add a shroud over tangential injection ports to help with the retention of the air being injected. These designs considerations could reduce the energy required to fill the grooves with air.

Bibliography

- Adrian, R. (2007). Hairpin vortex organization in wall turbulence. *Physics of Fluids*, 4 (041301). doi:10.1063/1.2717527.
- Abu Rowin, W., Hou, J. and Ghaemi, S. (2017) Inner and outer layer turbulence over a superhydrophobic surface with low roughness level at low Reynolds number. *Phys. Fluids* 29, 095106
- Aljallis, E., Sarshar, M. A., Datla, R., Sikka, V., Jones, A., & Choi, C.-H. (2013). Experimental study of skin friction drag reduction on superhydrophobic flat plates in high Reynolds number boundary layer flow. *Physics of Fluids*, 25(2), 025103. doi:10.1063/1.4791602.
- Al-Shemmeri, Tarik (2012) *Engineering Fluid Mechanics*. Ventus Publishing ApS. pp.17–18. ISBN 978-87-403-0114-4.
- Anderson, J. (2005) Ludwig Prandtl's Boundary Layer. *Physics Today*, 58, 12, pp. 42-48.
- Ash, R. L. (1973). On the theory of compliant wall drag reduction in turbulent boundary layers. NASA CR-238 7.
- Balasubramanian, A., Miller, A., and Rediniotis, O. (2004) Microstructured hydrophobic skin for hydrodynamic drag reduction. *AIAA Journal*, 42 (2), pp. 411-414.
- Baek, S. J., and S. J. Lee. (1996). A New Two-Frame Particle Tracking Algorithm Using Match Probability. *Experiments in Fluids* 22 (1): 23–32. doi:10.1007/BF01893303.
- Barbier, C., E. Jenner, and B. D'Urso. (2012) "Drag reduction with superhydrophobic riblets." In *ASME 2012 International Mechanical Engineering Congress and Exposition*, 199–205. Houston: ASME. doi:10.1115/IMECE2012-86029.
- Barthlott, W., & Neinhuis, C. (1997). Purity of the sacred lotus, or escape from contamination in biological surfaces. *Planta*, 202(1), 1–8.
- Bechert, D. W., and M. Bartenwerfer. (1989). "The Viscous Flow on Surfaces with Longitudinal Ribs." *Journal of Fluid Mechanics* 206 (September): 105–29. doi:10.1017/S0022112089002247.
- Bechert, D. W., M. Bruse, W. Hage, J. G. T. Van Der Hoeven, and G. Hoppe. (1997). "Experiments on Drag-Reducing Surfaces and Their Optimization with an Adjustable Geometry." *Journal of Fluid Mechanics* 338 (May): 59–87. doi:10.1017/S0022112096004673.
- Bezuijen, S. (2017) Hydrodynamic drag reduction in turbulent boundary layer flow using riblets. MSc Thesis. Delft University of Technology

- Bidkar, R. A., L. Leblanc, A. J. Kulkarni, V. Bahadur, S. L. Ceccio, and M. Perlin. (2014). "Skin-Friction Drag Reduction in the Turbulent Regime Using Random-Textured Hydrophobic Surfaces." *Physics of Fluids* 26 (8): 085108. doi:10.1063/1.4892902.
- Bixler, G. D. and Bhushan, B. (2013) Fluid drag reduction with shark-skin riblet inspired microstructured surfaces. *Adv. Funct. Mater.*, 23: 4507–4528. doi:10.1002/adfm.201203683
- Blackwelder, R. F., and H. Eckelmann. (1979). Streamwise vortices associated with the bursting phenomenon. *Journal of Fluid Mechanics*, 94 (03), pp. 577–594. doi:10.1017/S0022112079001191.
- Bodgevich, V. G. and Evseev, A. R. (1976). The distribution of skin friction in a turbulent boundary layer of water beyond the location of gas injection. *Investigations of Boundary Layer Control (in Russian)*, vol. 62. Thermophysics Institute Publishing House.
- Bobji, M.S., Kumar, S.V., Asthana, A., Govardhan, R.N. (2009) Underwater sustainability of the "Cassie" state of wetting. *Langmuir - American Chemical Society*, **25**, 20.
- Bonaccorso, E., Butt, H. J., Craig, V. S. (2003) Surface roughness and hydrodynamic boundary slip of a newtonian fluid in a completely wetting system. *Phys Rev Lett.* 90(14):144501.
- Brzek B., Cal R. B., Johansson T. G., and Castillo L. (2008) Transitionally rough zero pressure gradient turbulent boundary layers. *Exp. Fluids* 44 (1), 115–124.
- Cebeci, T., and Smith, A. (1968). A finite-difference solution of the incompressible turbulent boundary-layer equations by an Eddy-Viscosity concept. *Proceedings of the 1968 AFOSR-IFP-Stanford Conference on Computation of Turbulent Boundary Layers. Vol 1*, Stanford University, pp. 346-355.
- Cebeci, T., and Smith, A. (1974). *Analysis of turbulent boundary layers*. Academic Press Inc.
- Cebeci, T, Mosinskis, G. J., Smith, A. M. (1970) Calculation of viscous drag and turbulent boundary layer separation on two dimensional and axisymmetric bodies in incompressible flows. Douglas Aircraft Company.
- Ceccio, S. (2010). Frictional drag reduction of external flows with bubble and gas injection. *Annual Review of Fluid Mechanics*, 42, pp. 183-203. doi:10.1146/annurev-fluid-121108-145504.
- Cengel, Y, and Cimbala, J. (2014) *Fluid Mechanics: Fundamentals and Applications*, Third Edition. McGraw-Hill. New York, NY. ISBN 978-0-07-338032-2
- Chan, L., Macdonald, M., Chung, D., Hutchins, N. & Ooi, A. (2015) A systematic investigation of roughness height and wavelength in turbulent pipe flow in the transitionally rough regime. *J. Fluid Mech.* 771, 743–777.

- Choi, H., Sagong, W., Kim, C., Choi, S., and Jeon, W. (2008). Does the sailfish skin reduce the skin friction like the shark skin? *Physics of Fluids Journal*, 20, (101510) pp. 1-10. doi: 10.1063/1.3005861
- Choi, K. S., Gadd, G. E., Pearcey, H. H., Savill, A. M. and Svensson, S. (1989) Test of drag-reducing polyme coated on a riblet surface. *App Sci Research*. 46: 209-216.
- Clark, H. and Deutsch, S. (1991). Microbubble skin friction reduction on an axisymmetric body under the influence of applied axial pressure gradients. *Phys. Fluids A* 3, pp. 2948–2954.
- Crees, T., Kaminski, C., Ferguson, J., Laframboise, J. M., Forrest, A., Williams, J., MacNeil, E., Hopkin, D., Pederson, R. (2010). Preparing for UNCLOS - An historic AUV deployment in the canadian high arctic. *IEEE / OES Autonomous Underwater Vehicles*. doi: 10.1109/AUV.2010.5779651
- Coward, A. (2004) Recommissioning an inoperable icing water tunnel as a flow visualization water tunnel. MSc. Thesis. University of Alberta.
- Daniello, R. J., Waterhouse, N. E. and Rothstein, J. P. (2009) Drag reduction in turbulent flows over superhydrophobic surfaces. *Phys. Fluids*, 21, 85103
- Daschiel, G. (2015). Strategies to reduce friction losses and their implications for the energy efficient design of internal flow domains, pp. 1-2. *Karlsruher Institut für Technologie (KIT)*. doi: 10.5445/KSP/1000043770
- Davari, A. (2014). Viscous drag reduction on axisymmetric bodies using helical riblets. *Int J of Advanced Design and Manufacturing Technology*, vol 7. No 4. E-ISSN: 2383-4447.
- Deutsch, S., and Castano, J. (1986) Microbubble skin friction reduction on an axisymmetric body. *Physics of Fluids* 29, 3590 (1986); doi: 10.1063/1.865786
- Deutsch, S, Pal S (1990) Local shear stress measurement on an axisymmetric body in a microbubble modified flow field. *Phys Fluids A2*:2140–2146
- Deutsch, S., Moeny, M., Fontaine, A. and Petrie, H. (2003) Microbubble drag reduction in rough walled turbulent boundary layers. *Proc. ASME Fluids Engineering Division Summer Meeting 2003*, pp. 1–9.
- Elbing, B. R., Winkel, E. S., Lay, K. A., Ceccio, S. L., Dowling, D. R., and Perlin, M. (2008). Bubble-induced skin-friction drag reduction and the abrupt transition to air-layer drag reduction. *Journal of Fluid Mechanics*, 612, pp. 201–236. doi:10.1017/S0022112008003029
- Ferrante, A., Elghobashi, S. (2004). On the physical mechanism of drag reduction in a spatially developing turbulent boundary layer laden with microbubbles. *Journal of Fluid Mechanics*, 503, pp. 345–355.

- Ferrante, A., Elghobashi, S. (2005). Reynolds number effect of drag reduction in a microbubble-laden spatially developing turbulent boundary layer. *Journal of Fluid Mechanics*, 543, pp. 93–106.
- Feng, Y., Goree, J., and Liu, B. (2011). Errors in Particle Tracking Velocimetry with High Speed Cameras. *Rev. Sci. Instrum.*, 82(053707):1–7.
- Fontaine, A. A. and Deutsch, S. (1992). The influence of the type of gas on the reduction of skin friction drag by microbubble injection. *Exps. Fluids* 13, pp. 128–136.
- Fu, Y. F., Yuan, C. Q., and Bai, X. Q. (2017) Marine drag reduction of shark skin inspired riblet surfaces. *Biosurface and Biotribology* 3 (2017) 11–24
- Gabillet, C., Colin, C., and Fabre, J. (2002). Experimental study of bubble injection in a turbulent boundary layer. *International Journal of Multiphase Flow*, 28, pp. 553-578.
- Gad-el-Hak, M. (1989). *Frontiers in experimental fluid mechanics*. Springer-Verlag. doi: 10.1007/978-3-642-83831-6.
- Gad-el-Hak, M., Pollard, A., and Bonnet, J. (1998). *Flow control: fundamentals and practices*. Springer-Verlag. ISBN 3-540-63936-5.
- Gad-el-Hak, M. 2013. Comment on ‘Experimental Study of Skin Friction Drag Reduction on Superhydrophobic Flat Plates in High Reynolds Number Boundary Layer Flow. *Physics of Fluids* 25 (7): 079101. doi:10.1063/1.4816362.
- Garcia-Mayoral, R., and J. Jimenez. (2011). “Drag Reduction by Riblets.” *Philosophical Transactions of the Royal Society A: Mathematical, Physical and Engineering Sciences* 369 (1940): 1412–27. doi:10.1098/rsta.2010.0359.
- Gao, X., and Jiang, L. (2004) Biophysics: water-repellent legs of water striders. *Nature*.432(7013):36.
- George, W. (2013). *Lectures in Turbulence for the 21st Century*. Department of Aeronautics. Imperial College of London. London, UK.
- Gillerist, M. C., and Reidy, L. W. (1989) 4.4 Drag and noise measurements on an underwater vehicle with a riblet surface coating. *Drag reduction in fluid flows, techniques for friction control*.
- Goldstein, D., R. Handler, and L. Sirovich. (1995). Direct Numerical Simulation of Turbulent Flow over a Modeled Riblet Covered Surface. *Journal of Fluid Mechanics* 302 (November): 333–76. doi:10.1017/S0022112095004125.
- Golovin, K. B., J. W. Gose, M. Perlin, S. L. Ceccio, and A. Tuteja. (2016). “Bioinspired Surfaces for Turbulent Drag Reduction.” *Philosophical Transactions of the Royal Society A:*

- Mathematical, Physical and Engineering Sciences 374 (2073): 20160189. doi:10.1098/rsta.2016.0189.
- Gore, R., and Crowe, C. (1989). Effect of particle size on modulating turbulent intensity. *International Journal of Multiphase Flow*, 15, pp. 279-285.
- Granville, P. S. (1953). The calculation of the viscous drag of bodies of revolution. The David W. Taylor Model Basin Report 849, July 1953.
- Hooshmand, A., R. Youngs, J. M. Wallace, and J. L. Balint. (1983). "An Experimental Study of Changes in the Structure of a Turbulent Boundary Layer due to Surface Geometry Changes." In 21st Aerospace Sciences Meeting, 83–230. Reston, Virginia: American Institute of Aeronautics and Astronautics. doi:10.2514/6.1983-230.
- Hou, J. (2016) Particle image velocimetry/ tracking in turbulent flow over riblet surfaces with superhydrophobic coating. MSc Thesis. University of Alberta.
- Hou, J., Vajdi Hokmabad, B., and Ghaemi, S. (2017) Three-dimensional measurement of turbulent flow over a riblet surface. *Exp Thermal and Fluid Science*. Vol 85, pp 229-239
- Jagadeesh, P., Murali, K., and Idichandy, V. G. (2008) Experimental investigation of hydrodynamic force coefficients over AUV hull form. *Ocean Engineering*. Vol. 36: 1, pp 113-118. <https://doi.org/10.1016/j.oceaneng.2008.11.008>
- Jiang, J., Shi, Y., and Pan, G. (2013) Computation of hydrodynamic coefficients of portable autonomous underwater vehicle. *APCOM & ISCM*. Singapore.
- Joseph, N. (2015) Effective slip lengths for Stoke flow over rough, mixed-slip surfaces. PhD Thesis. Victoria University of Wellington.
- Joseph, P., Cottin-Bizonne, C., Benoît, J.-M., Ybert, C., Journet, C., Tabeling, P. & Bocquet, L. (2006) Slippage of water past superhydrophobic carbon nanotube forests in microchannels. *Phys. Rev. Lett.* 97, 156104. (doi:10.1103/PhysRevLett.97.156104)
- Kato, H., Miura, K., Yamaguchi, H. and Miyanaga, M. (1998). Experimental study on the microbubble ejection method for frictional drag reduction. *J Mar Sci Technol* 3, pp. 122-129.
- Kawamura, T., Moriguchi, Y., Kato, H., Kakugawa, A. and Kodama, Y. (2003). Effect of bubble size on the microbubble drag reduction of a turbulent boundary layer. *Proc. ASME Fluids Engng Conf. Summer Meeting 2003*, pp. 1–8.
- Keane, R. D., Adrian, R. J. (1990) Optimization of particle image velocimeters. Part I: Double pulsed systems. *Meas. Sci. Technol*, 1:1202–1215.

- Kim, H., M. Moon, and K. Kim. (2011). Multi-objective optimization of a cooling channel with staggered elliptic dimples. *Energy* 36 (5). Elsevier Ltd, pp. 3419–3428. doi:10.1016/j.energy.2011.03.043.
- Kim, J., P. Moin, and R. Moser. (1987). Turbulence statistics in fully developed channel flow at low reynolds number. *Journal of Fluid Mechanics*, 177, pp. 133–166. doi:10.1017/S0022112087000892.
- Kim, S. H. (2008) Fabrication of Superhydrophobic Surfaces. *Journal of Adhesion Science and Technology* 22 (3-4): 235–50. doi:10.1163/156856108X305156.
- Kitawa, A., Hishida, K. and Kodama, Y. (2005) Flow structure of microbubble-laden turbulent channel flow measured by PIV combined with the shadow image technique. *Experiments in Fluids*, 38, pp. 466-475. doi: 10.1007/s00348-004-0926-8.
- Kline, S., Reynolds, W., Schraub, F., and Runstadler, P. (1967). The structure of turbulent boundary layers. *Journal of Fluid Mechanics*, 30 (04), pp. 741-773. doi:10.1017/S0022112067001740.
- Kodama, Y., Kakugawa, A., Takahashi, T., Nagaya, S. and Sugiyama, K. (2002). Microbubbles: drag reduction mechanism and applicability to ships. 24th Symp. Naval Hydrodyn. pp. 1–19.
- Kodama, Y., Hori, T., Kawashima, M. M. and Hinatsu, M. (2006). A full-scale microbubble experiment using a cement carrier. *Eur. Drag Reduction and Flow Control Meeting*, Ischia, Italy, pp. 1–2.
- Koeltzsch, K., Dinklacker, A. and Grundmann, R. (2002). Flow over convergent and divergent wall riblets. *Experiments in Fluids*, 33, pp. 346-350
- Konovalov, S. F., Lashkov, Y. A., Mikhailov, V. V., Fadeev, I. V., and Shapovalov G., K. (1991) Effect of longitudinal riblets on axisymmetric body drag. Moscow. Translated from *Izvestiya Rossiiskoi Akademii Nauk, Mekhanika Zhidkosti i Gaza*, No.2, pp. 174-178
- Kundu, P., Cohen, I., Dowling, D. (2012). *Fluid Mechanics*. 5th Edition. Elsevier.
- Kunert, C., and Harting, J. (2007) Roughness induced boundary slip in microchannel flows. *Physical Review Letters* 99, 176001.
- Lay, K., Yakushiji, R., Makiharju, S., Perlin, M., and Ceccio, S. (2010). Partial cavity drag reduction at high Reynolds number. *Journal of Ship Research*, 54, pp. 109–119.
- Lazos, B. (1989) Effects of contamination on riblet performance. *Journal of Aircraft*, Vol. 26, No. 7, pp. 684-686. <https://doi.org/10.2514/3.45821>
- Legner, H. (1984). Simple model for gas bubble drag reduction. *Physics of Fluids*, 27, pp. 2788–2790.

- Lee, T., Charrault, E., and Neto, C. (2014) Interfacial slip on rough, patterned and soft surfaces: A review of experiments and simulations. *Advances in Colloid and Interface Science* 210, pp 21–38
- Lee, S., and Y. Choi. (2008). Decrement of spanwise vortices by a drag-reducing riblet surface. *Journal of Turbulence*: 1–15. doi:10.1080/14685240802251517.
- Lindken, R., Merzkirch, W. (2002) A novel PIV technique for measurements in multiphase flows and its application to two-phase bubbly flows. *Exp in Fluids*, 33, 814-825.
- Ling, H., Srinivasan, S., Golovin, K., McKinley, G. H., Tuteja, A. and Katz, J. (2016) High-resolution velocity measurement in the inner part of turbulent boundary layers over super-hydrophobic surfaces. *J. Fluid Mech.*, 801, 670–703
- Lo, T. S., L’vov, V.S., Procaccia, I. (2006). Drag reduction by compressible bubbles. *Phys. Rev. E* 73:036308.
- Loadstar™ (November, 2017) Retrieved from <http://www.loadstarsensors.com/what-is-a-load-cell.html>
- Lu, J., Fernández, A. and Tryggvason, G. (2005). The effect of bubbles on the wall drag of a turbulent channel flow. *Phys. Fluids* 17, 095102.
- Lumley, J. (1973). Drag reduction in turbulent flow by polymer additives. *Journal of Polymer Science: Macromolecular Reviews*, 7, pp. 263-290. doi:10.1002/pol.1973.230070104
- Lumley, J. (1977). Drag reduction in two phase and polymer flows. *Physics of Fluid* 20, S64-70. doi: 10.1063/1.861760.
- L’vov, V., Pomyalov, A., Procaccia, I., and Tiberkeish, V. (2005) Drag reduction by microbubbles in turbulent flow: the limit of minutes bubbles. *Physical Review Letters*, 94 (174502).
- Lyu, S., Nguyen, D.C.; ., Hwang, W., Yoon, B. (2013) Experimental drag reduction study of super-hydrophobic surface with dual-scale structures. *Applied Surface Science* 286:206-211
- Madavan, N., Deutsch, S. and Merkle, C. (1984). Reduction of turbulent skin friction by microbubbles. *Phys. Fluids* 27, pp. 356–363.
- Madavan, N., Deutsch, S., Merkle, C. (1985a). Measurements of local skin friction in a microbubble modified turbulent boundary layer. *Journal of Fluid Mechanics*, 156, pp. 237–256.
- Madavan, N., Deutsch, S., Merkle, C. (1985b). Numerical investigation into the mechanisms of microbubble drag reduction. *Journal of Fluid Engineering*, 107, pp. 370–377.

- Mäkiharju, S., Elbing, B., Wiggins, A., Schinasi, S., Vanden-Broeck, J., Perlin, M., and Ceccio, S. (2013a) On the scaling of air entrainment from a ventilated partial cavity. *Journal of Fluid Mechanics*, 732, pp. 47–76.
- Mäkiharju, S., Gabillet, C., Paik, B., Chang, N., Perlin, M., and Ceccio, S. (2013b) Time-resolved two-dimensional X-ray densitometry of a two-phase flow downstream of a ventilated cavity. *Experiments of Fluids*, 54(7), 1561.
- Martell, M. B., J. B. Perot, and J. P. Rothstein. (2009) Direct Numerical Simulations of Turbulent Flows over Superhydrophobic Surfaces. *Journal of Fluid Mechanics* 620 (February): 31–41. doi:10.1017/S0022112008004916.
- Martell, M. B., J. P. Rothstein, and J. B. Perot. (2010) An Analysis of Superhydrophobic Turbulent Drag Reduction Mechanisms Using Direct Numerical Simulation. *Physics of Fluids* 22 (6): 065102. doi:10.1063/1.3432514.
- Masliyah, J., Jauhari, R., and Gray, M. (1994). Drag coefficient for air bubbles rising along an inclined surface. *Chemical Engineering Science*, 49, pp. 1905–1911
- McCormick, M. E. and Battacharyya, R. (1973). Drag reduction of a submersible hull by electrolysis. *Naval Engrs J.* 85, pp. 11–16.
- McCutcheon, S.C., Martin, J.L, Barnwell, T.O. Jr. (1993) *Water Quality in Maidment, D.R.* (Editor). *Handbook of Hydrology*, McGraw-Hill. New York, NY
- Meng, J. and Uhlman, J. (1998). Microbubble formation and splitting in a turbulent boundary layer for turbulence reduction. *Proc. Intl Symp. Seawater Drag Reduction*, pp. 341–355.
- Merkle, C. and Deutsch, S. (1992). Microbubble drag reduction in liquid turbulent boundary layers. *Appl. Mech. Rev.* 45, pp. 103–127.
- Min, T., and J. Kim. (2004) Effects of Hydrophobic Surface on Skin-Friction Drag. *Physics of Fluids* 16 (7): 0–3. doi:10.1063/1.1755723.
- Mongruel A, Chastel T, Asmolov ES, Vinogradova OI. (2013) Effective hydrodynamic boundary conditions for microtextured surfaces. *Phys Rev E*;87:011002.
- Murai, Y., Fukuda, H., Oishi, Y., Kodama, Y. and Yamamoto, Fujio (2006). Skin friction reduction by large air bubbles in a horizontal channel flow. *Int J of Multiphase Flow*, 33, pp: 147-163. doi: 10.1016/j.ijmultiphaseflow.2006.08.008.
- Murai, Y. (2014). Frictional drag reduction by bubble injection. *Experiments in Fluids*, 55:1773. doi: 10.1007/s00348-014-1773-x.
- Nagamatsu, T., Kodama, T., Kakugawa, A., Takai, M., Murakami, K., Ishikawa., Kamiirisa, H., Ogiwara, S., Yoshida, Y., Suzuki, T., Toda, Y., Kato, H., Ikemoto, A., Yamatani, S., Imo, S. and Yamashita, K. (2002). A full-scale experiment on microbubbles for skin friction

- reduction using SEIUN MARU. Part 2: The full-scale experiment. *J. Soc. Naval Arch. Japan* 192, pp. 15–28.
- Ng., E., and Lou, Y. (2016). *Bio-inspired surfaces and applications*. World Scientific Publishing Co. Pte. Ltd. Singapore.
- Nunes, J. V., Lins, A. R., Ferreira, W., Barbosa, A. G. (2014) Numerical analysis of turbulent fluid flow drag coefficient for optimizing the AUV hull design. *Open J. of Fluid Dynamics*, 4, pp. 263-277.
- Norconk, M. P. (2011) *A Comprehensive Review and Application of Particle Image Velocimetry*. Michigan Technological University. <http://digitalcommons.mtu.edu/etds/392>.
- Oishi, Y., and Murai, Y. (2014). Horizontal turbulent channel flow interacted by a single large bubble. *Experimental Thermal and Fluid Science*, 55, pp. 128–139
- Ou J., Rothstein J. P. (2004) Laminar drag reduction in microchannels using ultrahydrophobic surfaces. *Phys. Fluids* 16, 4635
- Ou J., Rothstein J. P. (2005) Direct velocity measurements of the flow past drag-reducing ultrahydrophobic surfaces. *Phys. Fluids* 17, 103606. doi:10.1063/1.2109867(doi:10.1063/1.2109867)
- Park, H., Sun, G. and Kim, C. J. (2014) Superhydrophobic turbulent drag reduction as a function of surface grating parameters. *J. Fluid Mech.*, 747, 722–734
- Peng, D., Wen, J., Dong, S., Ouahsine, A., and Haibao, H. (2017) Maintenance of air layer and drag reduction on superhydrophobic surface. *Ocean Engineering*.130,pp 328-335
- Perry, A., Schofield, W., & Joubert, P. (1969). Rough wall turbulent boundary layers. *Journal of Fluid Mechanics*, 37(2), 383-413. doi:10.1017/S0022112069000619
- Poetes, R, Holtzmann, K., Franze, K., Steiner, U. (2010) Metastable underwater superhydrophobicity *Phys Rev Lett*.105(16):166104. Epub 2010 Oct 14.
- Pope, S. (2000). *Turbulent Flows*. Cambridge University Press.
- Prandtl, L. in *Verhandlungen des dritten internationalen Mathematiker-Kongresses in Heidelberg* (1904), Krazer, A., ed., Teubner, Leipzig, Germany (1905), p. 484. English trans. in *Early Developments of Modern Aerodynamics*, Ackroyd, J. A. K., Axcell, B. P. Ruban, A. I., eds., Butterworth-Heinemann, Oxford, U.K. (2001), p. 77.
- Prasad AK (2000) Stereoscopic particle image velocimetry. *Exp Fluids* 29:103–116
- Prince, J. F., Maynes, D., Crockett, J. (2014) Pressure drop measurements in turbulent channel flow over superhydrophobic surfaces with riblets. *ASME 2014 12th International*

Conference on Nanochannels, Microchannels and Minichannels. ISBN: 978-0-7918-4627-8

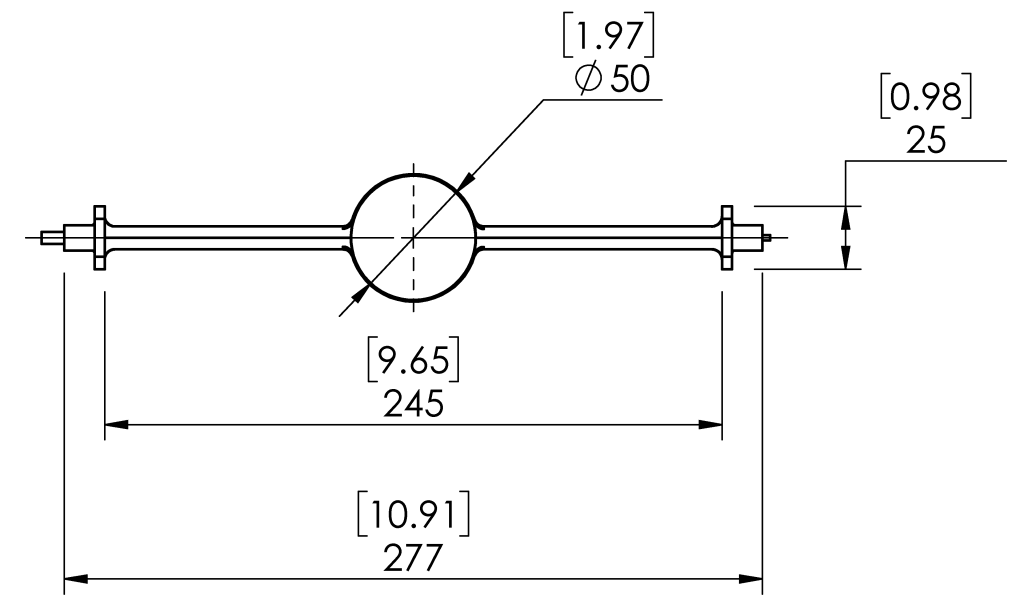
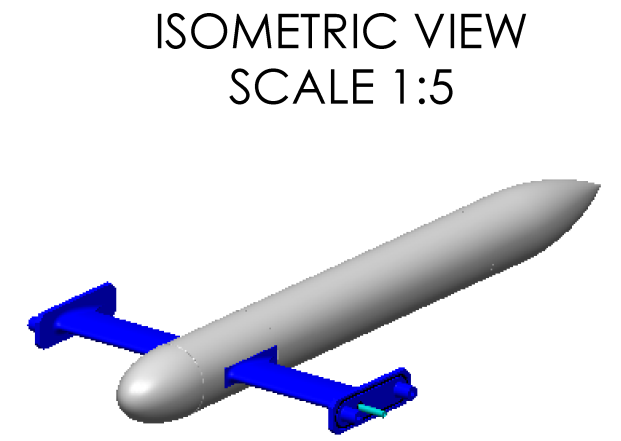
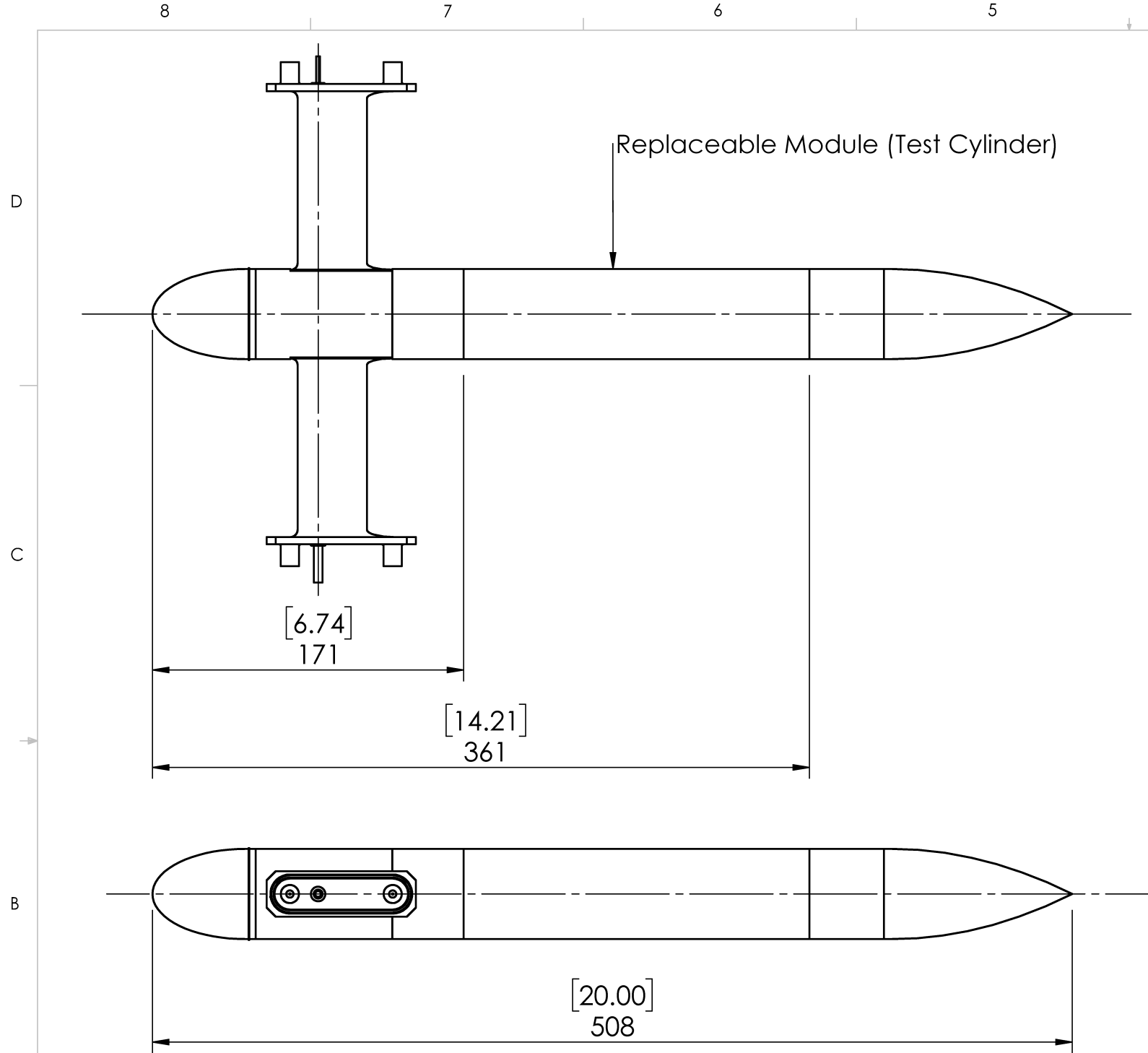
- Rastegari, A. and Akhavan, R. (2015) On the mechanism of turbulent drag reduction with superhydrophobic surfaces. *J. Fluid Mech.*, 773, R4
- Raffel, M., C. E. Willert, S. T. Wereley, and J. Kompenhans. (2007) *Particle Image Velocimetry*. Springer. Experimental Fluid Mechanics. Berlin, Heidelberg: Springer Berlin Heidelberg. doi:10.1007/978-3-540-72308-0.
- Rastegari, A., and R. Akhavan. (2015) On the Mechanism of Turbulent Drag Reduction with Super-Hydrophobic Surfaces. *Journal of Fluid Mechanics* 773 (June): R4. doi:10.1017/jfm.2015.266.
- Reed, J. and Weinstein, L. (1989) Flow visualization study of grooved surface/surfactant/air-sheet interaction. AIAA 2nd Shear Flow Conference. AIAA-89-0962.
- Reed, J. (1994) Using grooved surfaces to improve the efficiency of air injection drag reduction methods in hydrodynamics flows. *J. of Ship Research*. Vol. 38, No. 2, pp. 133-136.
- Robinson, S. (1991). Coherent motions in the turbulent boundary layer. *Annual Review of Fluid Mechanics*, 23, pp. 601-639.
- Rothstein, J. P. (2010). Slip on superhydrophobic surfaces. *Annual Review of Fluid Mechanics*, 42, pp. 89–109. doi:10.1146/annurev-fluid-121108-145558.
- Samaha, M. A., Ochanda, F. O., Tafreshi, H. V., Tepper, G. C. and Gad-el-Hak, M. (2011) In Situ, non-invasive characterization of superhydrophobic coatings. *Rev. Sci. Instrum.* 82, 045109
- Samaha, M. A., Tafreshi, H. V. and Gad-el-Hak, M. (2012) Influence of Flow on Longevity of Superhydrophobic Coatings. *Langmuir*, 28, 9759–9766
- Sanders, W. C., Winkel, E. S., Dowling, D. R., Perlin, M., and Ceccio, S. L. (2006). Bubble friction drag reduction in a high-Reynolds-number flat-plate turbulent boundary layer. *Journal of Fluid Mechanics*, 552(-1), 353. doi:10.1017/S0022112006008688
- Sangani, A., Kang, S., Tsao, H., and Koch, D. (1997). Rheology of dense bubble suspensions. *Physics of Fluids*, 9(6), pp.1540–1561.
- Saravi SS, Cheng K. (2013) A review of drag reduction by riblets and micro-textures in the turbulent boundary layers. *Eur. Sci. J.* 9, 62–81.
- Schlichting, H., and Gersten, K. (2000). *Boundary Layer Theory*. 8th Edition. Springer.
- Shen, X., Perlin, M. and Ceccio, S. L. (2006). Influence of bubble size on micro-bubble drag reduction. *Exps. Fluids* 41, pp. 415–424.

- Shereena, S. G., Vengadesan, S., Idichandy, V. G. and Bhattacharyya, S.K. (2013) CFD of drag reduction in axisymmetric underwater vehicles using air jets. *Engineering Applications of Computational Fluid Mechanics*. Vol 7, No. 2, pp. 193-209.
- Sirovich, L., and Karlsson, S. (1997) Turbulent drag reduction by passive mechanisms, (February), pp. 728–730.
- Smith, C., and Metzler, S. (1983) The characteristics of low-speed streaks in the near-wall region of a turbulent boundary layer. *Journal of Fluid Mechanics*, 129 (April), pp 27-54. doi:10.1017/S0022112083000634.
- Spalart, P. (1988) Direct simulation of a turbulent boundary layer up to $Re_\theta=1410$. *Journal of Fluid Mechanics*, 187, pp. 61-98.
- Takahashi, T., Kakugawa, A., Nagaya, S., Yanagihara, T. and Kodama, Y. (2001) Mechanisms and scale effects of skin friction reduction by microbubbles. *Proc. 2nd Symp. on the Smart Control of Turbulence*, University of Tokyo, pp. 1–9.
- Tropea, C., Yarin A., Foss, J. (2007) *Springer Handbook of Experimental Fluid Mechanics*. Springer-Verlag Berlin Heidelberg. 978-3-540-30299-5.
- Vadji Hokmabad, B., and Ghaemi, S. (2016) Turbulent flow over wetted and non-wetted superhydrophobic counterparts with random structure. *Phys. Fluids*, 28, 15112, (2016).
- Vadji Hokmabad, B., and Ghaemi, S. (2017) Effect of flow and particle-plastron collision on the longevity of superhydrophobicity, *Scientific Reports*, 7, 41448
- Verho, T., Bower, C., Andrew, P., Franssila, S., Ikkala, O. and Ras, R. H. A. (2011) Mechanically Durable Superhydrophobic Surfaces. *Adv. Mater.*, 23: 673–678. doi:10.1002/adma.201003129
- Vinogradova, O. and Belyaev, A (2011) Wetting, roughness and flow boundary conditions *J. Phys.: Condens. Matter* 23 184104
- Vinogradova, O. I., and Yakubov, G. E. (2006) Surface roughness and hydrodynamic boundary conditions. *Physical Review E* 73, 045302.
- VPG Transducers. (2015) Load Cell Accuracy in Relation to the Conditions of Use. Technical Note VPGT-02. Document 11864.
- Wallace, J. M., H. Eckelmann, and R. S. Brodkey. (1972) The wall region in turbulent shear flow. *Journal of Fluid Mechanics*, 54 (01), pp. 39–48. doi:10.1017/S0022112072000515.
- Walsh, M. J. (1979) Drag characteristics of v-groove and transverse curvature riblets. In *Symposium on Viscous Flow Drag Reduction*, 168–84. Dallas.1983. “Riblets as a Viscous Drag Reduction Technique.” *AIAA Journal* 21 (4): 485–86. doi:10.2514/3.60126.

- Walsh, M., and A. Lindemann. (1984) Optimization and application of riblets for turbulent drag reduction. In 22nd Aerospace Sciences Meeting, 1–10. Reston, Virginia: American Institute of Aeronautics and Astronautics. doi:10.2514/6.1984-347.
- Walsh, M. J. (1990) Viscous drag reduction in boundary layers: Riblets. AIAA, pp. 203-261. doi:10.2514/5.9781600865978.0203.0261.
- Wenzel, R. N. (1936) Resistance of solid surfaces to wetting by water. *Ind. Eng. Chem.*, 28(8), 988–994. doi:10.1021/ie50320a024
- Winkel, E. S. (2007) High Reynolds number flat plate turbulent boundary layer measurements and skin friction drag reduction with gas or polymer injection. Doctoral thesis, University of Michigan.
- Winkel, White, C. M., and Mungal, M. G. (2008) Mechanics and prediction of turbulent drag reduction with polymer additives. *Annual Review of Fluid Mechanics*, 40(1), pp. 235–256. doi:10.1146/annurev.fluid.40.111406.102156.
- Woolford, B., Prince, J., Maynes, D. and Webb, B. W. (2009) Particle image velocimetry characterization of turbulent channel flow with rib patterned superhydrophobic walls. *Phys. Fluids* 21, 085106
- Wu, C., He, S., Zhu, D., Gu, M. (2006) Numerical simulation of microbubble flow around an axisymmetric body. *Journal of Hydrodynamics* 18(3), pp. 217-222.
- Xu, M., Sun, G. and Kim, C. (2014) Infinite lifetime of underwater superhydrophobic states. *Physical review letters*, 113, 136103. Doi: 10.1103/PhysRevLett.113.136103.
- Yan, Y. Y., N. Gao, and W. Barthlott. (2011) Mimicking Natural Superhydrophobic Surfaces and Grasping the Wetting Process: A Review on Recent Progress in Preparing Superhydrophobic Surfaces. *Advances in Colloid and Interface Science* 169 (2). Elsevier B.V.: 80–105. doi:10.1016/j.cis.2011.08.005.
- Young, A. D. (1939). The calculation of the total skin-friction drags of bodies of revolution at zero incidence. R and M Rept. No. 1874.
- Yu, X., Wang, Y., Huang, C., Wei, Y., and Fang, X. (2015). Experiment and simulation on air layer drag reduction of high-speed underwater axisymmetric projectile. *European Journal of Mechanics B/Fluids*, 52, pp. 45-54.
- Zhang, J., Tian, H., Yao, Hao, P., and Jiang, N. (2015) Mechanisms of drag reduction of superhydrophobic surfaces in a turbulent boundary layer flow. *Exp. Fluids*, 56, 179
- Zhang, S., Ouyang, X., Li, J., Gao, S., Han, S., Liu, L., and Wei, H. (2015) Underwater drag-reducing effect of superhydrophobic submarine model. *Langmuir - American Chemical Society*, 31 (1), pp. 587-593. doi: 10.102/la504451k.

Zhen, N., Handler, R., Zhang, Q., Oeth, C. (2013). Evolution of a hairpin vortex in a shear-thinning fluid governed by a power-law model. *Physics of Fluids*, 25(110703).

Appendix A. Drawings

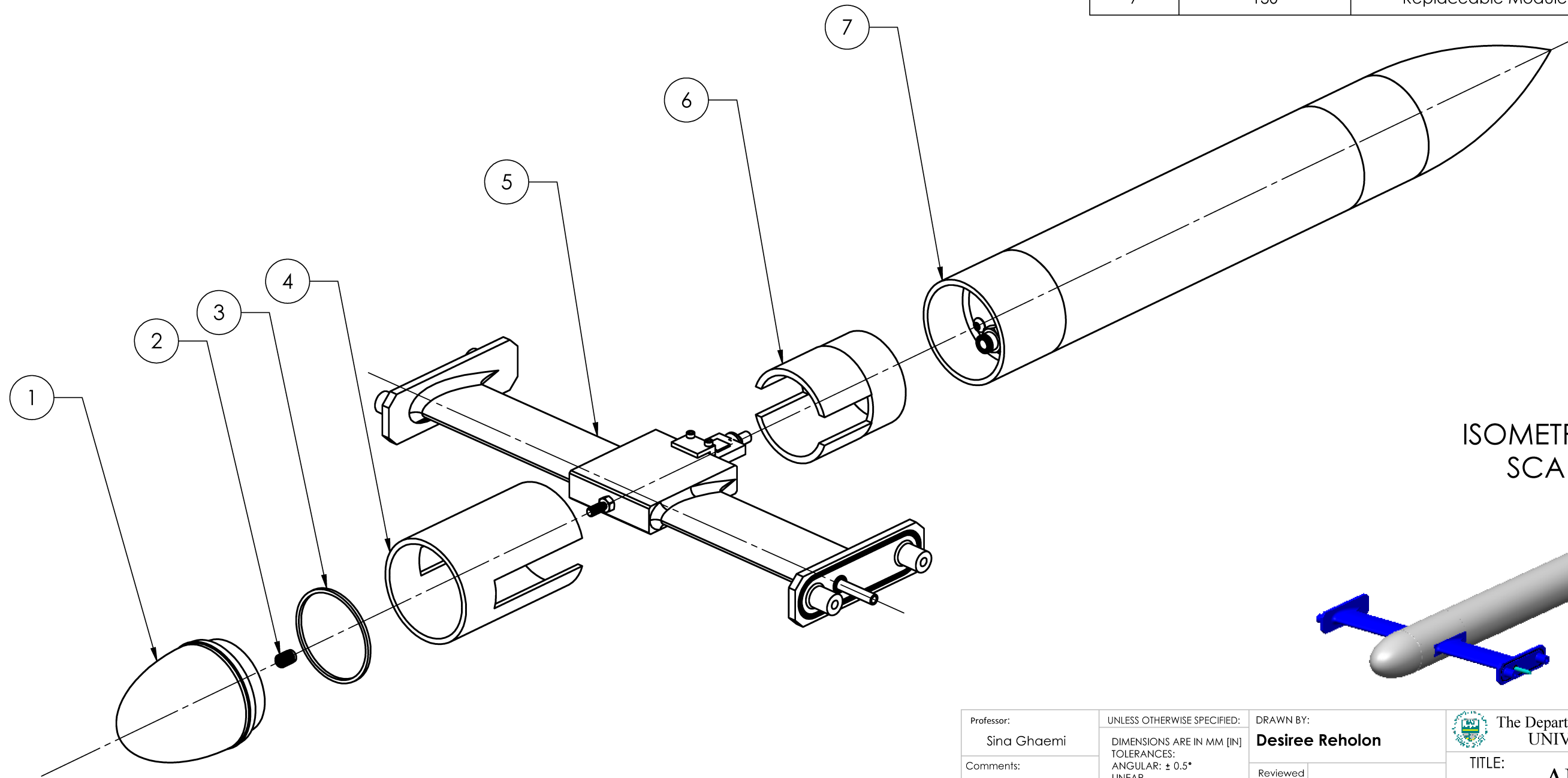


Professor: Sina Ghaemi	UNLESS OTHERWISE SPECIFIED: DIMENSIONS ARE IN MM [IN] TOLERANCES: ANGULAR: $\pm 0.5^\circ$ LINEAR X = ± 0.5 X.X = ± 0.1 X.XX = ± 0.025 SURFACE FINISH μm 0.6 DO NOT SCALE DRAWING	DRAWN BY: Desiree Reholon	The Department of Mechanical Engineering UNIVERSITY OF ALBERTA			
Comments:		Reviewed by:	TITLE: AUV Model Assembly			
	MATERIAL:	Sold Model By Desiree Reholon	Monday, January 15, 2018 2:57:14 PM	SIZE B	Part supplier/manufacturer	REV 0
		DRAWING No.: AUV-100-01	Sunday, May 22, 2016 5:11:12 PM	SCALE: 1:3	Mass: 1052gr	SHEET 1 OF 3

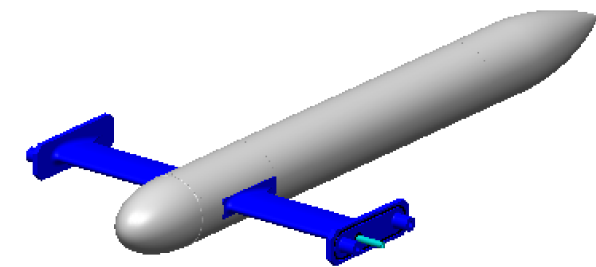
NOTES:

1. For assembly instructions see Drawing No. AUV-100-02
2. O-Rings are identified by the numbering 01X.
3. Screws and Nuts by the numbering 02X.
4. Pressure fittings by the numbering 04X.

ITEM No.	PART No.	DESCRIPTION	QTY.
1	101	Nose	1
2	021	Thread Insert, M4x0.7, length 10mm	1
3	011	O-Ring, Oil-Resistant Buna-N, Dash Number 030	1
4	102	Central Body Section	1
5	120	Hydrofoil & Load Cell Assembly	1
6	103	Sleeve Bearing	1
7	130	Replaceable Module Assembly	1



ISOMETRIC VIEW
SCALE 1:5



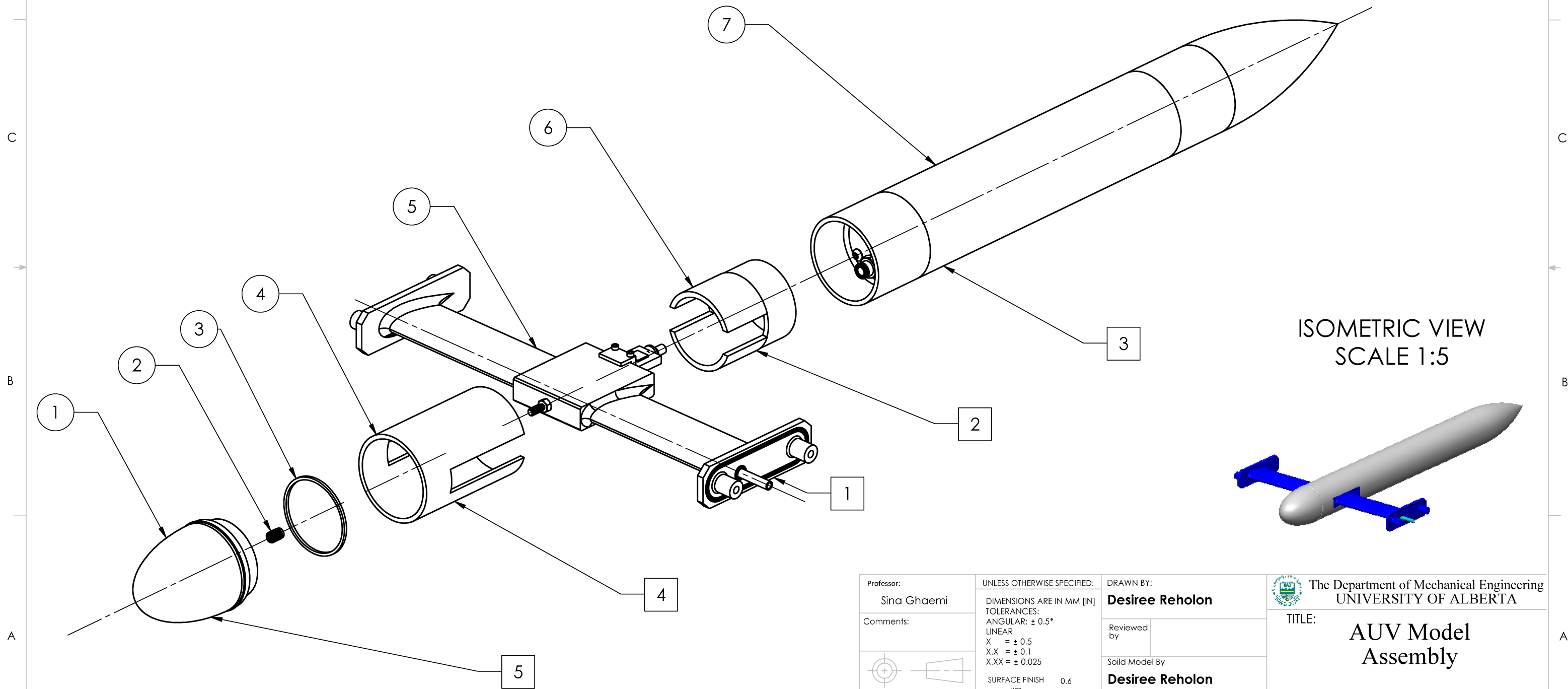
SOLIDWORKS Educational Product. For Instructional Use Only

Professor: Sina Ghaemi	UNLESS OTHERWISE SPECIFIED: DIMENSIONS ARE IN MM [IN] TOLERANCES: ANGULAR: ± 0.5° LINEAR X = ± 0.5 X.X = ± 0.1 X.XX = ± 0.025 SURFACE FINISH 0.6 µm DO NOT SCALE DRAWING	DRAWN BY: Desiree Reholon	The Department of Mechanical Engineering UNIVERSITY OF ALBERTA	
Comments:		Reviewed by:	TITLE: AUV Model Assembly	
MATERIAL:	DRAWING No.: AUV-100-02	Soild Model By: Desiree Reholon	SCALE: 1:2	Part supplier/manufacturer
		Monday, January 15, 2018 2:57:14 PM	REV 0	Mass: 1052gr
		Sunday, May 22, 2016 5:11:12 PM	SHEET 2 OF 3	

ASSEMBLY INSTRUCTIONS (SQUARE IDENTIFIERS):

- 1 Prepare Assemble 120 (item 5).
- 2 Place the sleeve bearing in item 5.
- 3 Prepare Assemble 130 (item 7) without the front seal. The front seal is first attached to the load cell using a thread stud. Then the rest of the assemble 130 is screwed to the front seal.
- 4 Item 3 is press fitted to assembly 120 (item5).
- 5 Item 2 and 3 are installed on item 1, which goes through item 3 and is threaded to the end available at assembly 120 (item 5).

ITEM No.	PART No.	DESCRIPTION	QTY.
1	101	Nose	1
2	021	Thread Insert, M4x0.7, length 10mm	1
3	011	O-Ring, Oil-Resistant Buna-N, Dash Number 030	1
4	102	Central Body Section	1
5	120	Hydrofoil & Load Cell Assembly	1
6	103	Sleeve Bearing	1
7	130	Replaceable Module Assembly	

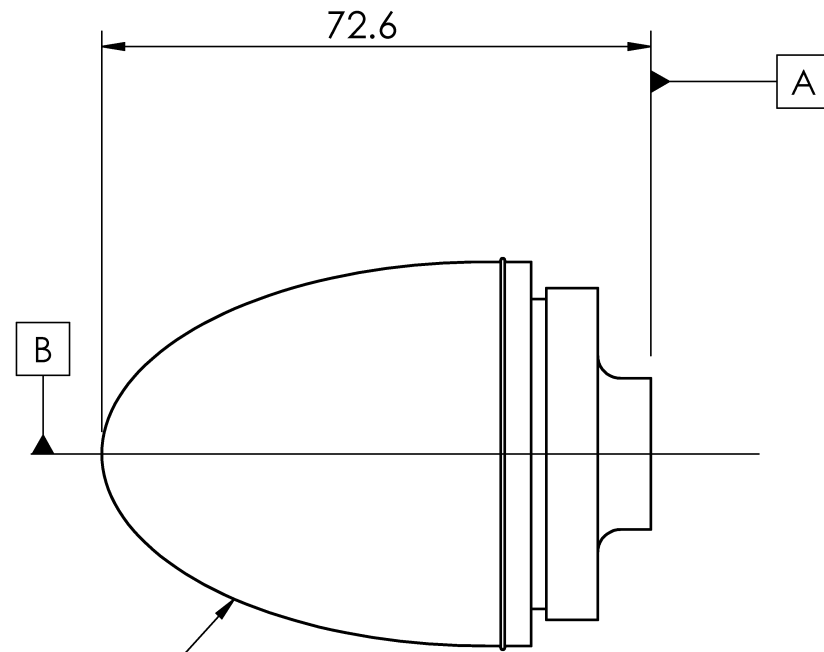


ISOMETRIC VIEW
SCALE 1:5

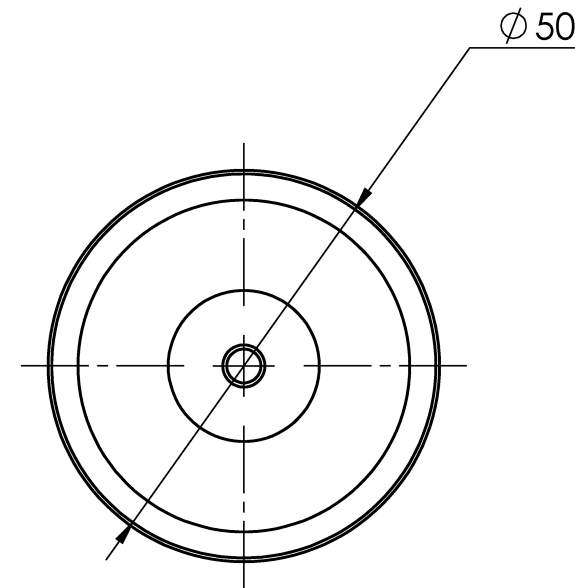
SOLIDWORKS Educational Product. For Instructional Use Only

Professor: Sina Ghaemi	UNLESS OTHERWISE SPECIFIED: DIMENSIONS ARE IN MM [IN] TOLERANCES: ANGULAR: ± 0.5° LINEAR X = ± 0.5 X.X = ± 0.1 X.XX = ± 0.025 SURFACE FINISH µm 0.6 DO NOT SCALE DRAWING	DRAWN BY: Desiree Reholon	The Department of Mechanical Engineering UNIVERSITY OF ALBERTA			
Comments:		Reviewed by:				
MATERIAL:		Sold Model By: Desiree Reholon	TITLE: AUV Model Assembly			
DRAWING No.: AUV-100-03		Monday, January 15, 2018 2:57:14 PM	<table border="1"> <tr> <td>SIZE B</td> <td>Part supplier/manufacturer</td> <td>REV 0</td> </tr> </table>	SIZE B	Part supplier/manufacturer	REV 0
SIZE B	Part supplier/manufacturer	REV 0				
		Sunday, May 22, 2016 5:11:12 PM	<table border="1"> <tr> <td>SCALE: 1:2</td> <td>Mass: 1052gr</td> <td>SHEET 3 OF 3</td> </tr> </table>	SCALE: 1:2	Mass: 1052gr	SHEET 3 OF 3
SCALE: 1:2	Mass: 1052gr	SHEET 3 OF 3				

ISOMETRIC VIEW
SCALE 1:2



Curvature Equation
Semi-ellipse $D=2d$

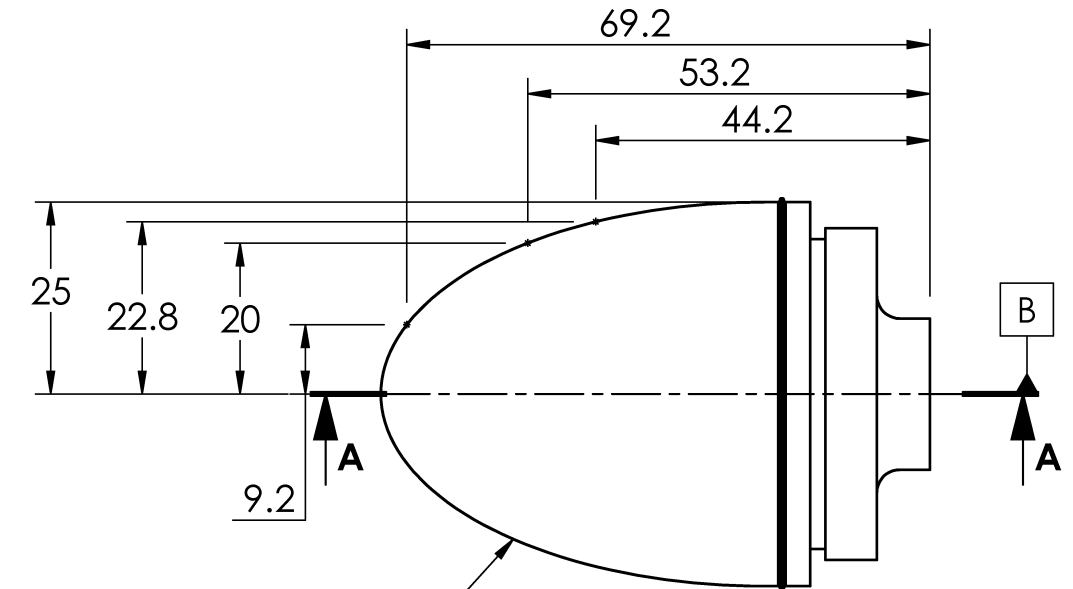
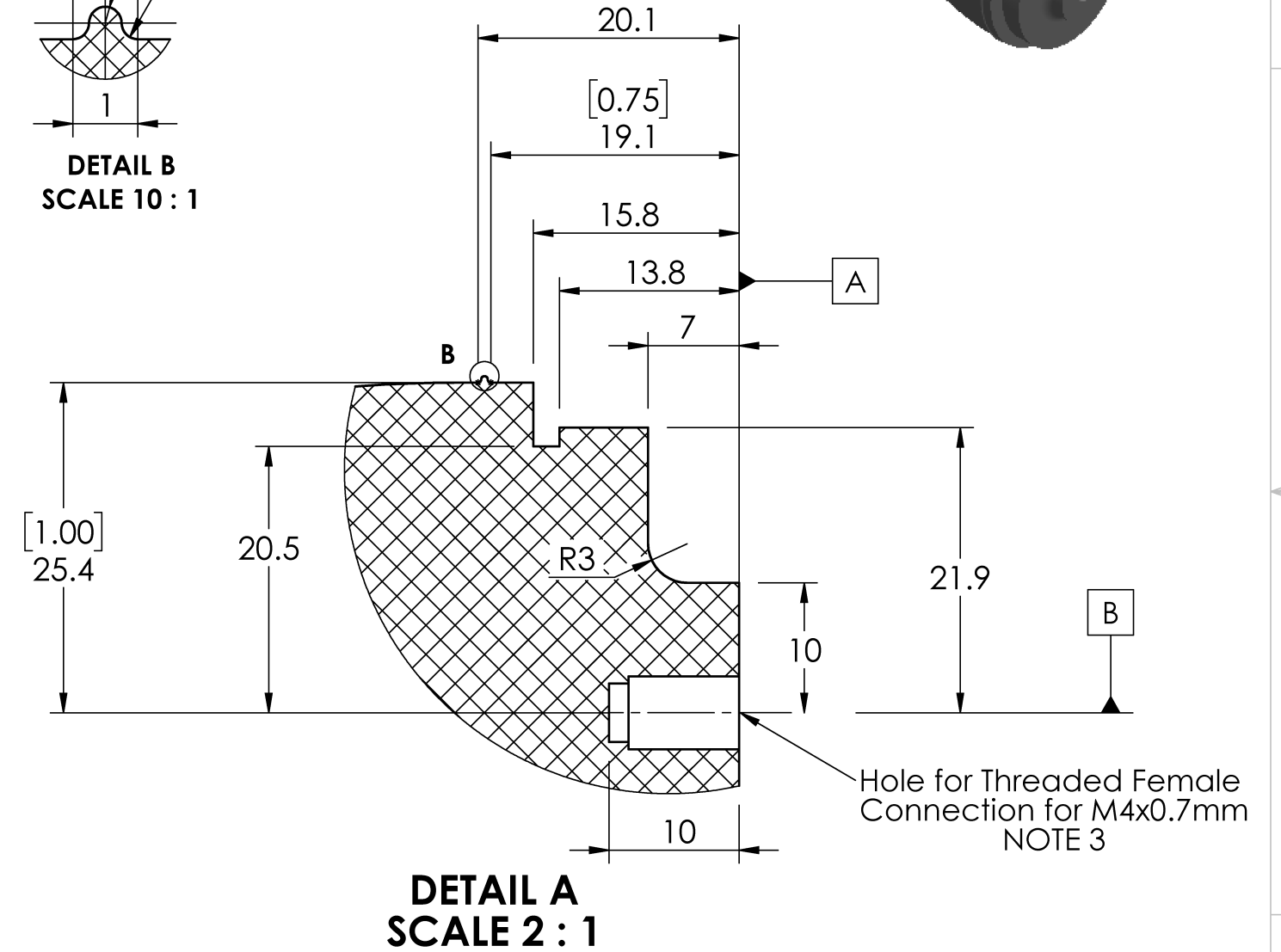
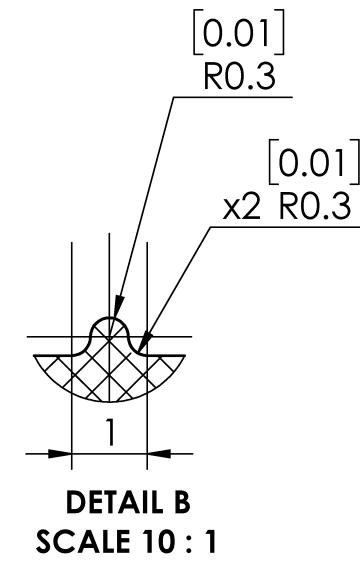
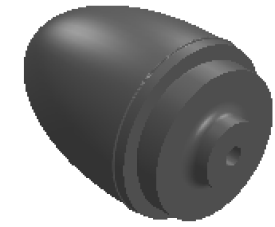


NOTES:

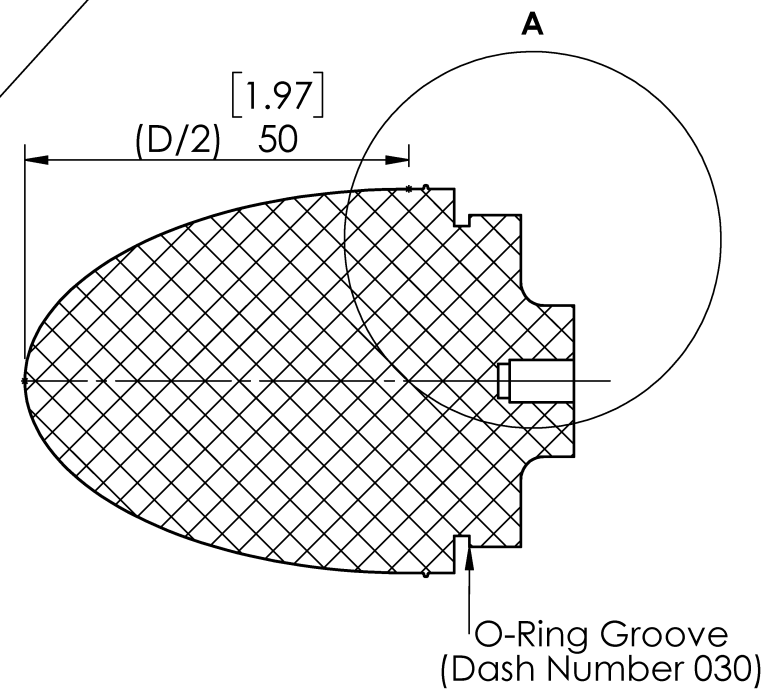
1. Manufacture procedure: 3D Printing.
2. Quantity required: 1.
3. Thread to be made by a tap for plastic (Close-End Hole Threading, M4x0.7, length 10mm).

Professor: Sina Ghaemi	UNLESS OTHERWISE SPECIFIED: DIMENSIONS ARE IN MM [IN] TOLERANCES: ANGULAR: $\pm 0.5^\circ$ LINEAR X = ± 0.5 X.X = ± 0.1 X.XX = ± 0.025	DRAWN BY: Desiree Reholon	The Department of Mechanical Engineering UNIVERSITY OF ALBERTA		
Comments:	SURFACE FINISH 0.6 μm DO NOT SCALE DRAWING	Reviewed by:	TITLE: Nose		
		Soild Model By: Desiree Reholon	SIZE B	Part supplier/manufacturer 101	REV 0
MATERIAL: Ployjet Vero	DRAWING No.: AUV-101-01	Monday, January 15, 2018 4:47:18 PM	SCALE: 1:1	Mass: 98gr	SHEET 1 OF 2
		Thursday, April 07, 2016 8:53:05 AM			

ISOMETRIC VIEW
SCALE 1:2



Curvature Equation
Semi-ellipse $D=2d$



SECTION A-A

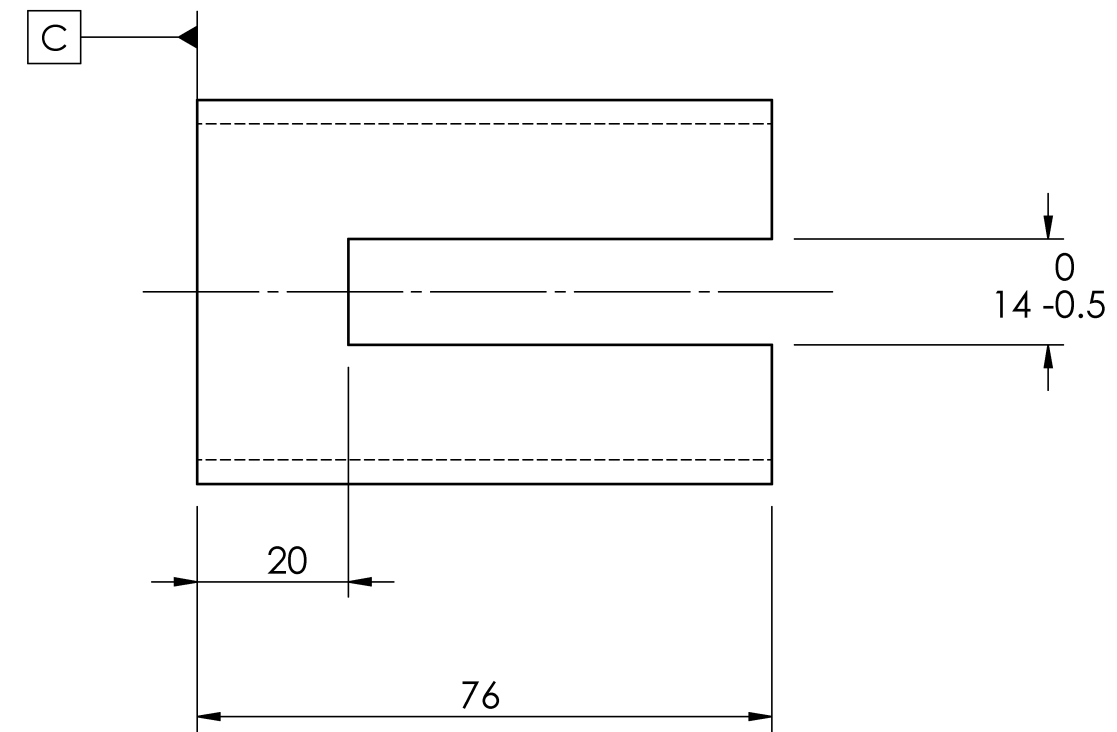
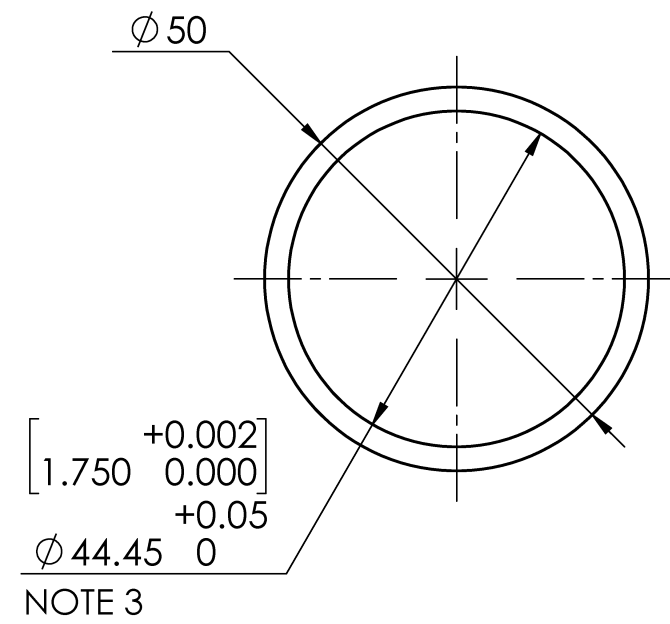
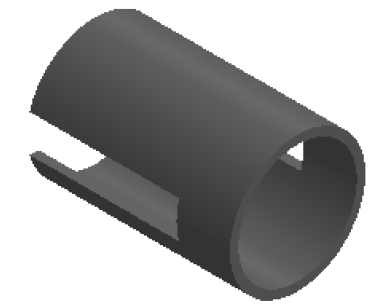
NOTES:

1. Manufacture procedure: 3D Printing.
2. Quantity required: 1.
3. Thread to be made by a tap for plastic (Close-End Hole Threading, M4x0.7, length 10mm).

SOLIDWORKS Educational Product. For Instructional Use Only

Professor: Sina Ghaemi	UNLESS OTHERWISE SPECIFIED: DIMENSIONS ARE IN MM [IN] TOLERANCES: ANGULAR: $\pm 0.5^\circ$ LINEAR X = ± 0.5 X.X = ± 0.1 X.XX = ± 0.025 SURFACE FINISH μm 0.6 DO NOT SCALE DRAWING	DRAWN BY: Desiree Reholon	The Department of Mechanical Engineering UNIVERSITY OF ALBERTA TITLE: Nose
Comments:		Reviewed by:	
		Solid Model By: Desiree Reholon	SIZE B
MATERIAL: Ployjet Vero	DRAWING No.: AUV-101-02	Monday, January 15, 2018 4:47:18 PM Thursday, April 07, 2016 8:53:05 AM	Part supplier/manufacturer 101 REV 0
			SCALE: 1:1 Mass: 98gr SHEET 2 OF 2

ISOMETRIC VIEW
SCALE 1:2

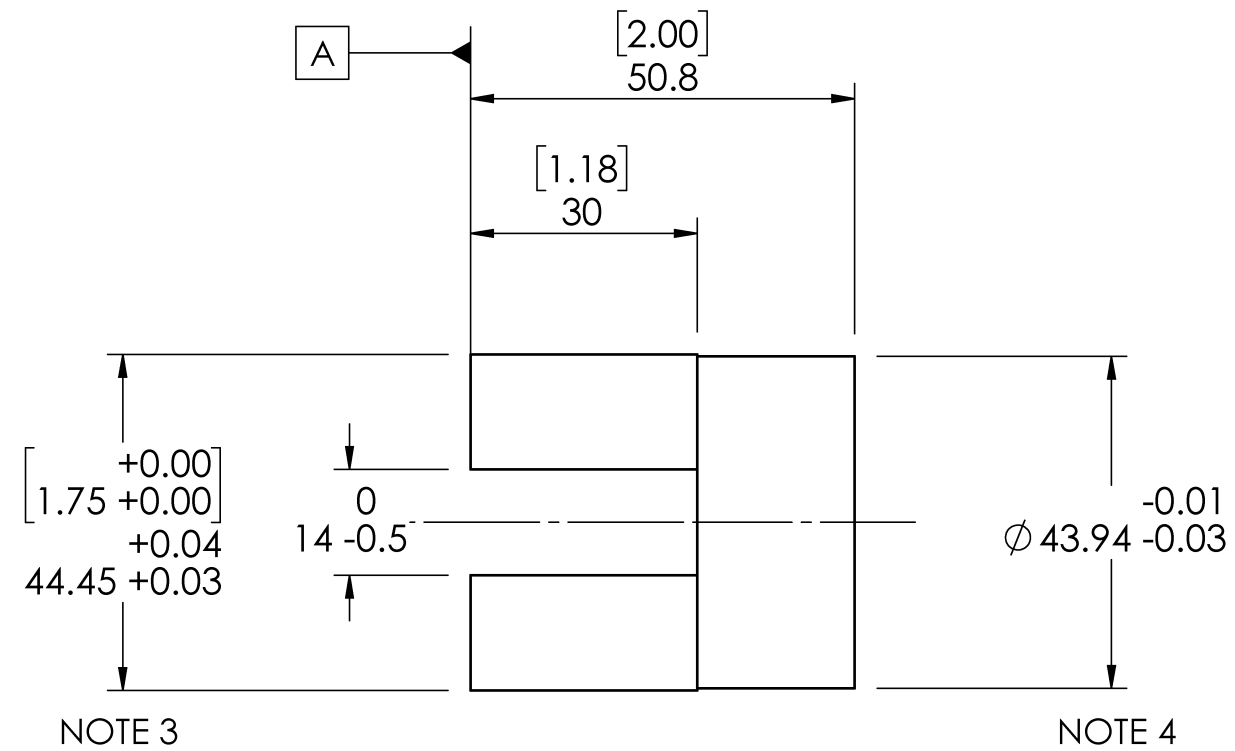
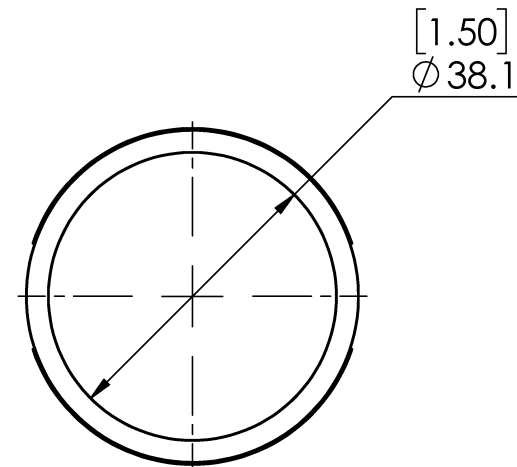
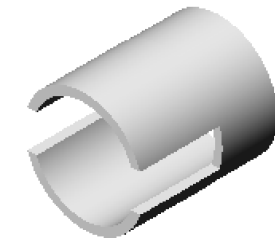


- NOTES:
1. Raw material: 2 OD x 1.75 ID, Aluminum 6061, Round Tube.
 2. Quantity required: 1.
 3. Tolerance considering the O-Ring compression when the part is in contact with the nose (Part No. 101).

SOLIDWORKS Educational Product. For Instructional Use Only

Professor: Sina Ghaemi	UNLESS OTHERWISE SPECIFIED: DIMENSIONS ARE IN MM [IN] TOLERANCES: ANGULAR: ± 0.5° LINEAR X = ± 0.5 X.X = ± 0.1 X.XX = ± 0.025 SURFACE FINISH 0.6 µm DO NOT SCALE DRAWING	DRAWN BY: Desiree Reholon	The Department of Mechanical Engineering UNIVERSITY OF ALBERTA TITLE: Central Body Section						
Comments:		Reviewed by:							
MATERIAL: Aluminum 6061	DRAWING No.: AUV-102-01	Monday, January 15, 2018 4:47:59 PM	Soild Model By: Desiree Reholon						
		Sunday, March 20, 2016 7:56:03 PM	<table border="1"> <tr> <td>SIZE B</td> <td>Part supplier/manufacturer 102</td> <td>REV 0</td> </tr> <tr> <td>SCALE: 1:1</td> <td>Mass: 84gr</td> <td>SHEET 1 OF 1</td> </tr> </table>	SIZE B	Part supplier/manufacturer 102	REV 0	SCALE: 1:1	Mass: 84gr	SHEET 1 OF 1
SIZE B	Part supplier/manufacturer 102	REV 0							
SCALE: 1:1	Mass: 84gr	SHEET 1 OF 1							

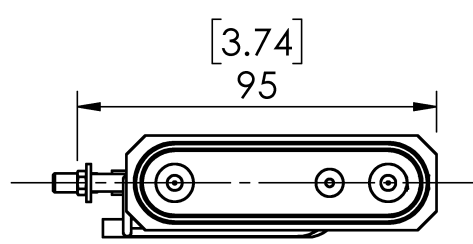
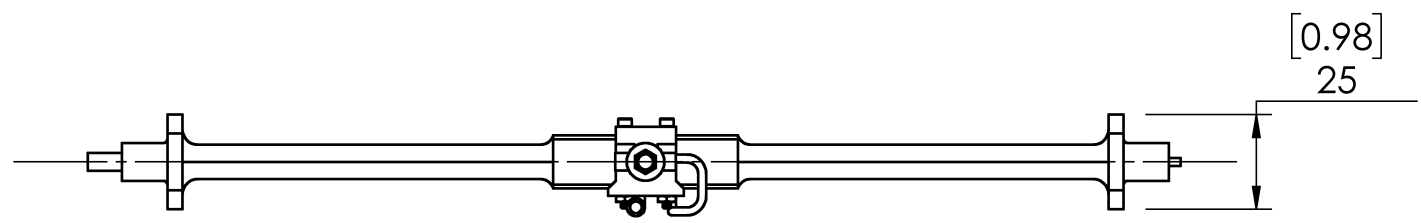
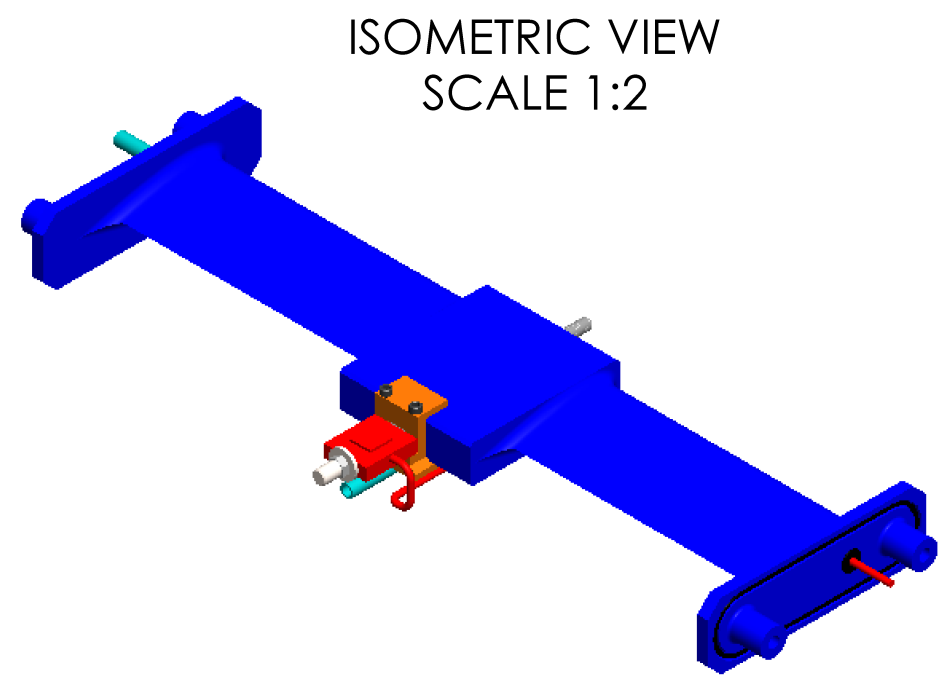
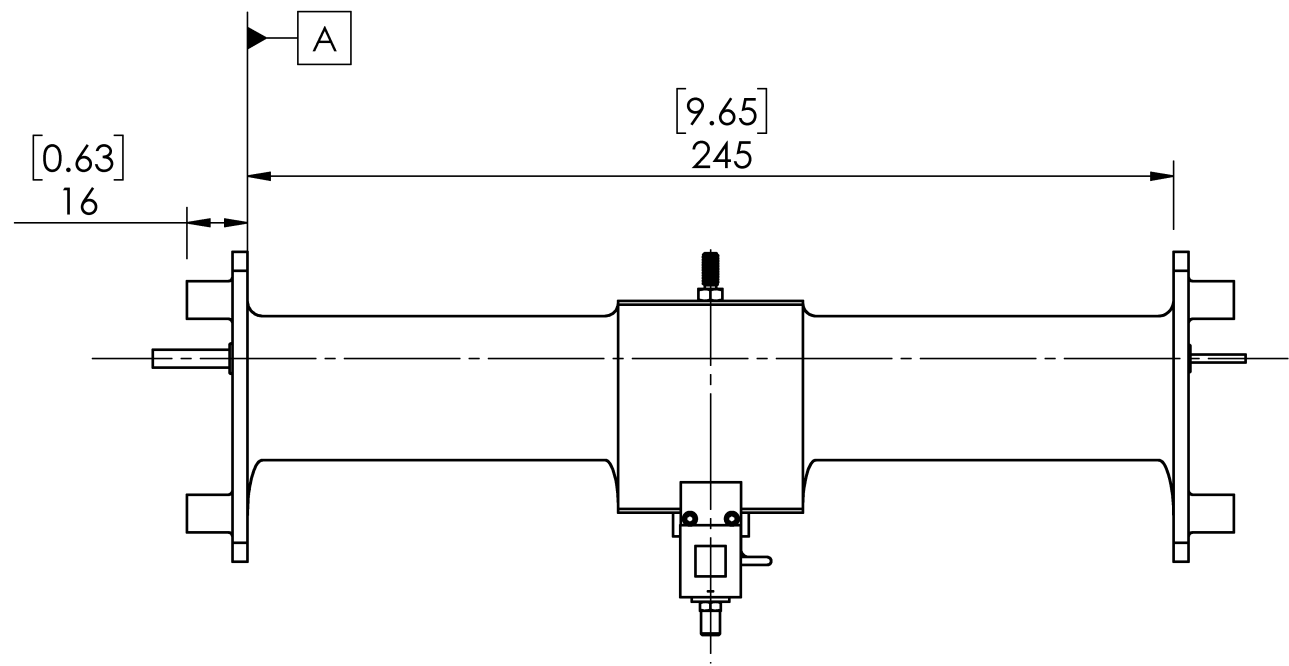
ISOMETRIC VIEW
SCALE 1:2



NOTES:

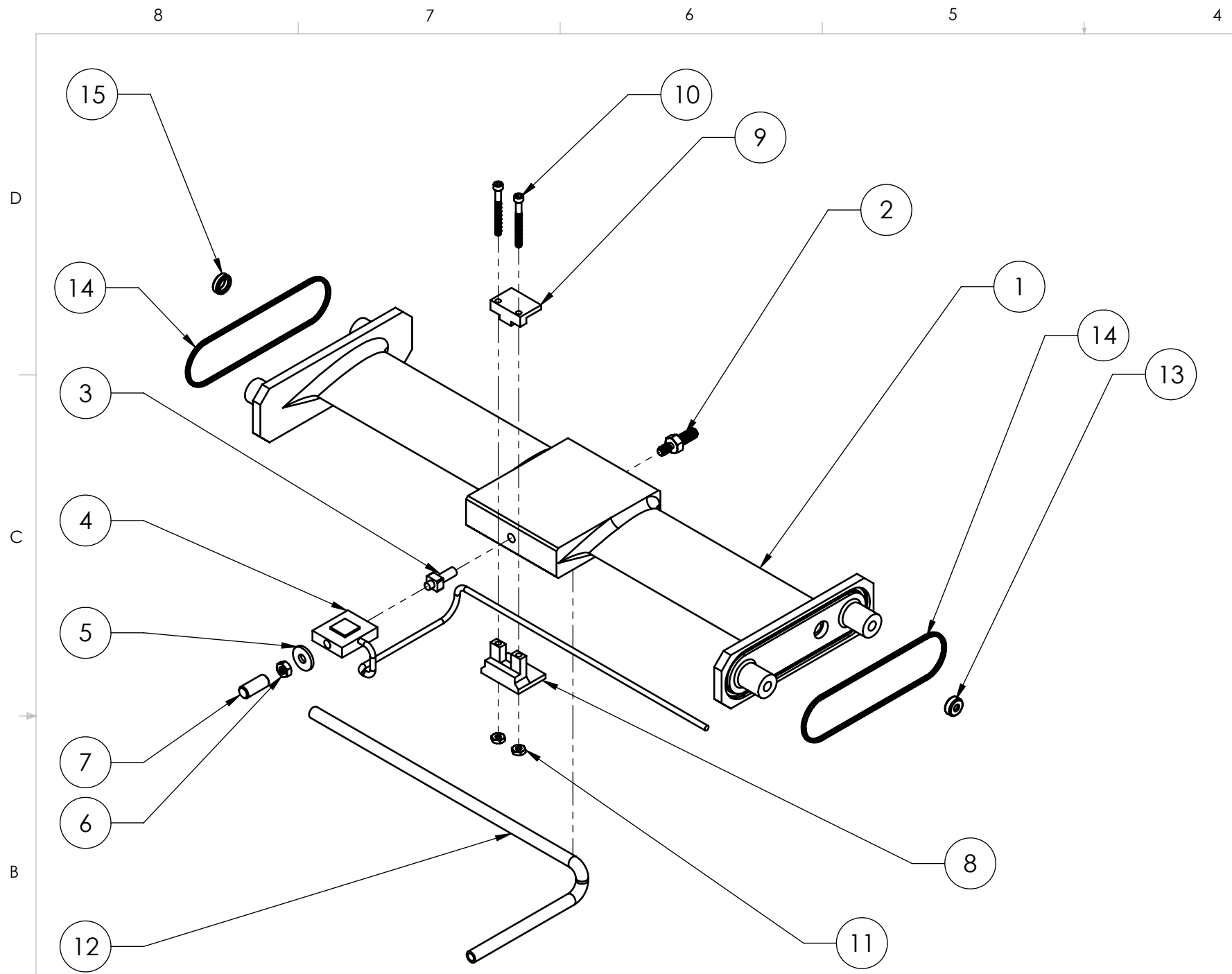
1. Raw material: 1.75 OD x 1.5 ID, Teflon, Round Tube.
2. Quantity required: 1.
3. Tolerance considering the compression of this section with part No. 102.
4. Tolerance considering a loose fit with the part No. 131

Professor: Sina Ghaemi	UNLESS OTHERWISE SPECIFIED: DIMENSIONS ARE IN MM [IN] TOLERANCES: ANGULAR: ± 0.5° LINEAR X = ± 0.5 X.X = ± 0.1 X.XX = ± 0.025 SURFACE FINISH 0.6 µm DO NOT SCALE DRAWING	DRAWN BY: Desiree Reholon	The Department of Mechanical Engineering UNIVERSITY OF ALBERTA TITLE: Sleeve Bearing
Comments:		Reviewed by:	
		Soild Model By: Desiree Reholon	SIZE B
MATERIAL: Teflon		Monday, January 15, 2018 11:04:37 AM	Part supplier/manufacturer 103
DRAWING No.: AUV-103-01		Friday, March 18, 2011 7:38:34 AM	REV 0
			SCALE: 2:1 Mass: 40gr SHEET 1 OF 1



SOLIDWORKS Educational Product. For Instructional Use Only

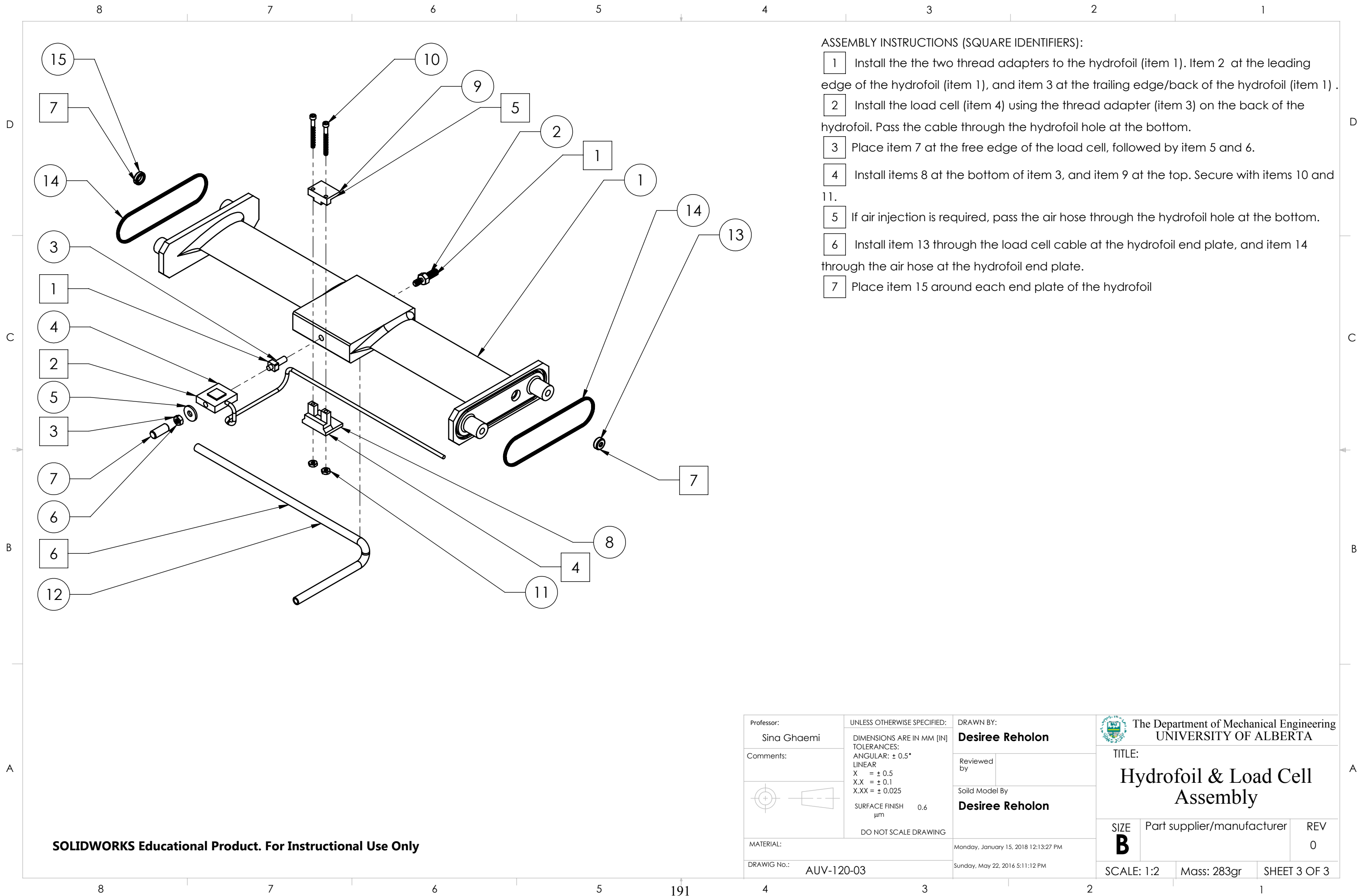
Professor: Sina Ghaemi	UNLESS OTHERWISE SPECIFIED: DIMENSIONS ARE IN MM [IN] TOLERANCES: ANGULAR: $\pm 0.5^\circ$ LINEAR X = ± 0.5 X.X = ± 0.1 X.XX = ± 0.025 SURFACE FINISH 0.6 μm DO NOT SCALE DRAWING	DRAWN BY: Desiree Reholon	The Department of Mechanical Engineering UNIVERSITY OF ALBERTA	
Comments:		Reviewed by:	TITLE: Hydrofoil & Load Cell Assembly	
		Solid Model By: Desiree Reholon	Monday, January 15, 2018 12:13:27 PM	Part supplier/manufacturer
MATERIAL:		Sunday, May 22, 2016 5:11:12 PM	REV 0	REV
DRAWING No.: AUV-120-01			SCALE: 1:2	Mass: 283gr
				SHEET 1 OF 3



ITEM	PART No.	DESCRIPTION	QTY.
1	121	Hydrofoil	1
2	022	Thread Adapter 6-32 to M4 x 0.7 mm Thread Size	1
3	023	Thread Adapter M3x0.5 Male to #6-32-2A Male	1
4	125	LSB210 Submersible Jr S-Beam Load Cell	1
5	024	Washer (M3)	1
6	025	Hex. Nut, M3	1
7	026	Threaded Stud, M3 x 12.7mm	1
8	122	Load Cell Support, Bottom	1
9	123	Load Cell Support, Top	1
10	027	Screw, 0-80 x 19 mm	2
11	028	Hexagonal Nuts (0-80)	2
12	031	Flexible High-Pressure Nylon Tubing Semi-Clear, 0.109" ID, 3/16" OD	1
13	012	O-Ring, 1/16 Fractional Width, Dash Number 008 (9452K317)	1
14	013	O-Ring, 3/32 Fractional Width, Dash Number 103 (9452K16)	1
15	014	O-Ring, 1/16, Fractional Width, Dash Number 034 (5308T143)	2

SOLIDWORKS Educational Product. For Instructional Use Only

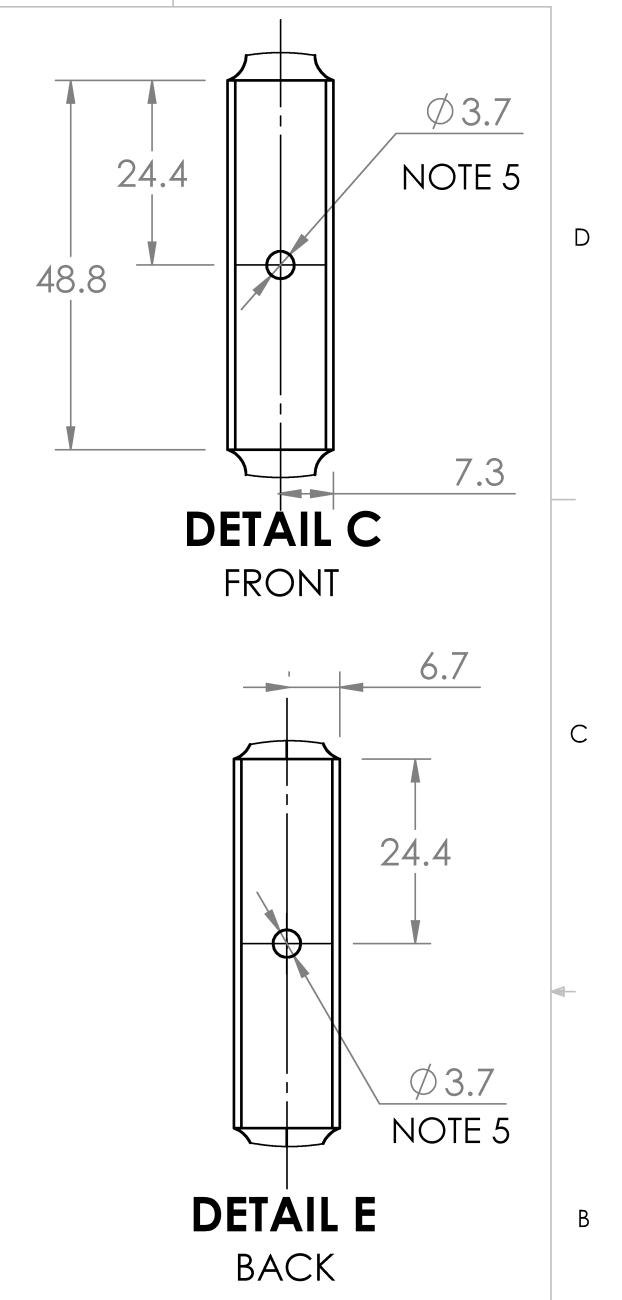
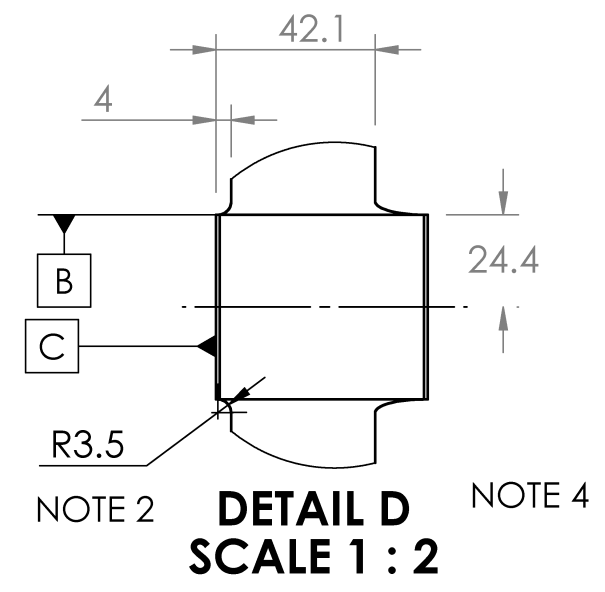
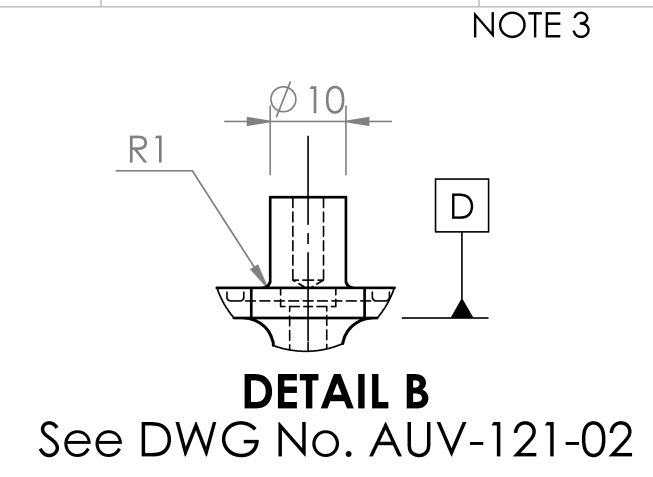
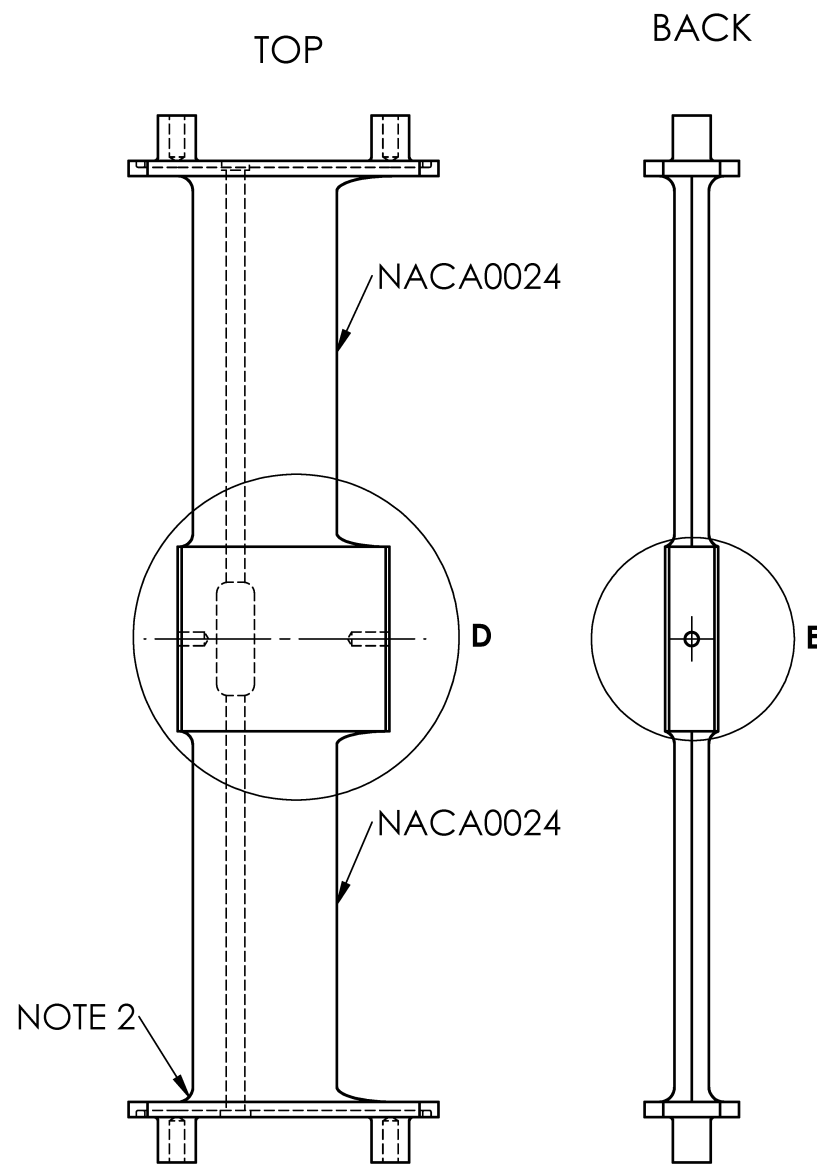
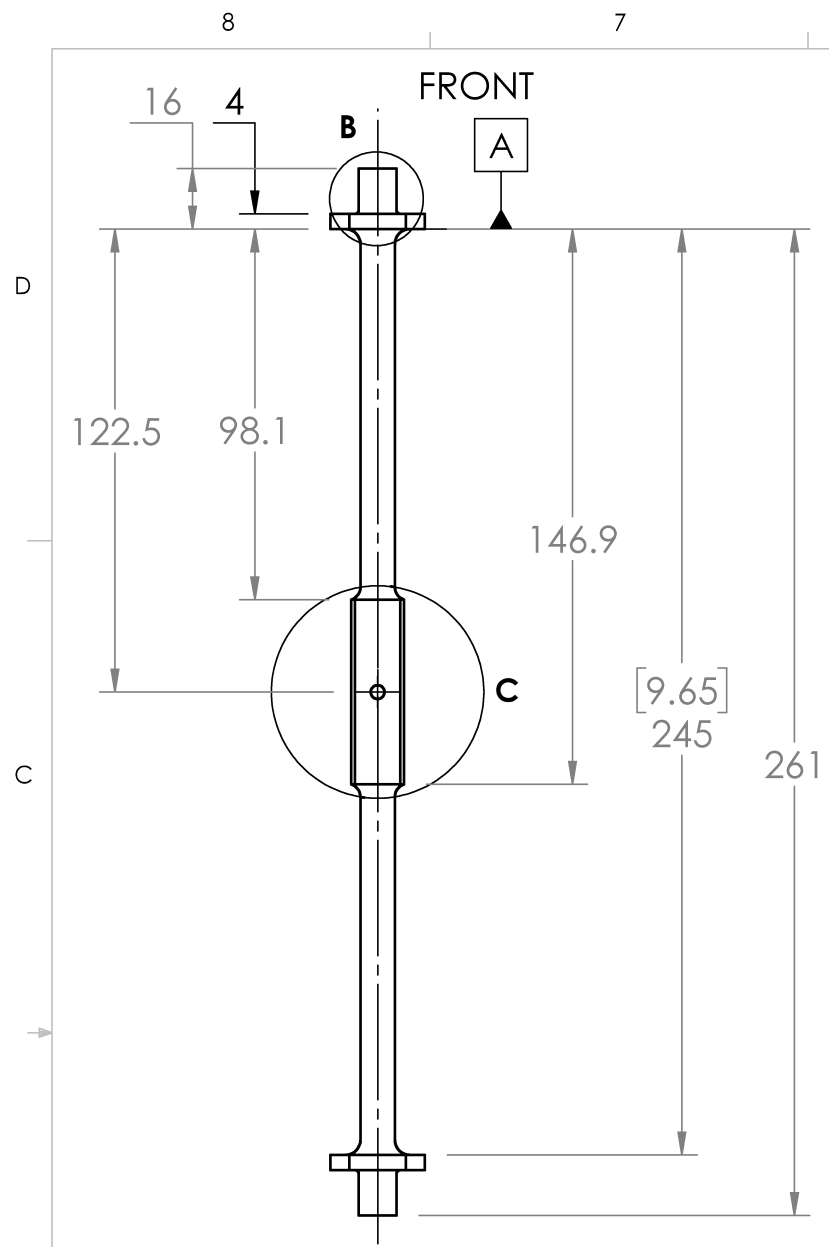
Professor: Sina Ghaemi	UNLESS OTHERWISE SPECIFIED: DIMENSIONS ARE IN MM [IN] TOLERANCES: ANGULAR: ± 0.5° LINEAR X = ± 0.5 X.X = ± 0.1 X.XX = ± 0.025 SURFACE FINISH µm 0.6 DO NOT SCALE DRAWING	DRAWN BY: Desiree Reholon	The Department of Mechanical Engineering UNIVERSITY OF ALBERTA	
Comments:		Reviewed by:	TITLE: Hydrofoil & Load Cell Assembly	
		Solid Model By: Desiree Reholon	SIZE B	Part supplier/manufacturer
MATERIAL:		Monday, January 15, 2018 12:13:27 PM	REV 0	
DRAWING No.: AUV-120-02		Sunday, May 22, 2016 5:11:12 PM	SCALE: 1:2	Mass: 283gr
				SHEET 2 OF 3



ASSEMBLY INSTRUCTIONS (SQUARE IDENTIFIERS):

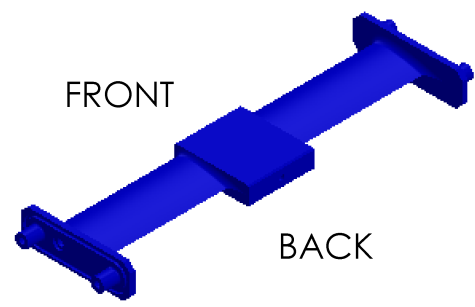
- 1 Install the the two thread adapters to the hydrofoil (item 1). Item 2 at the leading edge of the hydrofoil (item 1), and item 3 at the trailing edge/back of the hydrofoil (item 1).
- 2 Install the load cell (item 4) using the thread adapter (item 3) on the back of the hydrofoil. Pass the cable through the hydrofoil hole at the bottom.
- 3 Place item 7 at the free edge of the load cell, followed by item 5 and 6.
- 4 Install items 8 at the bottom of item 3, and item 9 at the top. Secure with items 10 and 11.
- 5 If air injection is required, pass the air hose through the hydrofoil hole at the bottom.
- 6 Install item 13 through the load cell cable at the hydrofoil end plate, and item 14 through the air hose at the hydrofoil end plate.
- 7 Place item 15 around each end plate of the hydrofoil

Professor: Sina Ghaemi	UNLESS OTHERWISE SPECIFIED: DIMENSIONS ARE IN MM [IN] TOLERANCES: ANGULAR: ± 0.5° LINEAR X = ± 0.5 X.X = ± 0.1 X.XX = ± 0.025 SURFACE FINISH 0.6 µm DO NOT SCALE DRAWING	DRAWN BY: Desiree Reholon	The Department of Mechanical Engineering UNIVERSITY OF ALBERTA TITLE: Hydrofoil & Load Cell Assembly
Comments:		Reviewed by:	
MATERIAL:		Sold Model By: Desiree Reholon	SIZE B
DRAWING No.: AUV-120-03		Monday, January 15, 2018 12:13:27 PM	Part supplier/manufacture
		Sunday, May 22, 2016 5:11:12 PM	REV 0
			SCALE: 1:2
			Mass: 283gr
			SHEET 3 OF 3



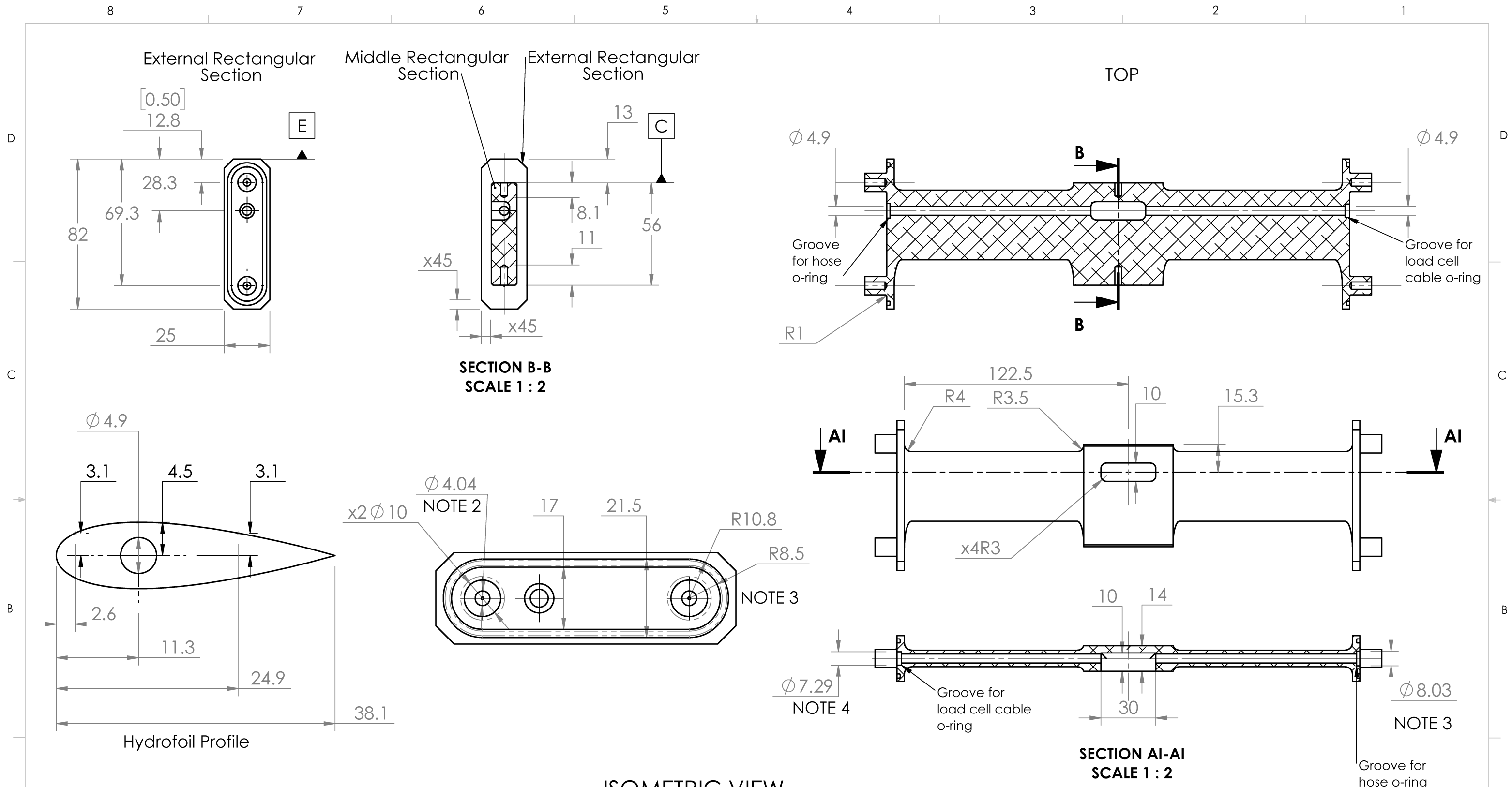
- NOTES:
1. Manufacture procedure: CNC/Milling. Raw material: 6061, T6 Aluminum. Anodizing process is required.
 2. Fillet all around the hydrofoil (NACA 0024) section.
 3. O-Ring Groove.
 4. Screw clearance hole for #10-32, all through. Normal Fit.
 5. Threaded Female Connection for #6-32, 7mm length for hole in Detail C and 10mm for hole in Detail E. Close Fit.

ISOMETRIC VIEW
SCALE 1:4



SOLIDWORKS Educational Product. For Instructional Use Only

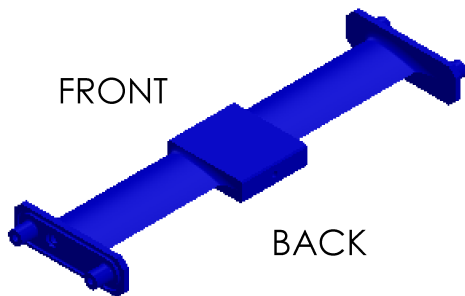
Professor: Sina Ghaemi	UNLESS OTHERWISE SPECIFIED: DIMENSIONS ARE IN MM [IN] TOLERANCES: ANGULAR: ± 0.5° LINEAR X = ± 0.5 X.X = ± 0.1 X.XX = ± 0.025 SURFACE FINISH µm 0.6 DO NOT SCALE DRAWING	DRAWN BY: Desiree Reholon	The Department of Mechanical Engineering UNIVERSITY OF ALBERTA TITLE: Hydrofoil						
Comments:	Reviewed by:	Soild Model By: Desiree Reholon							
MATERIAL: Aluminum 6061with anodizing	DRAWING No.: AUV-121-01 (1/2)	Tuesday, August 15, 2017 12:24:39 PM	<table border="1"> <tr> <td>SIZE B</td> <td>Part supplier/manufacturer 121</td> <td>REV 0</td> </tr> <tr> <td>SCALE: 1:2</td> <td>Mass: 259gr</td> <td>SHEET 1 OF 2</td> </tr> </table>	SIZE B	Part supplier/manufacturer 121	REV 0	SCALE: 1:2	Mass: 259gr	SHEET 1 OF 2
SIZE B	Part supplier/manufacturer 121	REV 0							
SCALE: 1:2	Mass: 259gr	SHEET 1 OF 2							



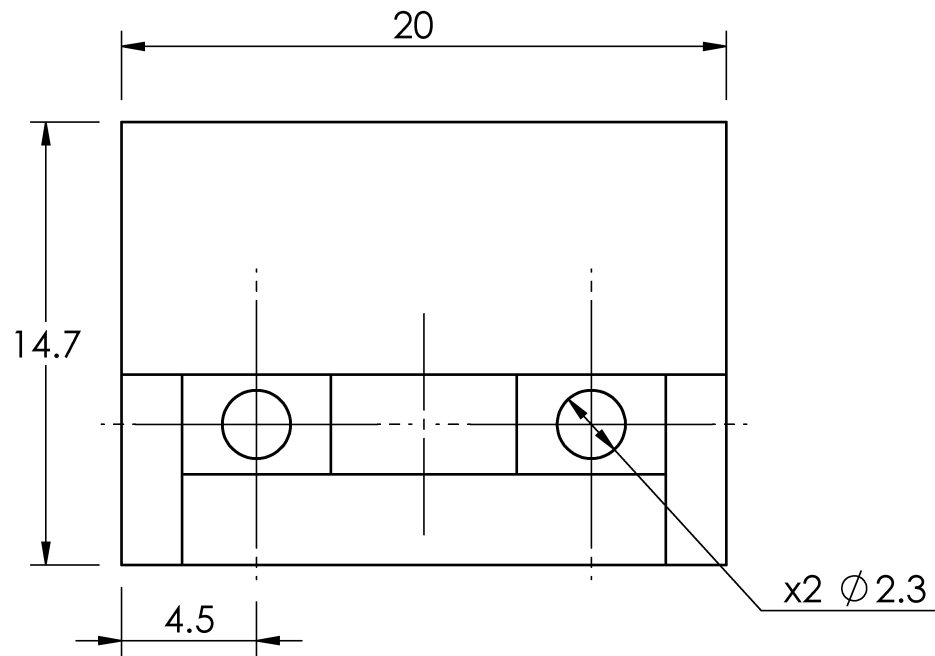
- NOTES:
1. Threaded Female Connection for #6-32, Close Fit.
 2. Threaded Female Connection for #10-32, 12mm length.
 3. O-ring groove, depth 1.75mm.
 4. O-ring groove, depth 2.5mm.

SOLIDWORKS Educational Product. For Instructional Use Only

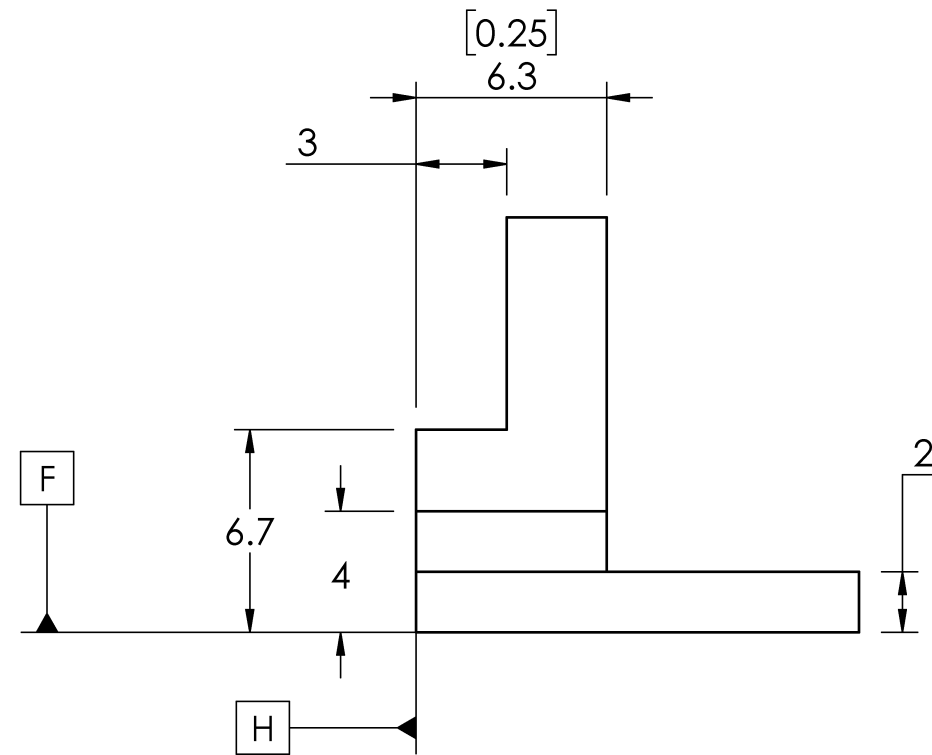
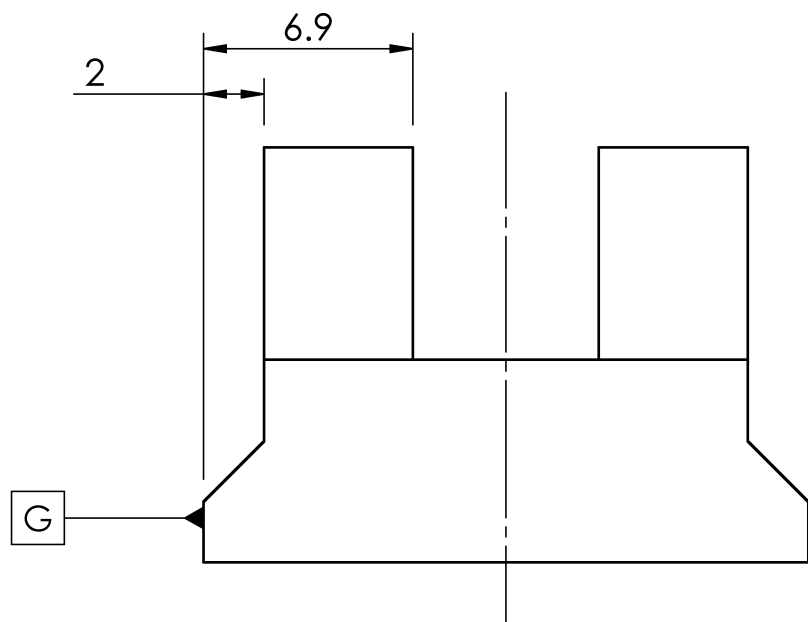
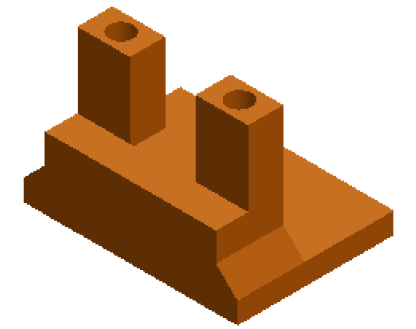
ISOMETRIC VIEW
SCALE 1:4



Professor: Sina Ghaemi	UNLESS OTHERWISE SPECIFIED: DIMENSIONS ARE IN MM [IN] TOLERANCES: ANGULAR: $\pm 0.5^\circ$ LINEAR X = ± 0.5 X.X = ± 0.1 X.XX = ± 0.025 SURFACE FINISH μm 0.6 DO NOT SCALE DRAWING	DRAWN BY: Desiree Reholon	The Department of Mechanical Engineering UNIVERSITY OF ALBERTA TITLE: Hydrofoil						
Comments:	Reviewed by:	Soild Model By: Desiree Reholon							
MATERIAL: Aluminum 6061 with anodizing	DRAWING No.: AUV-121-02 (2/2)	Tuesday, August 15, 2017 12:24:39 PM	<table border="1"> <tr> <td>SIZE</td> <td>Part supplier/manufacturer</td> <td>REV</td> </tr> <tr> <td>B</td> <td>121</td> <td>0</td> </tr> </table>	SIZE	Part supplier/manufacturer	REV	B	121	0
SIZE	Part supplier/manufacturer	REV							
B	121	0							
SCALE: 1:2		Mass: 259gr	SHEET 2 OF 2						


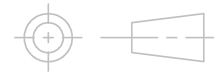


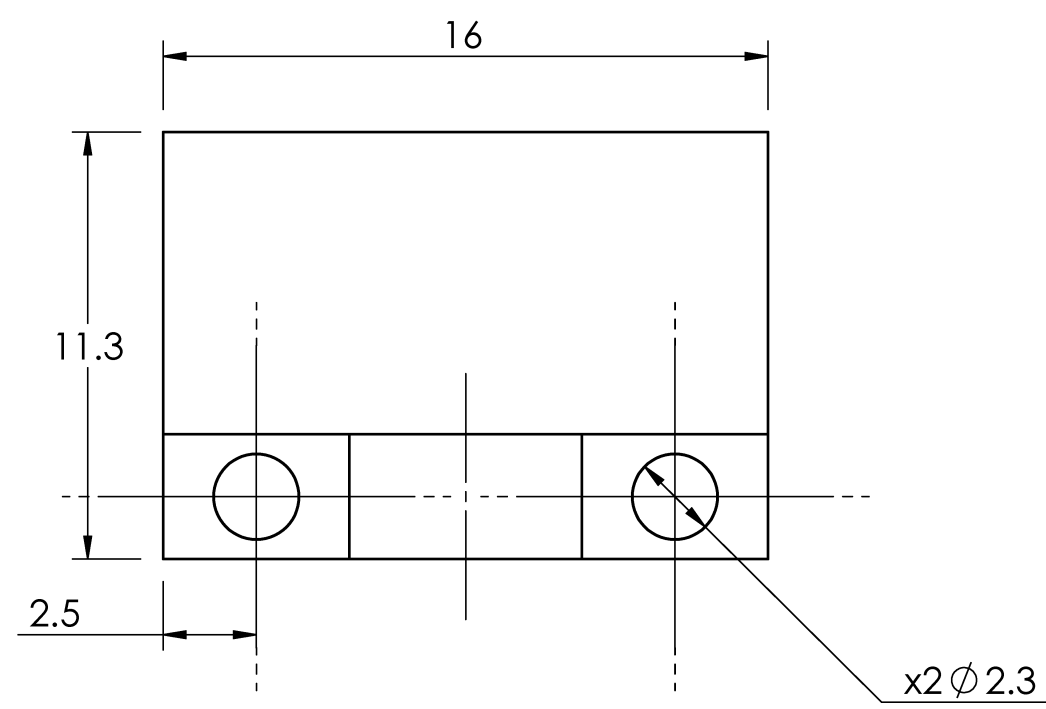
ISOMETRIC VIEW
SCALE 2:1



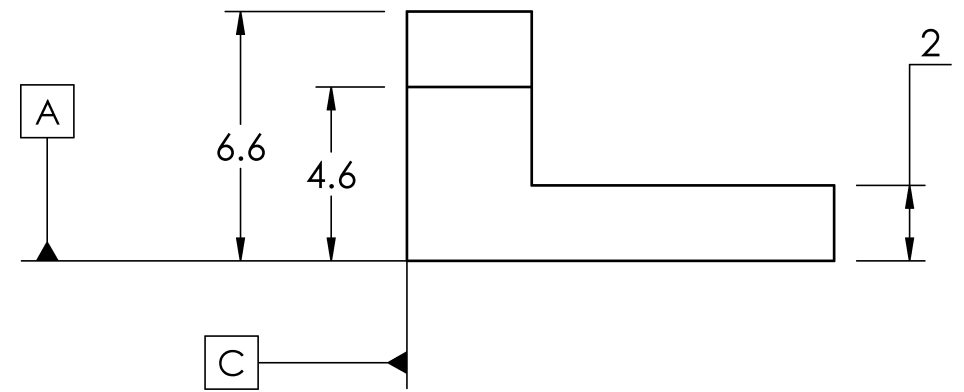
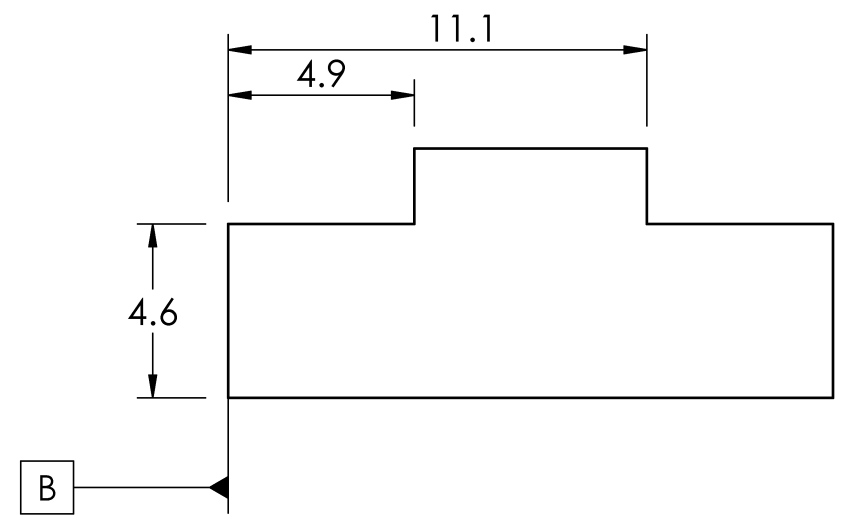
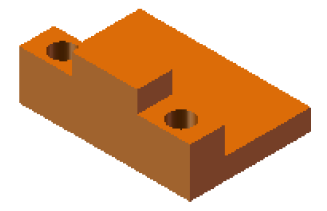
- NOTES:
1. Manufacture procedure: 3D printed, ABS
 2. Hole, all through

SOLIDWORKS Educational Product. For Instructional Use Only

Professor: Sina Ghaemi	UNLESS OTHERWISE SPECIFIED: DIMENSIONS ARE IN MM [IN] TOLERANCES: ANGULAR: $\pm 0.5^\circ$ LINEAR X = ± 0.5 X.X = ± 0.1 X.XX = ± 0.025 SURFACE FINISH μm 0.6 DO NOT SCALE DRAWING	DRAWN BY: Desiree Reholon	 The Department of Mechanical Engineering UNIVERSITY OF ALBERTA
Comments:		Reviewed by:	
	MATERIAL: ABS	Soild Model By: Desiree Reholon	SIZE B
DRAWING No.: AUV-122-01	Monday, January 15, 2018 11:44:49 AM	Part supplier/manufacturer 122	REV 0
	Wednesday, February 22, 2017 3:23:28 PM	SCALE: 4:1	Mass: 1.22gr
			SHEET 1 OF 1



ISOMETRIC VIEW
SCALE 2:1



- NOTES:
1. Manufacture procedure: 3D printed, ABS
 2. Hole, all through

SOLIDWORKS Educational Product. For Instructional Use Only

Professor: Sina Ghaemi	UNLESS OTHERWISE SPECIFIED: DIMENSIONS ARE IN MM [IN] TOLERANCES: ANGULAR: ± 0.5° LINEAR X = ± 0.5 X.X = ± 0.1 X.XX = ± 0.025	DRAWN BY: Desiree Reholon	The Department of Mechanical Engineering UNIVERSITY OF ALBERTA TITLE: Load Cell Support Top			
Comments:		Reviewed by:				
		SURFACE FINISH µm 0.6	Soild Model By Desiree Reholon	SIZE B	Part supplier/manufacturer 123	REV 0
	MATERIAL: ABS	DO NOT SCALE DRAWING	Monday, January 15, 2018 11:44:06 AM	SCALE: 4:1	Mass: 0.50gr	SHEET 1 OF 1
DRAWIG No.: AUV-123-01		Wednesday, February 22, 2017 5:28:12 PM				

8 7 6 5 4 3 2 1

D
C
B
A

D
C
B
A

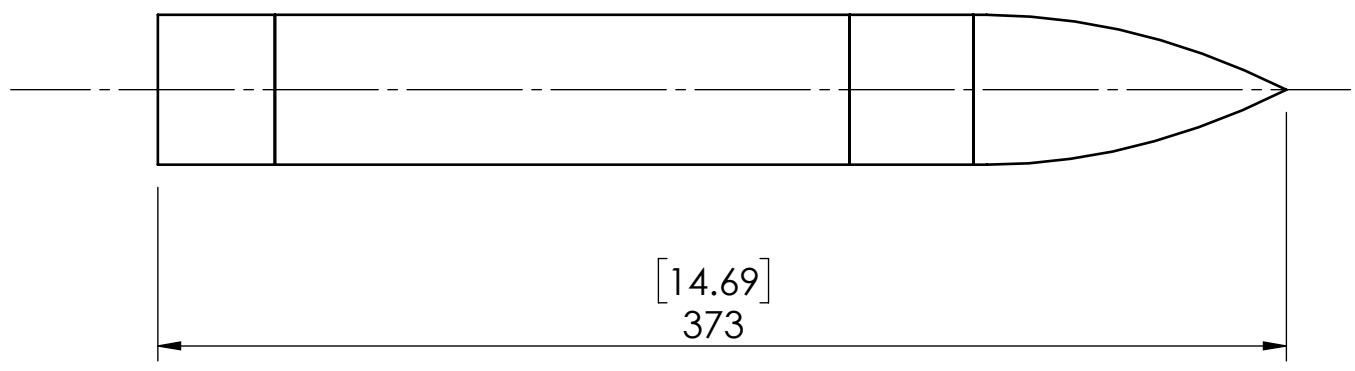
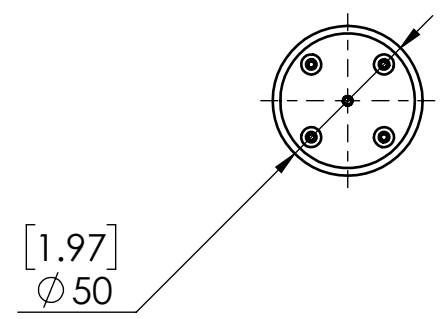
8 7 6 5 4 3 2 1

8 7 6 5 4 3 2 1

D

D

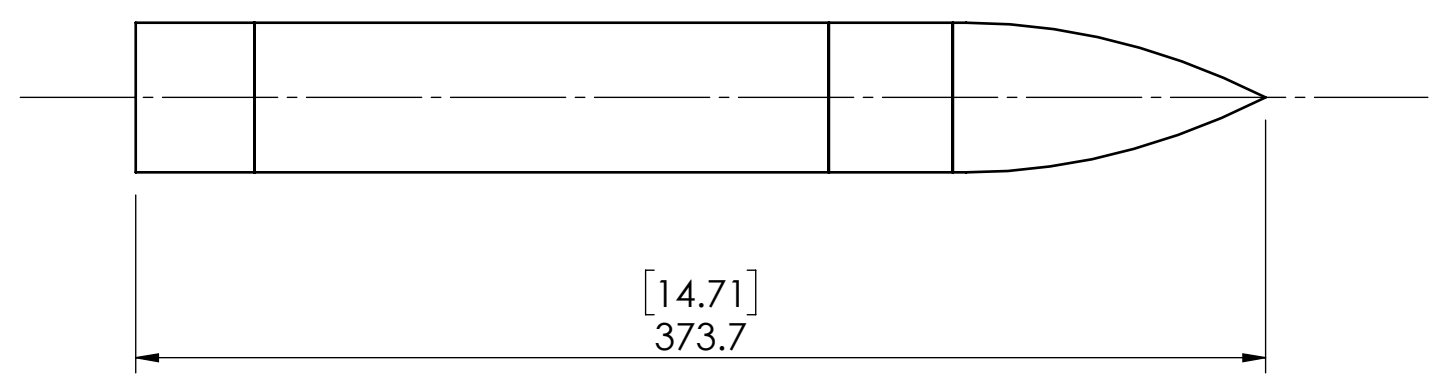
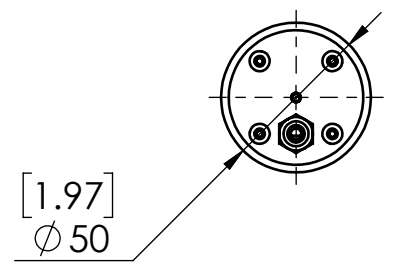
AUV-131a



C

C

AUV-131b
(For Air Injection)



B

B

A

A

SOLIDWORKS Educational Product. For Instructional Use Only

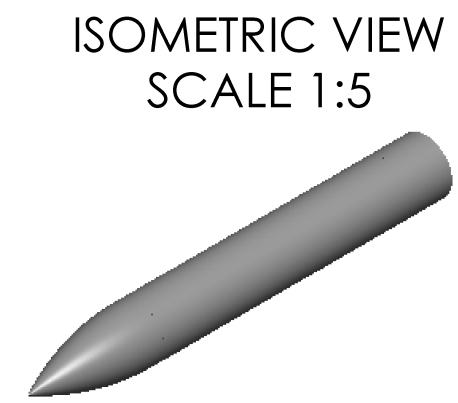
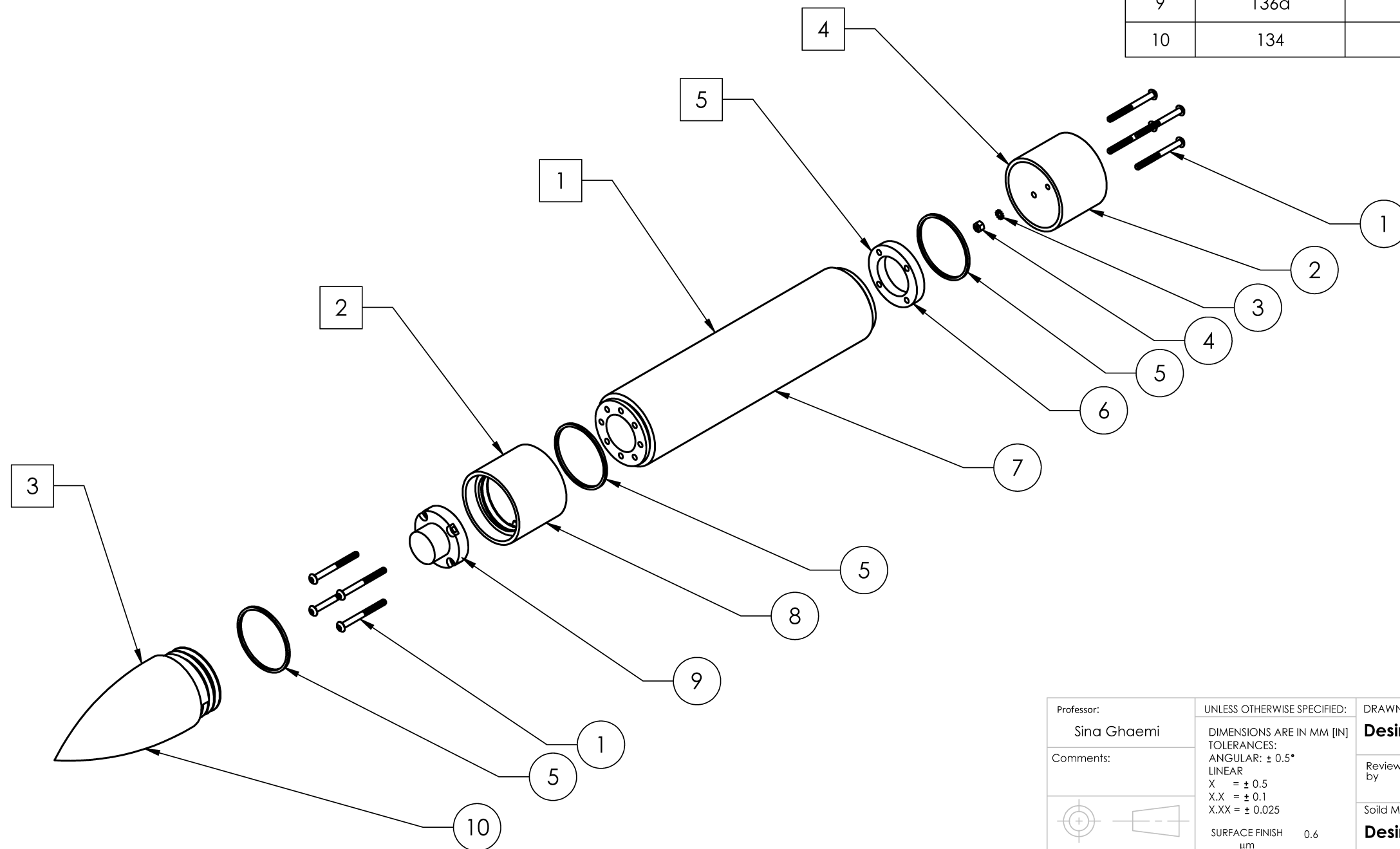
Professor: Sina Ghaemi	UNLESS OTHERWISE SPECIFIED: DIMENSIONS ARE IN MM [IN] TOLERANCES: ANGULAR: ± 0.5° LINEAR X = ± 0.5 X.X = ± 0.1 X.XX = ± 0.025 SURFACE FINISH 0.6 µm DO NOT SCALE DRAWING	DRAWN BY: Desiree Reholon	The Department of Mechanical Engineering UNIVERSITY OF ALBERTA TITLE: Replaceable Module Assembly
Comments:		Reviewed by:	
		Soild Model By Desiree Reholon	Part supplier/manufacturer 130
MATERIAL:		Monday, January 15, 2018 4:42:25 PM	REV 0
DRAWING No.: AUV-130a/b-01		Sunday, May 22, 2016 5:11:12 PM	SCALE: 1:2.5 Mass: SHEET 1 OF 3

8 7 6 5 4 3 2 1

ASSEMBLY INSTRUCTIONS (SQUARE IDENTIFIERS):

- 1 Install the o-rings (items 011) on the grooves available for it on item 132a and 134.
- 2 Place item 8 in item 7, followed by item 9 inside item 8. Align all the holes and fix them with the screws (item 1).
- 3 Install item 10 to item 8.
- 4 Attach item 2 to sub-assembly AUV-120 with items 3 and 4, using the torque wrench.
- 5 Place item 6 over item 7 and align the holes, to finally attach the front seal to item 7 with the screws (item 1).

ITEM	PART No.	DESCRIPTION	QTY.
1	029	Sealing Pan Head Phillips Machine Screw. Buna-N O-Ring, 6-32 Thread, 1-1/4" Length	8
2	131a	Front Seal	1
3	030	Lock Washer M3	1
4	031	Class 04 Steel Thin Hex Nut - DIN 439B. Zinc Plated, M3x0.5 Thread Size, 5.5mm Wide, 1.8mm High	1
5	011	O-Ring Oil-Resistant Buna-N, Dash Number 030	2
6	135a	Front Balance Weigh	1
7	132a	Control Replaceable Module	1
8	133	Back seal	1
9	136a	Back Balance Weigh	1
10	134	Tail	1



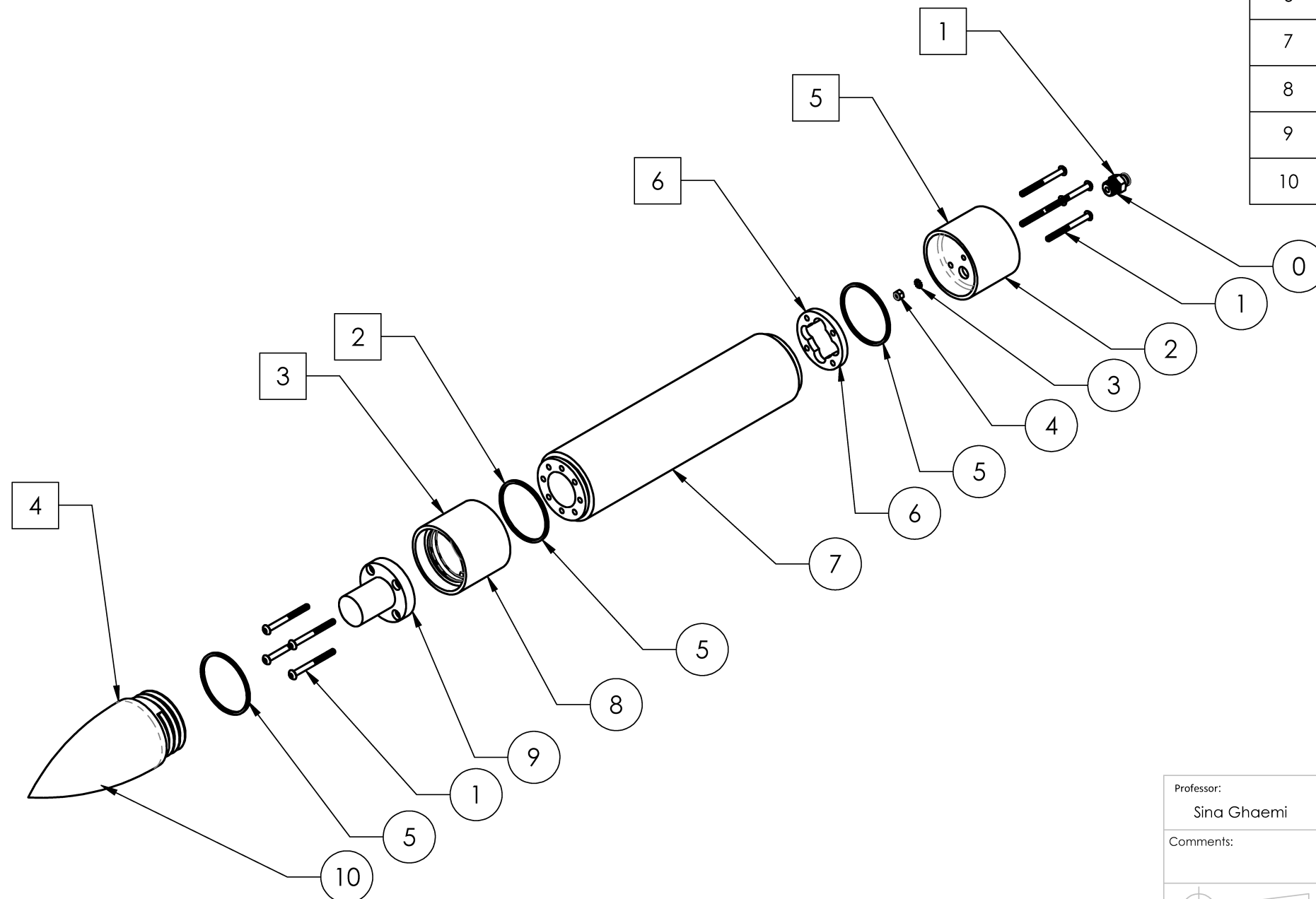
SOLIDWORKS Educational Product. For Instructional Use Only

Professor: Sina Ghaemi	UNLESS OTHERWISE SPECIFIED: DIMENSIONS ARE IN MM [IN] TOLERANCES: ANGULAR: ± 0.5° LINEAR X = ± 0.5 X.X = ± 0.1 X.XX = ± 0.025 SURFACE FINISH µm 0.6 DO NOT SCALE DRAWING	DRAWN BY: Desiree Reholon	The Department of Mechanical Engineering UNIVERSITY OF ALBERTA TITLE: Replaceable Module Assembly - Control
Comments:		Reviewed by: Solid Model By: Desiree Reholon	
MATERIAL:		Monday, January 15, 2018 4:42:25 PM	SIZE B Part supplier/manufacturer 130a REV 0
DRAWING No.: AUV-130a-01		Sunday, May 22, 2016 5:11:12 PM	SCALE: 1:2.5 Mass: 614gr SHEET 2 OF 3

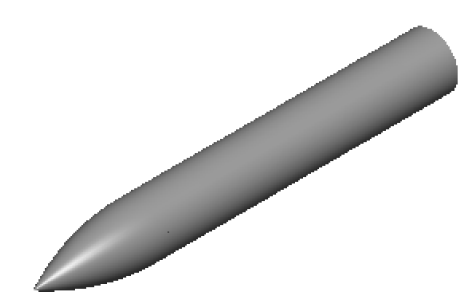
ASSEMBLY INSTRUCTIONS (SQUARE IDENTIFIERS):

- 1 Install item 0 in item 2.
- 2 Install the o-rings (items 011) on the grooves available for it on item 132b and 134.
- 3 Place item 8 in item 7, followed by item 9 inside item 8. Align all the holes and fix them with the screws (item 1).
- 4 Install item 10 to item 8.
- 5 Attach item 2 to sub-assembly AUV-120 with items 3 and 4, using the torque wrench.
- 6 Place item 6 over item 7 and align the holes, to finally attach the front seal to item 7 with the screws (item 1).

ITEM	PART No.	DESCRIPTION	QTY.
0	040	Push-to-Connect Tube Fitting for Air & Water, Straight Adapter, 3/16" Tube OD x 1/8 NPT Male	1
1	029	Sealing Pan Head Phillips Machine Screw. Buna-N O-Ring, 6-32 Thread, 1-1/4" Length	8
2	131a	Front Seal	1
3	030	Lock Washer M3	1
4	031	Class 04 Steel Thin Hex Nut - DIN 439B. Zinc Plated, M3x0.5 Thread Size, 5.5mm Wide, 1.8mm High	1
5	011	O-Ring Oil-Resistant Buna-N, Dash Number 030	2
6	135b	Front Balance Weigth	1
7	132b	Porous Replaceable Module	1
8	136b	Back seal	1
9	138	Back Balance Weigth	1
10	134	Tail	1



ISOMETRIC VIEW
SCALE 1:5



SOLIDWORKS Educational Product. For Instructional Use Only

Professor: Sina Ghaemi	UNLESS OTHERWISE SPECIFIED: DIMENSIONS ARE IN MM [IN] TOLERANCES: ANGULAR: ± 0.5° LINEAR X = ± 0.5 X.X = ± 0.1 X.XX = ± 0.025 SURFACE FINISH µm 0.6 DO NOT SCALE DRAWING	DRAWN BY: Desiree Reholon	The Department of Mechanical Engineering UNIVERSITY OF ALBERTA TITLE: Replaceable Module Assembly - Air Injection						
Comments:		Reviewed by:							
MATERIAL:		Sold Model By: Desiree Reholon	<table border="1"> <tr> <td>SIZE</td> <td>Part supplier/manufacturer</td> <td>REV</td> </tr> <tr> <td>B</td> <td>130b</td> <td>0</td> </tr> </table>	SIZE	Part supplier/manufacturer	REV	B	130b	0
SIZE	Part supplier/manufacturer	REV							
B	130b	0							
DRAWING No.: AUV-130b-01		Monday, January 15, 2018 4:42:04 PM Sunday, May 22, 2016 5:11:12 PM	<table border="1"> <tr> <td>SCALE: 1:2.5</td> <td>Mass: 593gr</td> <td>SHEET 3 OF 3</td> </tr> </table>	SCALE: 1:2.5	Mass: 593gr	SHEET 3 OF 3			
SCALE: 1:2.5	Mass: 593gr	SHEET 3 OF 3							

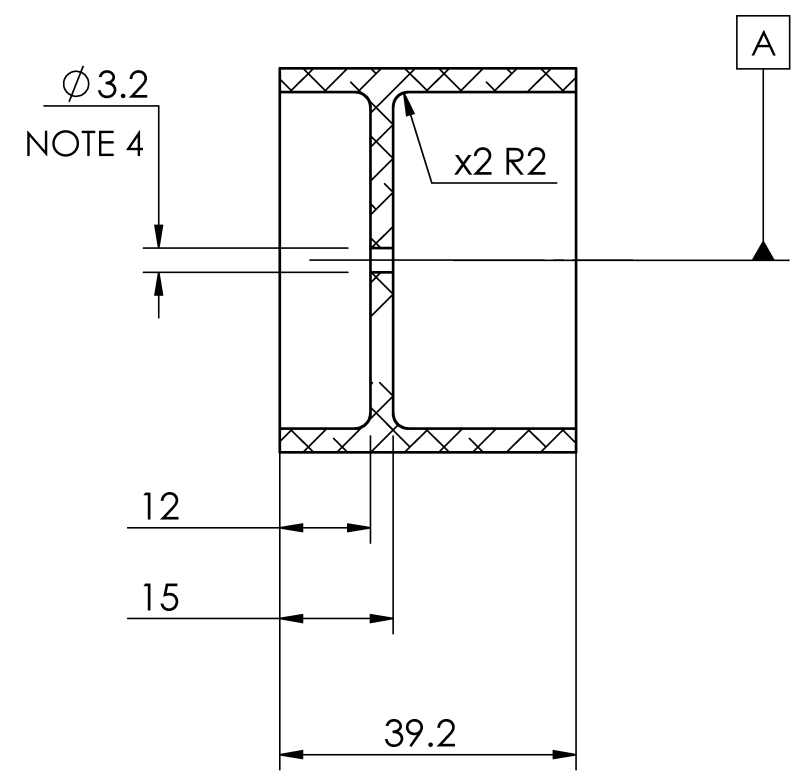
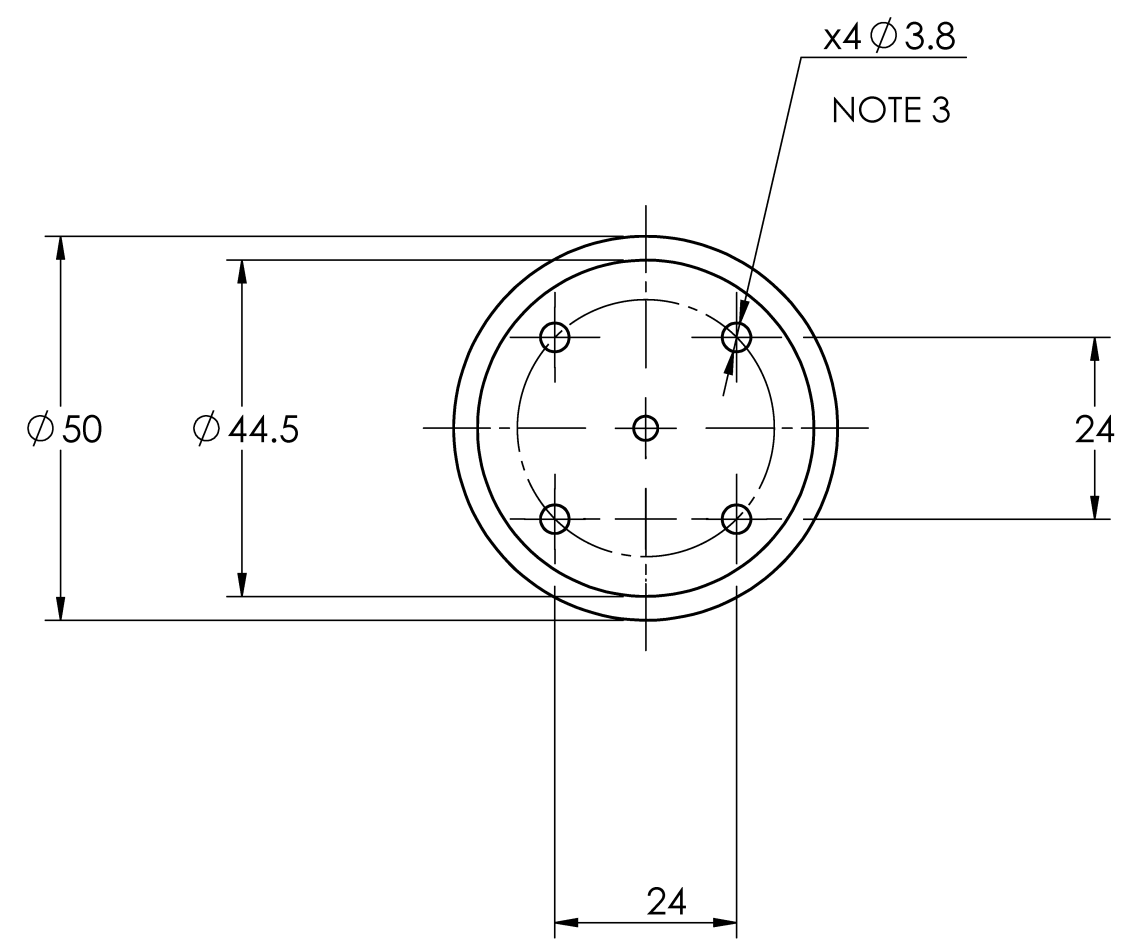
8 7 6 5 4 3 2 1

D

C

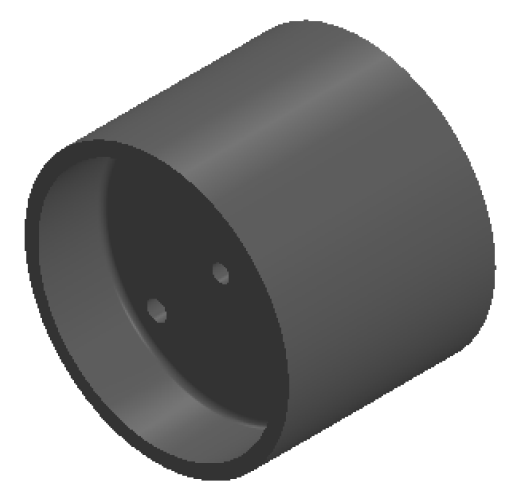
B

A



A

ISOMETRIC VIEW

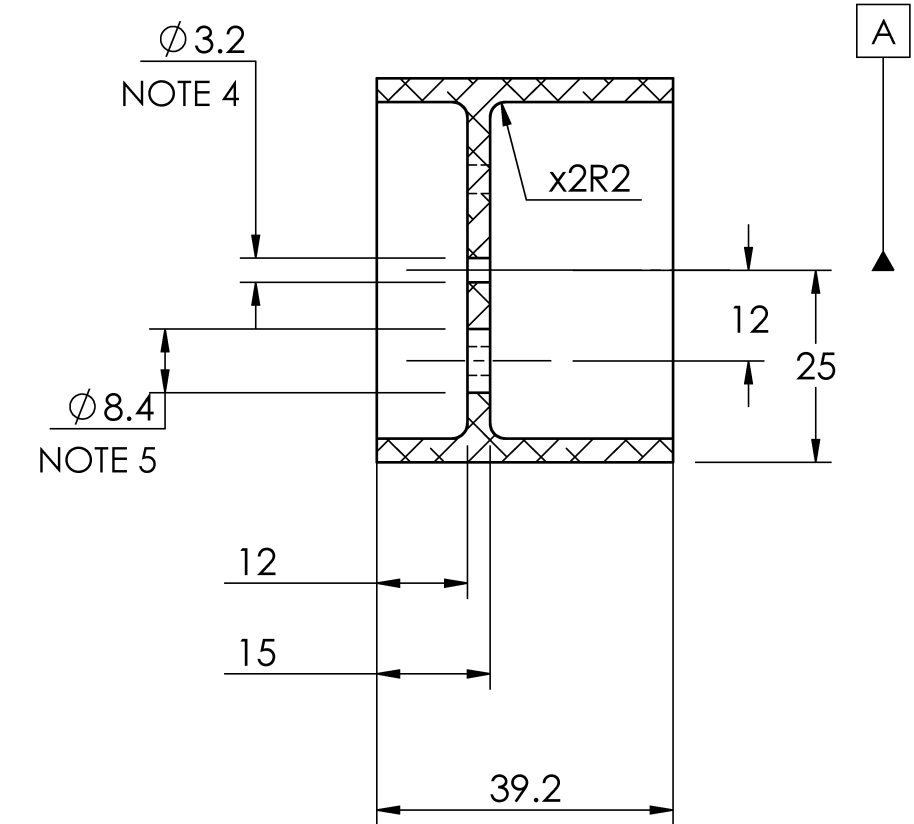
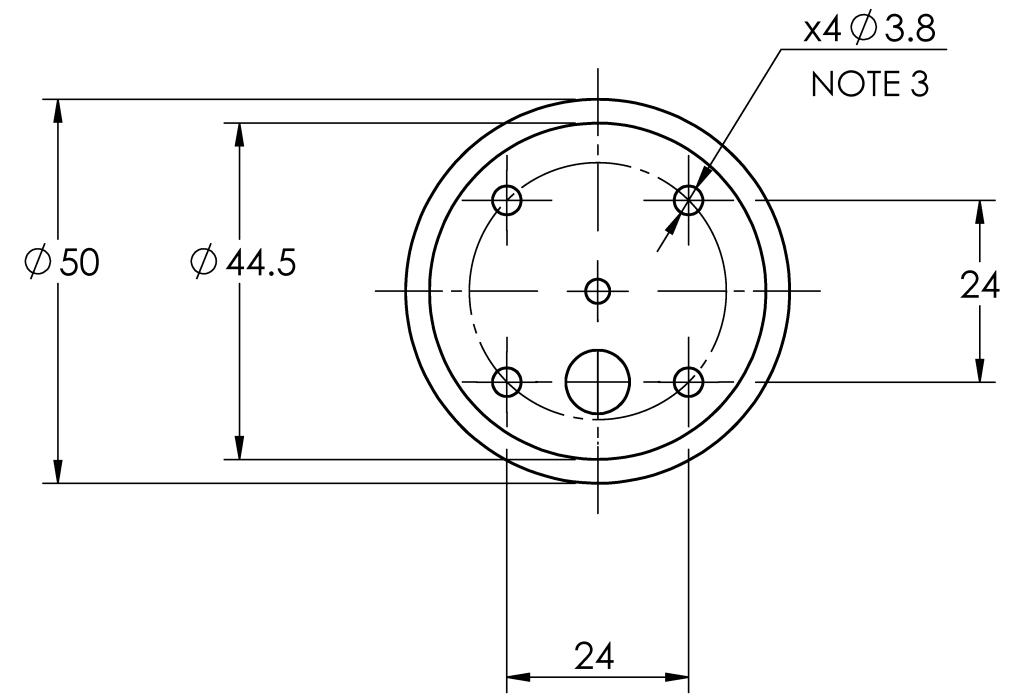


- NOTES:
1. Manufacture procedure: CNC/Milling.
 2. Quantity required: 1.
 3. Threaded Female Connection for #6-32, all through. Close Fit.
 4. Threaded Female Connection for M3x0.5mm, all through. Close Fit.

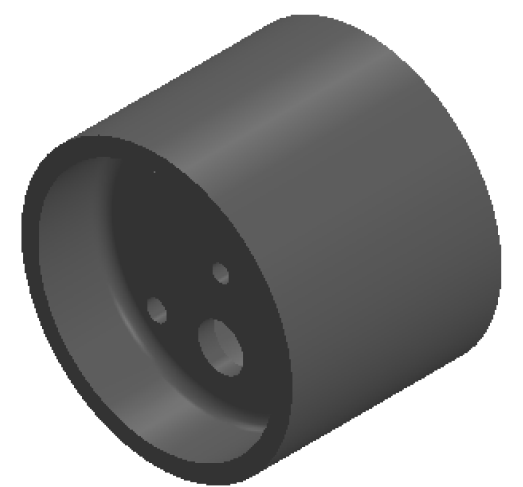
SOLIDWORKS Educational Product. For Instructional Use Only

Professor: Sina Ghaemi	UNLESS OTHERWISE SPECIFIED: DIMENSIONS ARE IN MM [IN] TOLERANCES: ANGULAR: $\pm 0.5^\circ$ LINEAR X = ± 0.5 X.X = ± 0.1 X.XX = ± 0.025 SURFACE FINISH μm 0.6 DO NOT SCALE DRAWING	DRAWN BY: Desiree Reholon	The Department of Mechanical Engineering UNIVERSITY OF ALBERTA TITLE: Front Seal Baseline Assembly
Comments:		Reviewed by:	
MATERIAL: UHMW Polyethylene	DRAWING No.: AUV-131a-01	Soild Model By: Desiree Reholon	SIZE B Part supplier/manufacturer 131a REV 0
		Monday, January 15, 2018 4:43:43 PM	SCALE: 1:1 Mass: 73gr SHEET 1 OF 1
		Sunday, March 20, 2016 7:13:53 PM	

8 7 6 5 4 3 2 1



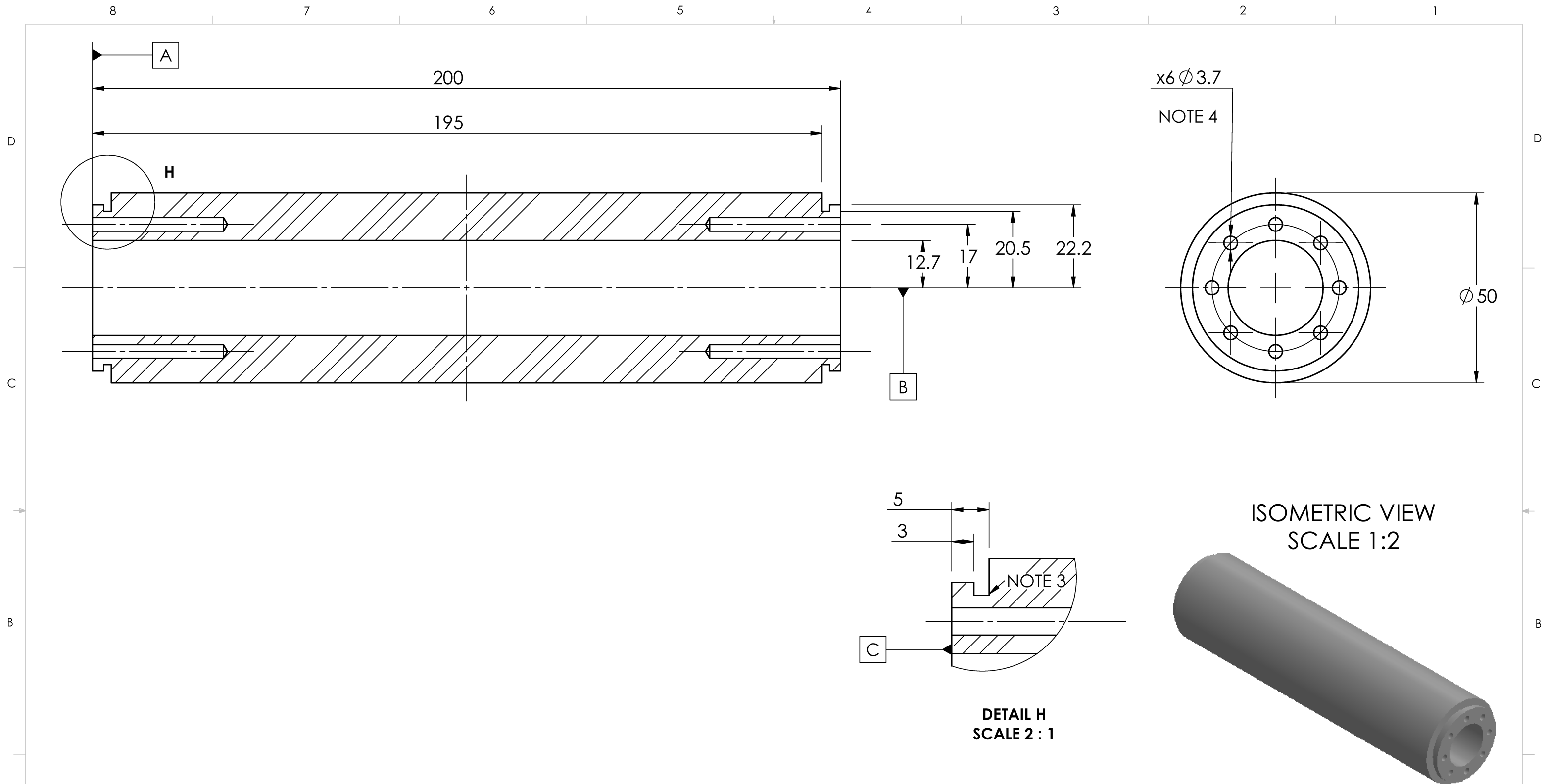
ISOMETRIC VIEW



- NOTES:
1. Manufacture procedure: CNC/Milling.
 2. Quantity required: 1.
 3. Threaded Female Connection for #6-32, all through. Close Fit.
 4. Threaded Female Connection for M3x0.5mm, all through. Close Fit.
 5. Threaded Female Connection for 1/8 NPT Pipe, all through. Close Fit.

SOLIDWORKS Educational Product. For Instructional Use Only

Professor: Sina Ghaemi	UNLESS OTHERWISE SPECIFIED: DIMENSIONS ARE IN MM [IN] TOLERANCES: ANGULAR: $\pm 0.5^\circ$ LINEAR X = ± 0.5 X.X = ± 0.1 X.XX = ± 0.025 SURFACE FINISH μm 0.6 DO NOT SCALE DRAWING	DRAWN BY: Desiree Reholon	The Department of Mechanical Engineering UNIVERSITY OF ALBERTA TITLE: Front Seal Test Assembly
Comments:		Reviewed by: Desiree Reholon	
MATERIAL: Aluminum 6061	DRAWING No.: AUV-131b-01	Monday, January 15, 2018 4:43:43 PM	SIZE B
		Sunday, March 20, 2016 7:13:53 PM	Part supplier/manufacturer 131b REV 0
			SCALE: 1:1 Mass: 62gr SHEET 1 OF 1



x6 ϕ 3.7
NOTE 4

12.7 17 20.5 22.2

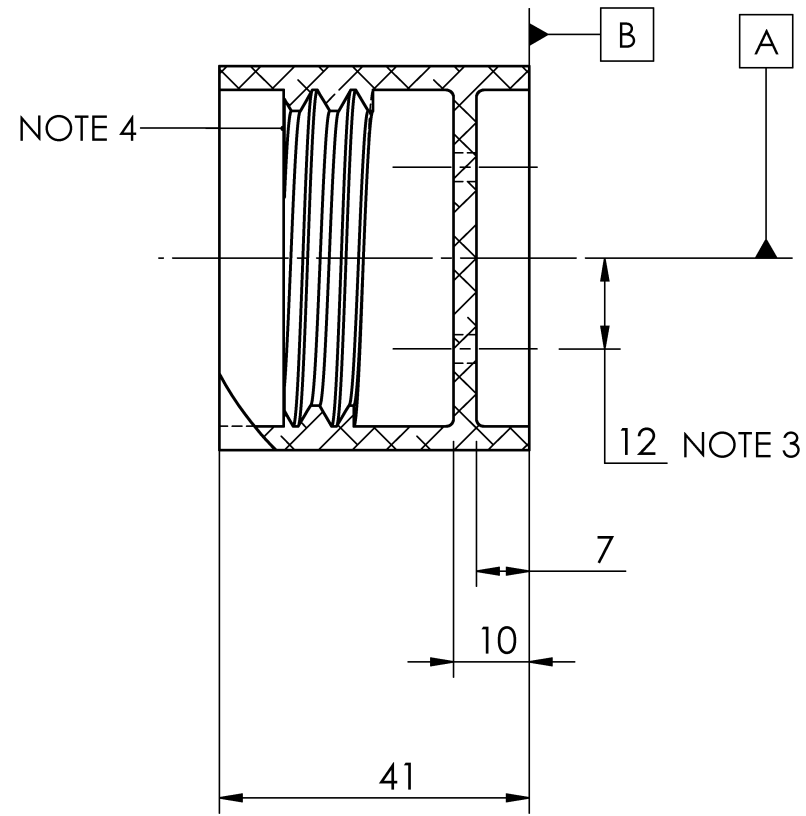
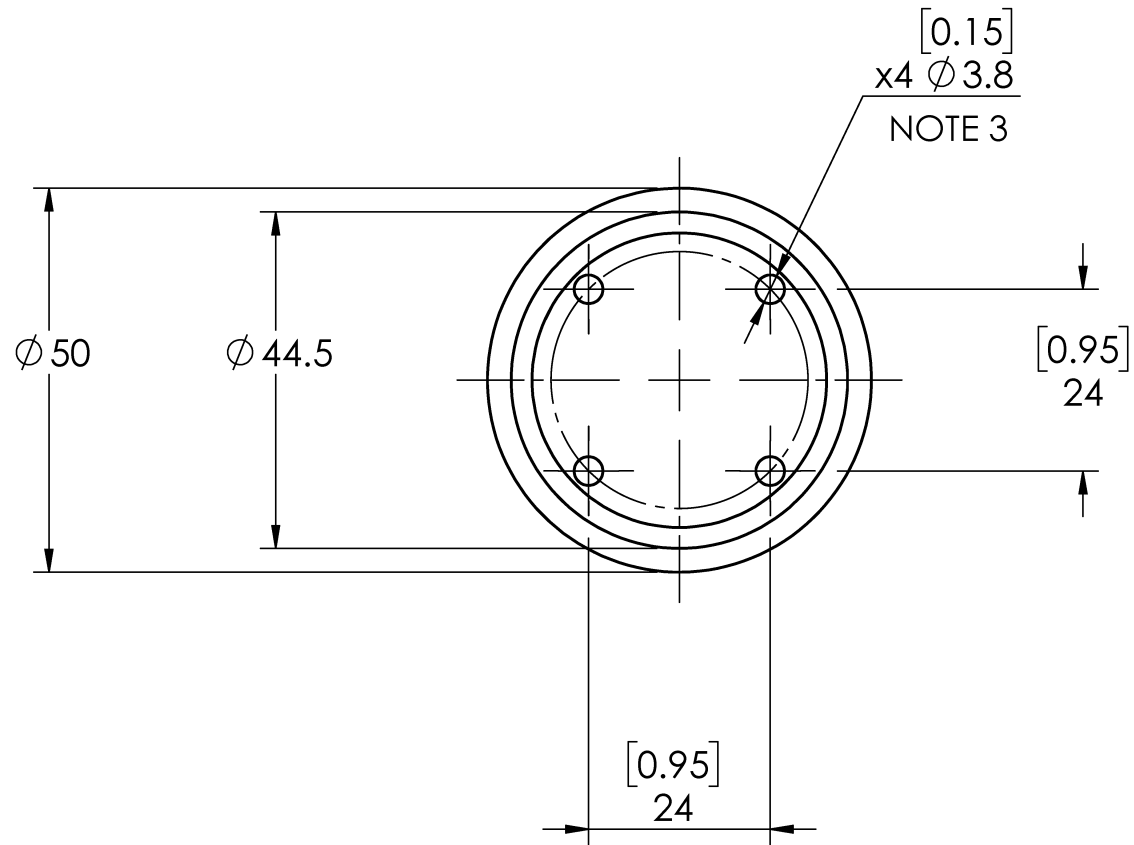
ISOMETRIC VIEW
SCALE 1:2

DETAIL H
SCALE 2:1

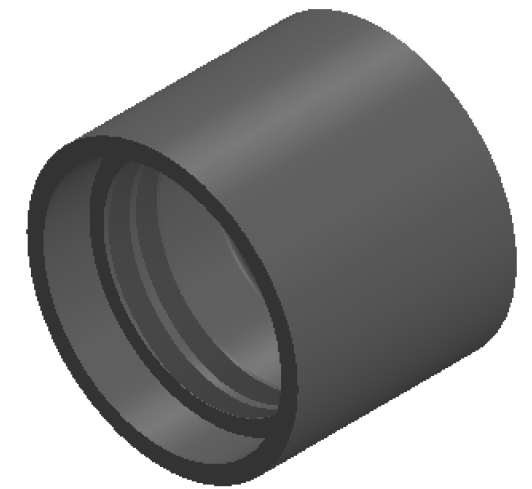
- NOTES:
1. 133a correspond to the Baseline Replaceable Module, and 133b correspond to the Test Replaceable Module (UHMW-PE - Hydrophobic 2 OD x .500 wall x 1.00 ID, 10 microns porous).
 2. Manufacture procedure: CNC/Milling.
 3. O-Ring Groove.
 4. Threaded Female Connection for #6-32, 30mm length. Close Fit.

Professor: Sina Ghaemi	UNLESS OTHERWISE SPECIFIED: DIMENSIONS ARE IN MM [IN] TOLERANCES: ANGULAR: $\pm 0.5^\circ$ LINEAR X = ± 0.5 X.X = ± 0.1 X.XX = ± 0.025 SURFACE FINISH μm 0.6 DO NOT SCALE DRAWING	DRAWN BY: Desiree Reholon	The Department of Mechanical Engineering UNIVERSITY OF ALBERTA TITLE: Replaceable Module
Comments:		Reviewed by:	
MATERIAL: UHMW Polyethylene	DRAWING No.: AUV-132b-01	Sold Model By: Desiree Reholon	SIZE B
		Monday, January 15, 2018 2:37:51 PM	Part supplier/manufacturer 132ab
		Sunday, March 20, 2016 7:56:03 PM	REV 0
			SCALE: 1:1 Mass: 200/180 SHEET 1 OF 1

SOLIDWORKS Educational Product. For Instructional Use Only



ISOMETRIC VIEW

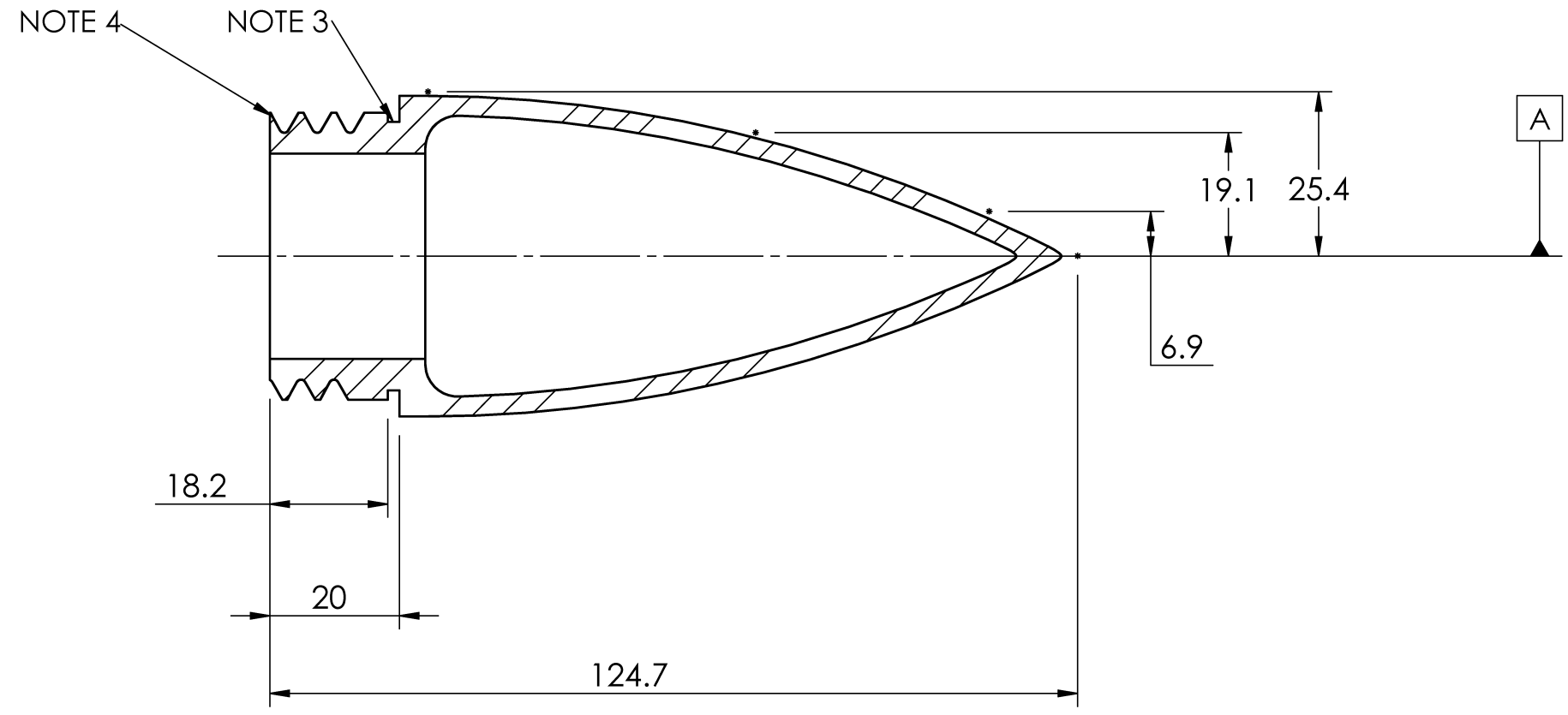
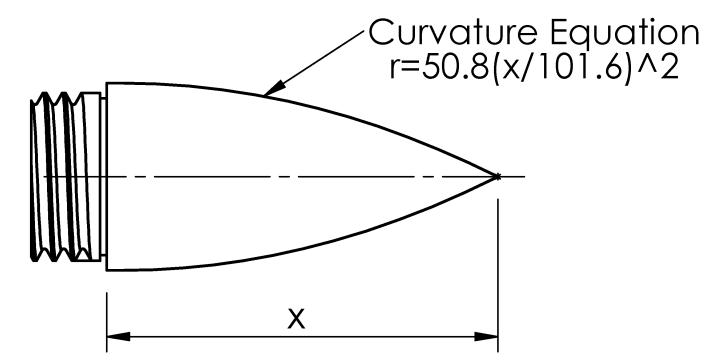


NOTES:

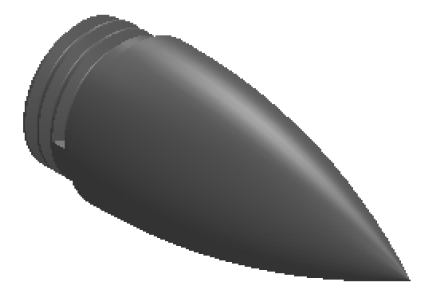
1. Manufacture procedure: CNC/Milling.
2. Quantity required: 1.
3. Threaded Female Connection for #6-32, all through. Close Fit.
4. Threaded Male Connection.

SOLIDWORKS Educational Product. For Instructional Use Only

Professor: Sina Ghaemi	UNLESS OTHERWISE SPECIFIED: DIMENSIONS ARE IN MM [IN] TOLERANCES: ANGULAR: $\pm 0.5^\circ$ LINEAR X = ± 0.5 X.X = ± 0.1 X.XX = ± 0.025 SURFACE FINISH 0.6 μm DO NOT SCALE DRAWING	DRAWN BY: Desiree Reholon	The Department of Mechanical Engineering UNIVERSITY OF ALBERTA TITLE: Aft Seal
Comments:		Reviewed by:	
MATERIAL: Aluminum 6061	DRAWING No.: AUV-133-01	Monday, January 15, 2018 4:49:20 PM	SIZE B
		Sunday, March 20, 2016 7:13:53 PM	Part supplier/manufacturer 133
			REV 0
			SCALE: 1:1 Mass: 61gr SHEET 1 OF 1



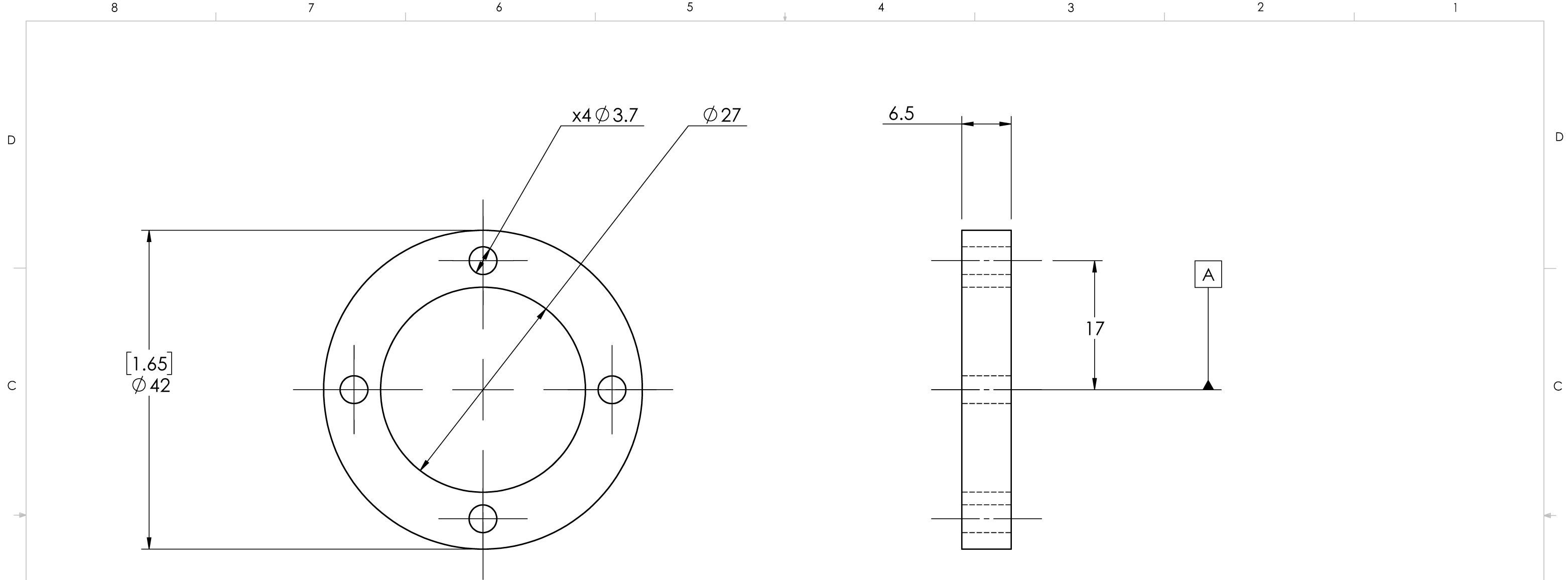
ISOMETRIC VIEW



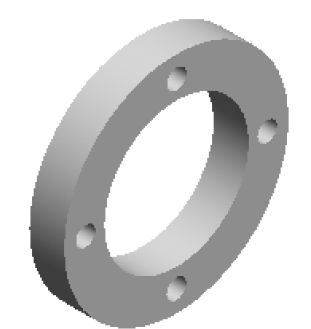
- NOTES:
1. Manufacture procedure: 3D Printing, PolyJet Vero.
 2. Quantity required: 1.
 3. O-Ring Groove.
 4. Threaded Male Connection.

Professor: Sina Ghaemi	UNLESS OTHERWISE SPECIFIED: DIMENSIONS ARE IN MM [IN] TOLERANCES: ANGULAR: ± 0.5° LINEAR X = ± 0.5 X.X = ± 0.1 X.XX = ± 0.025 SURFACE FINISH 0.6 µm DO NOT SCALE DRAWING	DRAWN BY: Desiree Reholon
Comments:		Reviewed by:
		Solid Model By Desiree Reholon
MATERIAL: PolyJet Vero		Monday, January 15, 2018 4:41:59 PM
DRAWING No.: AUV-134-01		Thursday, April 07, 2016 9:43:08 AM

The Department of Mechanical Engineering UNIVERSITY OF ALBERTA		
TITLE: Tail		
SIZE B	Part supplier/manufacturer 134	REV 0
SCALE: 1:1	Mass: 57gr	SHEET 1 OF 1



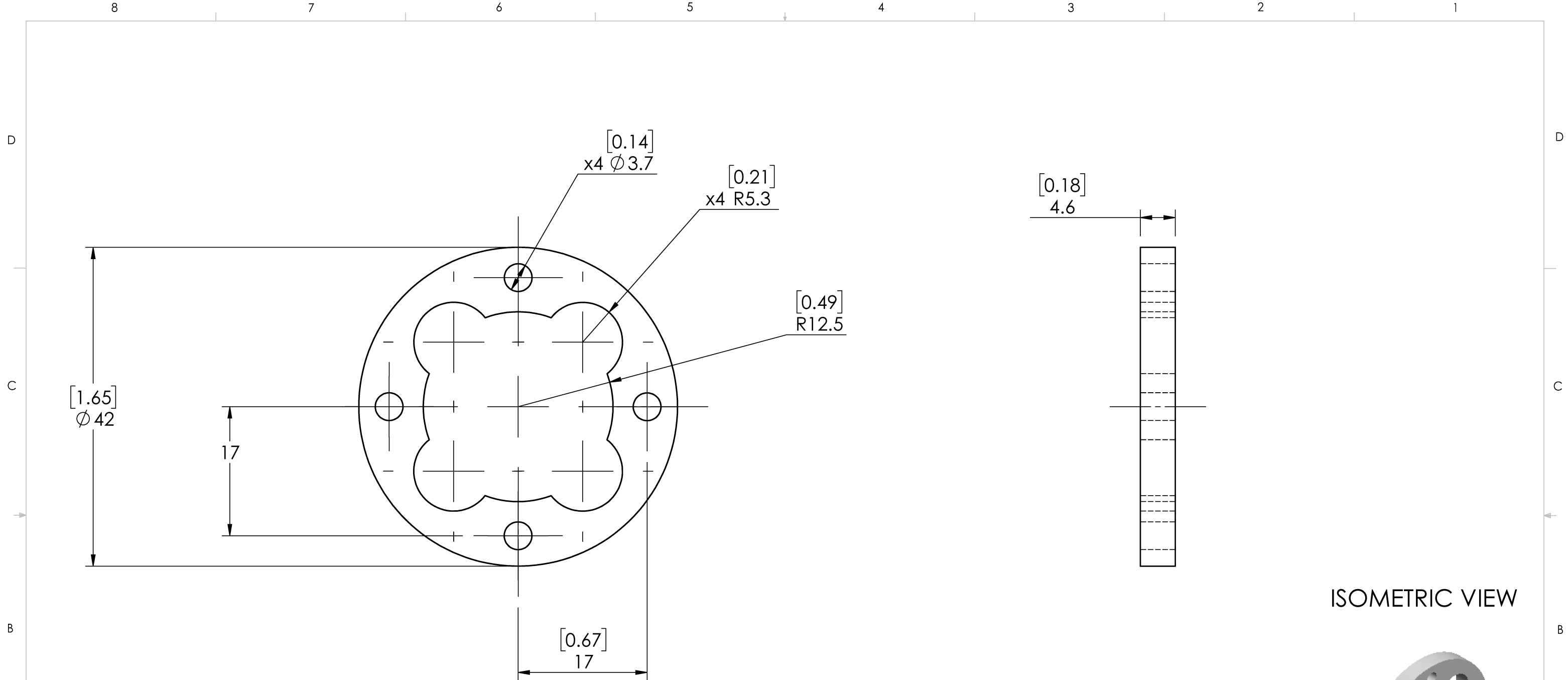
ISOMETRIC VIEW



- NOTES:
1. Manufacture procedure: CNC/Milling.
 2. Quantity required: 1.

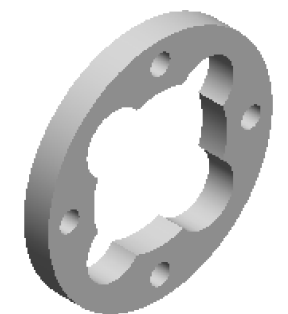
SOLIDWORKS Educational Product. For Instructional Use Only

Professor: Sina Ghaemi	UNLESS OTHERWISE SPECIFIED: DIMENSIONS ARE IN MM [IN] TOLERANCES: ANGULAR: ± 0.5° LINEAR X = ± 0.5 X.X = ± 0.1 X.XX = ± 0.025 SURFACE FINISH 0.6 µm DO NOT SCALE DRAWING	DRAWN BY: Desiree Reholon	The Department of Mechanical Engineering UNIVERSITY OF ALBERTA TITLE: Front Balance Weight for Smooth Surface
Comments:		Reviewed by: Desiree Reholon	
MATERIAL: Stainless Steel	DRAWING No.: AUV-135a-01	Soild Model By: Desiree Reholon	SIZE B Part supplier/manufacturer 135a REV 0
		Monday, November 13, 2017 1:05:57 PM Friday, January 13, 2017 1:48:18 PM	SCALE: 2:1 Mass: 40 gr SHEET 1 OF 1



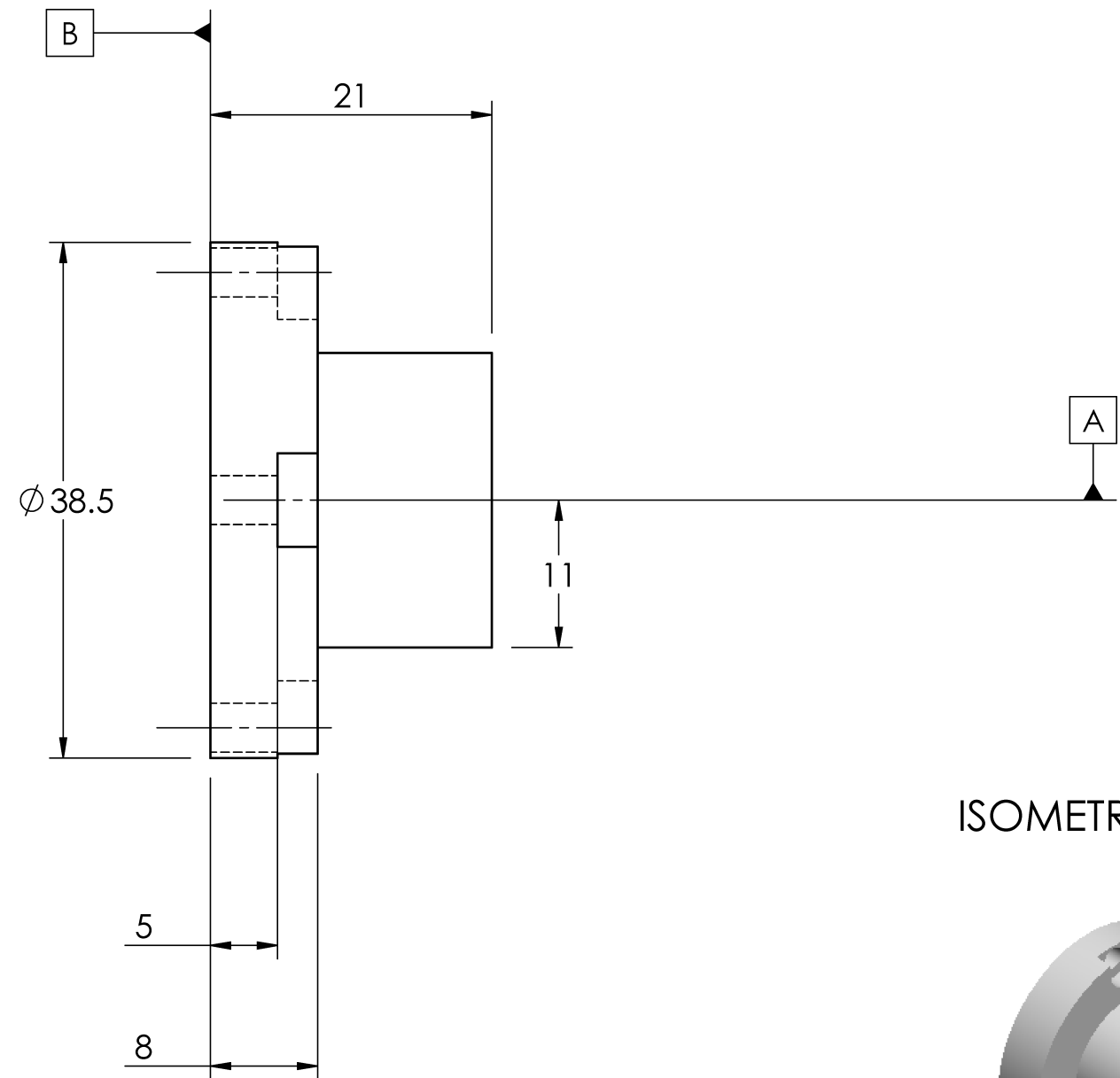
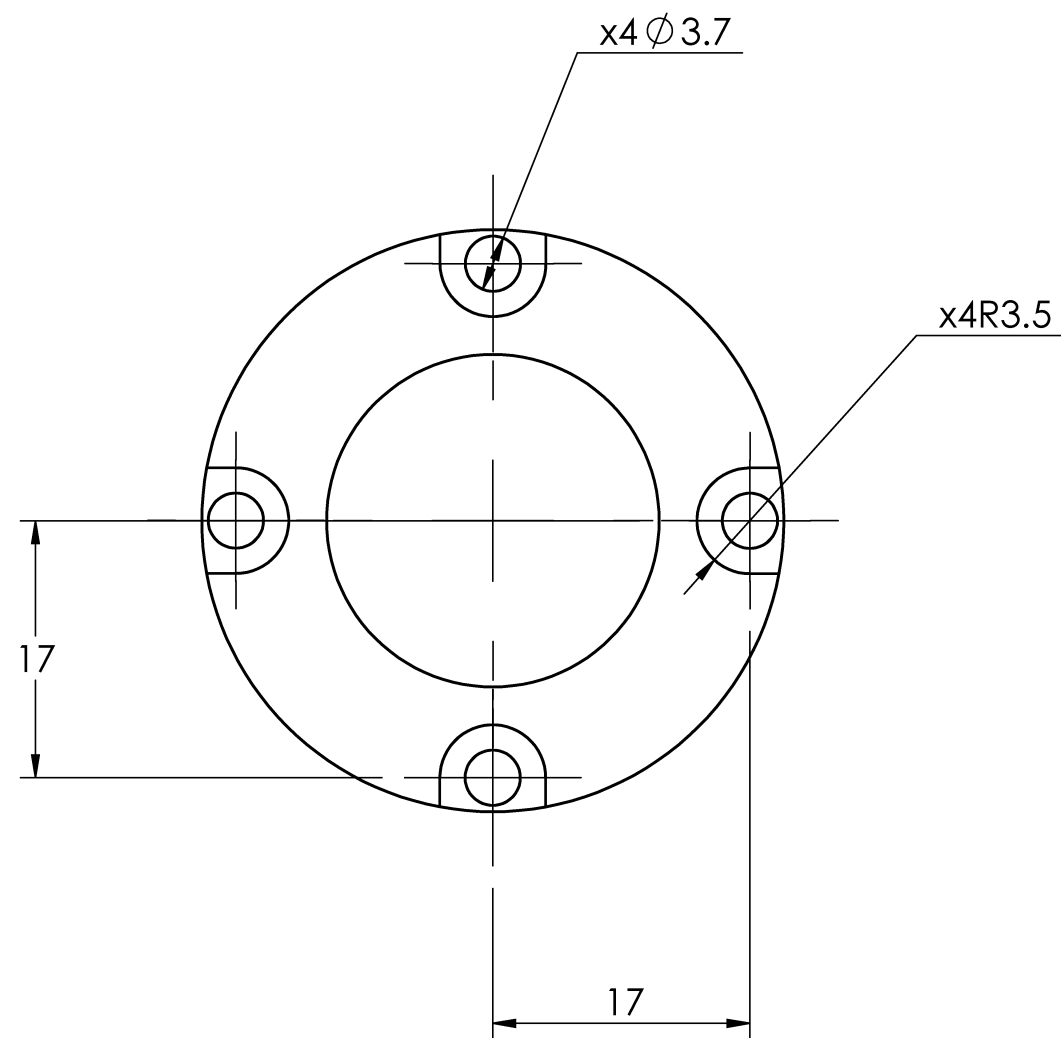
- NOTES:
1. Manufacture procedure: CNC/Milling.
 2. Quantity required: 1.

ISOMETRIC VIEW

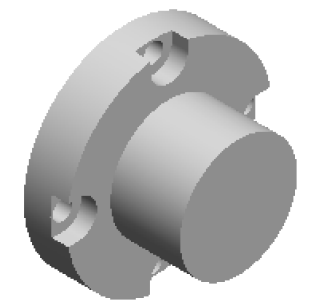


SOLIDWORKS Educational Product. For Instructional Use Only

Professor: Sina Ghaemi	UNLESS OTHERWISE SPECIFIED: DIMENSIONS ARE IN MM [IN] TOLERANCES: ANGULAR: $\pm 0.5^\circ$ LINEAR X = ± 0.5 X.X = ± 0.1 X.XX = ± 0.025 SURFACE FINISH 0.6 μm DO NOT SCALE DRAWING	DRAWN BY: Desiree Reholon	The Department of Mechanical Engineering UNIVERSITY OF ALBERTA TITLE: Front Balance Weight for Porous Surface
Comments:		Reviewed by:	
		Solid Model By: Desiree Reholon	SIZE Part supplier/manufacturer B 135b REV 0
MATERIAL: Stainless Steel		Monday, November 13, 2017 1:05:11 PM	SCALE: 2:1 Mass: 20 gr SHEET 1 OF 1
DRAWING No.: AUV-135b-01		Friday, January 13, 2017 1:48:18 PM	



ISOMETRIC VIEW

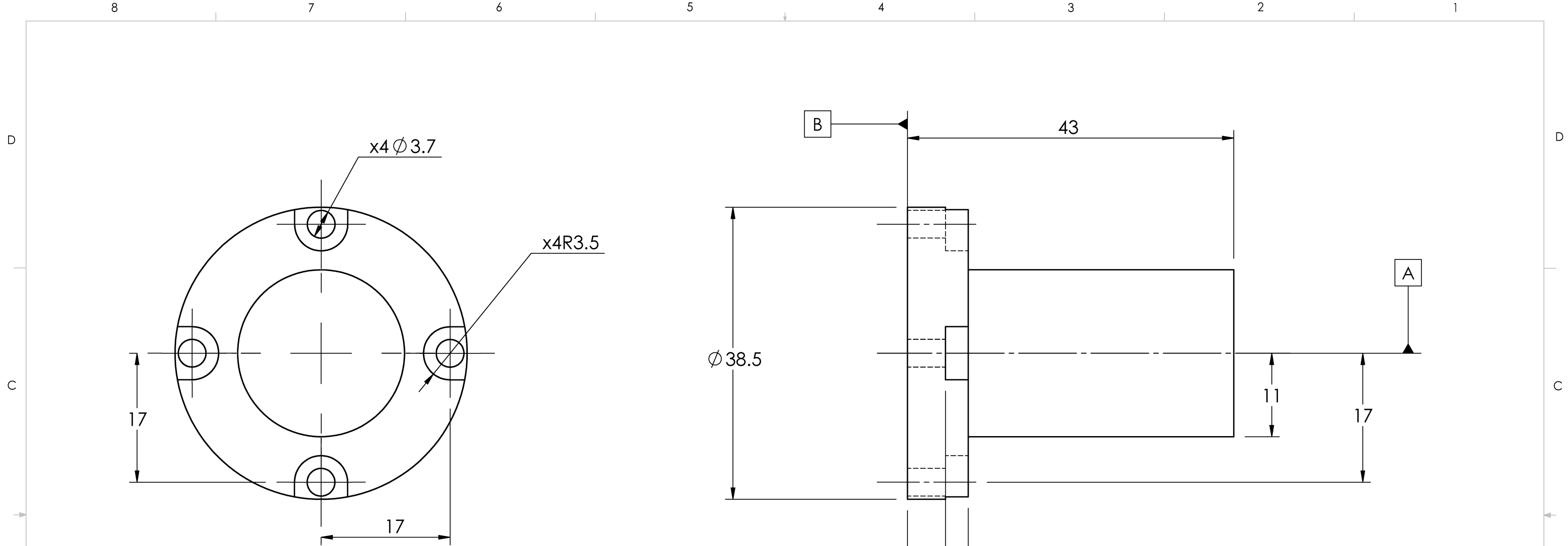


NOTES:

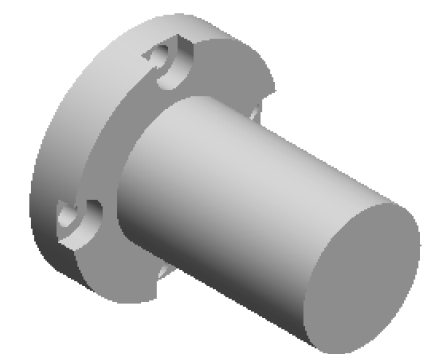
1. Manufacture procedure: CNC/Milling.
2. Quantity required: 1.

SOLIDWORKS Educational Product. For Instructional Use Only

Professor: Sina Ghaemi	UNLESS OTHERWISE SPECIFIED: DIMENSIONS ARE IN MM [IN] TOLERANCES: ANGULAR: $\pm 0.5^\circ$ LINEAR X = ± 0.5 X.X = ± 0.1 X.XX = ± 0.025 SURFACE FINISH μm 0.6 DO NOT SCALE DRAWING	DRAWN BY: Desiree Reholon	The Department of Mechanical Engineering UNIVERSITY OF ALBERTA	
Comments:		Reviewed by:	TITLE: Back Balance Weight for Smooth Surface	
		Solid Model By: Desiree Reholon	Monday, November 13, 2017 1:03:48 PM	
MATERIAL: Stainless Steel		DRAWING No.: AUV-136a-01	Friday, January 13, 2017 1:48:18 PM	
		SIZE B	Part supplier/manufacturer 136a	REV 0
		SCALE: 2:1	Mass: 135 gr	SHEET 1 OF 1



ISOMETRIC VIEW



NOTES:

1. Manufacture procedure: CNC/Milling.
2. Quantity required: 1.

SOLIDWORKS Educational Product. For Instructional Use Only

Professor: Sina Ghaemi	UNLESS OTHERWISE SPECIFIED: DIMENSIONS ARE IN MM [IN] TOLERANCES: ANGULAR: ± 0.5° LINEAR X = ± 0.5 X.X = ± 0.1 X.XX = ± 0.025 SURFACE FINISH 0.6 µm DO NOT SCALE DRAWING	DRAWN BY: Desiree Reholon	The Department of Mechanical Engineering UNIVERSITY OF ALBERTA TITLE: Back Balance Weight for Porous Surface
Comments:		Reviewed by:	
MATERIAL: Stainless Steel	DRAWING No.: AUV-136b-01	Soild Model By: Desiree Reholon	SIZE B Part supplier/manufacturer 136b REV 0
		Monday, November 13, 2017 1:05:16 PM	SCALE: 2:1
		Friday, January 13, 2017 1:48:18 PM	Mass: 170 gr
			SHEET 1 OF 1

Appendix B. Data Distribution of the Drag Coefficient

The following section presents for a sample data set of the load cell the calculated drag coefficient (C_D) as a function of time (Figure B.1) and the probability density function (PDF, Figure B.2). The data used for this analysis correspond to one data point of the smooth surface collected at the Re number = 1.5×10^6 , after 40 min of submersion of the load cell in the flow stream.

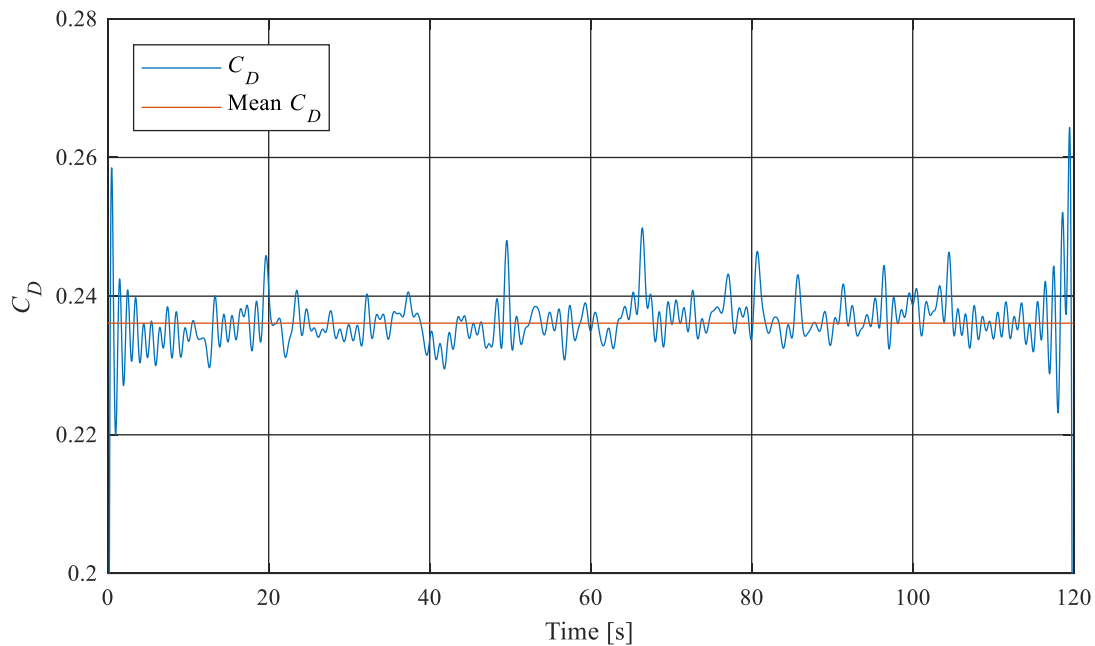


Figure B.1. Drag coefficient (C_D) as a function of time.

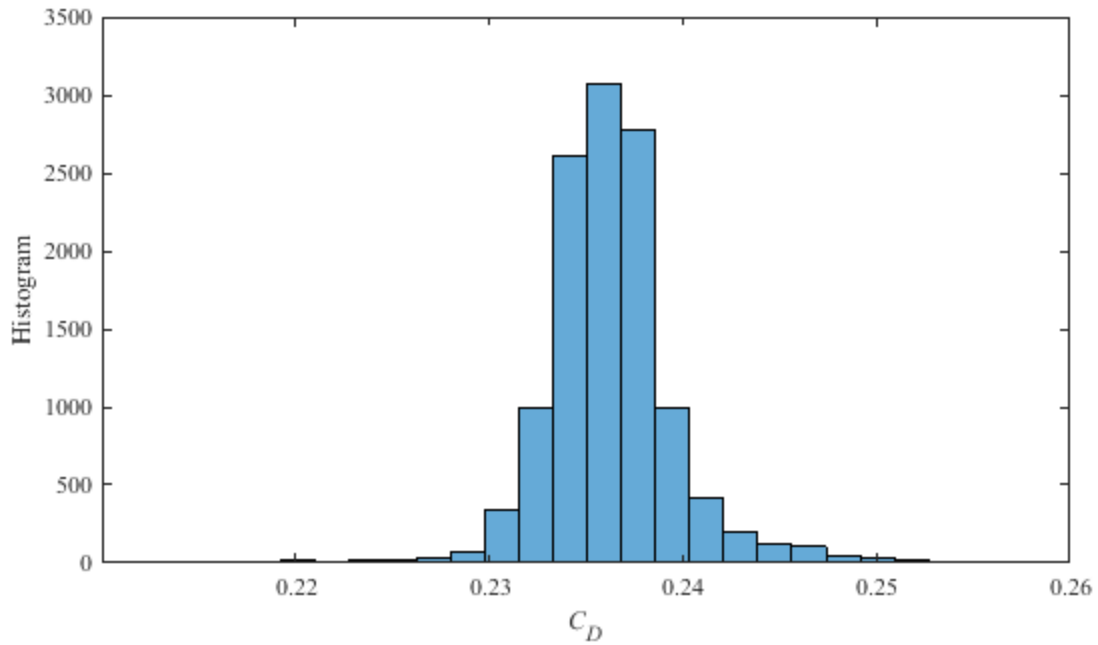


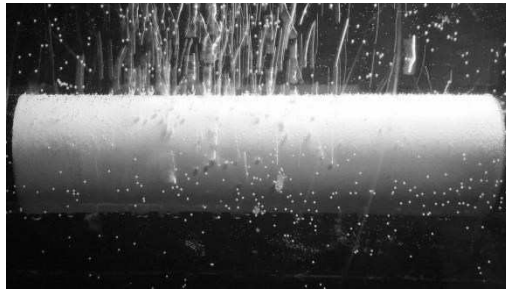
Figure B.2. Histogram for the drag coefficient (C_D) at Re number = 1.5×10^6 using the smooth surface

The C_D as function of time, displayed in Figure B.1, shows that the measurement varies around the average value and not present a substantial decay or increase over the range of time tested. In Figure B.2 is possible to observe that the data has a Gaussian distribution around the mean value. Hence, the use of the standard deviation as an indicator of the dispersion of the data is of significance.

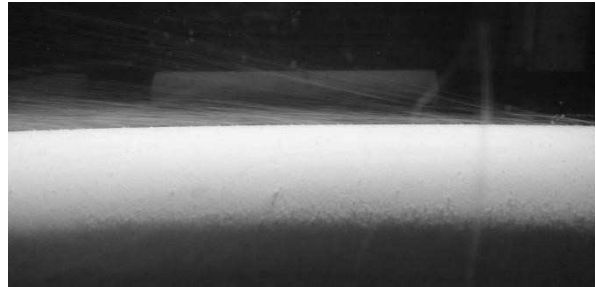
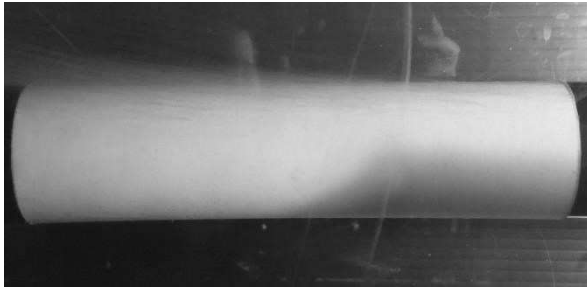
Appendix C. Pictures of the Porous Surface Tests

C.1 Low air injection rates (LAIR)

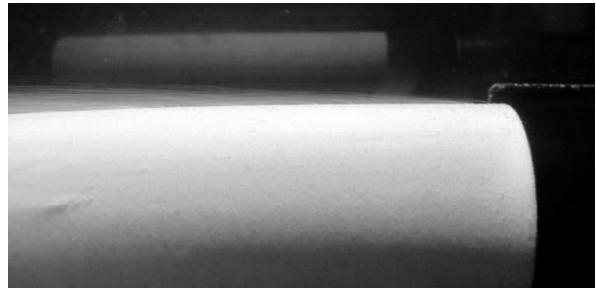
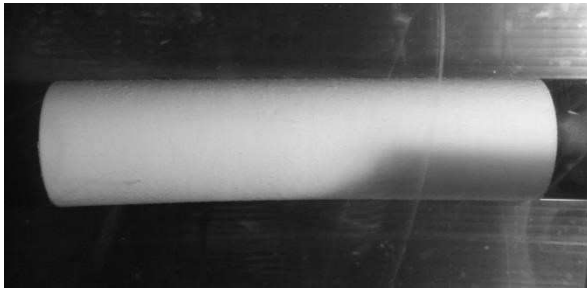
C.1.1 $Q_a = 0.15$ L/min



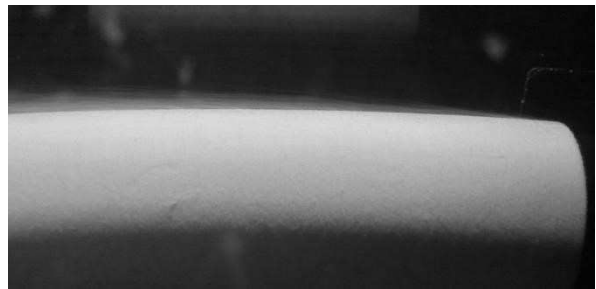
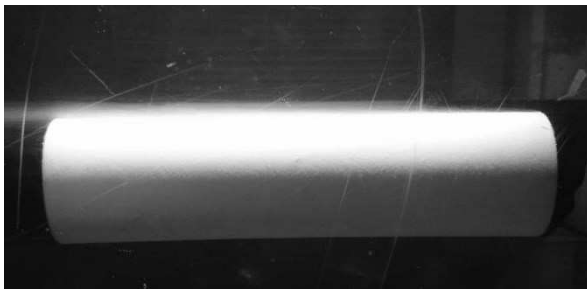
$Q_a = 0.15$ L/min. Static water



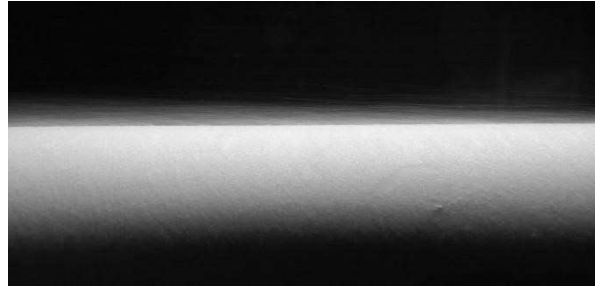
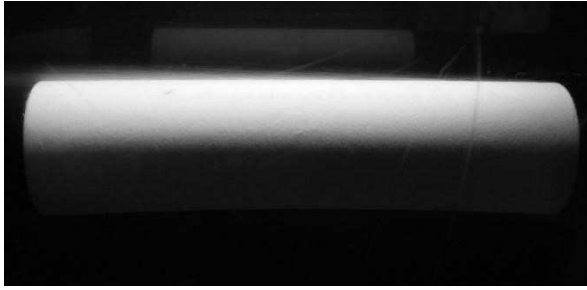
$Q_a = 0.15$ L/min. $Re = 5.0 \times 10^5$



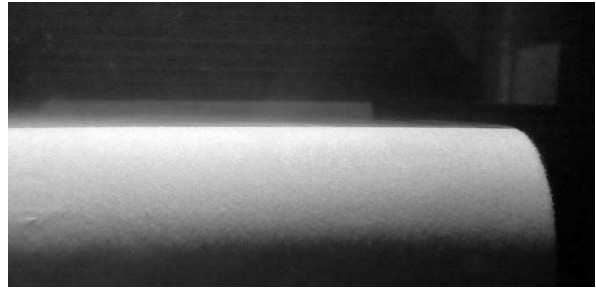
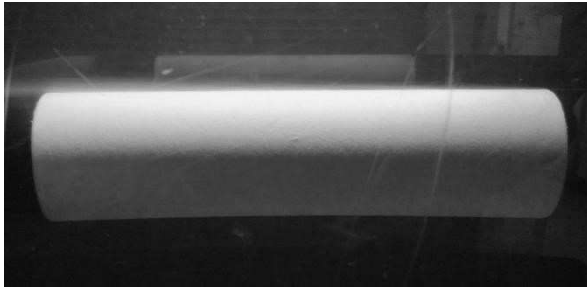
$Q_a = 0.15$ L/min. $Re = 7.0 \times 10^5$



$Q_a = 0.15 \text{ L/min. } Re = 1.0 \times 10^6$

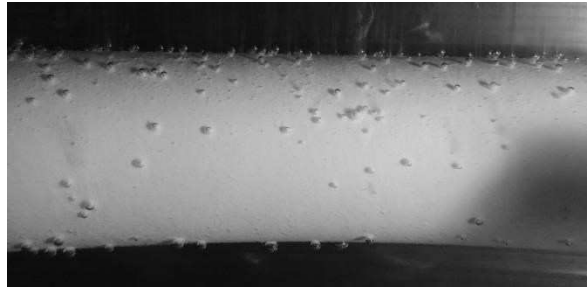


$Q_a = 0.15 \text{ L/min. } Re = 1.2 \times 10^6$

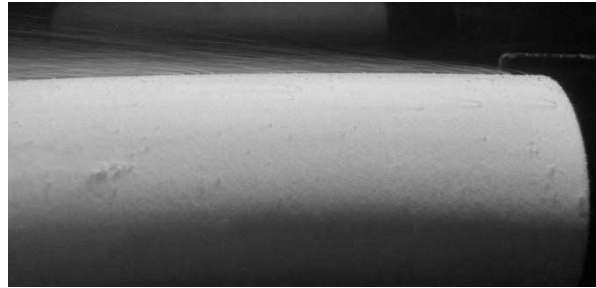


$Q_a = 0.15 \text{ L/min. } Re = 1.5 \times 10^6$

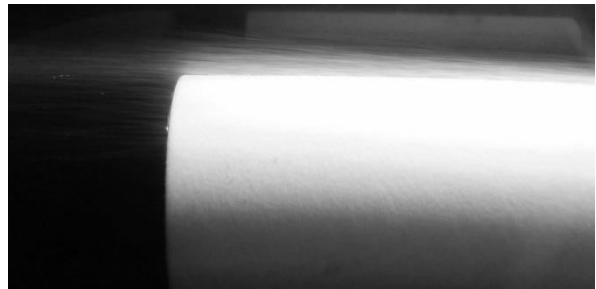
C.1.2 $Q_a = 0.25$ L/min



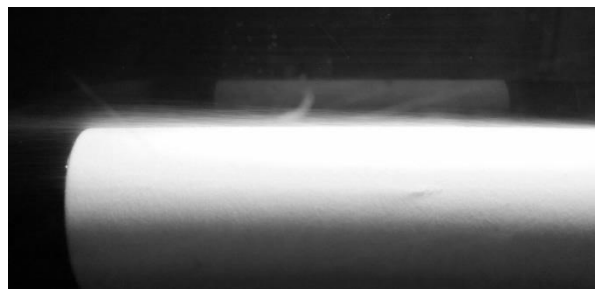
$Q_a = 0.25$ L/min. Static water



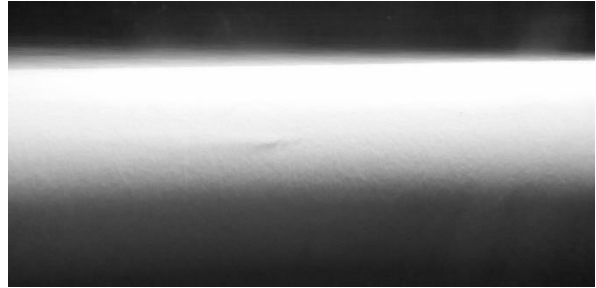
$Q_a = 0.25$ L/min. $Re = 5.0 \times 10^5$



$Q_a = 0.25$ L/min. $Re = 7.0 \times 10^5$



$Q_a = 0.25$ L/min. $Re = 1.0 \times 10^6$

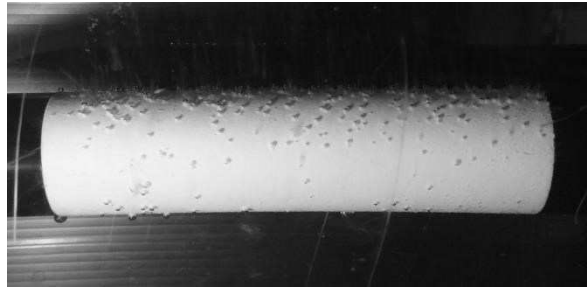


$Q_a = 0.25 \text{ L/min. } Re = 1.2 \times 10^6$

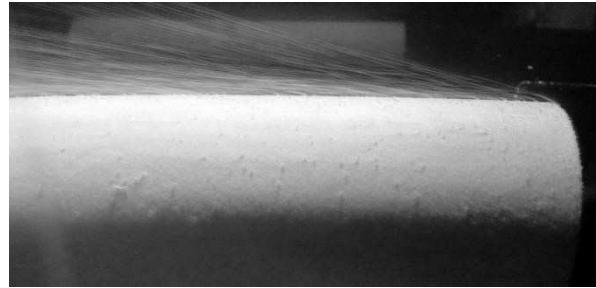
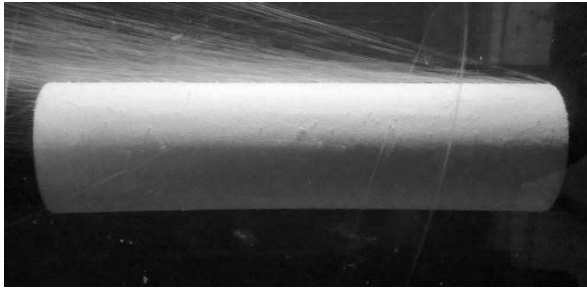


$Q_a = 0.25 \text{ L/min. } Re = 1.5 \times 10^6$

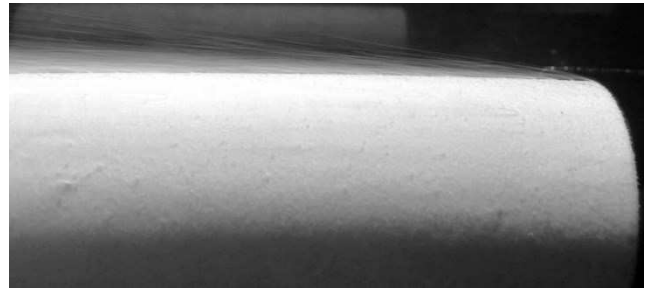
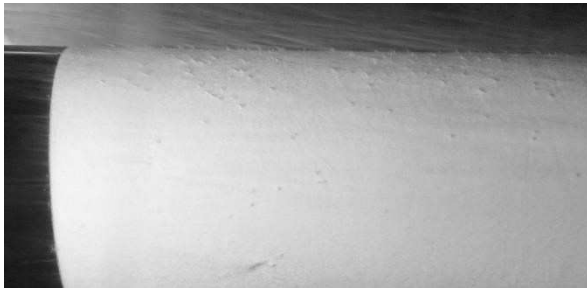
C.1.3 $Q_a = 0.5$ L/min



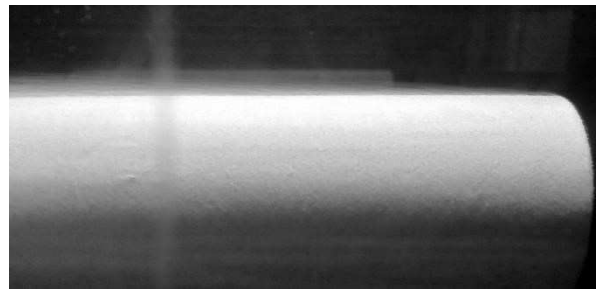
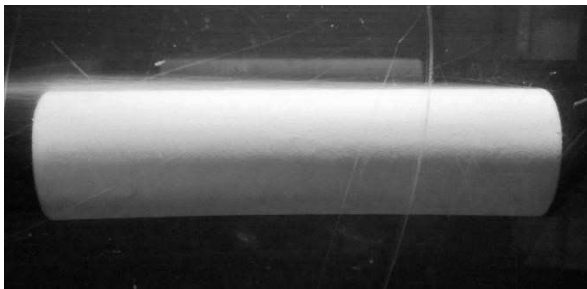
$Q_a = 0.5$ L/min. Static water



$Q_a = 0.5$ L/min. $Re = 5.0 \times 10^5$

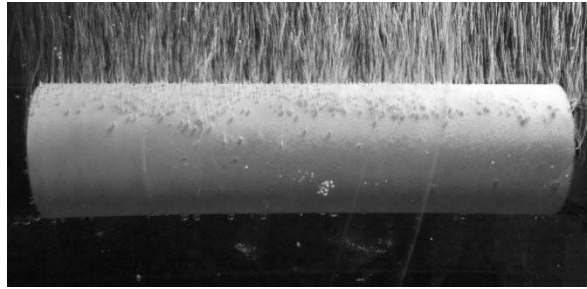


$Q_a = 0.5$ L/min. $Re = 7.0 \times 10^5$

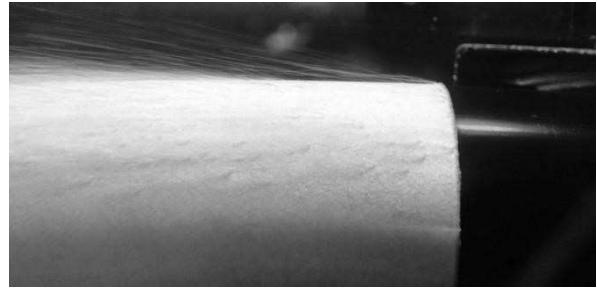
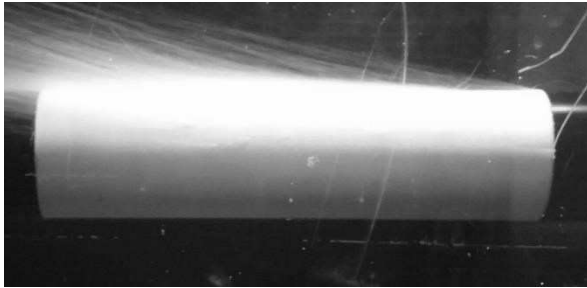


$Q_a = 0.5$ L/min. $Re = 1.5 \times 10^6$

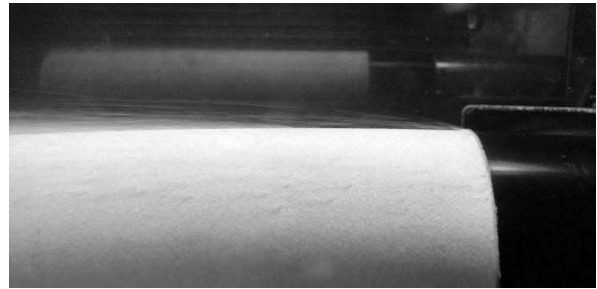
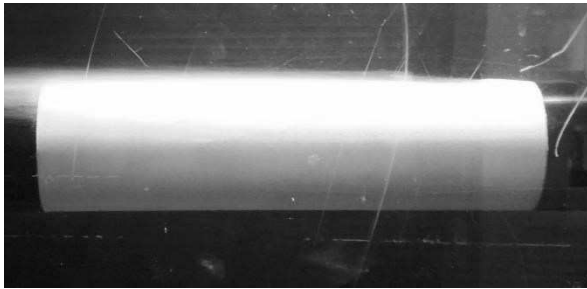
C.1.4 $Q_a = 1 \text{ L/min}$



$Q_a = 1 \text{ L/min}$. Static water

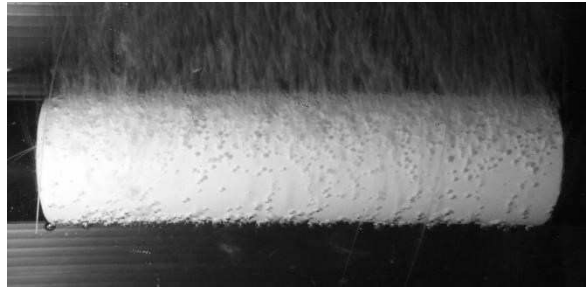


$Q_a = 1 \text{ L/min}$. $Re = 5.0 \times 10^5$

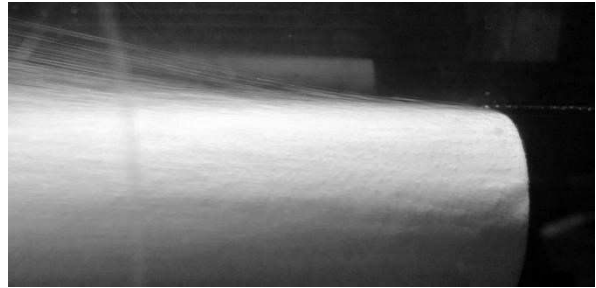
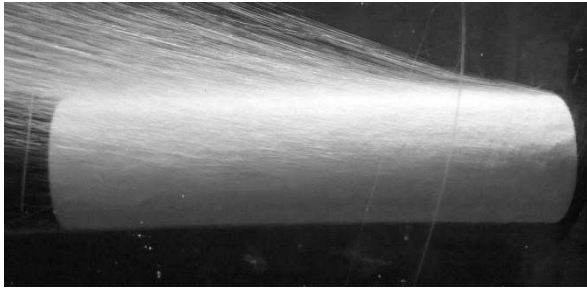


$Q_a = 1 \text{ L/min}$. $Re = 1.5 \times 10^6$

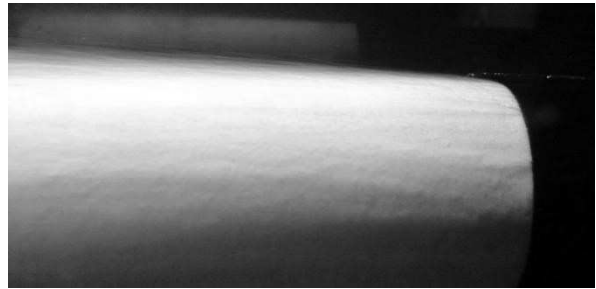
C.1.5 $Q_a = 5 \text{ L/min}$



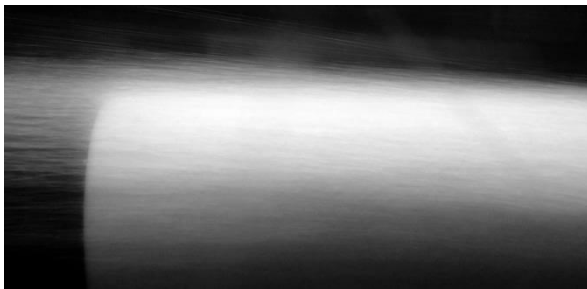
$Q_a = 5 \text{ L/min}$. Static water



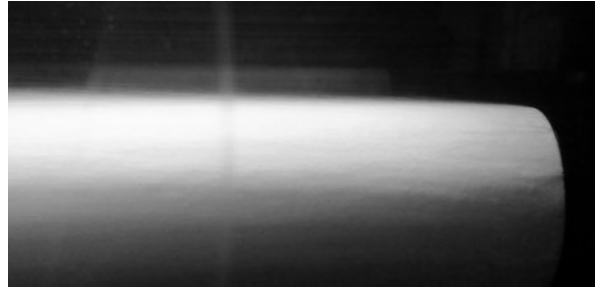
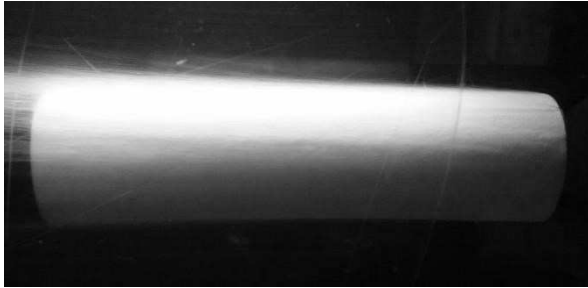
$Q_a = 5 \text{ L/min}$. $Re = 5.0 \times 10^5$



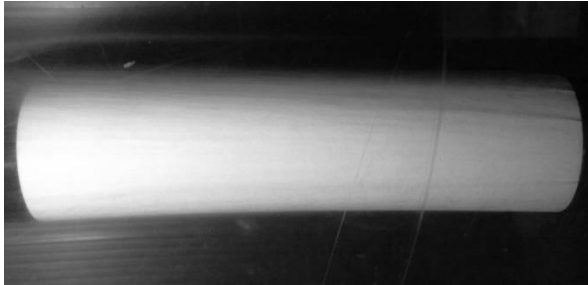
$Q_a = 5 \text{ L/min}$. $Re = 7.0 \times 10^5$



$Q_a = 5 \text{ L/min}$. $Re = 1.0 \times 10^6$



$Q_a = 5 \text{ L/min. } Re = 1.2 \times 10^6$



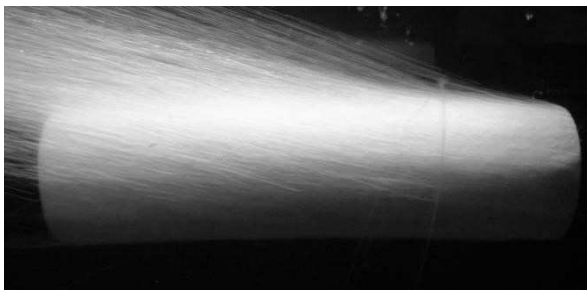
$Q_a = 5 \text{ L/min. } Re = 1.5 \times 10^6$

C.2 High air injection rates (HAIR)

C.2.1 $Q_a = 10$ L/min



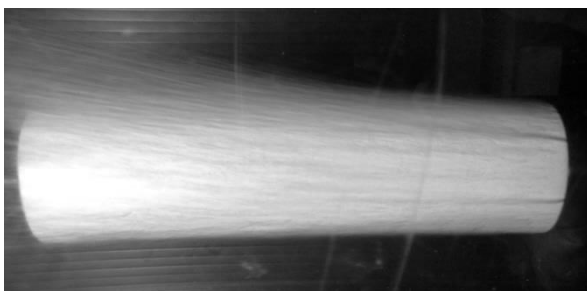
$Q_a = 10$ L/min. Static water



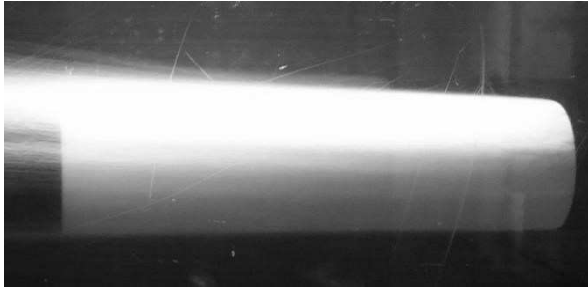
$Q_a = 10$ L/min. $Re = 5.0 \times 10^5$



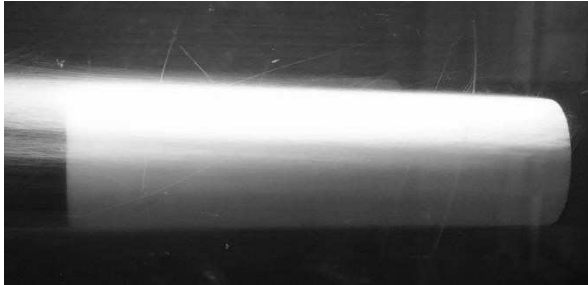
$Q_a = 10$ L/min. $Re = 7.0 \times 10^5$



$Q_a = 10$ L/min. $Re = 1.0 \times 10^6$



$Q_a = 10 \text{ L/min. } Re = 1.2 \times 10^6$



$Q_a = 10 \text{ L/min. } Re = 1.5 \times 10^6$

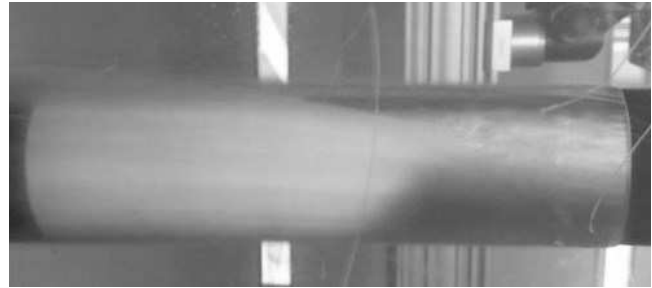
C.2.2 $Q_a = 15$ L/min



$Q_a = 15$ L/min. Static water

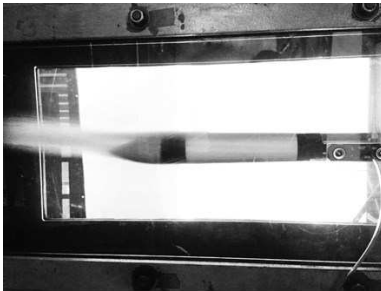


$Q_a = 15$ L/min. $Re = 5.0 \times 10^5$

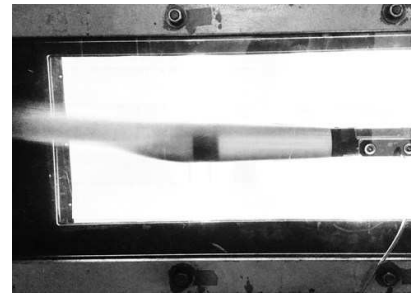


c) $Q_a = 15$ L/min. $Re = 1.5 \times 10^6$

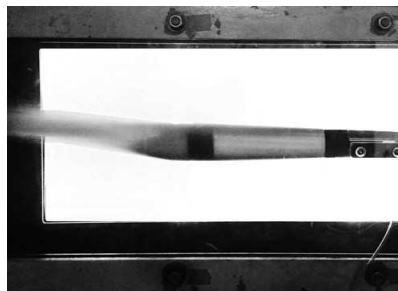
C.2.3 $Q_a = 25$ L/min, 35 L/min and 45 L/min



$Q_a = 25$ L/min. $Re = 1.5 \times 10^6$



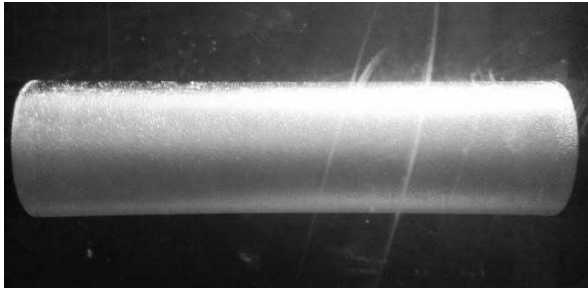
a) $Q_a = 35$ L/min. $Re = 1.5 \times 10^6$



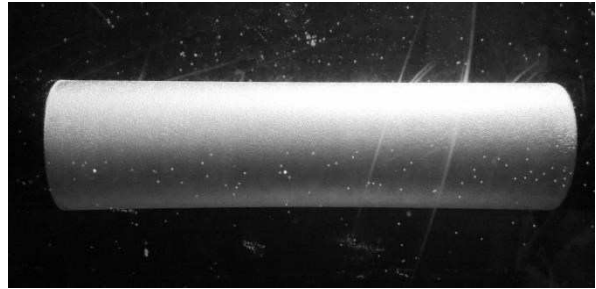
$Q_a = 45$ L/min. $Re = 1.5 \times 10^6$

C.3 Porous superhydrophobic surface (SHS)

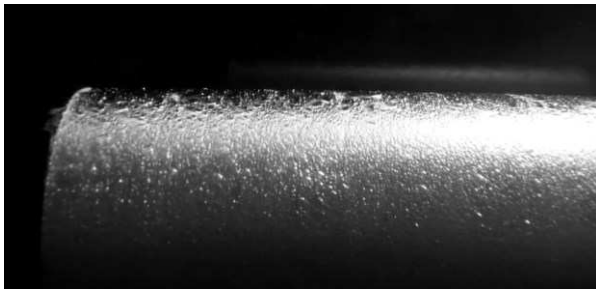
C.3.1 $Q_a = 0$ L/min



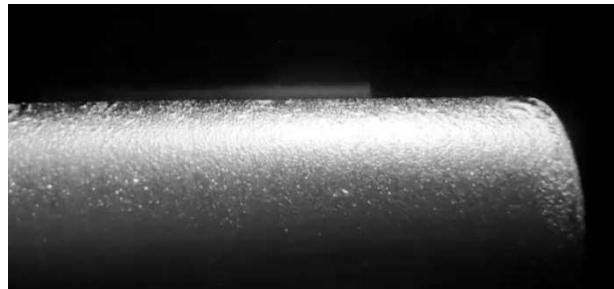
Beginning of the test. No air injection. Static water.



End of the test. No air injection. Static water.

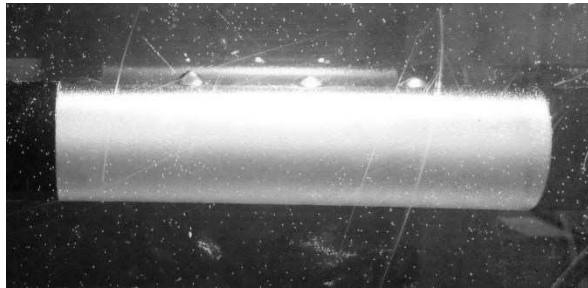


Back section of the module. No air injection.
 $Re = 1.5 \times 10^6$.

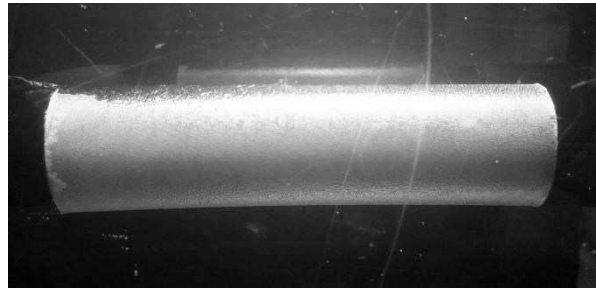


Front section of the module. No air injection.
 $Re = 1.5 \times 10^6$.

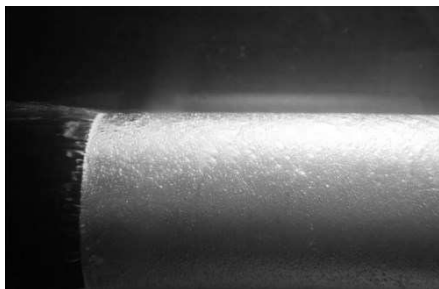
C.3.2 $Q_a = 0.15$ L/min



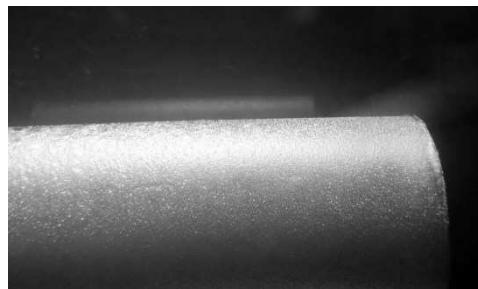
Beginning of the test. $Q_a = 0.15$ L/min. Static water.



$Q_a = 0.15$ L/min. $Re = 5 \times 10^5$

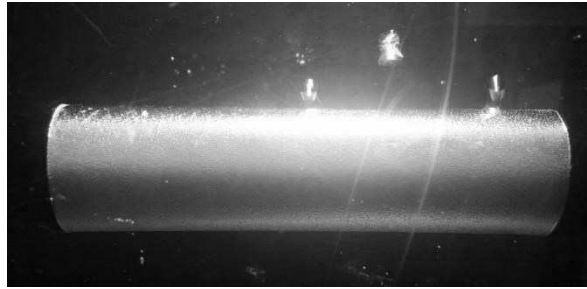


Back section of the module. $Q_a = 0.25$ L/min.
 $Re = 1.5 \times 10^6$

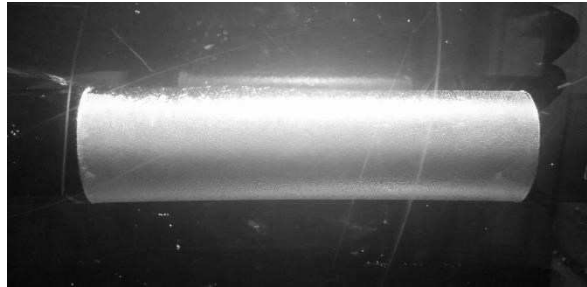


Front section of the module. $Q_a = 0.25$ L/min.
 $Re = 1.5 \times 10^6$

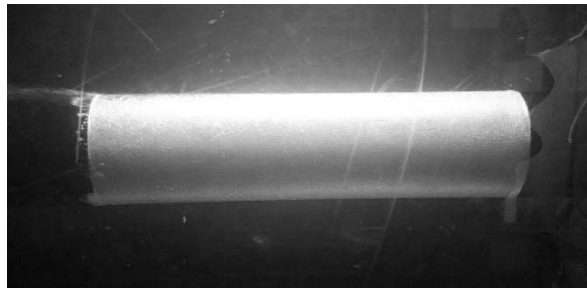
C.3.3 $Q_a = 0.25$ L/min



Beginning of the test. $Q_a = 0.25$ L/min. Static water.



$Q_a = 0.25$ L/min. $Re = 5 \times 10^5$.



$Q_a = 0.25$ L/min. $Re = 1.5 \times 10^6$.

Appendix D. Permissions for Use of Figures

1. Figure 2.4

13/12/2017

RightsLink Printable License

CAMBRIDGE UNIVERSITY PRESS LICENSE TERMS AND CONDITIONS

Dec 13, 2017

This Agreement between University of ALberta -- Desiree Reholon Inojosa ("You") and Cambridge University Press ("Cambridge University Press") consists of your license details and the terms and conditions provided by Cambridge University Press and Copyright Clearance Center.

License Number	4247071406156
License date	Dec 13, 2017
Licensed Content Publisher	Cambridge University Press
Licensed Content Publication	The Journal of Fluid Mechanics
Licensed Content Title	The structure of turbulent boundary layers
Licensed Content Author	S. J. Kline, W. C. Reynolds, F. A. Schraub, P. W. Runstadler
Licensed Content Date	Mar 28, 2006
Licensed Content Volume	30
Licensed Content Issue	4
Start page	741
End page	773
Type of Use	Dissertation/Thesis
Requestor type	Not-for-profit
Portion	Text extract
Number of pages requested	1
Order reference number	
Territory for reuse	World
Title of your thesis / dissertation	Application of passive drag reduction techniques on a scaled-down underwater vehicle
Expected completion date	Jan 2018
Estimated size(pages)	200
Requestor Location	University of ALberta 10150 83 Av NW Edmonton, AB T6E 2C4 Canada Attn: Desiree Reholon
Publisher Tax ID	123258667RT0001
Billing Type	Invoice
Billing Address	University of ALberta 10150 83 Av NW Edmonton, AB T6E 2C4 Canada Attn: Desiree Reholon

2. Figure 2.6

13/12/2017 Rightslink® by Copyright Clearance Center

 **Copyright Clearance Center**

 **RightsLink®**

[Home](#) [Account Info](#) [Help](#) 

 **ANNUAL REVIEWS**

Title: Coherent Motions in the Turbulent Boundary Layer

Author: S K Robinson

Publication: Annual Review of Fluid Mechanics

Publisher: Annual Reviews

Date: Jan 1, 1991

Copyright © 1991, Annual Reviews

Logged in as:
Desiree Reholon Inojosa
University of Alberta
Account #: 3001228269

[LOGOUT](#)

Permission Not Required

Material may be republished in a thesis / dissertation without obtaining additional permission from Annual Reviews, providing that the author and the original source of publication are fully acknowledged.

[BACK](#) [CLOSE WINDOW](#)

Copyright © 2017 [Copyright Clearance Center, Inc.](#) All Rights Reserved. [Privacy statement.](#) [Terms and Conditions.](#) Comments? We would like to hear from you. E-mail us at customercare@copyright.com

3. Figure 2.10

Confirmation Number: 11686717
Order Date: 12/12/2017

If you paid by credit card, your order will be finalized and your card will be charged within 24 hours. If you choose to be invoiced, you can change or cancel your order until the invoice is generated.

Payment Information

Desiree Reholon Inojosa
University of ALberta
reholoni@ualberta.ca
+1 (780) 966-3236
Payment Method: n/a

Order Details

Journal of Physics : Condensed Matter

Order detail ID: 70850464
Order License Id: 4246611204247
ISSN: 0953-8984
Publication Type: Journal
Volume:
Issue:
Start page:
Publisher: IOP Publishing

Permission Status:  **Granted**
Permission type: Republish or display content
Type of use: Thesis/Dissertation

Requestor type Academic institution

Format Print, Electronic

Portion image/photo

Number of images/photos requested 1

The requesting person/organization Desiree Reholon / University of Alberta

Title or numeric reference of the portion(s) Application of passive drag reduction techniques on a scaled-down underwater vehicle

Title of the article or chapter the portion is from Wetting, roughness and flow boundary conditions

12/12/2017

Copyright Clearance Center

Editor of portion(s)	N/A
Author of portion(s)	Olga I Vinogradova and Aleksey V Belyaev
Volume of serial or monograph	Volume 23, Number 18
Issue, if republishing an article from a serial	N/A
Page range of portion	15
Publication date of portion	20 April 2011
Rights for	Main product
Duration of use	Life of current edition
Creation of copies for the disabled	no
With minor editing privileges	no
For distribution to	Worldwide
In the following language(s)	Original language of publication
With incidental promotional use	no
Lifetime unit quantity of new product	Up to 499
Title	Application of passive drag reduction techniques on a scaled-down underwater vehicle
Instructor name	n/a
Institution name	n/a
Expected presentation date	Jan 2018

Note: This item will be invoiced or charged separately through CCC's [RightsLink](#) service. [More info](#)

\$ 0.00

4. Figure 2.14

12/12/2017

RightsLink Printable License

**SPRINGER LICENSE
TERMS AND CONDITIONS**


Dec 12, 2017

This Agreement between University of ALberta -- Desiree Reholon Inojosa ("You") and Springer ("Springer") consists of your license details and the terms and conditions provided by Springer and Copyright Clearance Center.


License Number	4246600965235
License date	Dec 12, 2017
Licensed Content Publisher	Springer
Licensed Content Publication	Experiments in Fluids
Licensed Content Title	Frictional drag reduction by bubble injection
Licensed Content Author	Yuichi Murai
Licensed Content Date	Jan 1, 2014
Licensed Content Volume	55
Licensed Content Issue	7
Type of Use	Thesis/Dissertation
Portion	Figures/tables/illustrations
Number of figures/tables/illustrations	1
Author of this Springer article	No
Order reference number	
Original figure numbers	Figure 4
Title of your thesis / dissertation	Application of passive drag reduction techniques on a scaled-down underwater vehicle
Expected completion date	Jan 2018
Estimated size(pages)	200
Requestor Location	University of ALberta 10150 83 Av NW Edmonton, AB T6E 2C4 Canada Attn: Desiree Reholon
Billing Type	Invoice
Billing Address	University of ALberta 10150 83 Av NW Edmonton, AB T6E 2C4 Canada Attn: Desiree Reholon
Total	0.00 CAD
Terms and Conditions	


5. Figure 2.15

12/12/2017 Rightslink® by Copyright Clearance Center

 **Copyright Clearance Center**

RightsLink®

[Home](#) [Account Info](#) [Help](#) 

 **ANNUAL REVIEWS**

Title: Friction Drag Reduction of External Flows with Bubble and Gas Injection

Author: Steven L. Ceccio

Publication: Annual Review of Fluid Mechanics

Publisher: Annual Reviews

Date: Jan 1, 2010

Copyright © 2010, Annual Reviews

Logged in as:
Desiree Reholon Inojosa
University of Alberta

[LOGOUT](#)

Permission Not Required

Material may be republished in a thesis / dissertation without obtaining additional permission from Annual Reviews, providing that the author and the original source of publication are fully acknowledged.

[BACK](#) [CLOSE WINDOW](#)

Copyright © 2017 [Copyright Clearance Center, Inc.](#) All Rights Reserved. [Privacy statement](#). [Terms and Conditions](#).
Comments? We would like to hear from you. E-mail us at customer-care@copyright.com

6. Figure 2.17

12/12/2017

RightsLink Printable License

**CAMBRIDGE UNIVERSITY PRESS LICENSE
TERMS AND CONDITIONS**

Dec 12, 2017

This Agreement between University of ALberta -- Desiree Reholon Inojosa ("You") and Cambridge University Press ("Cambridge University Press") consists of your license details and the terms and conditions provided by Cambridge University Press and Copyright Clearance Center.

License Number	4246601447243
License date	Dec 12, 2017
Licensed Content Publisher	Cambridge University Press
Licensed Content Publication	The Journal of Fluid Mechanics
Licensed Content Title	Experiments on drag-reducing surfaces and their optimization with an adjustable geometry
Licensed Content Author	D. W. BECHERT, M. BRUSE, W. HAGE, J. G. T. VAN DER HOEVEN, G. HOPPE
Licensed Content Date	May 10, 1997
Licensed Content Volume	338
Licensed Content Issue	undefined
Start page	59
End page	87
Type of Use	Dissertation/Thesis
Requestor type	Not-for-profit
Portion	Text extract
Number of pages requested	1
Order reference number	
Territory for reuse	World
Title of your thesis / dissertation	Application of passive drag reduction techniques on a scaled-down underwater vehicle
Expected completion date	Jan 2018
Estimated size(pages)	200
Requestor Location	University of ALberta 10150 83 Av NW
	Edmonton, AB T6E 2C4 Canada Attn: Desiree Reholon
Publisher Tax ID	123258667RT0001
Billing Type	Invoice
Billing Address	University of ALberta 10150 83 Av NW

Edmonton, AB T6E 2C4

7. Figure 2.20

12/12/2017

RightsLink Printable License

**SPRINGER LICENSE
TERMS AND CONDITIONS**

Dec 12, 2017

This Agreement between University of ALberta -- Desiree Reholon Inojosa ("You") and Springer ("Springer") consists of your license details and the terms and conditions provided by Springer and Copyright Clearance Center.

License Number	4246610250056
License date	Dec 12, 2017
Licensed Content Publisher	Springer
Licensed Content Publication	Springer eBook
Licensed Content Title	Physical and technical background
Licensed Content Author	Markus Raffel, Christan E. Willert, Jürgen Kompenhans
Licensed Content Date	Jan 1, 1998
Type of Use	Thesis/Dissertation
Portion	Figures/tables/illustrations
Number of figures/tables/illustrations	1
Author of this Springer article	No
Order reference number	
Original figure numbers	Figure 2.4
Title of your thesis / dissertation	Application of passive drag reduction techniques on a scaled-down underwater vehicle
Expected completion date	Jan 2018
Estimated size(pages)	200
Requestor Location	University of ALberta 10150 83 Av NW Edmonton, AB T6E 2C4 Canada Attn: Desiree Reholon
Billing Type	Invoice
Billing Address	University of ALberta 10150 83 Av NW Edmonton, AB T6E 2C4 Canada Attn: Desiree Reholon
Total	0.00 USD
Terms and Conditions	